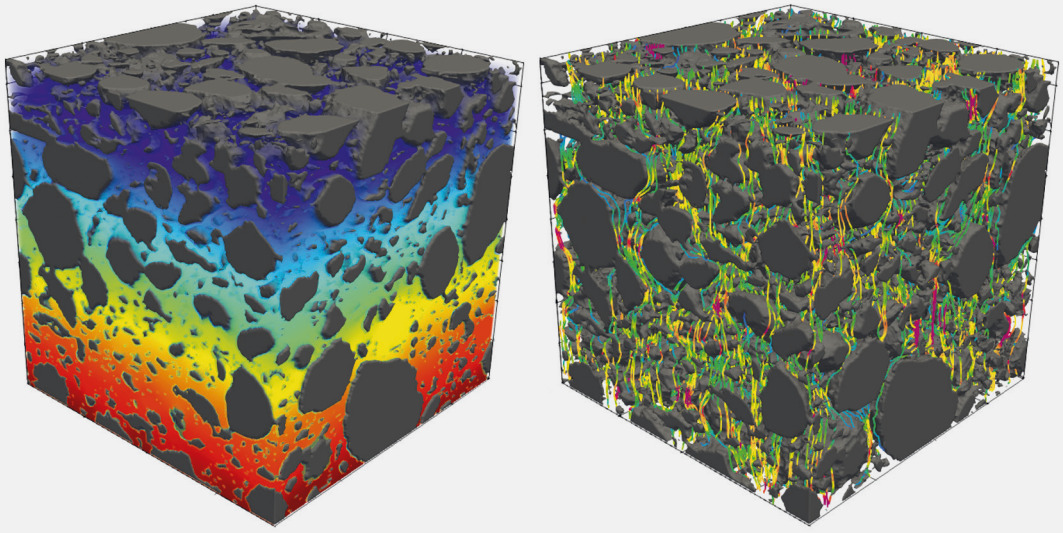

Pore-scale reactive transport modeling in cementitious materials: Development and application of a high-performance computing code based on the Lattice-Boltzmann method

Stephan Rohmen

Energie & Umwelt / Energy & Environment
Band / Volume 659
ISBN 978-3-95806-812-4

Mitglied der Helmholtz-Gemeinschaft

JÜLICH
Forschungszentrum

Schriften des Forschungszentrums Jülich
Reihe Energie & Umwelt / Energy & Environment Band / Volume 659

Forschungszentrum Jülich GmbH
Institut für Energie- und Klimaforschung (IEK)
Nukleare Entsorgung (IEK-6)

Pore-scale reactive transport modeling in cementitious materials: Development and application of a high-performance computing code based on the Lattice-Boltzmann method

Stephan Rohmen

Schriften des Forschungszentrums Jülich
Reihe Energie & Umwelt / Energy & Environment Band / Volume 659

ISSN 1866-1793 ISBN 978-3-95806-812-4

Bibliografische Information der Deutschen Nationalbibliothek.
Die Deutsche Nationalbibliothek verzeichnet diese Publikation in der
Deutschen Nationalbibliografie; detaillierte Bibliografische Daten
sind im Internet über http://dnb.d-nb.de abrufbar.

Herausgeber und Vertrieb:	Forschungszentrum Jülich GmbH Zentralbibliothek, Verlag 52425 Jülich Tel.: +49 2461 61-5368 Fax: +49 2461 61-6103 zb-publikation@fz-juelich.de www.fz-juelich.de/zb
Umschlaggestaltung:	Grafische Medien, Forschungszentrum Jülich GmbH
Druck:	Grafische Medien, Forschungszentrum Jülich GmbH
Copyright:	Forschungszentrum Jülich 2025

Schriften des Forschungszentrums Jülich
Reihe Energie & Umwelt / Energy & Environment, Band / Volume 659

D 82 (Diss. RWTH Aachen University, 2024)

ISSN 1866-1793
ISBN 978-3-95806-812-4

Vollständig frei verfügbar über das Publikationsportal des Forschungszentrums Jülich (JuSER)
unter www.fz-juelich.de/zb/openaccess.

Abstract

The presence of cementitious materials in the modern world is ubiquitous, since concrete is one of the most important construction materials in civil engineering. Cementitious materials are also commonly used in nuclear waste management, e.g. for solidification of radioactive wastes, or as construction and backfill material in deep geological repositories for radioactive wastes. In this context, cementitious materials provide barrier functions to reduce the migration of radionuclides in the repository near field. However, despite the vast application of cementitious materials in this context, the long-term evolution of several material properties is not yet fully understood, in particular the changes in fluid and solute transport properties induced by long-term alteration due to interaction of cementitious materials with groundwaters, taking into account the time scales relevant for nuclear waste disposal. Since alterations of the microstructure have significant effect on macroscopic transport properties of the materials, this work focuses on the improvement of the quantitative description of the alteration of cementitious materials at the pore-scale.

Pore-scale reactive transport models are appealing techniques to analyze the alteration of phase assemblage, microstructure, and transport properties in cementitious materials, to get deeper insights into their long-term macroscopic evolution. In this work, a Lattice-Boltzmann based approach was used to simulate degradation and alteration of cementitious materials due to interaction with groundwater. A modular reactive transport toolbox deployable in high-performance computing (HPC) environments was developed by coupling a Lattice-Boltzmann transport code (Palabos) to a geochemical solver (PhreeqC), which can account for fluid-mineral interactions controlled by thermodynamics and reaction kinetics, in the sequential non-iterative approach (SNIA) fashion.

After extensive optimization and validation, the code named iPP (interface-Palabos-PhreeqC) was applied to simulate in particular the alteration/leaching of a bespoke low-pH cementitious material destined for application in a nuclear waste repository, amongst other test cases. Input data for the simulations such as the microstructures of the non-degraded materials were derived from synthetically generated microstructures and by developing a segmentation algorithm, subsequently applied to μ-XCT image data of hardened cement pastes.

In the application case, a granite groundwater was used as leaching solution, leading to decalcification of calcium-silicate-hydrates (CSH) in the simulations in agreement with results from experiments and observations from underground research laboratories.

Due to saturation of the granitic water with respect to calcite, the simulation results revealed calcite precipitation on the surface of the cementitious material, which resulted in a partial clogging of the system. For an improved description of the precipitation of solids, different model assumptions were implemented in the reactive transport code (e.g. assuming local equilibrium or taking into account classical nucleation theory and/or porosity-controlled solubility effects) and tested. The results of the leaching simulations were analyzed, for example, with respect to the resulting phase assemblages, porosity

profiles and mass balances. Furthermore, the effect of the alteration processes on the effective diffusivity of the degraded cementitious material was analyzed.

Pore-scale reactive transport models such as iPP provide the means to enhance the understanding of the impact of long-term alteration processes (e.g. leaching by groundwater, carbonation, reactions at clay/cement interfaces, etc.) on the transport properties of cementitious barrier materials in nuclear waste repositories (e.g. with respect to solute transport/radionuclide migration, or gas transport, etc.) and can thus be employed as process models in support of the safety case. Moreover, an enhanced understanding of the evolution of transport properties on the pore-scale might facilitate the selection of optimized cementitious materials for specific purposes in repository design.

Zusammenfassung

Da Beton eines der wichtigsten Materialien im Bauwesen ist, treten zementbasierter Materialien in der modernen Welt allgegenwärtig auf. Darüber hinaus finden zementhaltige Materialien häufig Anwendung in der nuklearen Abfallentsorgung, zum Beispiel zur Verfestigung radioaktiver Abfälle oder als Bau- und Verfüllmaterial in Endlagern für radioaktive Abfälle. In diesem Zusammenhang übernehmen zementhaltige Materialien Barrierefunktionen, um die Migration von Radionukliden im Nahfeld des Endlagers zu reduzieren. Trotz der umfangreichen Anwendung zementhaltiger Materialien ist die langfristige Entwicklung mehrerer Materialeigenschaften jedoch noch nicht vollständig erforscht. Die Fragestellungen umfassen u.a. Veränderungen von Transporteigenschaften aufgrund von Degradation oder anderer Veränderungen des Materials. Die Transporteigenschaften umfassen zum Beispiel die Strömungsmechanik von Fluiden und die Diffusivität von gelösten Stoffen in diesen Materialien. Insbesondere die Erforschung von langfristigen Änderungen von Transporteigenschaften durch Wechselwirkungen zementhaltiger Materialien mit Grundwasser, unter Berücksichtigung der für die nukleare Abfallentsorgung relevanten Zeitskalen, sind von Interesse für die Endlagerforschung. Da Veränderungen der Mikrostruktur erhebliche Auswirkungen auf die makroskopischen Transporteigenschaften der Materialien haben, konzentriert sich diese Arbeit auf die Verbesserung der quantitativen Beschreibung der Veränderungen zementhaltiger Materialien auf dem Porenmaßstab.

Reaktive Transportmodelle im Porenmaßstab sind geeignete Techniken, um Veränderung der Phasenzusammensetzung, Mikrostruktur und Transporteigenschaften in zementhaltigen Materialien zu analysieren und um tiefere Einblicke in deren langfristige makroskopische Entwicklung zu erhalten. In dieser Arbeit wurde ein Lattice-Boltzmann basierter Ansatz verwendet, um die Degradation und Veränderung zementhaltiger Materialien aufgrund der Wechselwirkung mit Grundwasser zu simulieren. Durch die Kopplung eines Transportsoftwaremoduls, welches zur Transportsimulation von gelösten Stoffen verwendet wird, mit einem geochemischen Lösungsverfahren wurde eine modulare Software entwickelt, welche zur Simulation von reaktivem Stofftransport eingesetzt werden kann. Der Transport von gelösten Stoffen wurde auf Basis der Lattice-Boltzmann Methode implementiert und basiert auf dem Softwareframework Palabos, während zur thermodynamischen Modellierung der geochemische Gleichungslöser PhreeqC zum Einsatz kommt. In dieser Konstellation ist der geochemische Gleichungslöser in der Lage, die durch Thermodynamik und Reaktionskinetik getriebenen Fluid-Mineral-Wechselwirkungen zu berechnen. Die in dieser Arbeit entwickelte Kopplungssoftware berücksichtigt Fluid-Mineral-Wechselwirkungen mittels eines sequenziell nicht-iterativen Ansatzes (SNIA). Die Software wurde konzipiert um auf Hochleistungsrechnern (HPC) einsetzbar zu sein.

Nach umfangreicher Optimierung und Validierung wurde der Code mit dem Namen iPP (interface-Palabos-PhreeqC) eingesetzt um insbesondere die Veränderung und Auslaugung eines niedrig pH-Wert Zements zu simulieren. Dieser Zement ist für die Verwendung in einem Endlager für nukleare Abfälle bestimmt. Eingabedaten für die Simulationen, wie etwa die Mikrostrukturen des eingesetzten Zements, wurden zum einen aus synthetisch erzeugten Mikrostrukturen und zum anderen aus μ-CT Bilddaten gewonnen. Zur Gewinnung der Mikrostrukturinformation aus den Bilddaten wurde ein in dieser Arbeit neu entwickelter Segmentierungsalgorithmus angewendet.

In einem Anwendungsfall wurde ein Grundwasser aus Granitgestein als Auslaugungslösung verwendet, was zur Dekalzifizierung des Zements und insbesondere der Calcium-Silikat-Hydrats (CSH) Phase führte. Die Ergebnisse der Simulationen sind in Übereinstimmung mit Ergebnissen aus Experimenten und Beobachtungen aus unterirdischen Forschungslaboren.

Aufgrund der Sättigung des Granitwassers im Bezug auf Calcit, zeigten die Simulationsergebnisse eine Ausfällung von Calcit auf der Oberfläche des zementhaltigen Materials, was zu einer partiellen Abdichtung des Systems führte. Für eine verbesserte Beschreibung der Ausfällung von Feststoffen wurden verschiedene Modellannahmen im reaktiven Transportmodell implementiert und getestet. Diese umfassen z.B. die Annahme eines lokalen Gleichgewichts oder die Berücksichtigung der klassischen Nukleationstheorie und/oder der Einbeziehung von porositätskontrollierten Löslichkeitseffekten. Die Ergebnisse der Auslaugungssimulationen wurden hinsichtlich der resultierenden Phasenzusammensetzung, Porositätsverteilung und Massenbilanzen analysiert. Darüber hinaus wurde der Einfluss der Veränderungsprozesse auf die effektive Diffusivität von gelösten Stoffen innerhalb des degradierten Materials analysiert.

Porenmaßstabsmodelle für reaktiven Stofftransport wie iPP bieten die Möglichkeit, das Verständnis für den Einfluss von langfristigen Veränderungsprozessen (z.B. Auswaschung durch Grundwasser, Karbonatisierung, Reaktionen an Ton/Zement-Grenzflächen) auf die Transporteigenschaften von zementhaltigen Barrierematerialien in nuklearen Endlagern zu verbessern. Insbesondere im Hinblick auf den Transport von Fluiden, Radionuklidmigration oder Gastransport ist ein Erkenntnisgewinn von belang. Solche Modelle können daher als Prozessmodelle zur Unterstützung des Sicherheitskonzepts eingesetzt werden. Darüber hinaus könnte ein verbessertes Verständnis zur Evolution der Transporteigenschaften auf dem Porenmaßstab die Auswahl optimierter zementhaltiger Materialien für spezifische Zwecke im Design des Lagers erleichtern.

Contents

Part I

Introduction and scientific background

1 Introduction

1.1 Motivation

In our days, concrete is the most commonly used engineering material in the world [Pop92, pp.1]. In 2005 it was estimated that worldwide 11 billion tonnes of concrete are consumed per year [Meh05, p.3]. With respect to this tremendous usage, some authors are even naming the current mankind's epoch as the *concrete age*, as reference to terms as *iron age* [Emi17].

One reason for this widespread use is that concrete is quite resistant to water, it can easily be formed into arbitrary shapes during construction, it is cheap to produce and constituents are available in most countries [Meh05, pp.4]. For instance, it would be unfeasible to construct massively large structures as modern hydroelectricity producing dams with wood or steel only. Although cementitious materials have been used for several thousands of years, the knowledge about certain material properties is still incomplete. Moreover, most of these properties were derived in empirical ways during the time of usage.

In the field of nuclear waste management, cementitious materials are also commonly used. Besides the usage of concrete as one of the construction materials of a final repository, which serves for example as supporting structure of the host rock, cement is used as solidification/fixation agent of radioactive wastes, and in backfill construction materials. Furthermore, it is deemed to play an important role in barrier materials [Nag02]. Thus, the effect of cement influences the long-term safety character of a final repository significantly.

The usage of cement and concrete in particular in the field of nuclear waste management, e.g. for waste immobilization/solidification or as backfill and structural support in waste repositories stems not only from the general beneficial properties mentioned earlier. It was shown that hydrated cement has retention properties for certain safety relevant radionuclides. Some of these effects are due to the high pH in the pore water, which is buffered by hydrated cement phases and the presence of dissolved alkalis. A high pH essentially limits the solubility of many metal ions. Moreover, due to sorption of radionuclides on certain cement hydrates, further retention mechanisms are available [Lan18,Och16].

However, cementitious materials have a limited service life. In particular, they are incompatible with the environment and degrade over the long-time scales relevant for nuclear waste management. Several processes can lead to degradation of the matrix of cementitious materials. For example, concrete can experience physico-chemical alteration, degradation and weathering due to leaching with water with different composition.

These effects can be enhanced by specific aggressive species (e.g. Mg^{2+}, $SO_4{}^{2-}$) contained in the attacking medium. The terms used for these degradation effects are for example *calcium leaching*, *carbonation*, *sulfate attack* and *chloride attack*. These degradation effects alter the phase assemblage of the hydrated cement matrix and induce changes in the pore structure. Consequently, the diffusive, hydraulic and mechanical properties of cementitious material can be severely affected (e.g. [Ben92,Sto09]).

Although harnend cement paste (HCP) and concrete are by definition porous media, their diffusivity is rather limited compared to other porous materials typically found in geosciences. However, in the long term even small diffusivity can lead to significant transport of solutes and radionuclides in the near field of a final repository. Therefore, comprehensive knowledge about the evolution of cementitious materials, e.g. with respect to mineralogy and transport parameters, is mandatory to predict their long-term behavior of concrete structures during and after weathering. Further knowledge in the field of cement degradation mechanisms and interaction with different host rocks can therefore lead to a better understanding of repository evolution and help to build confidence in safety assessments. Modeling in this field of research is of particular importance since due to the long time scales of final waste repository services data cannot be gained from experiments alone.

In the line of addressing key issues for long-term safety related properties of cement based materials in nuclear waste disposal applications the CEBAMA project was initiated. Objectives of the CEBAMA project was to support implementations of geological disposal concepts. The aim was to develop a better understanding of the connection between porosities, transport processes and interaction between cement based materials and engineered and natural barriers of repositories [Dur20]. Most of the developments in this work were conducted in the framework of the CEBAMA project which was funded by the European Union's Horizon 2020 Framework Programme for Research and Innovation. Accordingly, there was an exchange of data among project partners participating in the CEBAMA project. Especially experiments which outcomes are providing image data and performing degradation experiments were of interest for the modeling studies in this work.

In contrast to reactive transport simulations at continuum scale, this thesis deals with physical and chemical processes at the pore-scale of cementitious materials. Effectively, the resulting conclusions from pore-scale simulations can serve as input and give insights about constitutive relations between key variables of macroscopic models, e.g. porosity and diffusivity. To this end, this thesis is dedicated to the modeling of reactive transport processes at the pore-scale. Pore-scale modeling is an emerging field of application next to classical continuum reactive transport models, which are rather applied to model processes at the macro-scale [Ste05a]. It has been shown that he Lattice-Boltzmann method (LBM) is a promising approach to tackle pore-scale transport processes. By using a reaction term within the context of the LBM, pore-scale reactive transport processes can be simulated [Kan06].

Although in literature there are some reactive transport models based on the LBM described (e.g. [Kan06,Pat18b,Yoo15]), the implementations are either not publicly available or have limitations in terms of capabilities and/or computational performance

and scalability. Most of the authors report implementations with simplified geochemical coupling, i.e. limited types of reacting species and types of reactions (e.g. [Kan06]). On the other hand, there are couplings with versatile geochemical solvers like PhreeqC (e.g. [Pat18b]) but have not high performance capabilities to scale on high performance cluster systems. Effectively, the applications were limited to simplified chemical systems and/or needed workarounds by using pre-computed look-up tables.

This study aims to push the boundary of these limitations by developing a new coupling code which can be applied in a flexible way. The coupling should contain the relevant physico-chemical models in pore-scale to be applied on cementitious systems. Moreover, the developed models are intended to be applied to simulate certain leaching scenarios with groundwaters in order to assess the influence of different model assumptions.

1.2 Aims of this work

A sophisticated reactive transport code is intended to be developed based on a coupling between an implementation of the Lattice-Boltzmann method for flow and solute transport and a geochemical simulator. The newly developed code should serve as a tool to tackle computationally expensive simulations at the pore-scale in cementitious systems. In order to solve computationally demanding problems cluster computers are using *distributed memory models*. The particular simulation codes must apply certain programming paradigms to make use of such. The implementation needs to fulfill certain requirement in terms of algorithmic design and data structure layout. Naturally, the developed framework is generic and can be readily applied to other porous materials without loss of generality. Thus, the aims of this work can be summarized as follows:

- Implementation of a reactive transport code based on a coupling between and implementation of the Lattice-Boltzmann method and a geochemical simulator
- Development aiming to produce a high performance cluster capable code which is scalable to solve huge problems
- Development of a multi-scale approach to simulate different kinds of porous media
- Addition of needed physical extensions to the numerical framework to simulate relevant physical properties at pore-scale
- Showing the capabilities with benchmarks against analytical solutions and comparisons to other numerical simulation codes
- Derivation of hydrated cement paste microstructure (geometry) from imaging techniques as input for pore-scale simulations
- Application of the reactive transport code to cementitious systems

- Simulation of mineralogical changes in cementitious materials due to leaching with groundwater
- Determination of effective diffusion coefficients of fresh and degraded cement pastes

1.3 Outline of the thesis

This thesis is split into three parts. The first part presents a review of key concepts of cement chemistry and reactive transport models (chapters 2 and 3). The differences between various reactive transport models are outlined and the need to develop a new pore-scale reactive transport code is justified. Moreover, chapter 3 provides the theoretical background of the Lattice-Boltzmann method. In particular, an introduction of the Boltzmann equation is presented which is in the following derivations transformed to the Lattice-Boltzmann equation. Subsequently, it is shown how the continuum equations can be recovered from the statistical mechanics approaches. The resulting equations are the basis of the development of the pore-scale modeling software.

The second part describes the methodology followed in this study. A rather comprehensive software engineering work was performed to develop the necessary software tools to fulfill the requirements. However, due to the sake of brevity in this thesis, only a succinct overview can be given. Chapter 4 introduces the strategy for the coupling of a Lattice-Boltzmann code with a geochemical solver, which is used in this work as basis of the pore-scale reactive transport model. To this end, a general approach how to couple pore-scale transport models to chemical solver is outlined. Afterwards, the focus is on the specific implementation of the reactive transport code.

Chapter 5 introduces the theoretical background and implementations to extend the pore-scale model by classical nucleation theory (CNT) and by the porosity-controlled solubility (PCS) effect. Both effects are known to be relevant in pore-scale approaches and found their applications within the simulations conducted for this study.

Chapter 6 presents the work done for the verification and validation of the numerical tool and shows the performance of the newly developed code (scalability) and the approaches implemented. It is also focused on the numerical limitations of the techniques.

With the advent of the third and last part of this work, the focus of the developed models and codes moves from abstract ideas towards literally concrete applications. Chapter 7 is a compilation of preliminary steps required for conducting reactive transport simulations of HCP and other cementitious materials. A description how microstructures of HCP can be derived for once from a numerical model and on the other hand from experimental data is presented. In particular, the microstructure of a low-pH cement paste is derived with a newly developed image segmentation technique based on μ-XCT volume image data.

Chapter 8 contains several results of application cases performed with the newly developed reactive transport coupling code. The previously derived microstructures and models are used as simulation input for reactive transport simulations and to estimate the diffusivity of cementitious materials. The calculations simulate the leaching of a

hardened low-pH cement paste with granitic water. Subsequently, the resulting microstructures and phase compositions after leaching are used as input to determine the effective diffusivities of the altered samples. The results are presented as a function of the exposure time for each kind of leaching simulation.

Finally, chapter 9 presents the main conclusions of this study. A brief discussion about limitations found within this work and suggestions about ways forward in future work along this line are given.

2 Cementitious materials

2.1 Introduction and cement chemistry notation

Concrete, as one of the most important cementitious materials, is a multi-scale and multi-component material. Thus, the material itself is a mixture of different ingredients. Most importantly, concrete is composed of hydrated cement, which serves as binding agent, and coarse aggregates. Due to the usage of cement as binder, concrete belongs to a material class called *cementitious materials*. The class of cementitious materials does also contain materials as grout and mortar.

The purpose of this chapter is to give the reader more insights about the importance of research in this field and emphasize the complexity of the material at hand. In particular, the raw products of cement, formation of hydration products and their properties, and a brief overview about degradation and alteration processes is given.

Concrete contains coarse aggregate particles (10 mm to 100 mm), sand (0.01 mm to 2 mm) and cement binder which hardens over time when mixed with water. On the other hand, for mortar more fine aggregate particles are mixed. During curing of the concrete or mortar, the cement binder undergoes hydration processes resulting into a cement paste composed of several phases. As a result, the HCP will consist of diffusive and non-diffusive phases and the residual reaction water will be located in capillary pores. Cementitious materials contain a significant porosity, in particular at the microscopic scale [Jen08]. The different phases which hydrated cement is composed of and their interactions render it as a complex chemical, thermodynamic and microstructural system.

In cement chemistry, chemical sum formulas are often expressed in the oxide nomenclature. For example Ca_3SiO_5 is noted as $3\,CaO \cdot SiO_2$. However, the notation does not refer to any structural properties of the chemical compound, i.e. the compound does not exist in an oxide separated state. Furthermore, it is also common to abbreviate the oxides with a single letter, for example C for CaO [Tay97, pp.3]. Most common abbreviations are found in table 2.1.

2.2 Types of cement

Unhydrated cement in general is composed of clinker minerals and supplementary cementitious materials (SCMs). Clinker can be separated into four phases: Alite or tricalciumsilicate (C3S), belite or dicalciumsilicate (C2S), aluminate or tricalciumaluminate (C3A), and ferrite or calciumaluminoferrite (C4AF). In particular, the clinker phases are very reactive in contact with water. In order to produce Ordinary Portland Cement

Table 2.1: Abbreviations of oxides commonly used in the domain of cement chemistry.

Abbreviation	Oxide	Abbreviation	Oxide
C	CaO	S	SiO_2
A	Al_2O_3	F	Fe_2O_3
M	MgO	K	K_2O
$\bar{S}$	SO_3	N	Na_2O
T	TiO_2	P	P_2O_5
H	H_2O	$\bar{C}$	CO_2

(OPC), referred to as CEM-I, the clinker phases are mixed with a few percent of calcium sulfate (gypsum) to produce the cement powder. There are other types of cement called composite or blended cements which contain SCMs as blast furnace slag (BFS), silica fume (SF), fly ash (FA) and other materials which are involved in the hydration process [Tay97, pp.261].

There is a wide range of cement types. Table 2.2 lists cement types according to DIN EN 197-1 in a simplified overview. Although different cement types in this table have similar constituents, e.g. Portland slag cement (CEM-II) and blast furnace slag (CEM-III), the compositions are different, i.e. CEM-III has a higher content of BFS than CEM-II. According to the standardization, the mass fraction of SCMs in CEM-II cements is limited to 6 % to 35 %, while CEM-III, CEM-IV and CEM-V cements contain higher fractions of SCMs [Zem02].

Table 2.2: List of cement types according to DIN EN 197-1 and their constituents [Zem02]. Abbreviations used: blast furnace slag (BFS), silica fume (SF), pozzolan (P), fly ash (FA), limestone (LS).

Type	Name	clinker	BFS	SF	P	FA	shale	LS
CEM-I	Portland cement	✓						
CEM-II	Portland slag cement	✓	✓					
	Portland SF cement	✓		✓				
	Portland pozzolan cement	✓			✓			
	Portland FA cement	✓				✓		
	Portland shale cement	✓					✓	
	Portland LS cement	✓						✓
	Portland composite cement	✓	✓	✓	✓	✓	✓	✓
CEM-III	Blast furnace cement	✓	✓					
CEM-IV	Pozzolan cement	✓		✓	✓	✓		
CEM-V	Composite cement	✓	✓		✓	✓		

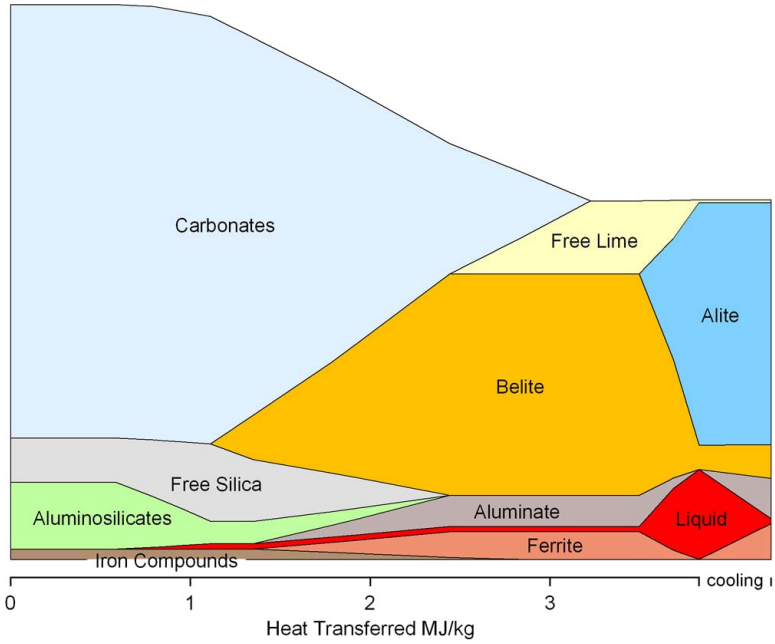

Figure 2.1: Schematic phase diagram of clinker produced as a function of mass normalized energy transferred into the material (`https://www.cementkilns.co.uk`, received at 15.01.2025).

2.3 Cement raw materials, hydration and microstructure

2.3.1 Clinker

In the manufacturing process to produce clinker, natural resources are used. The raw materials serve as sources for $CaCO_3$ (calcite), SiO_2 (quartz), aluminum oxide, and iron oxide. The raw materials usually used are limestone, quartz, and clays. Clinker is then produced by heating up a mixture of the raw materials to 1450 °C [Tay97, p. 56] which corresponds to 3.5 MJ kg^{-1} in figure 2.1. During the process of heating calcite is decomposed under release of CO_2, which leads to formation of CaO. At the same time the clay minerals decompose, too, and react with quartz and lime to form belite. Most of the excess CaO then reacts with a part of belite to form alite during further heating. During the cooling phase, the liquid melt crystallizes yielding mainly aluminate and ferrite. The resulting solidified melt is then ground and mixed with SCMs corresponding to the type of cement.

Depending on their sources, naturally occurring materials could incorporate certain amounts of impurities and have certain variances in their composition. The result-

ing clinker composition can thus vary considerably depending on the starting materials [Tay97, p.55]. Portland cement clinker are composed of 50 % to 70 % alite, 15 % to 30 % belite, 5 % to 10 % aluminate and 5 % to 15 % ferrite [Tay97, pp.1].

The complete ignition process is quite energy intensive and at the same time carbon dioxide is released into the atmosphere. The enthalpy of formation of one kg Portland cement clinker is about 1.76 MJ [Wor01]. Since this does not take into account the presence of water the real energy effort is much higher. Essentially, depending on the type of process and efficiency, an energy amount between 3.3 and 7.3 MJ must be expended [Meh05, p.205] [Wor01]. Stoichiometrically, the carbon dioxide footprint for Portland cement clinker is $0.5\,\mathrm{kgCO_2/kg}$. Approximately 50 % of carbon dioxide emissions originate from the chemical reactions occurring during the heating process while the rest is accounted for energy production. Estimated total yearly carbon emissions from cement production were reported to be 307×10^6 t for 1994, which were 5 % of the total emission world-wide [Wor01]. Since then, the absolute numbers have rather increased. In order to reduce the carbon dioxide footprint of cement production one approach is to produce blended cements which are incorporating supplementary cementitious materials. These numbers emphasize the importance for achieving deeper knowledge in the field of cement chemistry and understanding processes involved by adding SCMs to the cement mixture.

2.3.2 Hydration process

2.3.2.1 Overview

Bringing cement binder into contact with water immediately starts the process of hydration. During this process, clinker dissolves while various hydration products are formed. Each clinker mineral has different reactivity characteristics with respect to hydration with water, i.e. upon hydration alite and aluminate are consumed more rapidly than belite and ferrite [Tay97, pp. 1–3]. Some major hydration products of OPC (CEM-I) are:

- Calcium-silicate-hydrates (CSH)
- Portlandite ($Ca(OH)_2$)
- AFm (e.g. monosulfoaluminate, $Ca_4Al_2(OH)_{12}(SO_4) \cdot 6\,H_2O$)
- AFt (e.g. ettringite, $Ca_6Al_2(OH)_{12}(SO_4)_3 \cdot 26\,H_2O$)
- Others: e.g. hydrogarnet, strätlingite, hydrotalcite, etc.

The hydration process is sketched in figure 2.2. During hydration, porosity decreases as it is consequently filled by hydration products. In the early stages of hydration, AFt is formed, which is likely ettringite in gypsum containing OPC. Approximately at the same time, the CSH phase and portlandite start to form. After one day the AFt phase subsequently converts into an AFm phase while generating other more slowly forming hydration products (depicted as $C_4(A,H)H_{13}$). The hydration process is rather fast in

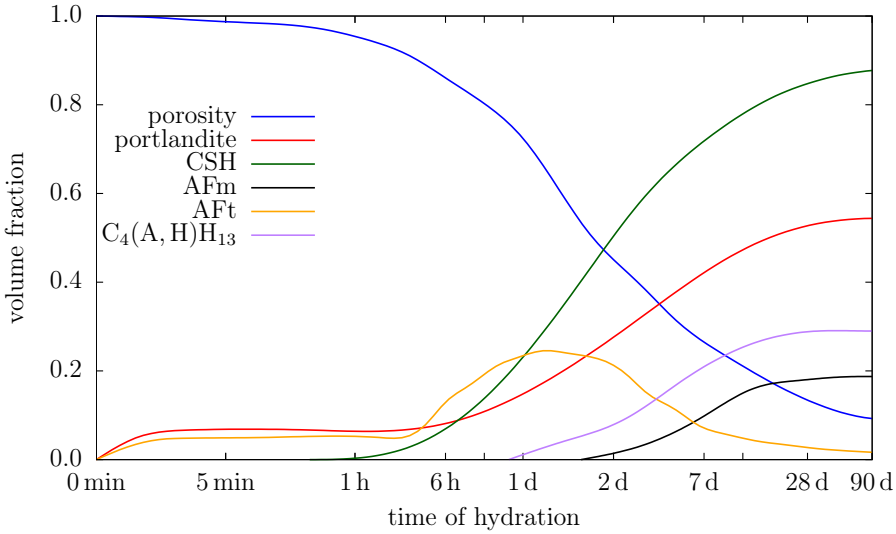

Figure 2.2: Fractions of the main hydration products formed and porosity evolution during hydration of OPC [Zem02]. The timescale is pseudo-logarithmic and only schematic.

the beginning but slows down significantly after a few days [Tay97, pp.222]. Although the shown plot is sketching the evolution of hydration products of OPC, most other types of cements show basically comparable kinetics of hydration. The composition of fractions of hydration products, however, can be significantly different. For example, although portlandite is a common hydration product in OPC, it might be absent in hydrated composite cements containing additional pozzolanic materials (e.g. silica fume). Moreover, high aluminate cement types may form a CASH phase, which is an aluminum containing CSH phase.

An important parameter for the hydration of cement is the water-to-cement ratio (w/c) of the mix, i.e. the mass of water divided by the mass of raw binder of the mix. The value is usually in the range of 0.3 to 0.6 [Tay97, p. 113]. This ratio affects various properties of the resulting hydrated cement. For example, without sufficient water the hydration of the cement is hindered, while high w/c ratios lead to a higher degree of hydration and a more porous structure. More details on the hydration processes are depicted in the following sections.

2.3.2.2 Degree of hydration

The degree of hydration is defined as the fraction of clinker consumed in relation to the initial amount present in the cement paste. From experimental studies it is known that hardened concrete, even after long in contact with water, may contain a signifi-

cant quantity of unhydrated cement. Thus, the degree of hydration does under certain circumstances not reach 100 % [Bej07,Mil66].

The reasons for this effect are diverse, while one of the obvious reasons is passivation. Most of the hydration products are formed quite rapidly upon dissolution of clinker. Effectively, the high concentration of dissolved species at the clinker surface leads to a preferential formation of hydration phases on the surface of the clinker grains. Hydration products are essentially less permeable for water than free pore space and effectively imposing a barrier. Furthermore, adsorption studies are indicating that the quantity of water contained in the pore space close to the clinker particles is in molecular dimensions, thus a few mono-layer in size. Due to adsorption forces the effective viscosity of water is rising in this domain. Therefore, due to a reduced diffusivity and permeability the reaction kinetic between water and clinker is subsequently reduced. Additionally, the lack of space to allow hydration products to form is also suggested as an explanation [Mil66].

Since the available pore space is of importance there is a relationship between w/c and the maximum degree of hydration. Several authors have derived semi-empirical relationships fitted to experimental data. For example, the degree of hydration α_{max} as function of w/c ratio according to Mills et al. is [Mil66]:

$$\alpha_{max} = \frac{1.031 w/c}{0.194 + w/c} \tag{2.1}$$

Bejaoui et al. [Bej07] reported:

$$\alpha_{max} = 0.239 + 0.745 \tanh\left(3.62\left(\frac{w}{c} - 0.095\right)\right) \tag{2.2}$$

Both functions are plotted in figure 2.3. Apparently, the model of Mills predicts that a maximum degree of hydration of only 85 % is achievable at a w/c ratio of one. At the same time the Bejaoui model suggest a degree of hydration of almost 100 %.

Although equations 2.1 and 2.2 describe the limiting value of the degree of hydration, the transient behavior towards the limit is not covered. Other authors have developed models to fill this gap, e.g. with the Parrot and Killoh model [Lot08]. The algorithmic approach is to determine the limiting reaction rate R_t. According to the model there are a nucleation and growth rate (R_t^{nucl}), a diffusion limited rate (R_t^{diff}) and a formation rate of a hydration shell (R_t^{shell}):

$$R_t^{nucl} = \frac{K_1}{N_1}\left(1 - \alpha_t\right)\left(-\ln\left(1 - \alpha_t\right)\right)^{1-N_1} \tag{2.3}$$

$$R_t^{diff} = \frac{K_2\left(1 - \alpha_t\right)^{2/3}}{1 - \left(1 - \alpha_t\right)^{1/3}} \tag{2.4}$$

$$R_t^{shell} = K_3\left(1 - \alpha_t\right)^{N_3} \tag{2.5}$$

The equations use various coefficients (K_1, K_2, K_3, N_1, N_3) which are tuned to reflect

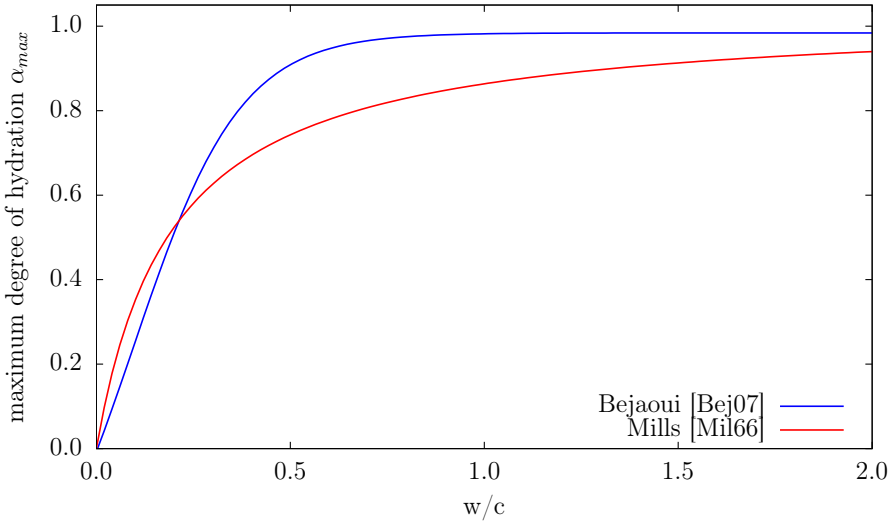

Figure 2.3: Maximum degree of hydration in dependency of the w/c ratio according to models of Bejaoui [Bej07] and Mills [Mil66].

w/c ratios and reactive surface areas [Lot08]. After determination of the rates, the minimum rate is used to iteratively calculate the degree of hydration in the next time step:

$$\alpha_t = \alpha_{t-1} + \Delta t R_{t-1} \tag{2.6}$$

With help of different coefficients for the four main clinker phases, it is possible to determine the evolution of the degrees of hydration evolution separately. Such an evolution for an OPC with a w/c-ratio of 0.4 is plotted in figure 2.4. In the plot, it is observable that alite and aluminate react faster than belite and ferrite. However, the total degree of hydration depends on the initial composition. As an example, a typical OPC clinker composition is assumed (weight fractions: 60 % alite, 25 % belite, 5 % aluminate, 10 % ferrite [Tay97, pp.1]) and the resulting degree of hydration of the clinker phases is plotted in orange in figure 2.4.

2.3.3 Hydration products

2.3.3.1 Calcium-silicate-hydrates (CSH)

During the course of hydration of cement clinkers, in particular of the calcium silicates alite and belite, general forms of *calcium silicate hydrates* (CSH) and calcium hydroxide (portlandite) are produced. The general term of calcium silicate hydrates is defined as a set of compounds which are composed of $c \cdot \mathrm{CaO}$ - $s \cdot \mathrm{Si_2O}$ - $h \cdot \mathrm{H_2O}$ with varying pre-factors c, s, and h. According to the cement chemistry notation, the compounds

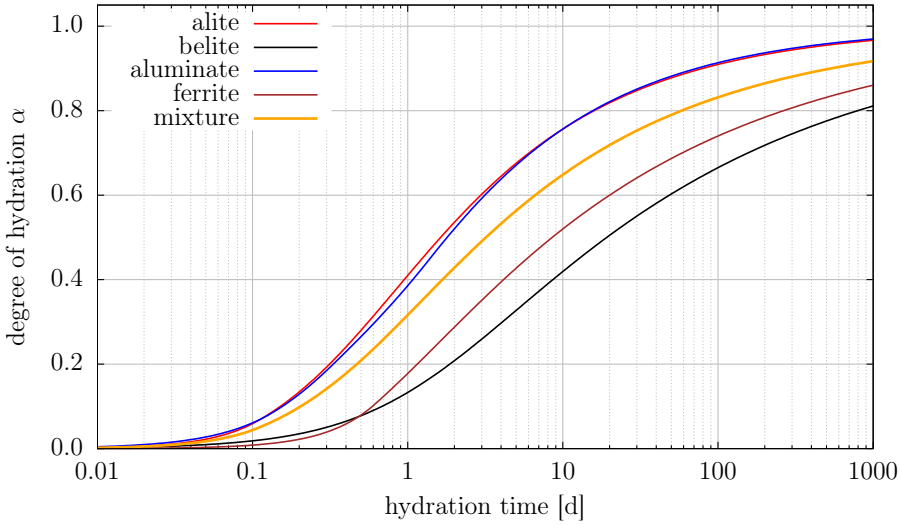

Figure 2.4: Degree of hydration of different clinker phases in dependency of the hydration time according to the model of Parrot and Killoh [Lot08]. The values for the mixture curve are determined by using the corresponding mass fractions of the clinker in typical OPC.

are shortcut with just CSH. There are more than 40 different compounds falling under this category [Gar04]. While most of these are crystalline phases, the most common occurrence in hydrated cement paste is a (amorphous to nano-crystalline) gel phase. CSH is also the main constituent of hardened cement pastes, accounting for more than 50 % of its volume [Meh05, p.29].

CSH gels have a continuous composition with respect to Ca-to-Si ratios (C/S) and are amorphous or nano-crystalline with limited long-range order. While hydration of calcium silicate clinker at ambient temperature mainly produces CSH-gel [Lot15], it is possible to transform CSH-gel to crystalline analogues with similar C/S ratios (e.g. tobermorite or jennite) with hydrothermal treatment [Gar04].

The equilibrium solution chemistry is related to the C/S ratio of the CSH phase. The higher the C/S of the CSH phase the higher the calcium and the lower the silicon equilibrium concentrations and vice versa. In general, CSH can be produced by reacting hydrous silica and calcium hydroxide in aqueous solution (i.e. $CaO + SiO_2 + H_2O$) or by hydration of calcium silicate clinker (e.g. $Ca_3SiO_2 + H_2O$), but both process would produce subtle different kind of CSH, namely CSH(I) and CSH(II) [Tay97, p. 132]. The C/S value of CSH(I) is limited between 0.7 and 1.45 while CSH(II) can achieve higher C/S values.

In the CSH(I) case the maximum C/S is limited by the solubility of portlandite and the lowest value by the solubility of amorphous silica. Accordingly, CSH with C/S values

lower than 0.7 are considered as mixture of CSH-0.7 and amorphous silica while values higher than 1.45 are interpreted as mixtures of CSH-1.45 and portlandite [Lot15].

On the other hand, if the CSH is produced from suspensions of alite or belite, which is the case in cement hydration, the situation may change. In that case a CSH(II) phase can be formed which has indeed a C/S value higher than 1.45. This can occur since during rapid reaction of clinker the activity of calcium hydroxide is higher and CSH is immediately precipitating [Lot15]. During dissolution of CSH(II), the equilibrium concentration is still limited by the solubility of portlandite, since CSH(II) is passivated by a layer of portlandite and CSH(I) upon contact with undersaturated solution.

2.3.3.2 Portlandite

Apart from the CSH phase, young cementitious materials based on Portland cement usually contain a significant amount of portlandite ($Ca(OH)_2$). Generally, 20 % to 25 % of the volume of hydrated OPC paste is occupied by portlandite. Portlandite tends to form crystals with a hexagonal-prism morphology [Meh05, p.29]. However, the addition of pozzolanic active SCMs consumes portlandite significantly while additional CSH is formed. Thus, the resulting portlandite content in the hydrated cement depends on the type of cement binder, water-to-cement ratio (w/c) and setting condition.

2.3.3.3 AFm phases

The abbreviation AFm stands for ***a**luminate/**f**errite-**m**ono-substituted*. Essentially, this refers to a phase whose oxide representation contains calcium oxide in companion with either aluminate (A) or ferrite (F) as fundamental component with a mono-substituted anion incorporated. The anions can be divalent, i.e. have a double negative charge. Thus, the existing substitutions with anions are versatile, most important anions are OH^-, $SO_2{}^-$, $CO_3{}^{2-}$. Although the ferrite variants are not exotic in hydrated cement paste, the aluminates are more frequent in terms of amount within the set of hydration products. Thus, this section focuses on the aluminate variants. Nevertheless, most of the phases mentioned here exist as a ferrite variant as well [Tay97, pp.157].

The general aluminate based formula reads $(Ca_2Al(OH)_6)^+ \cdot X^- \cdot y\,H_2O$ where X^- denotes a single charged anion. Usually, its layered structure incorporates a variable amount of water, hence $y\,H_2O$. The most common AFm phase in hydrated cement is calcium monosulfoaluminate ($Ca_4Al_2(OH)_{12}(SO_4) \cdot 6\,H_2O$ or $C_4A\bar{S}H_{12}$) and often short-cut as *monosulfate*. AFm-SO_3 crystallizes in hexagonal plates.

The carbonate analogue *monocarboaluminate* is only stable at low partial pressures of CO_2 ($p < 1 \times 10^{-8}$ atm). Higher carbonate concentrations lead to calcite formation [Dam94]. Due to the ingress of chloride ions in cementitious materials an AFm phase named *Friedel's salt* ($Ca_2Al(OH)_6(Cl) \cdot 2\,H_2O$) can be formed. Furthermore, there is a common phase named strätlingite (C_2ASH_8) in hydrated cements. It is an AFm phase having aluminosilicate as interlayer anion [Tay97, p.163]. Moreover, there is the hydroxy-AFm (C_4AH_{13}) phase [Mat07a], which is structurally related to *hydrocalumite* (C_4AH_{19}) [Tay97, p.159], which both are formed during the initial hydration of C_3A

[Meh05, pp.215]. In hydrated OPC with an initially higher C_3A content than 8 %, hydroxy-AFm is commonly found [Meh05, p.160]. Additionally, there is a series of AFm phases called C_2A hydrates, some of them are meta-stable at room temperature (e.g. C_2AH_8). Similar to C_4AH_{13}, C_2AH_8 converts slowly to hydrogarnet (C_3AH_6) at room temperature [Lot08,Pep54].

The list of AFm type phases eventually present in hydrated cement is extensive. For further information, the reader is referred to the literature (e.g. [Bla10b,Dam11,Tay97])

2.3.3.4 AFt phases

Analogue to the AFm phases, which are mono-substituted aluminate/ferrite phases, AFt phases incorporate tri-substituted anions. Ettringite ($Ca_6Al_2(OH)_{12}(SO_4)_3 \cdot 26\,H_2O$ or $C_6A\bar{S}_3H_{12}$) [Tay97, p.166] is one of the most important AFt phases and is formed in the initial process of hydration of aluminates in presence of sulfate ions. The sulfate ion concentration is quite high in the early stages of hydration because of the dissolution of gypsum. Ettringite emerges as needle shaped crystals with a high molar volume ($707\,cm^3\,mol^{-1}$ [Lot08]) compared to other hydration products. Thus, the reaction leads to an expansion and consequently reduction of porosity within the hydrates pore structure during the early setting. Ettringite formation is one of the main reasons for early solidification during the curing process. Later in the hydration process, when the residual gypsum content is dissolved and the sulfate ions are consumed, the sulfate concentration in the pore water is depleting. Consequently, ettringite becomes thermodynamically unstable with respect to monosulfoaluminate and is gradually converted into the monosulfate phase [Meh05, pp.216]. Moreover, ettringite plays and important role in the thermodynamic modeling of the hydration process of cement. Pore solutions of OPC are supersaturated with respect to ettringite, but the source of the kinetic barrier for precipitation is still under investigation [Lot08].

The existence of a carbonate analogue of ettringite $C_6A\bar{C}_3H_{32}$ was reported [Tay97, p.168], but also that it is unstable relative to calcium monocarboaluminate [Dam94]. However, some authors described a solid solution between ettringite and its carbonate analogue [Mat07b].

2.3.3.5 Others

One other known hydration product is hydrogarnet (C_3AH_6 or $Ca_3Al_2(OH)_{12}$), which is a minor phase in alumina rich cements [Tay97, p. 170]. It is assumed that the formation is often kinetically hindered. Hydrogarnet usually does not appear in OPC except after high temperature treatment [Dam11]. Additionally, there is a siliceous hydrogarnet phase ($C_3AS_{0.8}H_{4.4}$) which forms very slowly at room temperature [Lot08].

There are several other hydration products reported to be found in hydrated cement pastes. In particular the use of SCMs can yield an even more complex system. For example, addition of magnesium oxides can lead to formation of MSH [Lot19] and hydrotalcite. Moreover, the formation of a CASH phase (calcium aluminum silicate hydrate) is possible, which is an alumina enriched CSH phase. CASH phases are in particular

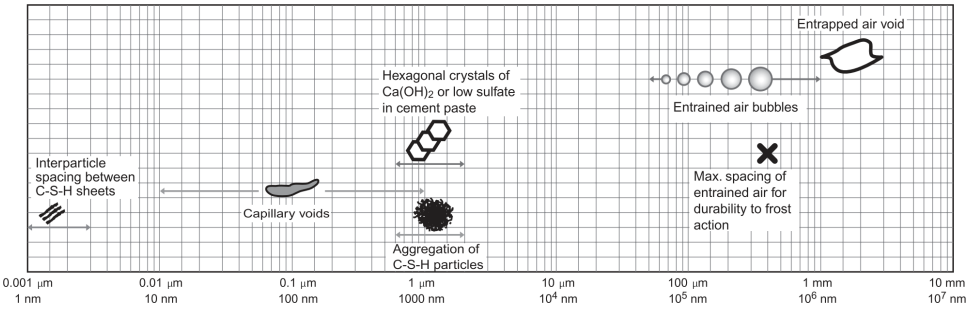

Figure 2.5: Schematic overview of dimensional range of solids and pores in a hydrated cement paste. The scales covered are in the range of seven orders of magnitude (1 nm to 10 mm) [Meh05, p.31].

found in high alumina cements [Och16, p.49] and low C/S CSH [LHô16]. Due to the chemical complexity of cementitious systems the investigation of the hydration product compositions, including but not limited to its thermodynamic and crystallographic properties, are still under intense research.

2.3.4 Microstructural properties and evolution

2.3.4.1 Pore size distribution

The overall pore size distribution of hydrated cement has a strong dependency on the curing time and the w/c ratio. In the early stages of hydration of high w/c ratio pastes, the capillary porosity voids are up to 5 µm. However, typical capillary pore size is 75 nm [Jen04], while pores in well-hydrated cement pastes with low w/c ratio may range within 10 nm to 50 nm [Meh05, p.32]. Additionally, hydrated cement and concrete can include air voids caused by the casting process (see figure 2.5).

On the lower end there is the gel porosity which accounts for a non-negligible volume fraction in hydrated cement paste. Similar as for the capillary porosity there are various reported values and ranges. Authors have reported that the size is likely in the range of 0.5 nm to 2.5 nm [Meh05, p.30] (see figure 2.5, left-hand side).

Moreover, different measurement techniques give further insights into the nature of the pore size distribution. For example, it is reported that the observed porosity determined with mercury intrusion porosimetry (MIP) is mainly in the range of 3 nm to 1000 nm for young pastes, while mature pastes show a range between 3 nm to 100 nm. For mature pastes of low w/c ratio almost all porosity is below 50 nm with the same technique. However, the data must be interpreted carefully, since MIP does actually give information about the pore-entry size, effectively hiding possibly present larger pores in the inside of the material [Tay97, pp.247].

According to *Power's model*, the fractional volume of total pores ϕ_T is empirically

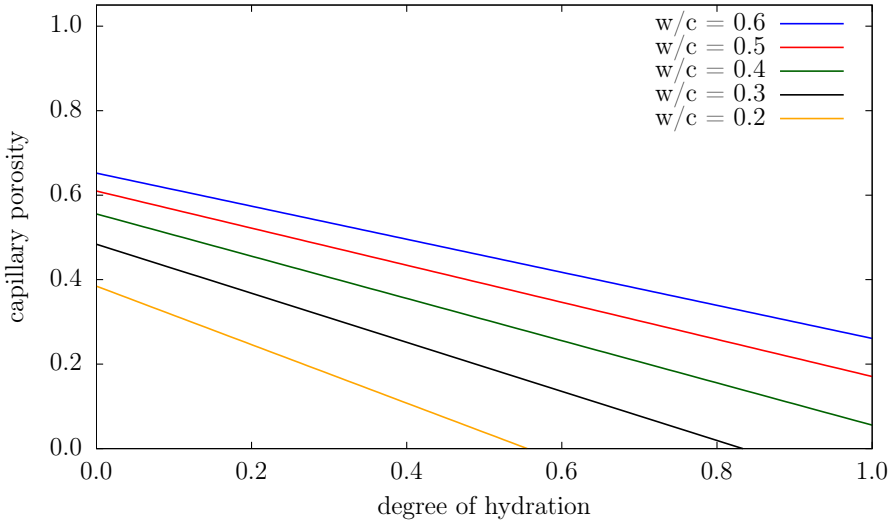

Figure 2.6: Capillary porosity in dependency of degree of hydration and different w/c ratios according to Power's model.

captured. The equation reads [Han86]:

$$\phi_T = \frac{w/c - 0.17\alpha}{w/c + 0.32} \tag{2.7}$$

In this equation α corresponds to the degree of hydration, which can potentially be estimated with equation 2.2, while w/c corresponds to the water content of the cement mixture.

2.3.4.2 Capillary porosity

Capillary porosity is defined as space which is neither filled by unhydrated clinker phases, SCMs nor hydration products. Since capillary porosity introduces significant pathways for diffusive and hydrodynamic transport in hydrated cementitious materials, it is an important parameter in the research and engineering domains.

While the absolute volume of the mixture of cement and water during hydration remains almost the same, the hydration products' density is approximately half the one of the anhydrous clinker phases. Effectively, most of the volume initially occupied by water is replaced by hydration products during hydration, while most of the water is consumed within the hydration process. Thus, an increase of the w/c ratio directly leads to an increase of capillary porosity. On the other hand, since further pore space will be filled by the formation of hydration products, the capillary porosity decreases with increasing degree of hydration [Jen08] [Meh05, pp.31].

Moreover, since the degree of hydration is proportional to the hydration time, hydrated cement at later stages has lower capillary porosity. However, degradation processes can change the tendency of porosity evolution. The amount of capillary porosity ϕ_c for OPC can be estimated with an empirical relation called *Power's model* [Han86]:

$$\phi_c = \frac{w/c - 0.36\alpha}{w/c + 0.32} \tag{2.8}$$

In this equation the same notation is used as before (compare to equation 2.7). As illustration of this model, the resulting capillary porosity as function of the degree of hydration for various w/c ratios are plotted in figure 2.6.

2.3.4.3 Gel porosity

Besides of the capillary porosity, HCP contains a smaller sized porosity called gel porosity. The pores of the size of nano-meters are mainly incorporated in the CSH phase. Gel porosity is incorporated in various types of CSH and independent of the CSH forming process, i.e. CSH(I) and CSH(II). Thus, it has to be interpreted as an intrinsic property of CSH. This is important because the gel porosity contributes to diffusive transport mechanisms within the HCP.

Although macroscopically CSH is a continuous phase, it contains multiple levels of heterogeneity. Surface area and porosity measurements indicate that there are at least two distinct morphologies present, which are called low density CSH (LD-CSH) and high density CSH (HD-CSH) [Jen94,Ten00]. Nanoindentation investigations are supporting this [Con04] and even indicate a third type called ultra-high density CSH (UHD-CSH) [Van10].

Further investigations have revealed that the ratio of LD- and HD-CSH in hardened cement pastes, M_r, depends on the w/c and degree of hydration (α). For OPC this mass relation M_r can be expressed by an empirical equation [Ten00]:

$$M_r = 3.017\frac{w}{c}\alpha - 1.347\alpha + 0.538 \tag{2.9}$$

With this relation it is possible to determine the mass fractions of LD- and HD-CSH. The obvious difference between LD- and HD-CSH is their density, which is different because of different intrinsic gel porosity. Despite the density differences, both types of CSH are considered to be composed of the same building blocks called *globules* but with different gel porosities. The gel porosities determined by BET measurements were 37.3 % and 23.7 % for LD- and HD-CSH, respectively [Ten00,Ulm04] (cf. table 2.3).

Furthermore, by drying LD- and HD-CSH separately, it has been shown that there is a higher mass difference in water than the gel porosity alone would explain, i.e. the measured difference in mass loss due to drying is higher than the 37.3 % and 23.7 % porosities recalculated in mass of water, respectively. The conclusion is that the globules themselves have an additional porosity called *intra-globules porosity*, which is embedded among the *basic building blocks*. In this model, the basic building blocks are considered

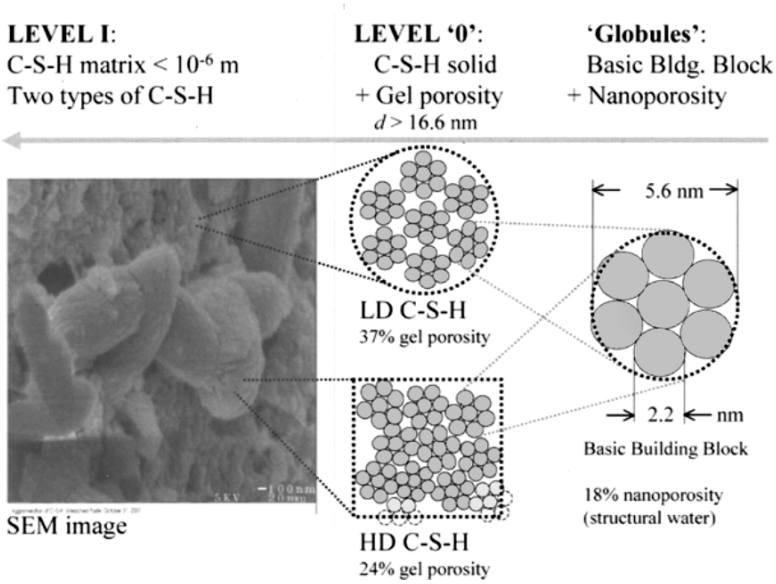

Figure 2.7: Schematic overview of the colloidal model of CSH [Jen04]. It consists of LD- and HD-CSH, globules and basic building blocks [Ulm04].

as solid particles with a size of 2.2 nm [Jen00,Ulm04] (cf. figure 2.7). The reported values for the density and the porosity of the CSH types, globule and basic building blocks are listed in table 2.3 [Ulm04].

Since the intra-globule porosity is considered as structural water, it is interpreted as non-contributing to diffusion processes within CSH. Furthermore, nitrogen accessible and inaccessible porosity in the CSH gel porosity have to be distinguished. Following this interpretation, LD-CSH has an additional porosity which can be accessed by nitrogen, which is not present in HD-CSH [Ten00]. In addition to the gel porosity, deeper analyses have shown that an additional porosity fraction does arise during the process of calcium leaching due to degradation of CSH [Sto09].

Table 2.3: Density and porosity values for constituents of CSH at different resolution levels. The data compiled in this table are values for water saturated (ρ_{sat}) and dry (ρ_{dry}) densities, and values for total (ϕ_{tot}) and gel (ϕ_{gel}) porosities [Ulm04]. The unit of the densities are in [g cm^{-3}].

Level		ρ_{sat}	ρ_{dry}	ϕ_{tot}	ϕ_{gel}
0: CSH solid	basic building block	2.80	2.80	0.00	0.00
	globule	2.48	2.30	0.18	0.00
1: CSH matrix	LD	1.93	1.44	0.49	0.37
	HD	2.13	1.75	0.37	0.24

2.4 Blended cements and low-pH cement

2.4.1 Blended cements

Blended cements are composite cement types which consists of OPC with additional inorganic materials (SCMs). The SCMs may contribute significantly to the hydration process. On one hand, one of the benefits of mixing SCMs to the usual Portland cement mixture is to save production costs compared to OPC and reduce the carbon dioxide footprint at the same time [Meh05, p.230].

On the other hand, there are several types of SCMs which can serve as agents to adjust desired properties of the cement hydration kinetics and/or improve durability and strengths of the resulting hardened concrete. Furthermore, improvements can be gained with respect to diffusivity, hydration heat and pore water pH [Tay97, p.261].

Most important SCMs are fly ash, ground granulated blast furnace slag, natural pozzolans and silica fume [Tay97, p.261]. Fly ash and slag are waste materials produced in large quantities but still serve some purpose when utilized in the production of cement. Since the focus in this work is on a special low-pH cement, the description here will be centered on the relevant SCMs used for the mixture, too.

2.4.2 Supplementary cementitious materials

2.4.2.1 Silica fume

Silica fume (SF) is a by-product of the silicon producing industry. For the production of silicon, quartz is reduced in an electric furnace while some SiO is lost as gas. In the contact with air, it is oxidized, resulting in finely dispersed particles with a size of 100 nm with a 95 % purity grade with respect to SiO_2.

Due to the high surface area, silica fume imposes a considerable pozzolanic reactivity during cement hydration and introduces an additional source of silicon. The finely dispersed reactive surface area of silica fume does also accelerate the reactions of clinker phases forming fine grains, filling gaps between other phases and grains. Thus, the effect on the cement paste in general is a reduction of capillary porosity and densification. The additional source term for silica leads to rapid consumption of portlandite within early stages of hydration. For the same reason the Ca/Si ratio of the CSH might be reduced compared to pure OPC [Tay97, p.285].

2.4.2.2 Blast furnace slag

Blast furnace slag (BFS) is a by-product of the iron and steel producing industry. Usually, the molten slag is cooled rapidly with water forming a glassy product, which is then grounded to powder. BFS is mainly composed of CaO, SiO_2, Al_2O_3 and MgO [Tay97, p.262]. Thus, adding blast furnace slag to the cement mixture introduces another source for calcium silicates. The environmental benefit is that no calcite needed to be transformed to calcium silicates, which would produce CO_2 as by-product which is released into the atmosphere.

In contrast to silica fume, finely grounded slag alone is able to hydrate by its own when in contact with water. However, the reaction kinetics are considerably slower compared to clinker reaction and thus BFS alone is not feasible for structural applications. On the other hand, the hydration kinetic is accelerated in the presence of calcium hydroxide and gypsum, which in this combination renders BFS to be feasible for as SCM in the cement hydration process [Meh05, pp.230]. Hydration of slag produces a CSH phase with a lower Ca/Si ratio than the hydration of OPC. Besides, BFS adds a significant source of magnesium to the cement hydration process. This could allow for the formation of magnesium silicate hydrate (MSH) and forms of hydrotalcite-type phases because of the aluminum content. These hydrotalcite phases can exists in different variants, e.g. as hydroxy or carbonate hydrotalcite, while in the presence of carbonates, the carbonate variant of hydrotalcite is preferably formed [Tay97, p. 173]. This process is even more dominant in the situation of degradation of concrete via carbonation. Similar to silica fume, the reactivity of BFS depends on its reactive surface area, i.e. the resulting particle sizes after grinding. Analyses have revealed that, for w/c ratios of 0.5 to 0.6 and a temperature of 20 °C, 30 % to 55 % of the slag reacts within 28 days and only 45 % to 75 % after 1 to 2 years. Increasing the fraction of slag in the cement mixture or decreasing the w/c ratio leads to a reduced consumption of BFS [Tay97, p.267].

2.4.3 Low-pH cement

Essentially, in this work the focus is on low-pH blended cement, which contains blast furnace slag and silica fume as SCMs. Consequently, the hydration tends to lower Ca/Si ratios for the CSH phase. Since portlandite is consumed and the CSH has a lower Ca/Si ratio, the Ca concentration in the pore solution is reduced. At the same time the pH in equilibrium is in the range of 10 to 11 and thus significantly lower than in cement pastes made from OPC (initial pH between 13 and 14).

Concretes containing a large amount of slag or pozzolanic reagents like silica fume in the cementitious material do usually outperform in certain properties those only containing Portland cement, e.g. with respect to reduced heat of hydration, or lower diffusivity. Furthermore, a high portlandite content as in OPC pastes would lead to a rather rapid leaching of calcium. If on the other hand the calcium is bound in form of CSH with moderate Ca/Si ratio, the equilibrium calcium concentration is reduced compared to that in presence of portlandite. Consequently, the gradient in the calcium concentration is lower, and thus the leaching rate is reduced [Meh05, p.188].

Moreover, silica fume has a high specific surface and leads to a high amount of nucleation sites due to finely dispersed particles. This leads to a reduced amount of capillary porosity effectively decreasing diffusive pathways. This effect provides another contribution towards reduced leaching and degradation rates.

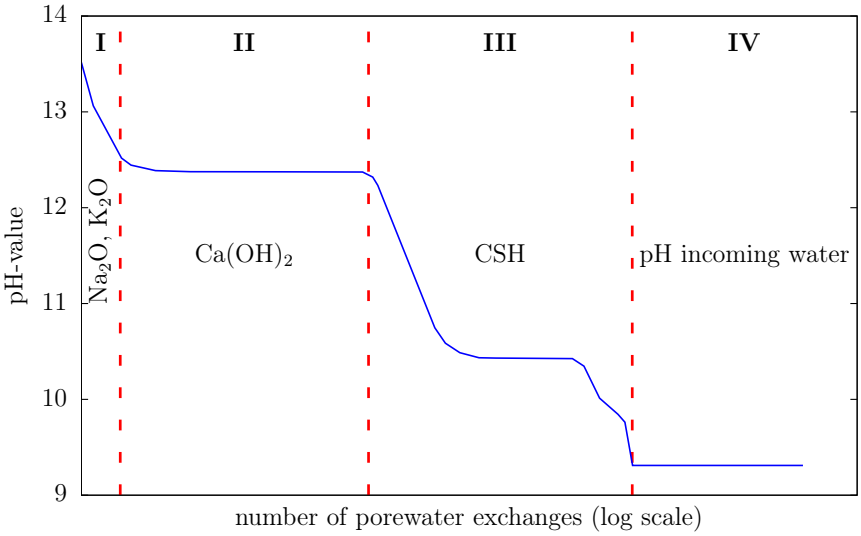

Figure 2.8: Schematic illustration of the evolution and drop of pH-value due to leaching. The pH controlling phases are depicted [Och16, p.12].

2.5 Alteration and degradation of hydrated cement

Cementitious materials are generally in thermodynamic disequilibrium with their environment, leading to alteration and degradation in the long-term, associated with changes in phase assemblage and transport properties. The degradation processes may affect the total porosity and pore-size distribution and thus cause changes in pore connectivity and induce microstructural changes. Resulting from this, different macroscopic properties as effective solute diffusivity, permeability or mechanical properties can be affected. The extent of these effects depends on the nature of the cementitious material and its intrinsic properties as well as on the degradation mechanism and the type of contacting solution.

2.5.1 Leaching of alkalis and calcium

Even in contact with ordinary (ground) water, hydrated cementitious materials experience certain degradation processes. In particular, alkalis and calcium are leached. In that sense, deionized water is quite aggressive to cementitious materials. Within this section, the processes involved in leaching and the resulting stages of leaching are briefly outlined (see also [Meh05, pp.154] [Och16, pp.11] [Tay97, pp.145]). The description is supported by figure 2.8.

OPC binder contains certain amounts of alkalis containing compounds as Na_2O and K_2O. In contact with water, these oxides form their corresponding hydroxides. Due to

the presence of these alkalis the pore water has a quite high pH of about 13.5. During stage I of leaching, i.e. due to pore water exchange, these highly alkaline ions are depleted rather quickly.

At the next stage (II), portlandite ($Ca(OH)_2$) is the dominant phase buffering the pH value in the pore water at about 12.5 at room temperature. Accordingly, the calcium concentration maintained in the pore solution is about $20\,\mathrm{mmol\,L^{-1}}$ [Och16, p.12]. The duration of this process depends on the amount of portlandite present in the hydrated cement. Thus, this stage might not be present, if no portlandite has been formed during hydration as it might be the case for low-pH cements containing a larger amount of additional silica. Nevertheless, at some point the portlandite is depleted and stage III comes into effect.

At the beginning of stage III, CSH is the pH controlling phase. Due to its continuous composition with respect to calcium content, the concentration of calcium in the equilibrated pore water evolves from $20\,\mathrm{mmol\,L^{-1}}$ to approximately $2\,\mathrm{mmol\,L^{-1}}$. Since the solubility of CSH is the controlling phase, the pH value is maintained initially above 12 but then decreases consecutively. For synthetic CSH phases without any other hydration product the pH drops to 10. During this process, the incongruent dissolution of CSH leads to a continuous decrease in Ca/Si ratio in the CSH phase. In a cementitious system the situation is more complex. For example, because calcium is present also in other hydration products, the decrease in the calcium concentration has an effect on these phases, too. Thus, later within stage III, other hydration products are dissolved and eventually depleted as well. However, the process itself depends on the type of cement and the composition of the leaching water. In particular, the starting pH-value in this stage is reduced in the case of low-pH cements. Further decalcification of CSH eventually results in formation of amorphous silica.

With the transition to stage IV, all hydrated cement components are completely dissolved. The pore fluid composition in concrete in this stage is solely maintained by aggregate minerals, possible degradation products (e.g., calcite in the case of carbonation and/or hydrotalcite if magnesium ions were present) and the incoming water [Och16, pp.12].

The porosity remains rather constant within stage I. In stage II, while portlandite dissolves, the porosity increases approximately linearly in the leached zone. Later in stage III, CSH transforms gradually from CSH-1.6 to a CSH with a lower C/S ratio, to finally CSH-0.8. This process involves effectively a shrinkage in the molar volume of CSH. Therefore, the porosity increases exponentially with respect to the number of pore water exchanges, until all CSH and other hydration products are degraded [Och16, p.14]. At the same time, while porosity increases, the mechanical strength of the hydrated cement paste also deteriorates [Gla08]. Experimental evidence revealed a dependency to the initial w/c ratio. An initially higher w/c ratio leads to higher porosity and thus higher diffusivity. This higher diffusivity subsequently leads to a faster depletion of portlandite [Hag05].

2.5.2 Carbonation

Carbon dioxide is an omnipresent gas in the earth's atmosphere, which has effects on the alteration of cement. Moreover, carbonates are commonly dissolved in ground waters. Carbonation is thus one of the major alteration processes experienced by cementitious materials. The whole process of carbonation comprises a sequence of different steps. In case of atmospheric conditions, initially the gaseous CO_2 is dissolved in the cement's pore water:

$$CO_{2(g)} \longrightarrow CO_{2(aq)} \tag{2.10}$$

As next step the dissolved carbon dioxide molecule dissociates into hydrogen carbonate and carbonate ions under release of protons.

$$CO_{2(aq)} + H_2O \rightleftharpoons H^+ + HCO^- \tag{2.11}$$

$$HCO^- \rightleftharpoons H^+ + {CO_2}^{2-} \tag{2.12}$$

In case of ingress of carbonate containing water, the latter stage is already given. Due to the high pH-value of the pore water, there is a high concentration of hydroxyl ions present [Gla08]. Those hydroxyl ions capture the released protons and form water, which leads to the effect that the dominant ionic species of carbonate in cement pore water is ${CO_2}^{2-}$. At this stage it is obvious that the process of carbonation involves a decrease of the concentration of hydroxyl ions and thus causes a decrease in pH-value.

Once the carbonate ion concentration increases in the pore water, there will be subsequently reaction among carbonate and other species in the pore water. Since cement pore water contains a high amount of calcium, the direct consequence is precipitation of calcium carbonate, e.g. in the form of calcite. The reduction of the calcium concentration in turn has an effect on the stability of calcium containing phases. In particular, portlandite and the CSH phase will release more calcium to compensate the disequilibrium. Thus, carbonation is also accelerating the effect of calcium leaching in portlandite and the CSH phase.

In the scope of usage of concrete as construction material, it is quite common to embed steel reinforcements into the concrete. Usually, the steel is well protected from corrosion due to the high pH-value of the cement pore water. However, due to the decrease of pH during carbonation, an increased rate of corrosion of the rebars can be initiated. Moreover, carbonate reaction with Friedel's salt, when present, can release chloride ions, which may reach the reinforcement and may accelerate corrosion.

Besides of the mineralogical changes, calcite has a higher molar volume than portlandite, i.e. $36.9\,cm^3\,mol^{-1}$ and $32.9\,cm^3\,mol^{-1}$ [Bal09], respectively. Therefore, the effect of carbonation is a reduction of porosity, as long the CSH phase is not significantly degraded. In particular this reduction occurs in the zone at the interface, closest to the source of carbonates. In turn, a decrease in porosity involves a decrease in diffusivity which consequently leads to a passivation effect due to hindered transport.

Due to the quite common effect of carbonation under normal atmospheric conditions, numerous research contributions about the kinetic carbonation rate were conducted

Table 2.4: Diffusion coefficients of carbon dioxide in air and water (20 °C) in addition to values for ionic carbonate species in water (25 °C).

Species	D $[10^{-9}\,m^2\,s^{-1}]$	reference
CO_2-air	1.60×10^4	[Hay17, p.6-259]
CO_2-aq	1.67	[Hay17, p.6-260]
CO_3^{2-}	0.923	[Hay17, p.5-75]
HCO_3^-	1.185	[Hay17, p.5-76]

and published (e.g. [Gla08]). Assuming a simplified model in which the pore space is saturated, i.e. completely filled with pore water without a gas phase, the diffusivity of carbonate ions would limit the carbonation rate to some extent. However, more detailed analyzes have revealed that under atmospheric conditions these assumptions did not prove true. Depending on the humidity, the pore structure of the hydrated cement paste is only partially saturated. To illustrate the effect, the different diffusion coefficients for carbonate species are given in table 2.4. The diffusion coefficient of aqueous carbon dioxide is four order of magnitudes lower than the one of carbon dioxide in air. Compared to the ionic carbonate species, this factor is even higher. Thus, CO_2 as gas can ingress deeper into the concrete structure in a smaller fraction of time, i.e. the carbonation rate is accelerated compared to saturated conditions. On the other hand, the presence of water is important to be able to dissolve CO_2 first, otherwise the steps of reaction described above are inhibited. Therefore, a complete dry pore structure would experience a reduced carbonation rate, too [Tay97, p. 357]. However, even though the rate in saturated conditions is reduced, carbonation still happens if the contacting water contains carbonate ions.

Additionally, the type of cement and the w/c ratio has consequences on the carbonation rate. For example, due to higher capillary porosity a higher w/c ratio causes a stronger carbonation effect. This correlation is expected, since a higher porosity means that the CO_2 and carbonates can ingress more easily deeper into the hydrated paste and at the same time it takes longer to clog the pores to gain a passivation effect.

2.5.3 Sulfate attack

Due to exposure of cementitious materials to sulfate containing chemical agents, groundwaters or due to environmental weathering (e.g. due to acidic rain), sulfate ions may ingress into the material. Due to interaction of aluminum containing phases (e.g. AFm) with elevated sulfate concentration, (secondary) ettringite can be formed:

$$C_4A\bar{S}H_{12} + 2\,SO_4^{2-} \rightleftharpoons C_6A\bar{S}_3H_{12} + 4\,OH^- \tag{2.13}$$

Since the molar volume of ettringite is higher than of monosulfate, this leads to a decrease in porosity and mechanical stresses inside the hardened cement paste. These internal stresses lead to expansion and can ultimately lead to the formation of macro

cracks [Meh05, p. 160].

Another effect which was reported is the formation of gypsum in contact with high-pH pore water. This effect can also occur when no aluminate species in the cement are present at all, e.g. in hydrated C_3S pastes. The formation of (expansive) gypsum can additionally contribute to the degradation of concrete due to sulfate attack [Gla08].

In general, the extent of the effect of sulfate attack depends on various properties of the hardened cement paste. Since the content of aluminates governs the amount of possible formation sites of ettringite, there is a correlation between the initial C_3A content and the expansion, i.e. the higher the aluminate content the higher the volume expansion. Another property which has a significant effect on the consequences of sulfate attack is the w/c ratio, since measurements revealed a significantly more pronounced loss in compressive strength with increasing w/c ratios [Gla08,Lee05]. This is likely connected to the process that a higher w/c ratio allows for faster sulfate ion penetration [Ouy88].

2.5.4 Other degradation processes

In addition, there are several other degradation processes affecting the properties of cementitious materials. One of the common ones is chloride attack which occurs mainly in saline environments, e.g. by seawater, leading in combination with aluminate phases to the formation of Friedel's salt. Friedel's salt has a molar volume of 271 $cm^3\,mol^{-1}$ [Bal09], which is higher than that of most other hydration products and can therefore also lead to volume expansion and cracking. Moreover, chloride ions accelerate the corrosion rate of iron reinforcements in concrete. Under oxidizing conditions, steel corrosion products induce volumetric expansions and cracking [Meh05, p.178].

Moreover, there are MSH and thaumasite phases which can form depending on environmental conditions. MSH can replace CSH upon presence of Mg. Thaumasite, which is a AFt type phase, forms preferable at lower temperatures [Gla08,Mat07b]. Besides MSH leads to a reduction in mechanical stability, it has a higher molar volume than CSH [Lot19]. Thaumasite has a quite high molar volume (329.40 $cm^3\,mol^{-1}$[Bla10b]) compared to other hydration products in general. Again, this may cause volume expansions which can lead to cracks during formation [Gla08].

2.6 Cementitious materials in nuclear waste management

In general, immobilization of radioactive waste significantly reduces the potential for release of radionuclides into the environment. The immobilization of low- and intermediate-level wastes using cements has been successfully applied for many years already. Essentially, using a cement matrix imposes a good thermal, chemical and mechanical stability of the treated waste [Ojo05, pp.205]. With a cement matrix it is possible to immobilize liquid and solid wastes at the same time (see also figure 2.9).

Besides of the immobilization purpose of radionuclides in the field of nuclear waste management, cement and concrete are also used as construction and backfill material

Figure 2.9: Drums containing solid, liquid and slurry intermediate-level waste immobilized with cement [Ojo05, p.226].

in final repositories. For example, concrete is used as lining and in support structures for tunnels and shafts. In addition to a clay sealing of waste disposal cells, it is planned to use further sealing plugs engineered from cementitious materials. Furthermore, even intermediate-level wastes are placed in high-performance reinforced concrete containers. Thus, depending on the disposal concept, cementitious materials serve as part of the engineered barrier systems [AND05]. The Belgian *Supercontainer* barrier concept for high level waste and spent fuel disposal is planned to use Portland cement as buffering system. In this concept, cementitious materials are utilized for corrosion protection of the carbon steel [Bel06].

Besides serving the mechanical and physical barrier function, cementitious materials have a significant effect on radiation shielding. This comes into play during the operation of the final repository in order to reduce radiological impact on operator personnel and employees [AND05] [Ojo05, p.206].

Moreover, certain radionuclides experience significant retention in cementitious materials. Numerous studies of uptake of safety relevant radionuclides in different cementitious materials and hydration phases have been performed during the last decades [Atk92,Gra20,Och16]. However, despite extensive research efforts, several sorption and retention mechanisms are still not completely understood. This might originate from the vast complexity of cementitious systems in terms of involved thermodynamic, chemical and mechanical properties. Moreover, experiments are often carried out at room temperature, while cementitious materials in a final repository might experience an elevated temperature. In this regard, a temperature of 55 °C is already sufficient to cause certain structural transformations of solid phases in hydrated cements [Atk92].

All in all, since the type of cement, curing conditions, treatment and exposure to different environmental conditions is affecting various chemical and physical properties, it is of paramount importance to fill the knowledge gaps. One envisaged result is to develop the tailor-made cement recipes for the various purposes in final repositories and disposal concepts.

3 Reactive transport modeling

A huge number of technological and environmental processes are known to consist of several individual processes, which encompass a chemical reaction and a solute transport term in a coupled manner. For example, the dissolution of a solid phase increases the local solute concentration, thus leading to an increase in diffusive fluxes. At the same time, transport of solutes can lead to a decrease of concentration and may therefore accelerate the dissolution of some solid phases. The same applies to mixing of different solutes via transport processes which can lead into precipitation of solid phases or production of gases. Moreover, thermal and/or pressure changes, which themselves obey transport processes, can induce chemical and mechanical alterations. The general domain of reactive transport modeling refers to calculation techniques which are dealing with the interaction between those coupled processes.

Reactive transport models have gained increasing importance in recent years as they became more mature and with the increase in computing power, since these models are generally computationally expensive. They are essential tools for the analysis of physical, chemical and biological processes on the one hand and helping to predict resulting alterations of complex geochemical systems on the other. The different processes can be individually described by mathematical formalism based on physical or chemical theories. The mathematical models are often expressed in form of partial differential equations, such as the Navier-Stokes equation or the diffusion equation, e.g. Fick's second law [Ste05a]. Moreover, when dealing with chemical equilibrium calculations, the problem to solve consists of a system of (non-)linear equations. The latter is usually solved with help of linear algebra techniques [Par99].

3.1 Transport modeling

3.1.1 Continuity equation

The continuity equation is fundamental to derive hydrodynamic and diffusive transport equations. It is an important statement to extend some aspects of the conservation laws. For example, conservation laws just state that mass, momentum and energy must be conserved in the modeled systems. However, this does not forbid that mass is transported without actual movement between two states. From experience, however, it is known that most processes involve a continuous transition from one state to another. Moreover, the continuity equation is fundamental to derive the diffusion equation [Wit15, pp.25].

The continuity equation is derived with help of Gauss's divergence theorem. In simple words, the divergence theorem states that the surface integral of the flux passing the

surface equals the volume integral of the divergences of the flux inside the volume. It has to be noted that flux in this case is a pure mathematical term and can refer to different physical properties as mass or heat. In the context of fluid dynamics, this means that the amount of fluid moving through a surface enclosing a volume equals the sum of all divergences in flux inside the volume. From this statement, the following equation is deduced [Kha15, pp.51]:

$$\frac{\partial f}{\partial t} + \frac{\partial (fu)}{\partial x} = 0 \tag{3.1}$$

In this equation f is a scalar value, which can be for example density or concentration, and u corresponds to velocity. The second term consists of the spatial derivative of the flux which corresponds to the divergence. For generalization for arbitrary dimensions the nabla operator ∇ is often used to express the spatial divergence. Furthermore, since the flux j is the product of the scalar value and velocity, i.e. $j = fu$, the equation is rewritten as:

$$\frac{\partial f}{\partial t} + \nabla j = 0 \tag{3.2}$$

3.1.2 Navier-Stokes equation

Hydrodynamic fluid flow is usually described by the Navier-Stokes equation, which is an important partial differential equation implemented in reactive transport modeling codes which incorporate fluid flow. Essentially, the Navier-Stokes equation describes the momentum conservation of a fluid:

$$\rho \left(\frac{\partial u}{\partial t} + (u \cdot \nabla) u \right) = -\nabla p + \mu \nabla^2 u + \rho F_e \tag{3.3}$$

In this equation, ρ corresponds to fluid density, μ is the dynamic viscosity, u the velocity vector while F_e is a possible external force, which could for example refer to g which is the gravitational force. Additionally, using the continuity equation 3.2 and assuming that the medium is incompressible, i.e. ρ is constant, the following additional constraint is defined:

$$\nabla u = 0 \tag{3.4}$$

Besides the external force term in the Navier-Stokes equation, the internal forces are separated into contributions from pressure a gradient ∇p and a friction term, which incorporates the effect of the fluid's viscosity. Basically, the Navier-Stokes equation 3.3 relates the product of density, which is mass normalized by volume, and acceleration (left-hand side, LHS) with forces acting on the fluid volume (right-hand side, RHS) [Łuk16, p.24]. Thus, this is essentially a volume normalized and extended form of Newton's second law:

$$ma = F \tag{3.5}$$

In this equation F corresponds to force, m to mass, while a is the acceleration.

Analytical solutions of the Navier-Stokes equation turned out to be very complicated to derive. In particular, the so-called *convective term* on LHS ($(u \cdot \nabla) u$) introduces a

non-linearity into the partial differential equation, which renders it difficult to solve. Thus, often numerical methods are applied to approximate solutions.

3.1.3 Solute transport: Advection-diffusion equation and porosity

The diffusion equation is one of the most important partial differential equation in reactive transport modeling. The equation describes transport processes due to Brownian motion of particles. Resulting from the solutions of the equation, new solute concentration profiles after progressed time can be determined. The diffusion equations mentioned in this section are usually implemented in some form in the algorithmic core of different reactive transport codes.

3.1.3.1 Diffusion equation

The derivation of the diffusion equation presented here is based on Fick's first law. Fick's first law is the basic relationship which describes the diffusive flux between different concentration potentials. It is the solute transport analogue to Fourier's law which deals with thermal conductivity. According to Fick's first law, the diffusive flux J is proportional to the diffusion coefficient D and the concentration gradient [Cra75, pp.2]:

$$J = -D\frac{\partial c}{\partial x} \tag{3.6}$$

The negative sign in front of the diffusion coefficient originates from the fact that diffusive flux is directed from high to low concentration potentials. This is a phenomenological description of the second law of thermodynamics, which states that heat cannot spontaneously flow from colder to hotter locations. Fick's first law is valid under steady-state conditions, i.e. there is no concentration change with time. With help of the continuity equation 3.2 it is possible to derive the differential equation reflecting transient concentration changes. Inserting the flux representation of equation 3.6 into 3.2 and reordering:

$$\frac{\partial c}{\partial t} = -\frac{\partial\left(-D\frac{\partial c}{\partial x}\right)}{\partial x} \tag{3.7}$$

Under assumption of a non-transient diffusion coefficient, the equation simplifies to the well-known form of the diffusion equation called Fick's second law [Cra75, p.4]:

$$\frac{\partial c}{\partial t} = D\frac{\partial^2 c}{\partial x^2} \tag{3.8}$$

3.1.3.2 Advection-diffusion equation

In the case of an advective flux component, the diffusion equation must be extended. The pure advection equation is derived from the continuity equation 3.2. For this, the

velocity field is assumed to be uniform and constant, which allows extracting u from the differential, leading to [Wit15, p.28]:

$$\frac{\partial c}{\partial t} + u\frac{\partial c}{\partial x} = 0 \tag{3.9}$$

Combining the advection equation with the diffusion equation yields the governing equation for the advection-diffusion processes [Moh11, pp.51]:

$$\frac{\partial c}{\partial t} + u\frac{\partial c}{\partial x} = D\frac{\partial^2 c}{x^2} \tag{3.10}$$

Similar as the equation describing Fick's first law, the diffusion coefficient used in the equations is also phenomenological, i.e. adjusted to model the macroscopic measured data. Usually, the coefficient is fitted to experimental results. For example, for calcium ions the determined diffusion coefficient in free water D_w is $2.2 \times 10^{-9}\,\mathrm{m^2\,s^{-1}}$. However, this value does not apply to a porous medium because of *tortuosity* effects. Tortuosity means that the solute needs to travel a longer pathway than without obstructions and direct connection. All in all, this leads to the term of *effective diffusivity* which is characterized by the effective diffusion coefficient D_e:

$$D_e = D_p\phi \tag{3.11}$$

$$D_p = D_w f(\phi) \tag{3.12}$$

In this equation $f(\phi)$ corresponds to a function which relates the porosity ϕ with the effect on diffusivity. In this process it is common to calculate the pore diffusion coefficient D_p first. A commonly known semi-empirical relation is Archie's law:

$$f(\phi) = \phi^m \tag{3.13}$$

In this equation m stands for the *cementation factor* which corresponds to the sensitivity on porosity changes, i.e. a higher value would reduce diffusivity more significantly. Depending on the morphology and microstructure of the porous media, the values may vary. A value of 1.5 corresponds to an analytical solution in which all obstructing particles are assumed to be perfect spheres.

Inserting D_e into equation 3.10 is valid only for systems without temporal gradients in porosity. However, when dealing with variations in porosity, one has to take into account porosity gradients in the transport equation:

$$\frac{\partial \phi c}{\partial t} = \frac{\partial J}{\partial x} \tag{3.14}$$

$$J = -\phi D_p\frac{\partial c}{\partial x} + \phi u c \tag{3.15}$$

It has also to be noted that in this work only Fickian diffusion processes are considered. Strictly speaking, Fickian description of diffusion is only valid for single diffusing

species systems while many solutes are dissociated as ions with different diffusion coefficients each. However, these ions are electrically coupled to maintain electroneutrality and described by the more sophisticated Nernst-Planck equation [Cus09, p. 164]. Some authors have used the Nernst-Planck equation to solve solute transport in their simulations [App17,Gal10,Yan14].

3.2 Thermodynamic modeling

Thermodynamic modeling is crucial for reactive transport simulations. Since the chemical alterations are governed by chemical equilibrium and kinetic reaction rates, stable and fast modeling algorithms are mandatory. Essentially, there are two schools of thermodynamic modeling techniques [Ste96], which are either based on:

- Gibbs energy minimization (GEM), or
- Law of mass action (LMA)

A chemical system is per definition in equilibrium when the amount of energy is minimal. Thus, the GEM method is about minimization of the total Gibbs energy while maintaining mass balances [Kul12]. On the other hand, the LMA method deals with optimization of mass balances directly with respect to equilibrium constants of the corresponding involved reactions. The law of mass action reads:

$$K = \prod a_i^m \tag{3.16}$$

In this equation m is the corresponding stoichiometric factor, while a stands for the chemical activity which corresponds to the concentration corrected by the activity coefficient γ.

$$a = \gamma c \tag{3.17}$$

There are several (empirical) models to determine the activity coefficients. Commonly the extended Debye-Hückel or Davies equations are used to correct the concentrations to express the activity term. Both models contain the ionic strength of the aqueous system. Furthermore, there is the SIT (Specific ion Interaction Theory) [Gre97] and Pitzer [Pit73] models. Different activity models have advantages and disadvantages in terms of demands on thermodynamic input data while some models have limited validity in a specific range of ionic strength. In particular, the activity models are introducing non-linearity into the system of equations to be solved [Par99].

Despite the advantages or disadvantages and different numerical approaches used to solve the corresponding governing equations, both LMA and GEM approaches essentially aim to solve the same class of problems. It can be seen as different point of views on the chemical process at hand. The interchangeability becomes clearer, when the connection between the Gibbs energy and the equilibrium constant is noticed:

$$\Delta G = -RT \ln K \tag{3.18}$$

However, both methods are conceptually not entirely equivalent. For once, the mathematical approach for finding a minimum is mathematically not equivalent to finding the root of a system of non-linear equations. Moreover, the view on constraints and relaxed parameters is inherently different. For example, the LMA approach maintains equilibrium in the system as fixed, while a variation in mass is allowed, thus relaxing the mass balance requirement. Iteratively, the total mass of each species is corrected until the correct mass balance is obtained again. On the other hand, the GEM method allows temporarily divergence from equilibrium but maintains the mass balance at all time. Mass is essentially transferred from one species to the other, with the driving force to minimize the Gibbs energy. During this process the conservation of mass in the system is maintained [Ste96].

For the LMA approach usually all equations for chemical reactions are rewritten in terms of *master species*, e.g. Ca^{2+} for calcium. Master species are also termed as *components* in other publications and text books. In general, the set of non-linear equations are approximated with systems of linear equations. Afterwards the Newton-Raphson method is used to solve this system of equations [Par99].

The LMA method has the benefits of simplicity in the implementation compared to the GEM methods [Lea16]. Furthermore, GEM is 2 to 10 times slower than LMA. However, GEM has benefits in the scope of solving more complex and non-ideal chemical systems [Kul12]. Both methods need thermodynamic data as input, which are different in kind though. Those data are given as input to the solver codes in the form of thermodynamic databases. These databases are usually compiled from various sources, which were derived by experiments as for instance calorimetry. The compilation of the database itself must be performed carefully, since the data need consistency among each other to yield meaningful results.

Important databases relevant for modeling of cementitious systems are ThermoChimie [Gif14], CEMDATA07 [Lot08,Mat07b], CEMDATA18 [Lot19] and the PSI/Nagra Chemical Thermodynamic Database [Tho14]. Some of them are, as of time of writing, available in formats for both GEM and LMA, while some only for one of these. Moreover, some have been converted by other authors from GEM to LMA format, e.g. CEMDATA07 [Jac12]. Since this work deals with cement chemistry the correctness, consistency and completeness of the used databases with respect to cement phases are of paramount importance to gain meaningful results.

3.3 Coupling of reaction and transport processes

There have been several methods proposed to couple the processes of reaction and transport at the same time. The most important are:

- **G**lobal **i**mplicit approach (GI)
- **S**equential **n**on-**i**terative **a**pproach (SNIA)
- **S**equential **i**terative **a**pproach (SIA)

The global implicit approach is about solving the reaction and transport terms at the same time. For this, usually a Jacobian matrix is constructed which in turn is used to solve the set of equations for example with Newton-Raphson methods. However, for complex multi-component systems, i.e. reaction and transport of multiple species at the same time, the matrix becomes excessively large which leads to a high memory consumption. Additionally, since the matrix contains the derivatives, the GI approach is computationally very intensive. Thus, with the currently available computational capabilities, the procedure might be effectively not applicable to very complex and large systems [Ste96].

The other common group of techniques to couple reaction and transport processes are the ones based on operator splitting. In these techniques, the reaction and transport terms are solved separately. Essentially, the results from the transport equation are sequentially plugged in as input for the equations solving the reactive part, while in turn the results of the reaction step are transferred back as input to the transport equations in the next time step [Ste96].

There are two classes of algorithms in operator splitting, namely a non-iterative and an iterative approach. For the non-iterative approach, the description provided above is almost complete. However, in order not to cause oscillations during application of the non-iterative operator splitting approach, the maximum time step length applied must obey the von Neumann criterion:

$$\frac{D\Delta t}{\Delta x^2} < \frac{1}{2} \tag{3.19}$$

In this equation D corresponds to the diffusion coefficient, Δt to the simulated time step length, while Δx is the spatial discretization.

Still, this method introduces some kind of error. To treat this, the iterative approach was developed. Here, during two time steps the coupling algorithm does mediate between reaction and transport algorithms until convergence in terms of e.g. concentrations is reached. The concrete implementation of the iterative approach is not clearly defined, since there are several methods possible [Ste96].

3.4 Reactive transport modeling approaches on different scales

There are two different approaches to solve reactive transport problems. On one hand, there are continuum approaches and on the other hand pore-scale transport methods. Both methods operate on different length and time scales. The main difference between both approaches is that pore-scale methods resolve the pore structure explicitly, while continuum transport models regard the porosity as an intrinsic property of the medium. Resolving the porosity explicitly allows for a more mechanistic modeling of the systems. However, pore-scale models are limited in time and length scales, while continuum models can operate on a wide range of applications. In the following sections a brief introduction of the two methods is given. However, in this work, the focus is on

a pore-scale modeling approach.

3.4.1 Continuum reactive transport modeling

Continuum reactive transport models solve the differential transport equations, presented in section 3.1, by discretization of the continuum equations. The general concept is to use representative elementary volumes (REVs), which capture the intrinsic properties of the medium, e.g. properties as porosity are not resolved explicitly. The size of the volume element must be chosen such that it reflects the required resolution. At the same time, the continuum description of the underlying system must still be valid.

A common approach in continuum modeling is to use meshes as spatial discretization and solve the governing equations for each node. The fineness of the mesh effectively controls the accuracy of the results in the spatial dimension. Often boundary conditions and interfaces are also implemented with a mesh approximation. In this context, a constant concentration interface, for instance when dissolving a mineral, is also imposed via a mesh, which approximates the surface of the grain [Mol15].

This is one of the reasons why continuum-based reactive transport modeling is usually applied on Darcy-scale. Darcy-scale means that the transport properties of the underlying pore structure are treated as an averaged bulk parameter. Furthermore, nodes in the pre-meshed domain of a continuum model can usually not reach for instance zero diffusivity without introducing numerical issues at the same time. Often this is circumvented by assigning very small values for the transport properties to the corresponding nodes. The evolution of the internal pore structure is still not covered in a mechanistic way, since the bulk is regarded as continuum. In reality, domains may be completely filled with non-diffusive solids, but its structure can evolve while moving physical boundaries.

There are different numerical techniques to perform the discretization. Depending on the scheme, the outcome may differ within the discretization accuracy. For example, the finite element method (FEM) and the finite volume method (FVM) have different control node locations. Thus, for instance, the interface locations may differ within the spatial discretization step.

There are several coupling codes following this technique, by coupling a geochemical solver with a continuum based transport code. One example is PhreeqC, which has an incorporated 1D transport module based on finite differences [Par13]. Some other examples for continuum scale reactive transport codes are depicted in table 3.1 [Ste15]. The table contains the underlying chemical solver and transport codes, if applicable.

Historically continuum based models were the first approach to simulate reactive transport systems. It is possible to use this approach to describe a large variety of systems, e.g. from short term lab experiments on centimeter scale up to repository systems on 100 m scales over 100,000s of years [Idi20,Nar14,Tri16].

3.4.2 Pore-scale reactive transport modeling

If it would be intended to use continuum approaches for simulations which resolve the pore structure, one would approximate grain boundaries with a mesh. This would be

Table 3.1: Selected examples of reactive transport codes based on continuum transport equations.

RTM code	transport	reaction	reference
iCP	COMSOL	PhreeqC	[Nar14]
OGS-GEMS	OpenGeoSys	GEMS	[Sha09]
HPx	HYDRUS	PhreeqC	[Jac05]
CrunchFlow	-	-	[Ste09]
PHT3D	MT3DMS	PhreeqC	[Pro10]

a static description of the grain geometry. In reality, however, due to dissolution the shape of the solid generally changes. To capture these possible geometrical alterations, an automatic remeshing process would be needed. This process is quite error-prone and computationally expensive. Given these shortcomings of continuum based approaches, in recent years pore-scale models were developed [Che98,Kan06,Lic07].

Classical pore-scale models treat solid and fluid domains in a distinct way. That said, the largest spatial scale is chosen to be able to distinguish between both domains and resolve solid surfaces. As an example, the model illustrated in figure 3.1, resolves quartz, calcium carbonate, clay and different iron containing phases domains explicitly. Furthermore, the growth of calcite and $FeCO_3$ on a $CaCO_3$ domain is contained in this model [Ste05a]. Essentially, in this resolution, concentration gradients are likely to be the driving force of reactions. On the other hand, in a continuum-scale model, the depicted phases would be mixed without any internal spatial information. At the same time, porosity would be an averaged property of the mixture and thus an effective diffusivity model would be needed.

It is known that microscopic heterogeneity may have significant effects on macroscopic transport properties such as permeability and effective diffusion coefficients [Mol15]. Pore-scale reactive transport models can thus be used to mechanistically describe the microscopic evolution of the pore structure and the heterogeneous distribution of hydrated phases and unhydrated binder components in cementitious materials. This approach can be used to address chemical degradation processes due to calcium leaching or carbonation of cementitious materials and their impact on physical and transport properties, such as porosity, pore-size distribution, permeability or diffusivity.

There are several approaches how to implement such pore-scale models. Examples for different methods of pore-scale techniques are for instance direct numerical simulation (DNS), Lattice-Boltzmann method (LBM), pore network modeling (PNM), or smooth particle hydrodynamic (SPH) [Yoo15]. Presenting all different approaches with their advantages and disadvantages would exceed the scope of this work. Focus is made on the Lattice-Boltzmann method, which is intended to be used as transport simulation method within this work. Several authors have successfully applied Lattice-Boltzmann (LB) based techniques to solve dissolution-precipitation governed problems (e.g. [Kan02]). A more thorough introduction to LBM is given below in section 3.5.

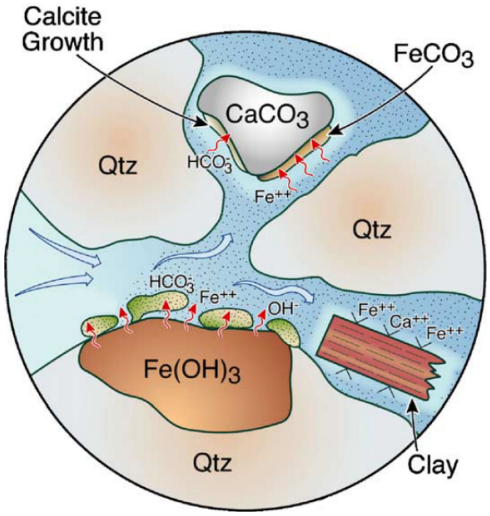

Figure 3.1: Schematics of pore-scale effects [Ste05a].

Although classical pore-scale models are an appealing approach to simulate reactive transport processes in a more mechanistic way, they are from their basic ideas limited to processes happening on small spatial and (consequentially) time scales. Depending on the pore size, the spatial resolution must resolve in the order of magnitude of 1 µm. Application of this discretization on macroscopic scale, e.g. on the scale of a repository system for nuclear waste, is virtually impossible with currently available computational capabilities. The approaches currently in development are rather to apply upscaling techniques. That means, microscopic and mesoscopic insights can be gained from pore-scale modeling approaches. In turn, these effects can be analyzed in terms of significance to macroscopic transport properties. The properties derived may be subsequently applied in upscaled models of a larger scope (e.g. [Lic07,Noi12,Poo22a]).

3.5 Lattice-Boltzmann method

3.5.1 Overview

Classical computational fluid dynamic (CFD) methods usually deal with direct numerical solution of the continuity and conservation laws, which might be for example diffusion and/or Navier-Stokes equations. The fluid in this regard is seen as a continuous medium which obeys certain continuity rules. In fact, each fluid is composed of microscopic particles which are interacting, just in a vast number and in a statistical way that it appears to be macroscopically a continuous medium. This view on the topic is successful for a vast amount of applications since, for example, the FEM gives satisfying results for a huge number of engineering applications. FEM uses a numerical discretization method

to solve the equations mentioned [Zie13, pp.1].

The LBM, on the other hand, is derived from a kinetic gas model (established as well-known Boltzmann equations in 1972 by Ludwig Boltzmann) which describes in its core the statistical mechanics behavior of particles and their interaction by elastic collisions [Suc01, p. 3]. Although initially aimed to give new insights into the thermodynamics of gases, it was subsequently shown that the theory of Boltzmann is consistent with continuum equations as the Navier-Stokes equation. The predecessors of the Lattice-Boltzmann methods were evolved from algorithms based on cellular automata namely lattice gas cellular automata (LGCA). In particular the HPP model, named after the initials of the authors Hardy, Pomeau and de Pazzis, is a foundation of the theoretical background of the Lattice-Boltzmann methods. However, the model revealed to be incomplete to derive the full Navier-Stokes equation [Wol05, pp.37]. An extension led to the Frisch-Hasslacher-Pomeau automaton (FHP) [Fri86], which was able to simulate the 2D Navier-Stokes equation [Suk07, pp.16]. Moreover, the LBM was first developed in the decade of 1980 [McN88] from the HPP and FHP models [Suc01, pp.17]. Since then, this method has shown its applicability and success in various fields and is still an active research field with respect to conceptual optimization.

Besides of the consistency with statistical mechanics and continuum equations, the Lattice-Boltzmann method has also advantages in terms of applicability compared to the earlier mentioned classical CFD methods. For example, the collision and streaming processes, which are the building blocks for the LBM, are computationally local. This means that the algorithmic parallelization on high performance computers is almost straight forward. Furthermore, geometric updates, e.g. with respect to pore structures, are rather easy to implement in LBM. Thus, multi-phase simulations, melting, dissolution and moving boundaries in general can be implemented explicitly. Of course, on the other hand, the so-called *standard*-Lattice-Boltzmann method has disadvantages. As later explained, the geometrical domain is usually represented as a lattice, thus rather limited to Cartesian aligned geometries. However, diagonal and roundly shaped geometries can either be approximated by a stair-case representation or by usage of recent developments in the field of off-lattice boundary conditions, which reduce this kind of geometrical inaccuracy. Furthermore, the simple Lattice-Boltzmann equations are derived with help of the Bhatnagar-Gross-Krook (BGK) approximation of the collision process of the Boltzmann equation. It has been analyzed by several authors that *standard* BGK-type LBM has its limits with simulating multi-phase flows with largely deviating viscosity or mixing media with different diffusion coefficients (e.g. [Suc01, pp.159], [Wol05, pp.102]). These kinds of limitations are addressed later on in this work, and it is explained how they were solved for the simulation of cementitious systems.

Nevertheless, in sections 3.5.2 through 3.5.5 the general concept of the derivation of the Lattice-Boltzmann method with the ideas of the Boltzmann kinetic gas theory is outlined. At the end, it is shown that also the Lattice-Boltzmann equation does actually recover the advection-diffusion equation, which is paramount for the simulation of solute transport phenomena at pore-scale.

The route starts at the assumptions Boltzmann made for deriving the Boltzmann equation followed by the concept, how the Boltzmann equation is discretized, from

which the general Lattice-Boltzmann equation emerges. Afterwards, it is shown how the Lattice-Boltzmann equation can be transformed into the advection-diffusion equation by the Chapman-Enscog multi-scale analysis [Cha70]. The multi-scale analysis part is the most complicated step in the derivations.

The derivation steps in this chapter are likely quite verbose for a reader with deeper mathematical background who would skip several steps for the sake of brevity. However, the aim of this detailed description is to give a better understanding for the broader audience. To the author's best knowledge, there is no comprehensive, correct and consistent presentation in literature in one standalone text book or publication. The information presented here are compiled from several literature references and translated into a consistent nomenclature. Additionally, several steps skipped in the derivations presented in most text books are explained in a more detailed way.

3.5.2 Introduction to the Boltzmann equation

The Boltzmann equation describes an ideal gas or fluid system in a statistical mechanics way. It assumes that there is a distribution function $f(x, v, t)$, which describes the number of gas molecules at time t, located at $x \pm dx$ with velocities $v \pm dv$ [Suc01, pp.4]. If there are no inter-particle collisions between two points in time (t and $t + dt$), the new position of the particles started at x are located at $x + dx = x + vdt$. Taking under consideration an external force F which exerts an acceleration $a = F/m$, where m is the particle's mass, the velocity will change to $v + dv = v + adt$ [Suk07, p.28]. Thus, it is possible to define:

$$f(x + dx, v + dv, t + dt) = f(x + vdt, v + adt, t + dt) \tag{3.20}$$

Following this, the particle number will not change, thus, the differential form is:

$$f(x + vdt, v + adt, t + dt)dxdv - f(x, v, t)dxdv = 0 \tag{3.21}$$

This equation is called streaming process. However, there are collisions involved, which leads to the effect that a number of particles will not arrive at $x + dx$ and that a number of particles will arrive additionally by another collision process originating from some neighboring points [Moh11, pp.15]. Introducing this effect, the RHS turns into the collision operator:

$$f(x + vdt, v + adt, t + dt)dxdv - f(x, v, t)dxdv = \Omega(f)dxdvdt \tag{3.22}$$

Dividing equation 3.22 by $dxdvdt$:

$$\frac{f(x + vdt, v + adt, t + dt) - f(x, v, t)}{dt} = \frac{df}{dt} = \Omega(f) \tag{3.23}$$

From previous definitions it is known that f is a function of x, v and t and thus:

$$df = \frac{\partial f}{\partial x}dx + \frac{\partial f}{\partial v}dv + \frac{\partial f}{\partial t}dt \tag{3.24}$$

Dividing by dt gives:

$$\frac{df}{dt} = \frac{\partial f}{\partial x}\frac{dx}{dt} + \frac{\partial f}{\partial v}\frac{dv}{dt} + \frac{\partial f}{\partial t} \tag{3.25}$$

Assuming $v = dx/dt$ (velocity) and $a = dv/dt$ (acceleration) the equation simplifies to:

$$\frac{df}{dt} = \frac{\partial f}{\partial x}v + \frac{\partial f}{\partial v}a + \frac{\partial f}{\partial t} \tag{3.26}$$

Therefore equation 3.23 can be expressed as:

$$\frac{\partial f}{\partial t} + \frac{\partial f}{\partial x}v + \frac{\partial f}{\partial v}a = \Omega(f) \tag{3.27}$$

For a system without an external force term, the acceleration term vanishes and the Boltzmann equation can be expressed in a general form with a gradient operator:

$$\frac{\partial f}{\partial t} + \vec{v} \cdot \vec{\nabla} f = \Omega(f) \tag{3.28}$$

Ω is a collision operator which depends on the particle distribution function f itself, while the equation is a so-called *integro-differential* equation [Moh11, p.17].

3.5.3 From the Boltzmann equation to the Lattice-Boltzmann equation

In the following paragraphs it will be shown how the Lattice-Boltzmann equation is derived from of the formerly determined general Boltzmann equation 3.28. The discretization of the velocity vector is the first step towards the Lattice-Boltzmann equation. In the following $\vec{e_i}$ is used as variable for the directional velocity vector i.

$$\frac{\partial f_i}{\partial t} + \vec{e_i} \cdot \vec{\nabla} f_i = \Omega_i \tag{3.29}$$

Discretization of the first term in time with a forward difference scheme yields:

$$\frac{\partial f_i}{\partial t} = \frac{f_i(\vec{x}, t + \Delta t) - f_i(\vec{x}, t)}{\Delta t} \tag{3.30}$$

Inserting in equation 3.29 and moving the space derivative to RHS results in:

$$\frac{f_i(\vec{x}, t + \Delta t) - f_i(\vec{x}, t)}{\Delta t} = -\vec{e_i} \cdot \vec{\nabla} f_i(\vec{x}, t) + \Omega(\vec{x}, t) \tag{3.31}$$

As next step, the spatial derivative is treated by an upwind scheme. The upwind treatment of the discrete Boltzmann equation means that the RHS in equation 3.31 must be evaluated one spatial step before the node in question at $\vec{x}$ [Mat10]. Thus, replacing $\vec{x}$ by $\vec{x} - \Delta\vec{x}$ gives:

$$\frac{f_i(\vec{x}, t + \Delta t) - f_i(\vec{x}, t)}{\Delta t} = -\vec{e_i} \cdot \vec{\nabla} f_i(\vec{x} - \Delta\vec{x}, t) + \Omega(\vec{x} - \Delta\vec{x}, t) \tag{3.32}$$

Substituting $\vec{x}$ with $\vec{x} + \vec{e_i}\Delta t$ and simplifying, the new equation defines the distribution functions for forward neighbors in the discrete direction $\vec{e_i}$:

$$\frac{f_i(\vec{x} + \Delta\vec{x}, t + \Delta t) - f_i(\vec{x} + \Delta\vec{x}, t)}{\Delta t} = -\vec{e_i} \cdot \vec{\nabla} f_i(\vec{x}, t) + \Omega(\vec{x}, t) \tag{3.33}$$

Since $\vec{e_i}$ is the discrete velocity it can be expanded to $\Delta\vec{x}/\Delta t$ and $\vec{\nabla} f$ is discretized with the same spacing as $\Delta\vec{x} = \vec{e_i}\Delta t$:

$$\vec{e_i} \cdot \vec{\nabla} f_i = \frac{\Delta x}{\Delta t} \frac{f_i(\vec{x} + \Delta\vec{x}, t) - f_i(\vec{x}, t)}{\Delta x} = \frac{f_i(\vec{x} + \Delta\vec{x}, t) - f_i(\vec{x}, t)}{\Delta t} \tag{3.34}$$

Subsequently inserted into equation 3.33 and after rearrangement, i.e. canceling of the $f_i(\vec{x} + \Delta\vec{x}, t)$ term and Δt, yields the general Lattice-Boltzmann equation:

$$f_i(\vec{x} + \Delta\vec{x}, t + \Delta t) = f_i(\vec{x}, t) + \Omega(\vec{x}, t) \tag{3.35}$$

There are different schemes which are defining the collision operator, e.g. single-relaxation-time (SRT) [Wol05, pp.163], two-relaxation-time (TRT) [Gin05a], or multi-relaxation-time (MRT) [Moh11, pp.101]. Usually, the collision operator needs also an implementation of the equilibrium function. The equilibrium functions must be defined in a way that is suitable for the simulated physical system.

For simplicity, only the single-relaxation-time (SRT) operator is introduced here. More complicated operators are discussed later in this work. The SRT operator is the simplest collision type and will be used in the Chapman-Enscog expansion later and thus allows the simplest derivation of the macroscopic equations. The derivation with more complex collision types would exceed the scope of this work. The SRT operator is derived from the so-called BGK collision approximation also used for approximating the collision integral of the Boltzmann equation [Bha54] [Moh11, pp.18].

$$\Omega_{BGK} = \frac{\Delta t}{\tau} \left(f_i^{eq}(\vec{x}, t) - f_i(\vec{x}, t) \right) \tag{3.36}$$

Thus, the complete BGK Lattice-Boltzmann equation reads:

$$f_i(\vec{x} + \Delta\vec{x}, t + \Delta t) = f_i(\vec{x}, t) + \frac{\Delta t}{\tau} \left(f_i^{eq}(\vec{x}, t) - f_i(\vec{x}, t) \right) \tag{3.37}$$

3.5.4 Moments of the distribution function and macroscopic constraints

In general, the Lattice-Boltzmann equation itself does not directly refer to the simulated physical system and its simulated equations, since it has a high degree of freedom in terms of mathematical ambiguity. Only with the idea in mind for interpreting the set of equations to simulate a certain physical system and to determine physical quantities it leads to a form allowing the numerical model to be useful for real world applications. Thus, additional inputs in form of constraints are mandatory [Che98]. Fundamental constraints are, for example, the conservation of mass and momentum.

Such constraints are plugged into the set of equations by defining the meaning of the moments of the particle distribution functions. One of such constraints needed to be satisfied for simulating the diffusion equation is the conservation of mass. Usually, the summation of the particle density function, called zeroth order moment, is set in relation to mass conservation (f_i is a short form of $f_i(\vec{x}, t)$), e.g. to the concentration c:

$$\sum_{i=0}^{q} f_i = c \tag{3.38}$$

It has to be noticed, that q is the number of microscopic particle velocities vectors. The same notation is used in this work unless otherwise stated. While for the advection-diffusion equation the mass conservation constraint is sufficient, for the simulation of the Navier-Stokes equation also the momentum must be conserved. Therefore, an additional constraint is set as first order moment of the distribution function:

$$\sum_{i=0}^{q} f_i \vec{e_i} = \vec{u}c \tag{3.39}$$

More physically demanding systems also need to have energy conservation implemented. To achieve this, the second order and higher moments are constrained as well. Since in this work energy conservation, in the hydrodynamic sense, is unimportant, it is omitted here for the sake of brevity.

3.5.5 From Lattice-Boltzmann to continuum equations: Chapman-Enscog expansion

The Chapman-Enscog expansion was initially developed to convert from gas kinetic Boltzmann equations to macroscopic continuum equations [Cha70]. The general idea of the application of the expansion technique on the discrete form of the Boltzmann equation is to show that the Lattice-Boltzmann equation is essentially solving the same equations as the continuum equations like the advection-diffusion equation or Navier-Stokes equation. In this work, focus is made on the advection-diffusion equation. For this analysis process, a series of approximations and derivations have to be performed.

The complete derivation is outlined in appendix A while the resulting equation reads:

$$\frac{\partial c}{\partial t} + \frac{\partial cu}{\partial x} = e_s^2 \left(\tau - \frac{1}{2}\right) \frac{\partial^2 c}{\partial x^2} + \left(\tau - \frac{1}{2}\right) u \cdot u \frac{\partial^2 c}{\partial x^2} \tag{3.40}$$

Finally, comparing equation 3.40, which was derived via Chapman-Enscog multi-scale analyses, with the continuum advection-diffusion equation

$$\frac{\partial c}{\partial t} + \frac{\partial cu}{\partial x} = D \frac{\partial^2 c}{\partial x^2} \tag{3.41}$$

shows that both equations are almost equivalent, if the second term on RHS in equation 3.40 is neglected and the diffusion coefficient D is reinterpreted as:

$$D_{LB} = e_s^2 \left(\tau - \frac{1}{2}\right) \tag{3.42}$$

Actually, the LHS and the first term on RHS are corresponding to the advection-diffusion equation. Equation 3.42 shows directly the relation between the Lattice-Boltzmann diffusion coefficient D_{LB} and purely numerical factors as the relaxation time τ and the so-called *lattice speed of sound* e_s^2. The second term on RHS in equation 3.40 is an error term, which is an artifact due to the usage of linear equilibrium function and an orthogonal lattice during the derivation of the sum of the second spatial derivative term (equation A.34). In this derivation this was chosen for the sake of simplicity. The error term then reads:

$$error = \left(\tau - \frac{1}{2}\right) u \cdot u \frac{\partial^2 c}{\partial x^2} \tag{3.43}$$

Higher order lattices with additional non-orthogonal microscopic velocity terms do not have this flaw and other researchers have also found this error [Lät07,Pat16a]. However, deeper analyses have revealed that the error term's correction is only about 1 % in the incompressible regime, i.e. for low velocities [Fle93]. Low velocity means a lattice velocity of lower than 0.3 Mach. Of course, this error term vanishes completely in case of a pure diffusive simulation without any advection term:

$$\frac{\partial c}{\partial t} = D_{LB} \frac{\partial^2 c}{\partial x^2} \tag{3.44}$$

All in all, in this chapter it was shown how the Lattice-Boltzmann equation was derived from the discretized form of the Boltzmann equation, and to the end with help of the Chapman-Enscog multi-scale technique, how it can be proven that it solves the continuum equations. In particular, the diffusion equation was recovered. With help of choosing other constraints and equilibrium functions also other physical models, such as the Navier-Stokes equation, can be solved. Since the diffusion process is the most important transport process in cementitious systems it was focused on recovering the diffusion equation.

Although some simplifications made are based on rough assumptions, the Chapman-

Enscog analyses have proven as powerful tool to mediate between the microscopic Lattice-Boltzmann equations and macroscopic continuum equations. By staying in certain boundaries of *secure* regimes, i.e. staying in the low Mach number incompressible regime, the derivations shown here are accurate enough to deliver physically meaningful results. More careful and accurate derivations, e.g. by respecting further error terms, can be used to explain inaccuracies in detail and to derive Lattice-Boltzmann models leading to more stable simulations and to more correct simulation results [Krä17]. For a more detailed view into the Chapman-Enscog based derivations, the reader is referred to more sophisticated text books (e.g. [Suc01,Wol05]) and publications (e.g. [Gin08,Vik14]) about Lattice-Boltzmann methods.

An interesting property of the Lattice-Boltzmann method is that the concentration gradient can be determined locally without any finite difference scheme. The local concentration gradient using a linear equilibrium function can be computed by using the first order moment of the LB velocity distribution [Per14]:

$$\frac{\partial c}{\partial x} = -\frac{1}{\tau e_s^2} \sum_{i=0}^{q} f_i \vec{e_i} \tag{3.45}$$

Essentially, this gradient can be used to calculate the diffusive flux by inserting it into equation 3.6. Additionally, equation 3.42 is used to substitute the diffusion coefficient. After simplification, the following equation is obtained, which allows to calculate the diffusive flux using only locally available properties:

$$J = \frac{1}{2\tau} \sum_{i=0}^{q} f_i \vec{e_i} \tag{3.46}$$

3.5.6 Formulation of the Lattice-Boltzmann method

The LBM is essentially the computational and algorithmic application of the mathematical foundation presented above. The equation mandatory to be numerically implemented consists of the Lattice-Boltzmann equation and the corresponding equilibrium functions and collision terms.

The algorithm can be implemented in different ways. For example, it could be thought that collision and streaming are different sub-steps in one time step iteration. Thus, the general Lattice-Boltzmann equation 3.35 can be split into a collision equation

$$f_i(\vec{x}, t)_c = \Omega(f_i(\vec{x}, t)) \tag{3.47}$$

and a streaming equation

$$f_i(\vec{x} + \Delta\vec{x}, t + \Delta t) = f_i(\vec{x}, t) + f_i(\vec{x}, t)_c \tag{3.48}$$

The effect of the collision operator is to relax the momentum towards the equilibrium. Effectively, the microscopic velocity distribution is distorted if evaluated after collision.

This has also an effect on the macroscopic variables as concentrations or flux. Thus, they should be evaluated after the streaming step. Although both operations are two distinct processes it is beneficial to implement both in one step as a swapping algorithm in order to save memory and increase CPU cache locality [Lat07].

The method itself has certain advantages compared to classical finite element methods. For example, geometric updates can be done in an explicit way by switching lattice node properties to bounce-back. In contrast, geometry updates in finite element methods must be done, for example, by more complicated remeshing and interpolation procedures. Additionally, parallelization is almost straight forward because most of the algorithm is almost purely local, i.e. ordinary collision steps only operate on variables available locally and streaming only affects direct neighboring lattice nodes.

Up to now only the basic and general framework of the Lattice-Boltzmann algorithm was introduced. Besides of the SRT/BGK collision model, there are TRT and MRT relaxation schemes. A similar derivation as presented above to recover the corresponding macroscopic equations and physical properties can be performed with TRT and MRT collision type. Due to the more complicated collision operator, the derivation is more complex than the one presented for the simple SRT scheme. For brevity in this work, it is referred to the original authors and textbooks [Gin08,Vik14,Moh11].

Additionally, the type of equilibrium function which is used in the collision operator is of great importance to simulate the corresponding physics. For example, to solve the Navier-Stokes equation, equilibrium functions up to second order are necessary. It is even possible to derive the Burnett equation with respecting higher order terms in the derivation and in the equilibrium function. Furthermore, there are special forms of equilibrium functions for example for porous media [Vik14].

3.5.7 Lattice structure and discrete velocity stencils

The Lattice-Boltzmann method uses a lattice which contains nodes. The nodes are usually connected to their corresponding neighbors with discrete velocity vectors (cf. figure 3.2). This is often called lattice type, discrete velocity scheme or stencil. In this work the terminology of velocity stencil is used.

In the Lattice-Boltzmann terminology, the lattice stencils are referred in a DnQm notation. A lattice stencil describes the connectivity of the microscopic discrete velocity vectors to neighboring lattice nodes. The n stands for the number of spatial dimensions, e.g. 2 for 2D and 3 for 3D, thus rendering the notation to D2Qm and D3Qm, respectively. The m in turn corresponds to the number of discrete microscopic velocities simulated. For example, D2Q5 means this is a lattice with two spatial dimensions and five discrete velocities. The meaning of the Q corresponds to the q variable within the moment sum equations mentioned in the derivation part of this chapter.

There are different lattice types which are satisfying different aspects of the mathematical model and stability behavior within simulations. For example, there are stencils with *rest velocity* (e.g. D1Q3 or D2Q5) and without it (e.g. D1Q2 or D2Q4). The rest velocity means the particle population with zero velocity vector, remaining at the lattice node during the streaming step, i.e. is not transported to neighboring nodes. Obviously,

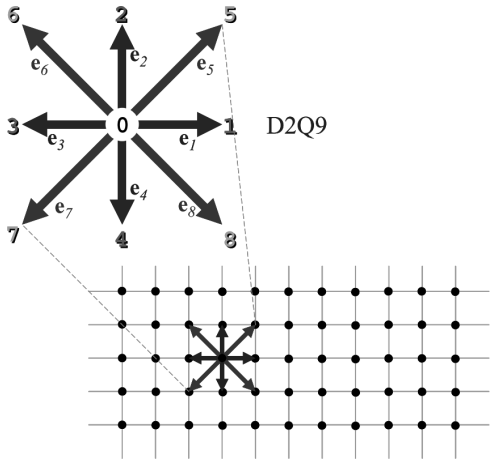

Figure 3.2: Schematics example of a 2D lattice (D2Q9 type) used for the Lattice-Boltzmann method [Suk07, p.32].

in the case of a 1D lattice to connect to the neighboring lattice nodes, there are only two populations mandatory. Meaning without a resting velocity population, there are only two populations, while including a rest velocity, three populations are necessary. However, lattice models with resting velocity show better computational stability [Per15]. Therefore, in the following only those with rest velocity are described in more detail and the rest velocity vectors are always referred to with the index zero.

A further property is the kind of connections the lattice nodes have to each other. There are lattice structures with orthogonal connections only and with additional diagonal connections (e.g. D2Q5 and D2Q9, respectively). Still, those lattice nodes are connected to the direct neighbors only. In contrast, there are even more sophisticated lattices which nodes are linked to nodes within a three node rim surrounding itself (e.g. D3Q39 and D3Q121, with more diagonal terms). High level lattices are mandatory for finding numerical solutions for equations beyond the Navier-Stokes equation (e.g. Burnett equation), which is also beyond the scope of this work. While the simplest Lattice-Boltzmann models are dealing with regular cartesian grid layouts, there are more exotic stencils with hexagonal layout (e.g. D2Q7) [Moh11, pp.89].

In addition to magnitude and direction of the discrete velocity vectors, there are the weighting factors w_i which need to be assigned to each vector. The distribution of the weightings is coupled to the type of lattice. One common feature of all stencils is that the sum of all weighting factors sums up to one, although due to geometrical and symmetry constraints the distribution is different. In the following, a selected set of typical cartesian stencils are presented with their vector components and weighting factors.

3.5.7.1 D2Q5

The simplest 2D layout with rest velocity is the D2Q5 structure. In the following, index zero corresponds to the rest velocity, while indices one through four correspond to link velocity vectors to the direct neighbors. There are no diagonal velocity populations present in this layout. A sketch of the connecting lines is show in figure 3.3.

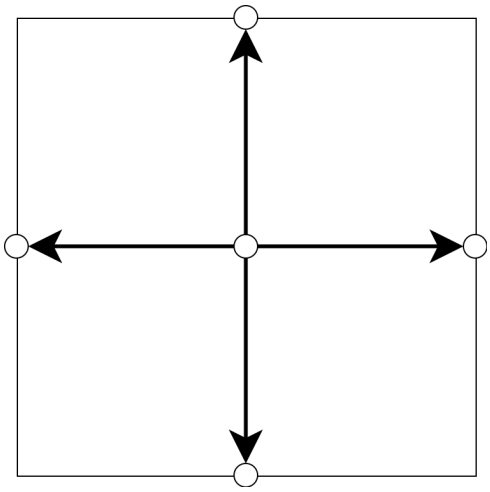

Figure 3.3: D2Q5 velocity stencil.

$$\begin{aligned} w_0 &= 1/3 \\ w_i &= 1/6 \quad i \in [1,4] \\ \vec{e}_0 &= (0,0) \\ \vec{e}_1 = (1,0) \quad \vec{e}_2 = (0,1) \quad \vec{e}_3 &= (-1,0) \quad \vec{e}_4 = (0,-1) \end{aligned} \tag{3.49}$$

This stencil is sufficient to simulate diffusive transport processes for a 2D model. In turn, for a numerical solution of the Navier-Stokes equation with the Lattice-Boltzmann method, this scheme is not applicable.

3.5.7.2 D2Q9

The D2Q9 lattice type is an extension of the D2Q5 layout. It adds diagonal links to the orthogonal connections of the D2Q5 type. The connection lines are depicted in figure 3.4

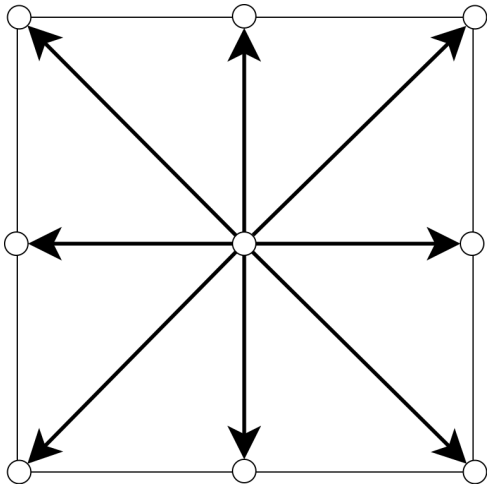

Figure 3.4: D2Q9 velocity stencil.

$$
\begin{aligned}
w_0 &= 4/9 \\
w_i &= 1/9 \quad i \in [1,4] \\
w_i &= 1/36 \quad i \in [5,8] \\
\vec{e}_0 &= (0,0) \\
\vec{e}_1 = (1,0) \quad \vec{e}_2 = (0,1) \quad \vec{e}_3 = (-1,0) \quad \vec{e}_4 &= (0,-1) \\
\vec{e}_5 = (1,1) \quad \vec{e}_6 = (-1,1) \quad \vec{e}_7 = (-1,-1) \quad \vec{e}_8 &= (1,-1)
\end{aligned}
\tag{3.50}
$$

For indices zero to four, the same description as for the D2Q5 layout in terms of directions is applicable, although the weighting factors w_i are different. Generally speaking, the diagonal vector components have a lower weight than the orthogonal connections. This lattice structure is more computationally intensive than D2Q5, but is capable of solving more complex transport and fluid dynamic equations.

3.5.7.3 D3Q7

The D2Q5 type is a 2D form of a stencil without diagonal components. Its extension to 3D leads to D3Q7. The outgoing velocity vectors are connecting to neighbors connected via the cube's faces only (see figure 3.5). The vectors with the indices one through six are the neighbor connecting directions.

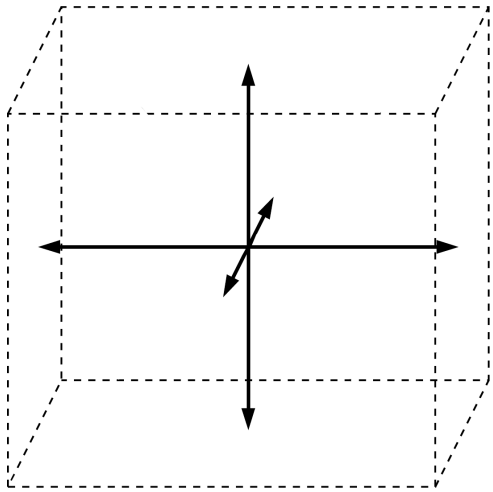

Figure 3.5: D3Q7 velocity stencil.

$$
\begin{aligned}
w_0 &= 1/4 \\
w_i &= 1/8 \quad i \in [1,6] \\
\vec{e}_0 &= (0,0,0) \\
\vec{e}_1 = (1,0,0) \quad \vec{e}_2 &= (0,1,0) \quad \vec{e}_3 = (-1,0,0) \\
\vec{e}_4 = (0,-1,0) \quad \vec{e}_5 &= (0,0,-1) \quad \vec{e}_6 = (0,0,1)
\end{aligned}
\tag{3.51}
$$

Similar to the D2Q5 structure, the numbers of velocity components are sufficient for solving the diffusion equation but not for the Navier-Stokes equation.

3.5.7.4 D3Q15

The last type of lattice structure presented here is the 15 velocity vector version of the cartesian 3D stencil. Basically, this is an extension of D3Q7 by diagonal vectors. The approach is similar to the extension of D2Q5 to D2Q9. The vector connections are shown in figure 3.6.

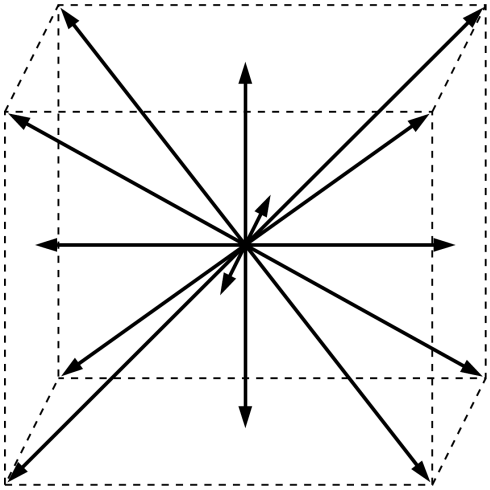

Figure 3.6: D3Q15 velocity stencil.

$$
\begin{aligned}
w_0 &= 2/9 \\
w_i &= 1/9 \quad i \in [1,6] \\
w_i &= 1/72 \quad i \in [7,14] \\
\vec{e}_0 &= (0,0,0) \\
\vec{e}_1 = (1,0,0) \quad \vec{e}_2 &= (0,1,0) \quad \vec{e}_3 = (-1,0,0) \\
\vec{e}_4 = (0,-1,0) \quad \vec{e}_5 &= (0,0,-1) \quad \vec{e}_6 = (0,0,1) \\
\vec{e}_7 = (1,1,1) \quad \vec{e}_8 &= (-1,1,1) \quad \vec{e}_9 = (-1,-1,1) \quad \vec{e}_{10} = (1,-1,1) \\
\vec{e}_{11} = (1,1,-1) \quad \vec{e}_{12} &= (-1,1,-1) \quad \vec{e}_{13} = (-1,-1,-1) \quad \vec{e}_{14} = (1,-1,-1)
\end{aligned}
\tag{3.52}
$$

Here, indices zero through six have the same meaning as for D3Q7, while the extended diagonal vectors are depicted with indices seven to 14. Again, due to the extension with diagonal links this stencil is more computationally intensive but allows for solving of more complex equations than the diffusion equation.

3.5.8 Collision operators

As already mentioned, there are several collision operators that have been developed for the Lattice-Boltzmann method. The simplest operator was already presented previously in equation 3.36, because a collision operator was required to perform the Chapman-Enscog multi-scale analysis. The choice of the operator depends not only on the physical property to be simulated but also on the combination with a corresponding equilibrium function. In this section, the collision operators analyzed and used in this work are only

outlined, while the combination of those yielding into a proper setup will be detailed later on in section 4.2.2.

3.5.8.1 Bounce-back

In principle, this operator just reflects the incoming particle distributions f_i^{in} back to their origin, hence the name bounce-back. This simple bounce-back algorithm can be applied to simulate a solid material.

$$f_i^{out} = f_{\hat{i}}^{in} \tag{3.53}$$

In this equation, the index $\hat{i}$ refers to the opposite direction than just a plain i. During the collision no relaxation towards equilibrium takes place. Since the particle pre-collision outgoing distribution function is undefined, the solid nodes are only computational entities, and no hydrodynamic properties or solute concentrations can be determined at those nodes. The same is true with regard to the determination of, e.g., solute concentration in solids, which is not a defined property.

In fact, the bounce-back collision imposes a no-slip condition midway between the solid and liquid node. If a slip condition is desired, a specular reflection algorithm would have to be implemented. However, this type of reflection would need more knowledge about the surrounding geometry. In case of non-diagonal lattice types (e.g. D2Q5), this does not matter, because the specular reflections would only be relevant for the diagonal microscopic Lattice-Boltzmann velocities (e.g. in the D2Q9 lattice stencil, see section 3.5.7).

3.5.8.2 Partial bounce-back

The main idea of a partial bounce-back collision is to simulate a partly hindered flux of fluid or solute. Although there are different ways in which this type of collision can be implemented, they have all in common that only a fraction of the incoming velocity populations are bounced back. In this work, it is focused on a mass conserving implementation of Walsh et al. [Wal09]. For this, between the ordinary SRT collision and streaming the incoming f_i^{in} and collided f_i^C populations are interpolated linearly with a modeling factor n_s. After that, the f_i^{out} populations are treated as usual and streamed to the neighboring nodes.

$$f_i^{out} = (1 - n_s)\, f_i^C + n_s f_{\hat{i}}^{in} \tag{3.54}$$

Again, the index $\hat{i}$ refers to the opposite direction. The limiting cases are when n_s reaches zero or one. A value of one corresponds to a pure bounce-back behavior as described above, while zero would fall back to a non-adjusted collision, i.e. simulating a non-hindered flux. A deeper analysis of the performance of this collision type is done later in the benchmark section 6.2.

3.5.8.3 Two-relaxation-time (TRT)

Although the SRT operator types are quite successful to simulate a large range of technical applications, certain limitations can show up yielding into numerical oscillations and/or inaccuracies. In the benchmark section 6.2 these issues are addressed in more detail. However, to overcome these limitations, the TRT collision scheme was developed.

The TRT collision splits the relaxation process into two steps, namely, relaxation with symmetric and asymmetric relaxation parameters [Moh11, pp.104]. With the TRT scheme, different physical conserved properties can be treated in a separate way. By this means, an increase in stability of the simulated macroscopic variables can be achieved [Gin05b]. The collision operator then reads:

$$\Omega_{TRT} = -\frac{\Delta t}{\tau_s}\left(f_i^s(\vec{x},t) - f_i^{seq}(\vec{x},t)\right) - \frac{\Delta t}{\tau_a}\left(f_i^a(\vec{x},t) - f_i^{aeq}(\vec{x},t)\right) \tag{3.55}$$

The symmetric $f_i^s(\vec{x},t)$ and asymmetric $f_i^a(\vec{x},t)$ populations are determined with:

$$f_i^s(\vec{x},t) = \frac{f_i + f_{\hat{i}}}{2} \tag{3.56}$$

$$f_i^a(\vec{x},t) = \frac{f_i - f_{\hat{i}}}{2} \tag{3.57}$$

Again, the indices with the hat $\hat{i}$ are corresponding to the opposite directions as i. The same way as for the incoming populations, the symmetric and asymmetric equilibrium functions ($f_i^{seq}(\vec{x},t)$ and $f_i^{aeq}(\vec{x},t)$, respectively) are determined.

In fact, the TRT collision type is a special case of the MRT collision. The general MRT collision type does perform a matrix multiplication with the particle distribution functions. In turn, TRT only relaxes with two different parameters instead of a whole matrix, thus it is a computational simplification compared to MRT. Additionally, the SRT collision can be seen as a special case of the TRT type. If both relaxation parameters, τ_s and τ_a reach the same value, equation 3.55 reduces to the simple SRT collision equation 3.36.

3.5.9 Equilibrium distribution functions

So far, the equilibrium distribution function was only mentioned but not defined. The equilibrium distribution function is usually used in the collision operator. In the Lattice-Boltzmann method the particle velocity distributions are relaxing towards the equilibrium with help of the collision operator. This is corresponding to Boltzmann's kinetic theory such that the velocity distribution of particles approaches the Maxwell-Boltzmann equilibrium. Since the Lattice-Boltzmann equation is based on a discretized form of the Boltzmann equation, also the equilibrium functions obey similar discretization aspects.

3.5.9.1 Standard

The standard Lattice-Boltzmann equilibrium function is derived by discretization of the Maxwell-Boltzmann equilibrium function. The Maxwell-Boltzmann distribution describes the probability that particles are in a certain interval of velocity dv.

$$f(\rho, v, T)dv = \rho \left(\frac{m}{2\pi k_b T}\right)^{d/2} e^{-\frac{m\nu^2}{2k_b T}} \tag{3.58}$$

In this equation d refers to the dimensional constant, i.e. equals to 3 for a 3D system. While ρ refers to the gas density in the original Maxwell-Boltzmann distribution function, in the framework of LBM it can be seen as the macroscopic variable to be simulated. In case of a hydrodynamic description (e.g. Navier-Stokes) it still refers to the fluid density, while in case of solving of the advection-diffusion equation it refers to solute concentration. Since advection-diffusion is the equation to be solved for porous media in this work, for further derivations it is replaced by the concentration c.

Furthermore, the relative particle velocity v in equation 3.58 can be extended to $\nu = v - u$, since ν is the fluctuation of the particle velocities around the macroscopic advective fluid flow velocity u, rendering v as the total velocity. Moreover, $m/(2k_bT)$ can be extracted and defined as a constant k. Inserting all modifications and respecting a 3D system yields to:

$$f(c, v, u) = c \left(\frac{k}{\pi}\right)^{3/2} e^{-k(v-u)^2} \tag{3.59}$$

Further expanding and separating the exponential terms gives:

$$f(c, v, u) = c \left(\frac{k}{\pi}\right)^{3/2} e^{-kv^2} e^{k2vu} e^{-ku^2} \tag{3.60}$$

Now, there are three factors besides of the concentration c:

$$w(v) = \left(\frac{k}{\pi}\right)^{3/2} e^{-kv^2} \tag{3.61}$$

$$A(v, u) = e^{k2vu} \tag{3.62}$$

$$B(u) = e^{-ku^2} \tag{3.63}$$

The first factor only depends on the absolute velocity v and will be further replaced by a discrete Lattice-Boltzmann weighting factor w. A and B are exponential functions, which will be expanded by a Taylor series. The Taylor series for the exponential function reads:

$$e^x = \sum_{n=0}^{\infty} \frac{x^n}{n!} = 1 + x + \frac{x^2}{2!} + \frac{x^3}{3!} + \frac{x^4}{4!} + ... \tag{3.64}$$

Inserting the series approximation into equation 3.60 and retaining terms up to second

order leads to:

$$f(c, v, u) = cw\left(1 + 2kvu + 2k^2(vu)^2 - ku^2\right) \tag{3.65}$$

As last step, the previously defined constant k is substituted by a discretized form of the *speed of sound* ($k = \frac{1}{2e_s^2}$, [Wol05, pp.168]) and the particle velocity is replaced by a discrete velocity vector $\vec{e_i}$:

$$f_i^{eq} = w_i c\left(1 + \frac{\vec{e_i} \cdot u}{e_s^2} + \frac{(\vec{e_i} \cdot \vec{u})^2}{2e_s^4} - \frac{\vec{u} \cdot \vec{u}}{2e_s^2}\right) \tag{3.66}$$

Equation 3.66 is the well-known Lattice-Boltzmann equilibrium function which treats advective velocity terms up to second order, which is sufficient to solve the Navier-Stokes equation for incompressible fluids. For advective-diffusive processes terms up to first order are sufficient. The equation simplifies to:

$$f_i^{eq} = w_i c\left(1 + \frac{\vec{e_i} \cdot \vec{u}_a}{e_s^2}\right) \tag{3.67}$$

The variable $\vec{u}_a$ corresponds to the advective fluid velocity and has to be set externally. For recovering the Navier-Stokes equation, equation 3.66 is mandatory because the quadratic velocity term must be respected. In this context u is also the fluid velocity but is calculated from the post-stream distribution function itself and not inserted from an external scalar field. Thus, the advective process must be solved in a distinct step for advection-diffusion simulations. This technique is also called *passive scalar* approach.

3.5.9.2 DV-SRT

The general idea of the *diffusion velocity* formulation is that the diffusion coefficient is split into a reference and a fluctuation around this value. The fluctuating value and concentration gradient is then interpreted as additional velocity term in the subsequent derivation [Per14].

$$D = D_{ref} + \tilde{D} \tag{3.68}$$

Following the derivation, the diffusive term is expressed as diffusion velocity $\vec{u}_d$ and added to the advective velocity $\vec{u}_a$.

$$\vec{u}_d = \frac{\frac{\tilde{D}}{\tau e_s^2}}{1 + \frac{\tilde{D}}{\tau e_s^2}}\left(\frac{\sum_i f_i \vec{e_i}}{c} - \vec{u}_a\right) \tag{3.69}$$

Furthermore, the diffusive velocity term has to be added to the advective term in equation 3.67 and yields to:

$$f_i^{eq} = w_i c\left(1 + \frac{\vec{e_i} \cdot (\vec{u}_d + \vec{u}_a)}{e_s^2}\right) \tag{3.70}$$

3.5.9.3 Partial bounce-back

The partial bounce-back (PBB) scheme evaluated in this work was developed by Walsh et al. [Wal09]. The authors reported using no specialized equilibrium function, thus the same as introduced in section 3.5.9.1. Thus, the ordinary *standard* equilibrium function 3.67, as derived above will be used in this work for all further evaluations using the PBB scheme.

3.5.9.4 P-TRT

In general, the TRT collision type can make use of the ordinary standard equilibrium functions as 3.67 or 3.66. However, there are specialized equilibrium functions in order to capture effects as intrinsic porosity. The equilibrium function to be presented here was published and analyzed in conjunction with the TRT collision operator [Vik14], accordingly it is named in this work as porosity-TRT (P-TRT) scheme.

The equilibrium function for all velocity vectors except of the resting population is defined as:

$$f_i^{eq} = \frac{c}{2}\left(c_\phi + \phi(\vec{e_i} \cdot \vec{u}) + \phi(\vec{u} \cdot \vec{u})\right) \quad i > 0 \tag{3.71}$$

ϕ stand for the medium's porosity while c_ϕ is a free parameter, which has to be chosen to satisfy stability. The rest velocity equilibrium is the complement:

$$f_0^{eq} = \phi c - \sum_1^q f_i^{eq} \tag{3.72}$$

The effective diffusion coefficient simulated is determined similar to the standard LBM scheme (see also equation 3.42), but with e_s^2 replaced by c_ϕ.

$$D_e^{LB} = c_\phi \left(\tau_a - \frac{1}{2}\right) \tag{3.73}$$

As already mentioned, c_ϕ is a free parameter to tune the simulation. Analysis of the P-TRT scheme revealed that it must be chosen within a range between zero and porosity divided by the model's dimensions d:

$$c_\phi \in \left[0, \frac{\phi}{d}\right] \tag{3.74}$$

Additionally, it has to be noted that the value for c_ϕ should be chosen as constant over the complete computational domain. Thus, the smallest porosity ϕ_{min} is governing the magnitude of c_ϕ:

$$c_\phi = \frac{\phi_{min}}{d} \tag{3.75}$$

In contrast to the ordinary SRT and TRT scheme, the P-TRT scheme does incorporate the porosity directly in the equilibrium function (see equation 3.71). A consequence is that the Lattice-Boltzmann velocity populations are *living* in an absolute amount (n)

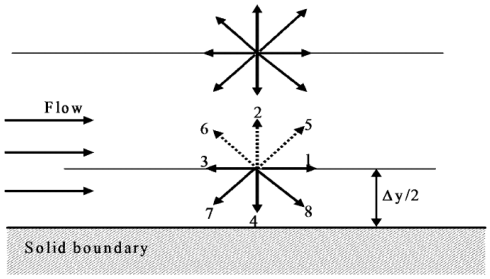

Figure 3.7: Illustration of the *wet* bounce-back closed boundary condition [Moh11, p.73].

domain instead of volume normalized amounts, i.e. concentrations. Following this, the first two moments of the distribution functions are:

$$\sum_{i=0}^{q} f_i = \phi c = n \tag{3.76}$$

$$\sum_{i=0}^{q} f_i e_i = \phi c u = n u \tag{3.77}$$

3.5.10 Boundary conditions

Similar as in the field of analysis of partial differential equations, a numerical simulation model does also require boundary conditions. They are important in the setup of the model to define what is beyond the boundaries of the model. With respect to various assumptions, they can for example be closed, constant or repetitive (periodic). This list is not exhaustive but the most important cases for this work.

3.5.10.1 Closed boundary

A closed boundary refers to an inert boundary imposing no transport, thus also called zero flux boundary. Within the Lattice-Boltzmann method there are several ways to impose a closed boundary condition. The most common approach is to apply a bounce-back condition. However, there are several conceptual types how to implement these [Moh11, pp.73]. The two most common variances are the so-called *wet* bounce-back (cf. figure 3.7) and full way bounce-back.

The full way bounce-back scheme refers to the same approach as described already in section 3.5.8.1, which just reflects incoming to outgoing populations during the collision step. This way, at the nodes at which this effect happens no macroscopic hydrodynamic properties can be determined. At the same time, they do not contribute to the simulation as a volume for solute [Flo11]. These nodes must only be regarded as computational entity.

On the other hand, the wet bounce-back still applies a proper collision operator,

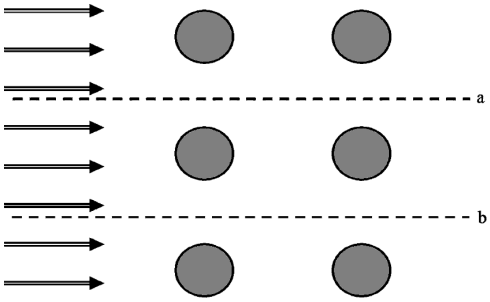

Figure 3.8: Example of a repeating geometry [Moh11, p. 80]. Gray colored obstacles are repeated vertically. This kind of repetition can be modeled with periodic boundary conditions by connecting surface a to b.

but the streaming step is altered instead. During streaming, the outgoing populations towards the boundary are redirected to the outgoing populations on the same node in the other direction. In the example of figure 3.7, populations 4, 7 and 8 are correspondingly assigned to 2, 5 and 6. This kind of boundary condition imposes a solid boundary which is one half of discretization width beyond the boundary node. Another difference to the full way bounce-back approach is that hydrodynamic properties are still obtainable. On the other hand, in order to implement such a wet boundary-condition, knowledge about the geometry is mandatory, while for the full way bounce-back scheme this does not apply. This is due to the fact that for flat, convex or concave corner nodes slightly different rules need to be applied.

3.5.10.2 Periodic boundary

In cases of a self-repeating geometry, it is beneficial to describe the geometrical model as a repeating sequence of the same geometry. For this kind of geometrical description of the model it is possible to implement the boundaries of the corresponding repeating dimensions as periodic (see also figure 3.8).

Effectively, this means that the solute or flux which is emitted on one side is re-injected on the other side. Within the Lattice-Boltzmann framework this can be quite easily achieved by assigning the outgoing distribution functions towards the boundary as incoming distribution function at the other end. For the example with the vertical periodicity in figure 3.8 this obeys the following relations:

$$f_{out}(x, a) = f_{in}(x, b) \tag{3.78}$$

$$f_{in}(x, a) = f_{out}(x, b) \tag{3.79}$$

By applying this rule, the periodic plane is located midway between the outer two lattice nodes which represent the last nodes in y direction. Similar conditions can be implemented the same way for arbitrary dimensions and axial directions.

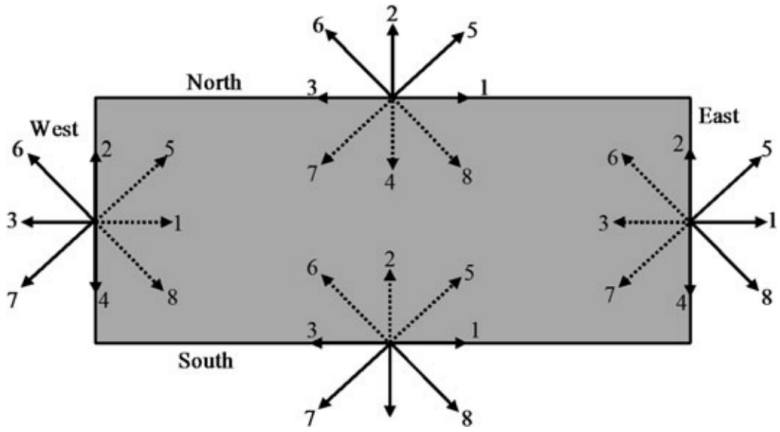

Figure 3.9: Schematic of lattice nodes at the boundary. The computational domain is depicted in gray and surrounded by west, south, east and north boundaries [Moh11, p. 76].

3.5.10.3 Constant concentration boundary (Dirichlet-type)

A Dirichlet-type boundary condition refers to a fixed value at the boundary. This value might be for example concentrations or density. As example, as shown in figure 3.9, a boundary node located at the south boundary must define incoming population values for velocity vectors 2, 5 and 6, since they affect the solution contained in the box. However, since the diffusion equation is to be solved in this work, it is sufficient to use Lattice-Boltzmann velocity stencils without diagonal terms to recover concentrations (see also section 3.5.7.1), i.e. for the south boundary, vectors 5 and 6 are not present.

Effectively, the only velocity vectors that need to be defined are 1, 2, 3, and 4 for west, south, east, and north, respectively. Based on this, a Dirichlet boundary condition can be implemented by determining the missing distribution function by calculating the difference between the boundary concentration c_b and the sum of all incoming distribution functions:

$$f_i = c_b - \sum_{j \neq i}^{q} f_j \tag{3.80}$$

Part II

Model development

4 Pore-scale reactive transport model development and implementation

4.1 General concept of the coupling code iPP

In the scope of this work a new coupling code named *iPP* was developed, which encompassed among other aspects the interaction between the geochemical solver and the transport code based on the Lattice-Boltzmann method. The coupling strategy used in this work was sequential non-iterative approach (SNIA). This means the time is marching in steps and within each iteration the updated concentrations are passed from the transport module to the reaction module. The transfer of the data from the transport algorithm to the chemical reaction solver is performed by *glue* code referred to as implementation of a coupling. As sketched in figure 4.1 the general idea is to programmatically transport the output data of the transport code as input for the chemical equilibrium calculations. In turn, the output of the chemical solver is used as input for the next transport calculation.

Besides of new solute concentrations after equilibration, also the change in solid phase composition and in porosity is determined. Porosity in turn has an effect on transport properties of the altered reaction cell, which is also fed back to the transport model. Within these cyclic iterations, a certain amount of simulated time is progressed. The time step worth for each iteration is determined by the transport model. After each

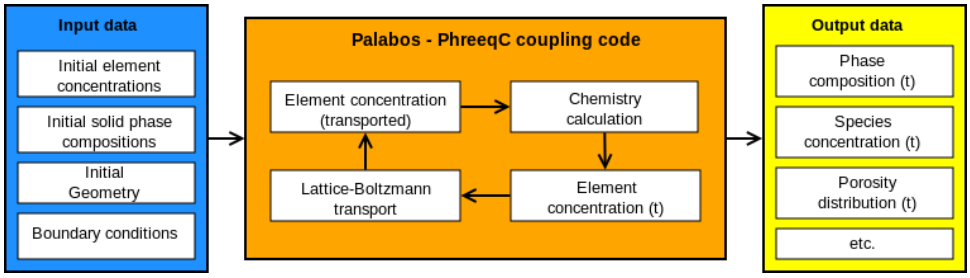

Figure 4.1: General idea of the coupling technique of iPP. The Lattice-Boltzmann code Palabos is incorporated within Lattice-Boltzmann transport while PhreeqC is executed within the chemistry calculation.

chemical reaction calculation the resulting properties can be written as output data (see also right-hand side of figure 4.1). For the implementation realized in this work, the output file format used is VTK [Sch06], which is a common file format supported by various scientific plotting tools (e.g. ParaView [Ahr05]).

The particular codes which were intended to couple are *Palabos* (**P**arallel **L**attice-**B**oltzmann **S**olver) and *PhreeqC*. Thus, the naming of iPP, is an acronym for **i**nterface **P**alabos **P**hreeqC. Palabos is a Lattice-Boltzmann programming framework. It shows promising capabilities and is easy to extend for specific purposes [Lat21]. On the other hand, PhreeqC is a well known, tested and validated geochemical speciation code, which solves equations based on the law of mass action [Par13].

4.2 Implementation of the Lattice-Boltzmann transport code

4.2.1 Lattice-Boltzmann framework Palabos

There are several LB solver implementations described in literature, e.g. HemeLB [Maz08], LB3D [Sch17], OpenLB [Kra21], PowerFlow [Loc02], Palabos [Lat21], SailFish [Jan14] and Yantra [Pat17]. Some of them are freely available and published under an open source license (e.g. OpenLB and Palabos), while the source code of others are either unpublished or under a commercial closed source license (e.g. PowerFlow). Moreover, the different codes are implemented in different programming languages as C, C++, Python or Fortran. Some implementations are even focused to run on accelerated graphics cards hardware as general-purpose computing graphics processing units (GPGPUs) infrastructure (e.g. SailFish). However, most of the codes listed here do not deal with the chemical reaction part and would need extensions to be coupled with a chemical solver.

In this work LBM was chosen because the method itself satisfies the requirement for flexible implementations of internal boundary conditions and efficient parallelization. A good CPU runtime performance is required, because of the expected complexity of the simulations dealing in particular with cementitious systems. In the model development section the Palabos Lattice-Boltzmann framework will be used as basis for the implementation of the transport model. Palabos is available under a free license and provides a proper foundation and infrastructure and has been tested in several benchmarks [Lat21]. Other codes have been revealed as not fulfilling the requirements or were not available freely. An accessible source code was valuable for the developments in this work to be able to extend the implementations as required. Although, for example, Yantra is a full reactive transport code coupled with PhreeqC, the code was not freely available at the start of this work and later inspections have revealed shortcomings in performance and software design. Palabos, and the derived implementations done for this work, deal much better with high performance computing aspects. Moreover, since plenty of extensions were required to tackle several effects in the reactive transport simulation, a sound foundation in software design of the underlying LBM code was mandatory, which

is actually provided by Palabos.

Palabos is a LBM programming framework which includes C++ class libraries which help to implement solutions for certain physical problems such as computational fluid dynamics with a Lattice Boltzmann approach. The library itself does not contain any command line or graphical user interface, thus from the Palabos point of view each problem has to be implemented in a programmatic way. As already mentioned, Palabos is implemented in C++ and thus the native way to make use of Palabos is to use the C++ programming interfaces. Additionally, there are wrappers for Java and Python but for the sake of performance they were not evaluated in the scope of the iPP development. The Palabos code is freely available under an open source license (AGPLv3). Therefore, derived software products must also be released under a GPL compatible license.

Although Palabos features already a vast amount of code, which is immediately capable of solving a lot of fluid dynamics problems [Lat21], the framework was just a foundation of the transport model developed for iPP. Nevertheless, Palabos implements already most of the needed framework for parallelization on shared and distributed memory computational models. Palabos as foundation with all its capability to extend and exchange parts of the Lattice-Boltzmann algorithms helped to speed up the development process, aiming to produce a reactive transport simulator for cementitious materials at pore-scale.

Palabos contains only the basic framework and some specialized collision models for Lattice-Boltzmann simulations. For example, there are already several implementations present for solving advective-diffusive and Navier-Stokes problems. Besides of SRT/BGK approaches, it contains also some sophisticated implementations for instance for regularized [Lat06] and entropic Lattice-Boltzmann collision operators. Palabos incorporates techniques for multi-phase flows and multi-fluid components as well. Multi-phase refers to separated phases as liquid and gas. At the same time, the gas and liquid can consist of the same component, e.g. water and water vapor [Suk07, pp.67]. Moreover, besides simple on-lattice boundary conditions as bounce-back, a set of different implementations for more complex and exotic off-lattice boundary conditions are present, e.g. Bouzidi, Filippova and Hänel and Guo conditions [Lat21], which are not detailed in this work.

4.2.2 Combination of equilibrium functions and collision operator and Palabos extensions

In the scope of this work, a large range of diffusivities are to be dealt with. Although in the Lattice-Boltzmann framework an arbitrary diffusion coefficient for one specific domain can be assumed, high contrasts in diffusion coefficients to other domains are of a special challenge. For the simple standard SRT scheme, the only mechanism to tune the diffusion coefficients is the relaxation parameter τ. Depending on the contrast of the diffusion coefficients, this might lead into numerical stability issues of the Lattice-Boltzmann transport simulation. However, there are other schemes which allow more flexibility.

Up to now, only the types of collision operators and equilibrium functions were pre-

Table 4.1: Analyzed Lattice-Boltzmann schemes and combinations treated in this work. The labels in the brackets indicate the equations referred to. For details the reader is advised to look up the corresponding derivations.

scheme	equilibrium function	collision operator	reference
SRT	linear (3.67)	SRT (3.36)	[Moh11,Yoo15]
PBB	linear (3.67)	PBB (SRT) (3.54)	[Wal09]
DV-SRT	DV (linear) (3.70)	SRT (3.36)	[Per14]
P-TRT	P-TRT (3.71)	TRT (3.55)	[Vik14]

sented. In order to set up a properly working simulation, a meaningful combination of these has to be chosen. The combinations analyzed in this work are depicted in table 4.1. These schemes have been chosen because of their simplicity to implement and promising properties to deal with a higher contrast of diffusion coefficients. The combinations listed in table 4.1 are called Lattice-Boltzmann schemes and ordered in increasing complexity. The fist column refers to the abbreviation used later on in this work. The abbreviations are standing for:

- SRT: (Standard) single-relaxation-time
- PBB: Partial bounce-back
- DV-SRT: Diffusion velocity - single-relaxation-time
- P-TRT: Porosity - two-relaxation-time

Important to notice is that SRT, PBB and DV are all single relaxation time schemes. However, PBB and DV are extended versions of it. If in this work the term SRT is used, it means the simple standard SRT scheme without any extension. At the same time, in this work the term TRT is used interchangeable to P-TRT and refers to the porosity aware TRT scheme. Since each of the depicted Lattice-Boltzmann schemes has benefits and drawbacks they are analyzed in more detail. The results with respect to the applicability on high contrasts of diffusion coefficients is outlined in the benchmark section 6.2.

The upstream Palabos version provides already the simple SRT scheme as implementation for advective-diffusive transport. However, in the starting phase of this work, there was no implementation of the DV [Per14] approach existing. With later versions of Palabos, a simple implementation but with fixed diffusivity factor was introduced, which still does not fulfill the requirements of this work. Moreover, there is a basic TRT collision operator implementation for solving the Navier-Stokes equation, but with a fixed symmetric relaxation parameter of 1.1. At the same time no implementation of the porosity aware P-TRT [Gin08,Vik14] operator was available nor any implementation serving diffusivity capabilities at all. Thus, the algorithms for partial-bounce-back [Wal09], DV-SRT [Per14] and P-TRT [Vik14] were implemented in the scope of this thesis as an extension of Palabos to be used in the framework of iPP.

4.2.3 Parametrization of the P-TRT scheme

While the simple standard SRT approach allows to tune the simulated diffusion coefficient or viscosity with only one value via the relaxation parameter τ, the TRT approach uses two parameters, τ_a and τ_s. Usually, the asymmetrical relaxation parameter τ_a is determined on the basis of the desired transport property, while the symmetrical parameter τ_s is chosen to optimize stability. Mathematical analyses have revealed that there is an intrinsic relation between both relaxation parameters which obeys [Gin10]:

$$M = \left(\tau_s - \frac{1}{2}\right)\left(\tau_a - \frac{1}{2}\right) \tag{4.1}$$

In equation 4.1, the value M corresponds to a so-called *magic* parameter. If the *magic* value is chosen properly, the stability of the simulation is ensured. With help of deeper analyses, a value of $1/4$ was obtained, whose choice leads to an independent stability disregarding which values for τ_a and τ_s were chosen [Gin10]. Thus, for this work the same *magic* parameter was adopted.

Moreover, the P-TRT scheme uses a variable c_ϕ, which needs a proper parametrization. According to equation 3.75, the value of c_ϕ must be chosen in a valid interval to ensure numerical stability. In order to obtain similar stability results irrespective of dimension, for all simulations the value for d in equation 3.75 was set to 3. Thus, the relation reads:

$$c_\phi = \frac{\phi_{min}}{3} \tag{4.2}$$

4.2.4 Unit conversion and reference diffusivity

Unit conversion within the domain of the Lattice-Boltzmann method is of importance to be understood initially, before grasping scaling effects of the simulations. The conversion is an intrinsic property of the method and is different to most other transport simulation methods, e.g. FEM.

As the Lattice-Boltzmann method is a discretized form of the statistical mechanics theory also time and space are discretized. Usually all Lattice-Boltzmann computations are performed in *lattice length* and *lattice time units*. It is numerically beneficial to express lattice length units (lu) dimensionless, i.e. the spatial and temporal discretization are always one unit apart and are without unit. Furthermore, the discretized velocity vectors in the Lattice-Boltzmann space are defined as spatial lattice units per discrete lattice time (lu/ltu). The time between two consecutive iteration steps must be coupled via the lattice speed.

Obviously, the spatial and temporal lattice units are different from the physical units the model is set up for. Thus, there are conversion factors required to translate between physical and lattice units. In the following, all conversion factors for the corresponding property are denoted with the subscript of c, e.g., L_c for the factor for length. The mapping between both systems can be done for all macroscopic quantities as length, time, energy, concentration, etc.

Length mapping is the basic and easiest property to convert. Assuming that the spatial discretization between two lattice nodes is Δx and lattice units are set to 1 lu, the spatial conversion factor is just:

$$L_c = \frac{\Delta x}{1lu} \tag{4.3}$$

As already mentioned, the velocity is also normalized to 1 lu/ltu thus requiring a relation for time conversion. This strongly depends on the physical system the Lattice-Boltzmann formulation is supposed to solve, e.g. diffusion or Navier-Stokes equation. For the sake of simplicity and relevance, the relation with respect to the diffusion equation is outlined here.

The physical diffusion coefficient D is defined as a product of the conversion factor D_c and the Lattice-Boltzmann diffusion coefficient D_{LB} as:

$$D = D_{LB}\, D_c \tag{4.4}$$

From the units of the diffusion coefficient ($\mathrm{m^2\,s^{-1}}$) it is known that there must be a conversion relation:

$$D_c = \frac{L_c^2}{T_c} \tag{4.5}$$

The relation between diffusion coefficient and the relaxation time is given by (cf. section 3.5.5):

$$D_{LB} = e_s^2 \left(\tau - \frac{1}{2}\right) \tag{4.6}$$

Combining equation 4.5 and 4.4, inserting in 4.6, and solving for the time conversion factor T_c leads to:

$$\Delta t = T_c = \frac{L_c^2}{D} e_s^2 \left(\tau - \frac{1}{2}\right) \tag{4.7}$$

Essentially, T_c equals to the amount of time one Lattice-Boltzmann iteration is worth, hence also Δt. This relation was derived via the macroscopic property of the diffusion coefficient. It contains only the spatial discretization, the macroscopic diffusion coefficient, and the relaxation parameter τ. It is interesting to notice, that the temporal discretization is directly bound to the diffusion coefficient and the spatial discretization. Thus, the Lattice-Boltzmann method does not allow to arbitrarily chose the magnitudes of time scales without changing τ. The choice of τ, however, is limited due to stability constrains. From equations 4.6 and 4.7 it is already deducible that τ cannot achieve values lower than $1/2$, without implying nonphysical conditions, i.e. a negative diffusion coefficient and a negative time step, respectively. Additionally, analyses about the stability range are conducted in the benchmark section 6.2.2.

Since Lattice-Boltzmann simulations are agnostic of physical units, i.e. dimensionless, also the Lattice-Boltzmann variant of the diffusion coefficient has no units. In fact, the Lattice-Boltzmann method has no concept of a diffusion coefficient at all and all algorithms are just using the relaxation parameter τ. Following this, the physical diffusion

coefficient is regarded as a conversion factor between spatial discretization and time discretization. Thus, the pure numerical result of a Lattice-Boltzmann simulation is irrespective from the assumed physical dimensions, i.e. there is no concept of a definition of an absolute physical size or diffusion coefficient for a domain. Rather an assumption of a *reference diffusion coefficient* allows then a conversion between space and time. This means, all diffusion coefficients in a Lattice-Boltzmann simulation are relative to a *reference diffusion coefficient*.

As an example, it is assumed that the spatial discretization is 1 mm while the reference diffusion coefficient D_{ref} is set to $1.0 \times 10^{-9}\,\mathrm{m^2\,s^{-1}}$. Using equation 4.7 and a reference relaxation parameter τ of unity, the resulting temporal discretization is 166.7 s. Now, it is assumed that a domain reflects an effective diffusion coefficient D_e of value $1.0 \times 10^{-10}\,\mathrm{m^2\,s^{-1}}$. Since this is a tenth of the reference value, then the τ parameter for this domain must be adjusted accordingly. Dividing the diffusion coefficient by the reference and using equation 4.6 gives:

$$\frac{D_e}{D_{ref}} = \frac{e_s^2\left(\tau - \frac{1}{2}\right)}{e_s^2\left(\tau_{ref} - \frac{1}{2}\right)} \tag{4.8}$$

After simplification and solving for τ:

$$\tau = \frac{D_e}{D_{ref}}\left(\tau_{ref} - \frac{1}{2}\right) + \frac{1}{2} \tag{4.9}$$

Under adoption of the physical values mentioned before, a relaxation parameter of $\tau = 0.55$ is obtained. If the model would only consist of domains with a diffusion coefficient of $1.0 \times 10^{-10}\,\mathrm{m^2\,s^{-1}}$, it would make sense to set the reference value to the same value. That way the simulation would run more efficient with respect to time steps. It is of course possible to increase the length of the time steps to some extent, by adjusting the reference relaxation parameter, in order to achieve a faster running simulation. However, this is impossible to do indefinitely without causing numerical oscillations and instabilities. A deeper analysis of numerical stability is presented in section 6.2.2.

Equation 4.7 applies to a typical simple SRT Lattice-Boltzmann scheme. In the case of a P-TRT scheme the conversion is more complicated, because the porosity and the related c_ϕ factor is involved:

$$\Delta t = T_c = \frac{L_c^2}{D} c_\phi \left(\tau_a - \frac{1}{2}\right) \tag{4.10}$$

Equation 4.10 defines the time step by using the asymmetric relaxation parameter τ_a. The symmetric relaxation parameter τ_s is calculated on-the-fly with help of the *magic number* of $1/4$ and equation 4.1 [Vik14].

4.3 Geochemical solver PhreeqC

4.3.1 Overview

For solving the chemical equilibrium a law of mass action approach was chosen. Freely available implementations of this technique have been tested for several decades, e.g. PhreeqC [Par13]. Several authors have incorporated the law of mass action approaches into reactive transport models (e.g. [Nar14]) and applied to cementitious systems as well (e.g. [Mar15,Pat18b]).

PhreeqC is a computer program, which is capable of calculating chemical reactions in aqueous systems. It is based on the equilibrium chemistry of aqueous solutions reacting with other phases as solid minerals, gases, solid solutions, etc. The approach to solve such problems is to apply the law of mass action and solve those equations numerically. Initial development took place already in 1980ies as *PHREEQE*. The initial acronym stands for **pH**-**RE**dox-**EQ**uilibrium. *PHREEQE* was implemented in FORTRAN and extended in the following years to support for example the solving of 1D diffusion problems.

In 1995 *PHREEQE* was ported to the C programming language and called PhreeqC. Apart from the porting to a more modern programming language, version 1 of PhreeqC was extended by capabilities to support more features including 1D advective transport, gas-phase and ion exchange equilibria. Subsequently, version 2 evolved which added features for solving problems like solid solution equilibria and kinetically controlled reactions. Eventually, with the third generation of PhreeqC, the algorithmic foundation to numerically solve stiff equations stemming from kinetic reactions and complex equilibrium setups were enhanced. Those revised algorithms allow to solve such problems in a more robust way.

Additionally, the code was refactored to bring into another form called *IPhreeqC* [Cha11]. This form allowed for the first time to use the code in another program to couple other algorithm and techniques to PhreeqC in a rather efficient way. Before that development, input files for the batch version of PhreeqC had to be written and re-read from PhreeqC each time. Writing files and re-reading them is a very inefficient way to passing data in a computer. However, IPhreeqC uses a string-based programming interface. Converting numerical values as floating point values to strings and back is again rather inefficient.

Finally, the most recent official achievement in the PhreeqC development process is the emergence of *PhreeqcRM*. The RM stands for *reaction module*. This version of PhreeqC is again improved compared to the IPhreeqC version in the sense that most of the data are no more passed via std::string or character array data types, which removes conversion overhead between numerical values and text based representations [Par15].

4.3.2 Saturation index

PhreeqC defines saturation with respect to phases in the form of *saturation indices* SI. The SI itself is the logarithmic saturation level of the solution:

$$SI = \log_{10}(SR) = \log_{10}\left(\frac{IAP}{K}\right) = \log_{10}(IAP) - \log_{10}(K) \tag{4.11}$$

In this equation IAP stands for *ion activity product*, K is the equilibrium constant and their ratio is the saturation ratio SR. The IAP is determined by the chemical activity a^{aq} of the species involved to form a specific phase, i.e. the concentration and some chemical activity model [Par13]. The resulting equation, omitting the activity model itself, reads (compare also to the general LMA equation 3.16):

$$IAP = \prod (a_i^{aq})^m \tag{4.12}$$

A SI value of zero corresponds to thermodynamic equilibrium, while values higher than zero indicate supersaturation. Furthermore, the PhreeqC input requires the *target* saturation index SI_T. If this is set to zero, PhreeqC simulates equilibrium conditions. PhreeqC tries to reach this target value by dissolving or precipitating solids as long there is either solid phase present or solute in the solution, respectively.

4.4 Coupling code iPP

4.4.1 Coupling scheme

4.4.1.1 Overview

Although the general coupling approach in iPP was already outlined, there are some more aspects to treat. In case of pore-scale reactive transport modeling one must distinguish between *homogeneous* and *heterogeneous* source and sink terms. The homogeneous reaction term corresponds to source and sink terms originating from the same reaction cell. For example, the precipitation of solids by supersaturation in a liquid reaction cell, which then ends in local mineralogical changes. On the other hand, there is a heterogeneous reaction term which alters adjacent reaction cells. For instance, when a cell is completely filled with some solid which does not contain any pore space by its own and is dissolving by equilibrating with one or more adjacent liquid cells. This kind of solid cells do not have any homogeneous reaction terms but have an effect on adjacent ones. In this section, the treatment of these aspects within iPP is explained while comparing to approaches used in other coupling codes.

Moreover, the initialization process with respect to equilibria, porosity and mass conservation is of importance. Initially, all reaction cells need to be initialized with input data. This encompasses boundary conditions, microstructure, phase compositions and solute concentrations. The initial phase composition given might not be in perfect equilibrium with the solution, which can cause dissolution or precipitation of solid phases,

which in turn alters the porosity. Upon porosity change, the solution is treated as if the same total amount of solute is contained in a modified pore volume which effectively changes the solute concentrations. These changes are usually quite small but cannot be neglected without violating the conservation of mass. The effect can be seen analogous to the compression or decompression of gases, although no real change of hydrodynamic pressure is simulated in the scope of this work. Thus, the initialization is also done in an iterative way without transport, to gain a stable system before starting the reactive transport calculation. Afterwards, the time marching is executed. The overall iteration reads:

1. Run transport module
2. Calculate post-transport concentrations
3. Update state in reaction module
4. Run reaction module
5. Update state in transport module
6. Write results if necessary
7. Repeat at 1 until end of simulation

The reaction module step (4) itself is separated into more sub-steps, which are treating various aspects of the dissolution and precipitation effects. A more detailed description of the scheme which is running in the reaction module is:

1. Run homogeneous reactions
2. Correct concentration by porosity change
3. Run heterogeneous reactions
4. Retrieve post-reaction concentrations and solid phase compositions from PhreeqC
5. Calculate post-reaction porosity
6. Treat negative porosities
7. Calculate new diffusion coefficients for transport module

As shown in the scheme above, first the homogeneous reactions are evaluated and afterwards the concentrations are corrected for porosity changes as described above. The resulting new concentrations are retrieved and saved intermediately. Afterwards, with help of the molar volumes of solids, the new solid phase compositions are used to convert to post-reaction porosity values. Note that the amounts of solid phases are specified in terms of concentration units (e.g. $\mathrm{mol\,L^{-1}}$). That way the numerical value is independent of the spatial discretization chosen for the simulations.

Since in rare cases an undershooting of the porosity lower than zero might occur, a mass conserved treatment of this non-physical state is applied. During the treatment the concentrations may be adjusted again. As last step, for each cell the new diffusion coefficients are calculated with help of porosity and solid phase composition, depending on the diffusivity model in use.

4.4.1.2 Homogeneous reaction term

The calculation of the homogeneous reaction term is relatively simple and well described in the literature, in contrast to the implementation of a heterogeneous reaction term. However, it is important to take some effects into consideration. As already mentioned, during dissolution and precipitation porosity can change, leading to a change in the solution volume. Depending on the porosity/diffusivity model used, newly formed precipitate can cause a switch of the reaction node to a heterogeneous reaction mode. Heterogeneous nodes do not participate in the transport of solute. In any case, changes in porosity cause changes in concentrations, which is similar to compression or decompression of gases. Without accounting for this effect, mass conservation is not guaranteed. Generally speaking, the total amount reaction term R_n is the difference between post-reaction n_r and post-transport n_t amounts of a solute.

$$R_n = n_r - n_t \tag{4.13}$$

Both total amount terms can be rewritten by the product of concentrations and corresponding porosities. Thus, the molar balance is converted to a concentration domain:

$$R_n = c_r\phi_r - c_t\phi_t \tag{4.14}$$

In order to recast the reaction term into the concentration domain, the total amount term must be normalized by the porosity:

$$R_c = \frac{R_n}{\phi} \tag{4.15}$$

To incorporate the source term, the general Lattice-Boltzmann equation is extended by the source term S:

$$f_i(\vec{x} + \Delta\vec{x}, t + \Delta t) = f_i(\vec{x}, t) + \Omega + S \tag{4.16}$$

Depending on the Lattice-Boltzmann scheme used, the source term must be defined accordingly. In absence of a velocity term, the SRT equilibrium equation reads:

$$f_i^{eq} = w_i c \tag{4.17}$$

Thus, it can be deduced that the additional source term has to be defined as:

$$S_i^{SRT} = w_i R_c \tag{4.18}$$

Similar to equation 4.17, the P-TRT equilibrium equation simplifies to:

$$f_{i>0}^{eq} = \frac{c_\phi}{2} c \tag{4.19}$$

The definition for the rest velocity remains the same:

$$f_0^{eq} = \phi c - \sum_1^n f_i^{eq} \tag{4.20}$$

Using the same deduction as for SRT, the source term for different velocity components is defined as:

$$S_{i>1}^{PTRT} = \frac{c_\phi}{2} R_c \tag{4.21}$$

Corresponding to equation 4.20 the rest velocity source term is:

$$S_0^{PTRT} = R_n - \sum_1^n S_i^{PTRT} \tag{4.22}$$

Thus, when homogeneous reactions occur in the liquid phase, a non-zero source term in the LB equation appears.

4.4.1.3 Heterogeneous reaction term

Heterogeneous reaction terms are usually implemented as ordinary LBM boundary condition [Yoo15]. Many of these implementations depend on geometrical properties at the fluid/solid interface such as surface normal [Hio13,Yu10], fluid node distance to solid interface [Lal03] or even boundary location movement and momentum transfer [Bou01]. Additionally, the reaction is often described as reaction rate instead of equilibrium condition at the surface [Che14,Hub11,Kan02]. Most of these approaches have in common that a non-negligible amount of bookkeeping about interface nodes and their topological features needs to be detected and updated during runtime.

Another approach is to introduce the heterogeneous reaction term as a pseudo homogeneous term adjacent to the solid interface node [Pat14]. By this means, no additional boundary conditions have to be setup and an external chemical solver can treat the homogeneous and heterogeneous reaction terms at the same time. Effectively, a source term is introduced at the corresponding fluid cell to correct the concentration, which is similar to the approach of Huber et al. [Hub11]. On the other hand, the location of the source and sink term is one cell adjacent to the solid node, too, thus a half spatial discretization step too far into the liquid domain.

Implementation wise with this technique, solid phases are shifted artificially into the fluid domain and equilibrated at the adjacent node. In turn, precipitated material at the adjacent cells is artificially moved and redistributed towards the solid interface site [Pat18a]. By artificially transporting solid material this whole approach leads to smearing of solid phases and spilling into other solid interface sites to some extent. Moreover,

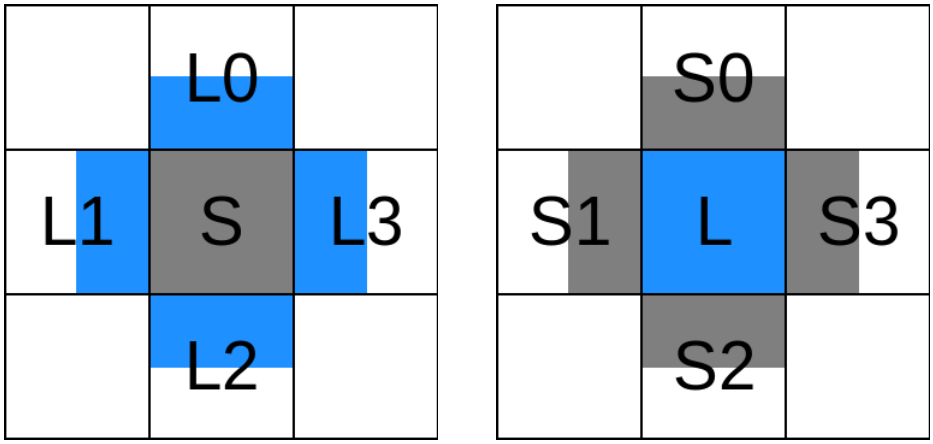

(a) Fluid cells L0 to L3 are exposing solute concentration and porosity to solid cell S.

(b) Solid cells S0 to S3 are effecting solute concentrations in fluid cell L.

Figure 4.2: Neighbors effecting solids and fluid nodes as internal boundary.

there is no control at the adjacent node for undershooting zero porosity after collecting and moving the precipitate towards the solid site. This leads effectively to porosities lower than zero, which needs a special distribution treatment, which is implemented as exceptional handling (e.g. observable in the Yantra source code [Pat18a]).

Furthermore, solutes of two different domains, which form precipitates when coming into contact, would separate both domains by a thin column of a solid interface node. Since only the solution of one domain is taken into account, no further precipitate can form. This effect does effectively prevent completely filling the solid reaction cell and thus avoids clogging artificially. In the published literature at the time of writing, Yantra was only applied to systems where solids are dissolved (Ca leaching in cementitious materials [Pat14,Pat18b]) and no clogging could occur at all, therefore this effect was presumably ignored. However, in this work, a more generic approach is mandatory since the simulations required a proper treatment of precipitation and clogging.

In order to overcome these limitations, another approach was developed in this work, which is related to the adjacent source node technique. In contrast to the Yantra approach, no solid phase is moved artificially. Instead, it is thought that the concentration in a fluid cell is defined by its reactive solid neighbors. For a 2D domain, as shown in figure 4.2b, there are at most 4 solid neighbors (S0 to S3) for each liquid node (L). In contrast, 4 liquid neighboring nodes are possible for each solid node (see figure 4.2a). Therefore, the effect of each solid node to the liquid node and vice versa is $1/4$. This approach can also be seen as a control volume defined around each solid interface node and average concentrations and porosities are determined by their fluid neighbors, while for simplification the neighboring effect of diagonal cells is excluded. In case of a 3D model, there are 6 neighbors and accordingly the neighbor effect is $1/6$.

Initially, the weighted porosity is determined:

$$\phi_n^w = w\phi_n \tag{4.23}$$

w is the neighbor weighting depending on the model's dimension d ($w = \frac{1}{2d}$) and ϕ_n is the neighbor's porosity. The average porosity is then:

$$\hat{\phi} = \sum_{n=0}^{N} \phi_n^w \tag{4.24}$$

Next, the averaged concentrations of each neighbor are weighted by their porosity fraction:

$$\phi_n^f = \frac{\phi_n^w}{\hat{\phi}} \tag{4.25}$$

$$\hat{c} = \sum_{n=0}^{N} c_n \phi_n^f \tag{4.26}$$

The averaged porosity $\hat{\phi}$ and concentrations $\hat{c}$ are inserted back into the corresponding chemical reaction cell of the solid interface node. After PhreeqC equilibrates the concentrations with the solid phase, the mole balance has to be distributed to the neighboring cells again in a pushing manner. The new concentration $\hat{c}_r$ is retrieved from PhreeqC for each solid interface cell. Afterwards, the concentration difference caused by a heterogeneous reaction term has to be determined by summing all solid neighbor effects:

$$\Delta c_n^{het} = \sum_{s=0}^{N} (\hat{c}_s^r - c_n) w \tag{4.27}$$

$$c_n^{het} = c_n + \Delta c_n^{het} \tag{4.28}$$

One major advantage of choosing to take only a fraction of 1/4 and 1/6 for 2D and 3D simulations, respectively, for each liquid cell control volume is that no concentration overshoot can happen if for example two solid nodes dissolve adjacent to the liquid node at the same time.

To compare how the results differ from the treatment of heterogeneous reaction terms as pseudo-homogeneous (see rationale in the paragraph in the beginning of this section), an example will be outlined here. Assuming two symmetrical domains with different solutes, which form a solid when coming into contact, e.g. in a 1D setup, thus ignoring L0 and L2 in figure 4.2a such that there is only L1 and L3 and a centering node. In a diffusive setup this solid will form at the center of both domains, when the solutes start to diffuse into the contact reaction cell S. The effect is that a thin single cell width barrier will be formed, apparently separating both domains depicted as L1 and L3. However, due to the treatment described here, the heterogeneous reaction term affects both domains symmetrically, i.e. even if completely clogged, the chemical equilibrium calculation takes into account both sides. After equilibration, the resulting concentrations

are evenly distributed to the liquid cells and thus a certain amount of solute from one domain is transported to the other like a tunneling effect, e.g. solutions of L1 and L3 in figure 4.2b are exchanged to some extent. This stops, when the thickness of the solid barrier increases to two discretization nodes, i.e. if there are at least two solid nodes between the domains L1 and L3. In that case, the redistribution of the solute due to the heterogeneous reaction term does only affect the corresponding side. However, completely separated domains might cause redissolution of the barrier and reopen pathways for the effect. Besides of other advantages, as better control of avoidance of negative porosities, it was assumed that this treatment is more robust and reasonable than implementation in other reactive pore-scale coupling codes, which assume heterogeneous reaction terms as pseudo-homogeneous, as implemented for example in Yantra [Pat14].

4.4.1.4 Treatment of low or negative porosities

There are cases where one solid node is in contact with two liquid nodes containing solutes, which in contact lead to precipitation of additional amounts of solids. For example, at one side of the solid node there are dissolved calcium ions present, while on the other side there is carbonate as solute. Thus, calcite will precipitate at the contacting solid node. This will continue as long as there is enough solute present. At some point, the resulting porosity in the solid node will converge towards zero. When the porosity falls below a certain threshold, in order to maintain a safety distance to prevent negative porosities, the chemical state of a cell with very low porosity is set to *dissolve_only* in the PhreeqC equilibrium phases input [Par13]. This safety margin used in this work is often chosen as 0.1 %. However, if the molar volume of the solid phase which precipitates and the concentrations adjacent to the solid node are high, it still might happen that the porosity undershoots zero.

To treat this nonphysical behavior locally, an algorithm was implemented which is used for finding a valid porosity state. The treatment developed within iPP used a root finding algorithm which is based on the Brent-Dekker method [Bre71], which does not need derivatives for solving the problem. During fixing the state, solute is removed or added and consecutively equilibrated until a positive porosity value close to zero within some tolerance is found. After finding the valid state the reaction cell has been stripped by some solid phase and the excess solute needs to be redistributed to the neighboring cells. This is added as source term to the neighboring cells during the transport simulation.

4.4.1.5 Interface evolution

During precipitation, the location of the newly formed solid is also a topic of debate. One common approach is to over-occupy interface nodes on the solid side with precipitated material until twice the volume is formed. In that event, a neighboring fluid cell is chosen to be filled with the surplus solid either by random sampling [Kan04] and/or with more complex probability functions [Che14]. This approach has several disadvantages. First, the boundary location movement is effectively delayed and introduces a geometrical error

for the time being over-occupied. Second, if the composition of the phase which has precipitated early is different to that formed later during the overfilling, there is always a mixture of earlier and later precipitates moved to the neighboring cells, although only the last over-occupying amount is intended to be transferred. This all could lead to smearing of the solid phases, which might not be desired. By using the new concept of treatment of homogeneous and heterogeneous reaction terms described above this effect is mitigated.

4.4.1.6 Interface diffusion coefficient

In order to have a proper effect of low diffusive domains on high diffusive domains, the diffusion coefficient assigned to the interface is often taken as a harmonic mean of the values is used in contrast to an arithmetic mean (e.g. [Cha92]). However, it turned out that this treatment is not perfectly right [Liu05]. Nevertheless, in this work it turned out that for the Lattice-Boltzmann method the adequate scheme is to assign the maximum diffusivity of the local neighborhood to an interface cell. Otherwise, the effect of a low diffusive domain on the high diffusive domain would be underestimated.

4.4.2 Local equilibrium assumption

The simplest assumption for reactive transport simulations is that the solution is always in local equilibrium with the solid phases it is in contact with. This assumption is valid if during the simulation concentration changes are dominated by transport characteristics rather than kinetically limited reaction rates. Moreover, as generic statement, inert solid phases are assumed to have no effect on solute concentrations. Inert solid phase domains are modeled as bounce-back nodes (see section 3.5.8.1) within the framework of Lattice-Boltzmann. Thus, they are only serving as computational entities and are not part of the chemical equilibrium treatment and hence do not need any thermodynamic properties assigned to.

4.4.3 Time marching, von Neumann criterion in LBM transport and spatial dimensions

As already mentioned, the time marching is governed by the transport model while the chemical solver is just following up. That said, too long time steps might introduce errors because of missing chemical equilibration in between. This source of error corresponds to the coupling of differential equations with a too coarse temporal discretization. According to this, certain stability criteria must be fulfilled to ensure a stable simulation, e.g. von Neumann criterion and Courant–Friedrichs–Lewy (CFL) condition. While the latter is important for convective processes, the von Neumann criterion must be respected for numerical solutions of diffusive processes within reactive transport models. Thus, it is important to note that the maximum time between two subsequent steps is restricted to:

$$\frac{D\Delta t}{\Delta x^2} < 0.5 \tag{4.29}$$

Although this criterion is a general stability restriction when dealing with discretized differential equations, there are some specific considerations for simulations based on the Lattice-Boltzmann method. In this case, the criterion is automatically satisfied by the choice of stable reference relaxation time parameters. According to equation 4.6, the lattice diffusion coefficient is 1/6 by the choice of a value of unity for τ. In terms of dimensionless lattice units the spatial and temporal discretization are both unity. All in all, it can be shown that the von Neumann criterion is satisfied:

$$\frac{D_{LB}\Delta t_{LB}}{\Delta x_{LB}^2} = \frac{1}{6} < 0.5 \tag{4.30}$$

Moreover, it has to be noted that within this work the Lattice-Boltzmann concentrations and solute amounts are modeled to be in the same scale as in physical units, i.e. in contrast to other properties there is no conversion factor involved or can be regarded as set to unity.

Another aspect of reactive transport modeling in a rather general way is that also in 2D simulations concentrations are in the units of mole per volume and not mole per area. This stems from the aspect that the third dimensions is assumed as unity in length. In other words, a 2D simulation in a XY-plane is regarded as pseudo 3D model with a homogeneous 1 m extend in Z-dimension. This peculiarity is not limited to the Lattice-Boltzmann method only, instead it is also applicable to other reactive transport simulation techniques, for example based on FEM or FVM approaches.

4.4.4 Software development

4.4.4.1 C++ template meta programming

The C++ programming language was used for the development of iPP. A programming technique allowed for better code optimizations was used to implement the coupling code. C++ has incorporated a widely used feature called *templates*. Templates were introduced to allow programming of generic container types like std::vector. Mostly by accident, after releasing the ISO C++-98 standard, programmers figured out that the template language feature is in fact Turing-complete. This allows execution of programmed code during compilation time which is coined *meta-programming*. Examples for this are the (static) generation of Fibonacci numbers or prime numbers during compile time but also compile time code generation. Taking advantage of such programming techniques allows writing code which generates other code during the compilation process, thus called *meta*-programming, referring to a higher layer of programming [Ale01,All16].

The intermediately produced code is not directly visible for the programmer in the first place, but allows the compiler to expand types, code structures and functionalities into intermediate code. The resulting binary code, generated by the compiler, could therefore be optimized in a way to include performance optimizing features of modern CPU architectures (e.g. SIMD vectorizations, sophisticated branch prediction, link time optimizations). iPP was widely programmed in such a way to minimize the coupling overhead at numerical hot-spots and allowing CPU and compiler enhancements to come

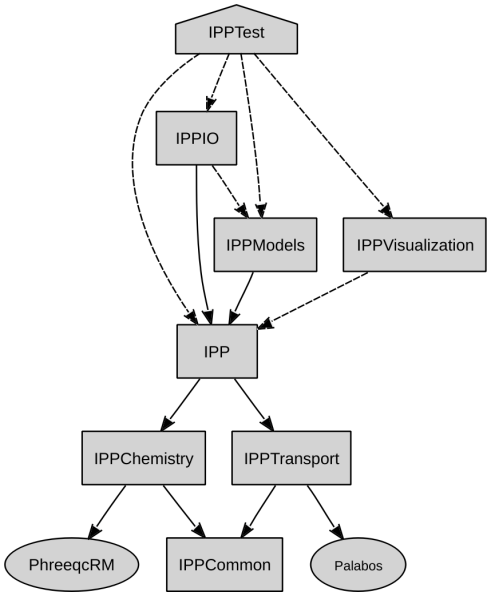

Figure 4.3: Simplified view on the software design of iPP. The arrows are indicating a dependency graph of different C++ libraries, e.g. *IPP* needs *IPPChemistry* and *IPPTransport*, while both need *IPPCommon*. Rectangular shapes are indicating internal libraries, ellipses are external libraries and the house-shaped icon is an actual run-able executable.

into effect.

4.4.4.2 Abstract interfaces and modularity

The coupling code iPP was designed in a modular form which allows to substitute several algorithmic details. The general structure looks as described in figure 4.3. It can be seen that the simulation coupling core is separated into several sub-modules which are interacting via abstract C++ interfaces. In its core, the iPP project is separated into several sub-libraries like *IPPChemistry* and *IPPTransport*. Each of them is responsible for one particular aspect within the simulation. The central library *IPP* works purely on C++ input data, which are then given into an initialization function. Subsequently, the simulation is run via an execution call.

There are various software modules for different aspects. For example, on the one hand there is the reaction module and on the other hand the transport module, while the SNIA marching is performed by an encapsulating module (*IPP*) which is only interacting with abstract representations of the concrete implementation of the transport and reaction codes. This allows to exchange the PhreeqcRM reaction module by another geochemical simulator (e.g. GEMS [Kul12] or Reaktoro [Lea16]) if needed. The same counts for

the transport code implementation, which can be exchanged, although the focus was on Palabos here.

Additionally, several other details, mostly related to modeling systems requirements, can be defined by programming a certain concrete implementation. For example, there is an abstract interface class called *AbstractPorosityCalc* which is used in iPP. The definition how the porosity is calculated, is then the responsibility of the concrete model implementation e.g. *TennisJenningsCSHPorosityCalc*. For example, this C++ class distinguishes between LD- and HD-CSH and takes into account the existence of their different gel porosities. Similarly, the diffusivity relation can be exchanged by overriding functions of *AbstractMultiScaleDiffusionCalc*. These mentioned concrete implementations are located in the *IPPModels* package shown in figure 4.3. However, it is up to the user to use these implementations or extend them by their will. As an example, the IPPTest executable was implemented, which makes use of the implementations in *IPPModels* and using *IPPIO* as user input library by reading JSON files [Int17]. Another software module called *IPPVisualization* allows direct visualization of simulation results during calculation.

4.4.4.3 Parallelization by using a distributed memory model

Pore-scale reactive transport simulations are computationally very demanding. Thus, the usage of high performance computing (HPC) facilities is required to simulate complex systems. In order to utilize computer clusters, parallelization is a mandatory requirement.

In order to take advantage of a distributed memory computing model, as used in most high performance computer clusters, iPP had to be implemented in a special way. Almost all code developed is parallelized by such a programming paradigm. A commonly used and de facto HPC standard for such implementations is Message Passing Interface (MPI). In contrast to OpenMP, MPI itself is not parallelizing any loops or performs any domain decomposition, since MPI is a specification of communication interfaces only. The main benefit of using a distributed memory model is the possibility to easily decompose certain computational problems into several compute nodes on a computer cluster. In the best case, each compute node can calculate a part of the problem by its own without the need of communicating to the others. The advantage is that there is no limitation on the amount of CPU cores used for a simulation (except for the size of the computing cluster), while OpenMP is limited to a single node calculation. One compute node, however, has a limited number of locally available CPU cores. In other words, besides of possible bottlenecks in the parallelization itself, the maximum number of CPU compute resources available might be restricting the performance gain.

On the other hand, compared to a shared memory model (e.g. OpenMP), distributed memory computation is much more demanding with respect to the programming work. All logic of domain decomposition must be implemented in the client code using a MPI library, which implements the MPI specification. Furthermore, all information exchange among the participating processes has to be programmed explicitly, because process A has no direct memory access to process B, in particular when process B is running on

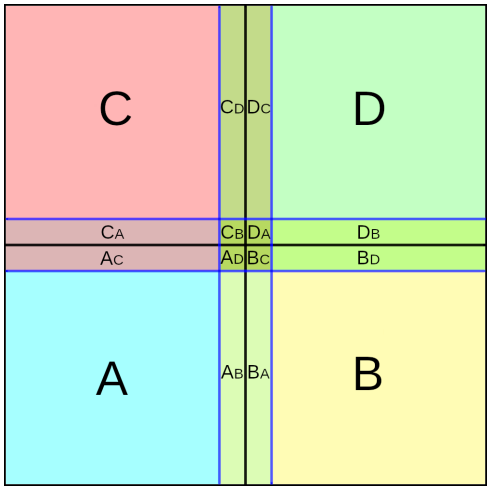

Figure 4.4: Decomposition technique of Palabos parallelization scheme. As example, this 2D domain is split up into four computational domains (A, B, C and D). Overlapping domains are depicted in intermediate colors.

another distinct compute node of a cluster. In the case of iPP, the development was done with *OpenMPI* while the code was directly portable to *Intel-MPI* and *ParaStationMPI* library, which are both used in an optimized form on the JURECA cluster at Forschungszentrum Jülich [Kra18].

Palabos offers already a domain decomposition infrastructure for MPI parallelization, which was exploited as far as possible. Still, a lot of algorithms had to be extended, which demanded knowledge about the internal data structures in order to implement them in a non-performance degrading way. In general, Palabos decomposes the total computational domain into preferable similar sized rectangles or cubes for 2D and 3D simulations, respectively. All domains still need to have some overlap to their adjacent domains in order to perform information exchange.

As an example, figure 4.4 sketches a 2D system decomposition. In this example, the complete domain is separated into four sub-domains (A, B, C and D) assigned each to another computing process. Each sub-domain contains multiple computational cells referring to the spatially discretized geometry. The process dealing with domain A is able to read data and write results to cells contained in the area of A, A_B, A_C and A_D. Additionally, process A has read-only access to the areas indicated with B_A, C_A, C_B, B_C, and D_A. The same scheme counts for the other processes B, C and D. For example, process B is writing results for instance to domain B_A which can then in turn be read by A.

For the shared memory computational model, the overhead of accessing the information of neighboring domains is quite low, hence the name *shared* indicates a shared usage. However, the distributed model needs an explicit transfer of data to adjacent processes.

This means, in order to have the possibility of reading the shared domains, the overlapping data must be synchronized to the corresponding memory of the adjacent processes. For example, when A has finished writing to A_B and B_C, the data must be copied into the corresponding read-only memory space of process B. By only copying mandatory data, the amount of data needed to be transferred is minimal and communication overhead is reduced. This idea of reduced communication is a quite general approach to deal with domain decomposed algorithms if there is exchange of data needed, i.e. it is applicable to FEM and Lattice-Boltzmann methods in a similar way. In the case of Lattice-Boltzmann algorithms, the information exchange takes place after the streaming step [Lat21].

4.4.4.4 User interface

The coupling code iPP itself is a C++ library which can be called by C++ program code, thus exposing a C++ programming interface, i.e. iPP has an application programming interface (API) for usage within an executable or another library. This is optimal, if a user of iPP intends to use the simulator within another program or software module. All input data have to be defined programmatically via a C++ configuration object, which is an instance of a class called *IPPConfig*. This configuration includes for example the size of the model, chemical compositions, geometric distribution of phases and the total running time of the simulation. In order to simplify the end-user utilization of iPP, a graphical user interface (GUI) can quite easily be implemented, which then directly defines the *IPPConfig* object. However, for the usage with non-GUI environments, as typically for high performance cluster log-in systems, this is not applicable, and a pure command line interface (CLI) capability was required. To this end, an easier to use end-user input format was designed. This format is based on a JSON data format [Int17] and partly utilizes the VTK image format [Sch06]. The benefit of using the JSON format is that it is quite readable and editable for humans in contrast to other formats like XML [Bra08]. An example for such JSON input is presented in appendix C. Details about the used models will be presented in the application part III.

4.4.4.5 Development efforts and output

The latest version of the coupling code consists of more than 40,000 source lines of code (SLOC). The SLOC number here is defined as the count of lines of code while not counting white space only or empty lines. However, the raw number of SLOC alone does not reflect the complexity to develop a software package. As already explained, the engineering effort involved is also depending on the generic nature with respect to the programming language paradigms used. The software architecture and design of iPP was focused on extensibility, flexibility, portability and with high performance computing capabilities in mind. All in all, the outcome is a modular and validated software library which might be the foundation of even more complex developments in the future.

4.4.5 Optimizations to PhreeqC, feature extensions and dynamic chemistry activity

Besides of the development of iPP, optimization work was undertaken within PhreeqcRM to enhance the performance of the coupling. Performance profiling revealed bad computational scalability with the default PhreeqcRM implementation. At several points unneeded overhead in the implementation were found, which limited computational scaling significantly. Within this work, several of these issues were treated in order to enhance performance of the Palabos-PhreeqC coupling. In the following paragraphs only the most significant improvements are detailed.

Although PhreeqcRM supports MPI parallelization during the PhreeqcRM::runCells() function call, concentration updates, requesting concentrations, and retrieving of auxiliary information (e.g. solid phase composition, pH, etc.) are implemented with a global MPI reduction and collecting step within the upstream available PhreeqcRM version. This reduction step implies that all concentration couplings to transport codes are forced to be done via the main process and cannot perform on a local process basis. Thus, this reduction procedure causes high communication overhead and a major performance drawback when utilizing parallelization on a high number of CPU nodes, leading eventually to negative scalability. In order to reduce this communication overhead, the PhreeqcRM code was optimized here, which led to a customized PhreeqcRM version allowing local coupling to the Lattice-Boltzmann transport code.

Additionally, several collective algorithms close to the programming interface within the official (upstream) version of PhreeqcRM are not optimized. Performance profiling and analyses revealed some hot spots which were then subsequently optimized with respect to memory allocations and cache alignment. These optimization tasks improved single thread performance as well.

Besides of concentration, pressure, and temperature updates, PhreeqcRM has no programming interface (API) to adjust certain other properties of reaction cells directly. For example, there is no API supported way to adjust the target saturation indices of the chemical equilibrium calculation. The only official way would be to execute a PhreeqC input with a *RunString()* call. As already mentioned, data parametrization via character strings is computationally expensive and can also lead to floating point rounding issues. Thus, depending on the number of reaction cells and the frequency of updates, the generation of a PhreeqC input string and re-parsing it within PhreeqcRM implies a huge unnecessary overhead. To reduce this overhead, the PhreeqcRM programming interface was extended to allow for the adjustment of additional parameters.

Apart from the changes within PhreeqcRM, another optimization was introduced with respect to dynamic chemistry activity. Since not all reaction cells are experiencing significant changes in the solute concentrations due to transport in each time step, the state with respect to chemical composition will also remain stagnant. An example is a reaction cell located away from the reaction interfaces and/or isolated by the events taking place at interfaces. Essentially, most of the domain might experience only slight concentration changes due to small concentration gradients. This observation was exploited for an optimization within the coupling code iPP called here dynamic chemistry

activity. Effectively, the chemical reaction calculation in a cell can be omitted when the relative changes in solute concentrations are lower than a certain threshold. This threshold can be configured via input data. Preliminary tests have shown that a threshold of 1 % did only introduce tiny errors during the simulations but led to significant performance improvement. Thus, if not stated otherwise, this threshold was used in all simulations in this work. These optimizations significantly improved the performance and scalability behavior of iPP (see section 6.4).

5 Departure from pure equilibrium assumptions

5.1 Overview

During the development of the pore-scale model and conducting various simulations of the leaching of hydrated cementitious materials with different waters, several issues were revealed. Most of them occurred because some pore-scale effects were not addressed properly in the simplified models. Thus, a re-evaluation of the complexity of the respected physical effects was necessary after each iteration. Each time the magnitude of contribution of possible missing effects were assessed, followed by an implementation of a model addressing the major contributing effect into the iPP code. In the following sections, the development of the assumptions and theoretical background behind them are outlined. Essentially, these models will be applied in chapter 8.3. In this chapter, two concepts of off-equilibrium models are described, addressing on the one hand the implementation of nucleation theory and on the other hand porosity controlled solubility. Both theories allow supersaturated solutions to some extent. It is known that in small pores both effects play a role (e.g. [Kas03,Poo16a]).

5.2 Inclusion of nucleation theory in pore-scale reactive transport simulations

5.2.1 Overview

Systems which are not in thermodynamic equilibrium experience a certain driving force towards equilibrium state. In case of solutions supersaturated with respect to one or more phases, eventually precipitation will occur. Although there is a driving force, the precipitation process is often not instantaneous, which is in contrast to the (assumed) instantaneous local equilibrium.

A common theory which describes this inhibition is the so-called classical nucleation theory, which represents the formation of nuclei in a supersaturated solution as a statistical process. Nucleation theory can be generally applied to both gas/liquid and liquid/solid systems [Kas03]. In the scope of this work, the precipitation of a solid from a solution is of primary interest and therefore the terminology of a liquid solution and a solid precipitated phase is used. It has been shown that nucleation is an important effect for pore-scale processes in reactive transport problems (e.g. [Li17,Pra17,Sta22]

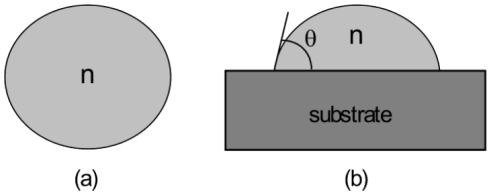

Figure 5.1: Illustration of a homogeneous (a) compared to a heterogeneous (b) nucleation process. The surface energy to overcome for HEN is lower because of the wetting angle θ on the substrate [Kas03].

Off-equilibrium conditions can technically also be simulated by kinetic reaction rates. It is evident that statistical events form another morphology in the microscopic scale than a smooth kinetically dominated precipitation. In this work, the heterogeneity emerging from particular precipitation events is analyzed.

5.2.2 Theoretical background

Classical nucleation theory distinguishes between homogeneous nucleation (HON) and heterogeneous nucleation (HEN). HON takes place in the free pore space in solution itself while HEN refers to the process of precipitation on another substrate [Kas00, pp.20]. In general, at moderate supersaturated conditions HEN prevails over HON [Kas03]. For instance, gas bubbles usually form preferable on surfaces or crystallization more likely occurs on another substrate than in the free volume of a liquid. This refers to a lower energy barrier for the HEN process.

To illustrate die differences in the energy barrier of HON and HEN, the processes are illustrated schematically in figure 5.1. Both processes lead to the creation of a nucleus of some size n. For HON the surface energy is governed by the precipitating material (cf. a in figure 5.1). On the other hand, for HEN the wetting angle θ on some substrate helps to reduce the effective surface energy (cf. b in figure 5.1). Since the wetting angle depends on the substrate, the effective surface energy for HEN does as well. A wetting angle of $\theta = 0°$ corresponds to a complete wetting of the substrate [Kas03]. The degree of wetting depends on several factors and is of complex nature. However, experiments suggests that structural similarity of the precipitate and the substrate improves the degree of wetting [Kas03,Mel65]. Resulting from this analogy it is obvious that HEN is governed by a lower surface energy than HON, since the HON case corresponds to the non-wetting limit of $\theta = 180°$.

Assuming an independent formation of single nuclei, the process of nucleation in general obeys a Poisson distribution whose probability can be calculated as follows [Goh10]:

$$P_n(t) = \frac{1}{n!}(JLt)^n \, e^{-JLt} \quad n \in 0, 1, 2, ... \tag{5.1}$$

where n is the number of nuclei, t the time, J the nucleation rate and L the physical

dimension in terms of volume or surface for HON and HEN, respectively. The probability for $n = 0$, i.e. a case where no nucleation has occurred, which is also called survival probability, simplifies to [Bra15]:

$$P_0(t) = e^{-JLt} \tag{5.2}$$

The complement of the survival gives the probability of having at least one nucleus in a certain frame of time and volume/surface:

$$p(t) = 1 - P_0(t) = 1 - e^{-JLt} \tag{5.3}$$

Since the nucleation rate is not directly obtainable experimentally, induction times are measured instead. The induction time is the time span between establishing supersaturation and the first detection of a precipitated phase and is a result of the statistical behavior of nucleation and crystal growth. Obviously, this detection does not perfectly give results for first occurrence of the first nuclei because the detection of very tiny crystallites is not always possible. Nevertheless, repeating the induction time measurements multiple times and plotting the data in a cumulative way a statistical pattern emerges, which obeys the Poisson distribution for nucleation events mentioned before.

Applying a proper growth law, which for example takes into account the delay between formation of nuclei and their detection, the nucleation rate can be derived with help of those plots [Bra15]. For this purpose, the measured data are fitted to equation 5.3 as plotted in figure 5.2. By this means, the nucleation rate for a certain supersaturation can be determined. Subsequently, the nucleation rate can be related to supersaturation.

A general form of the nucleation rate J is reported as [Pri14]:

$$J = J_0 e^{-\frac{\Delta G}{k_b T}} \tag{5.4}$$

In equation 5.4, J_0 stands for the pre-exponential factor and its unit is the same as for J, which is the volume or surface normalized nucleation rate for HON or HEN, i.e. $[1\,\mathrm{m}^{-3}\,\mathrm{s}^{-1}]$ or $[1\,\mathrm{m}^{-2}\,\mathrm{s}^{-1}]$, respectively. The term ΔG is the energy term which depends on the surface tension σ, the volume of a single nucleus ν and a geometrical factor β depending on the nucleus shape [Pri14]:

$$\Delta G = \frac{\beta \nu^2 \sigma^3}{(k_b T \ln(S))^2} \tag{5.5}$$

Additionally, in equation 5.5 the (super) saturation ratio $S = \mathrm{IAP}/K_{eq}$ (IAP stands for ion activity product), the Boltzmann constant k_b and the absolute temperature T are included. The shape factor for a spherical nucleus is defined as:

$$\beta = \frac{16\pi}{3} \tag{5.6}$$

For a cubical nucleus the shape factor is $\beta = 32$. The reasons behind the need of a

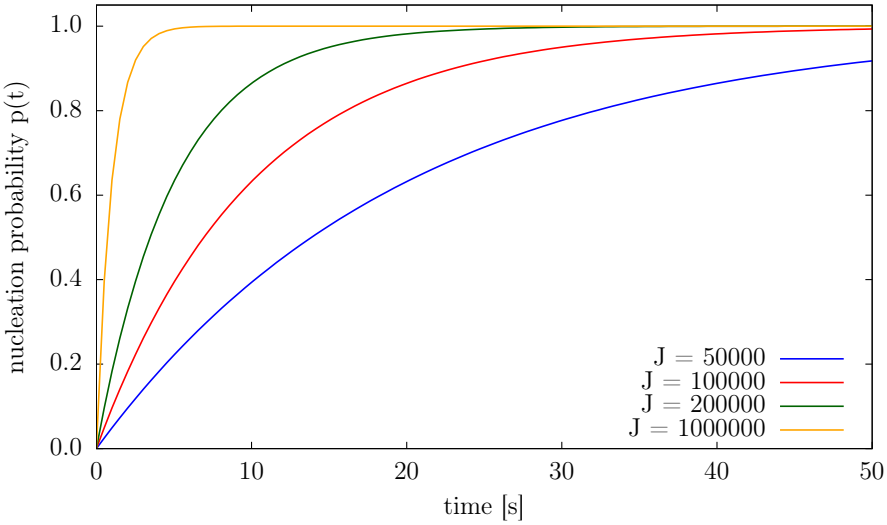

Figure 5.2: Nucleation probability for different nucleation rates J in a solution volume of 1 mL as a function of time.

conversion factor of $\pi/6$ are outlined in appendix B. Equation 5.5 is often simplified by extracting a factor B:

$$B = \frac{\beta \nu^2 \sigma^3}{(k_b T)^2} \tag{5.7}$$

resulting in:

$$\Delta G = \frac{B}{\ln^2(S)} \tag{5.8}$$

The pre-exponential factor J_0 in equation 5.4 also depends on several factors:

$$J_0 = 2\pi Z D N_0 N_1 d_c \tag{5.9}$$

where d_c is a normalization factor given as:

$$d_c = \frac{4\sigma\nu}{k_b T \ln(S)} \tag{5.10}$$

while N_0 is the number of nucleation sites, N_1 the particle concentration of monomers and D the diffusion coefficient, which is acting during monomer attachment. Z is the so-called *Zeldovich factor*, which is given as:

$$Z = \sqrt{\frac{\Delta G}{3\pi k_b T n_c^2}} \tag{5.11}$$

The definition of the Zeldovich factor includes the number of monomers of a critical nucleus:

$$n_c = \left(\frac{2\sigma\alpha}{3k_bT\ln(S)} \right)^3 \tag{5.12}$$

A nucleus is called critical if the size of it expresses the energy at the maximum of the energy barrier resulting from volume and surface energy in concurrency [Kas00, pp.29] (cf. equation 5.5 and figure B.1). α is the single nucleus surface area, which can be calculated by the sphere's volume-area relationship:

$$\alpha = 36^{1/3}\pi^{1/3}\nu^{3/3} \tag{5.13}$$

Inserting all equations into equation 5.9, simplifying and extracting a material dependent property constant C:

$$C = D\sqrt{\frac{k_b}{\sigma}} \tag{5.14}$$

results in a simplified form for J_0:

$$J_0 = N_0N_1C\ln(S) \tag{5.15}$$

Thus, it turns out that the pre-exponential factor J_0 also depends on the monomer concentrations and respective supersaturation of the phase. For HON it is assumed that every water molecule position can act as nucleation site. Following this, the number of nucleation sites N_0 for HON in liquid water can be estimated as the number of water molecules per volume. Thus, N_0 is estimated as $3.33 \times 10^{28}\,\mathrm{m}^{-3}$ [Pri14,Poo16b]. The situation changes when dealing with HEN. Here the number of nucleation sites on the substrate's surface is of importance. Equations 5.15 and 5.14 allow to define a relation for N_0:

$$N_0 = \frac{J_0}{N_1\ln(S)D\sqrt{\frac{k_b}{\sigma}}} \tag{5.16}$$

This relation is later used to determine the number of nucleation sites on a substrate.

5.2.3 Combination of nucleation probabilities

The probability of nucleation is regarded as a combination of multiple independently occurring processes, i.e. probability of HON in free water, probability of HEN on another substrate and probability of HEN on an identical phase. In order to determine, if a nucleation event takes place, the probabilities of all relevant processes have to be combined. Therefore, at each reaction cell in a reactive transport simulation, all three different probabilities are calculated. All three events are not mutually exclusive to each other (see also Venn-diagram in figure 5.3).

Thus, it is important to notice that the probability is not just the sum of the single probabilities, rather the combination of all three probabilities is determined according

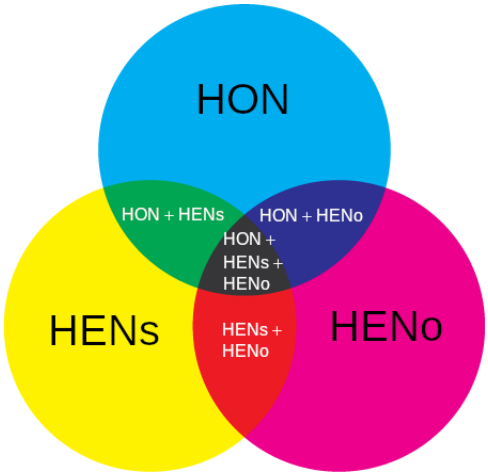

Figure 5.3: Venn-diagram of the three nucleation probabilities HON, HENs and HENo. The s and o subscripts at HEN stands for **s**elf and **o**ther, respectively, which refers to the substrate which is either of the same or of another type. The total probability corresponds to the black colored area in this scheme. However, since the processes are not mutually exclusive, the overlaps (e.g. green area, HON + HENs) must be accounted for only once.

to the union law:

$$\begin{aligned} p_{tot} = & \, p^{HON} + p^{HEN}_{self} + p^{HEN}_{other} \\ & - p^{HON} p^{HEN}_{self} \\ & - p^{HON} p^{HEN}_{other} \\ & - p^{HEN}_{self} p^{HEN}_{other} \\ & + p^{HON} p^{HEN}_{self} p^{HEN}_{other} \end{aligned} \tag{5.17}$$

Accordingly, while all single probabilities are in the interval of $0 \leq R \leq 1$, the total probability p_{tot} does not fall below zero nor exceed a value of one, therefore is limited to the same probability interval.

5.2.4 Implementation of CNT in iPP

5.2.4.1 Random sampling

If the condition for nucleation is not met, precipitation in the particular cell is suppressed via setting the *dissolve_only* flag in the PhreeqC reaction module. In the opposite case, if precipitation is allowed due to a nucleation event, this flag is disabled. Note that in the presented implementation the *dissolve_only* flag is set for all phases at the same

time, i.e. no precipitation is possible for any of the phases if no precipitation event has taken place yet. To determine if a nucleation event takes place in the following time step, a random number is generated for each cell and compared to the total nucleation probability (cf. equation 5.17). In the following, the algorithm is described how the random sampling is performed. It is shown how the mitigation of numerical artifacts is treated, if the probability is very small.

To avoid numerical floating point artifacts, it is beneficial to calculate the complement of the nucleation probability (survival probability) and taking the logarithm. Thus, using equations 5.3 and 5.17 and after simplification:

$$\ln P_{tot} = -\left(J^{HON} V_c + J^{HEN}_{self} A^{self}_e + J^{HEN}_{other} A^{other}_e\right) t \tag{5.18}$$

In equation 5.18 $\ln(P_{tot})$ is usually a negative value, except if the survival probability is one, i.e. either all nucleation rates are zero and/or corresponding volumes and surface areas are zero. The volume V_c in the term for HON refers to the absolute reaction cell volume, while A_e in the other terms are the effective surface areas of neighboring cells containing solid phases. The effective area is defined as the sum over all neighbors n:

$$A^S_e = \sum_{i=1}^{n} V^S_i A_c \tag{5.19}$$

A_c is the absolute interface surface area of a reaction cell to a neighboring cell while V^S_i corresponds to the volume fraction of the solid phase in question, either similar to the precipitating phase or a different kind of substrate.

In order to determine if a nucleation event will take place, for each reaction cell a uniformly distributed random number R in the interval of $0 < R \leq 1$ is generated. Nucleation occurs if the random number is higher than the survival probability P_{tot}, which holds also for the logarithmic form. Thus, the criterion reads:

$$\ln R > \ln P_{tot} \tag{5.20}$$

Therefore, the natural logarithm of the random number R is taken and compared to the logarithm of the survival probability defined in equation 5.18.

According to equation 5.9, the pre-exponential factor of the nucleation rate depends on the monomer concentration, e.g. for calcite nucleation this is $CaCO_3$(aq). These data can be determined by PhreeqC speciation calculations. Thus, within each iteration the concentrations for each cell are retrieved and plugged into equation 5.9.

5.2.4.2 Suppression of HEN in case of partially filled adjacent cells

Furthermore, another constraint was introduced in order to capture the aggregation of precipitating solids in one cell after another. If one would determine the probabilities of heterogeneous nucleation, assuming the adjacent cell contains homogeneously dispersed solids, even for very tiny amounts in adjacent cells, a potentially supersaturated solid in the cell would immediately nucleate, too. However, this is an oversimplification

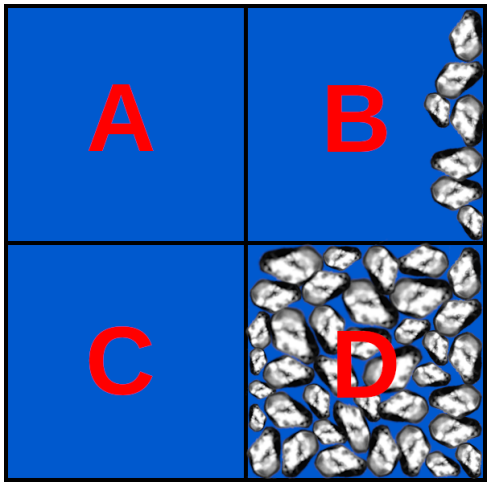

Figure 5.4: Schematic view of HEN cell filling process. Cell B is only partially filled while the precipitate in cell C is reaching towards cell C.

because in sub-cell resolution the precipitation would occur at the cell wall and not homogeneously distributed in the whole volume. Thus, the effect of HEN from partially filled cells on neighboring cells is limited.

This effect is sketched in figure 5.4. Cell B is partially filled with solid and precipitation occurred on the right-hand side of it. Obviously, there is not yet a solid phase connection to cell A. This is different in the case of cell D, which was already almost completely filled with solid. Effectively, the precipitation front will propagate towards cell C.

To capture this effect the assumption made was that if there had been at least one precipitation event before, further precipitation is always allowed in that certain reaction cell. That said, precipitation is allowed in equilibrium if at least a tiny amount of precipitated solid is already present. On the other hand, heterogeneous nucleation is suppressed if there is no other directly connected adjacent cell which is completely filled with a solid phase.

5.3 Porosity controlled solubility

5.3.1 Overview

Although the implementation of nucleation theory in a pore-scale model is capable of describing the location of newly precipitating solids, it does not limit the amount of additional precipitate in confined spaces. However, experimental evidences showed that there is another physical effect which prevents complete clogging in confined spaces [Sch99]. Precipitation in confined pores is not only limited due to reduction of transport pathways, but also by effects stemming from surface tension. This effect is called *porosity*

controlled solubility (PCS). PCS lead to the situation that the effective solubility is increased and thus higher than the thermodynamic solubility [Emm07,Liu17].

5.3.2 Effective solubility depending on pore size

Porosity controlled solubility describes an effect leading to the term effective solubility, which is higher than the thermodynamic equilibrium solubility. The effect gets more pronounced with decreasing pore size. For example, in 10 nm pores it was reported that the effective solubility of Na_2CO_3 is more than twice as high as the thermodynamic bulk solubility [Rij05]. The effective solubility can be described by the Kelvin equation. For cylindrical shaped pores the effective solubility product K_{eff} obeys the following relation [Sch04]:

$$\ln \frac{K_{eff}}{K_0} = \frac{\kappa V_m \sigma}{RT} \tag{5.21}$$

In equation 5.21 K_0 is the thermodynamic equilibrium constant, κ refers to the curvature of the pores, σ to the surface tension and V_m to the molar volume of the precipitating phase. If the pore is cylindrical, the end cap endings are interpreted as hemispherical and the curvature is expressed as $\kappa_E = 2/r$. In the case of a radial curvature of a cylinder, the curvature is defined as $\kappa_r = 1/r$ [Sch04]. Solving for K_{eff} and extracting the exponential factor as f gives:

$$K_{eff}^{A} = K_0 \, f \tag{5.22}$$

Inserting the corresponding curvature in equation 5.21 the effective equilibrium constants for axial and radial radii are:

$$K_{eff}^{A} = K_0 \, e^{\frac{2V_m\sigma}{RTr}} \tag{5.23}$$

$$K_{eff}^{R} = K_0 \, e^{\frac{V_m\sigma}{RTr}} \tag{5.24}$$

Usually, in the PhreeqC input the target saturation index SI_T (cf. equation 4.11) is set to zero to simulate equilibrium conditions. PhreeqC tries to reach this value by dissolving or precipitating solids as long there is either solid phase present or solute in the solution. While a SI value of zero corresponds to thermodynamic equilibrium, the adjusted one by curvature is defined as:

$$SI_{eff} = \log_{10}(IAP) - \log_{10}(K_{eff}) \tag{5.25}$$

Since $\log_{10}(K_{eff}) >= \log_{10}(K_0)$ the effective saturation index SI_{eff} is always lower or equal than SI. To determine the saturation index incorporating the effective equilibrium constant the new saturation index is adjusted by the difference of SI_{eff} and SI:

$$\Delta SI = SI_{eff} - SI \tag{5.26}$$

Since $SI = \log_{10}(IAP) - \log_{10}(K)$ the equation is extended and simplified afterwards:

$$\begin{aligned} \Delta SI &= (\log_{10}(IAP) - \log_{10}(K_{eff})) - (\log_{10}(IAP) - \log_{10}(K_0)) \\ \Delta SI &= \log_{10}(K_0)) - \log_{10}(K_{eff}) \end{aligned} \tag{5.27}$$

Inserting equations 5.22 and 5.21 followed by simplification yields to:

$$\begin{aligned} \Delta SI &= \log_{10}(K_0)) - (\log_{10}(K_0) + \log_{10}(f)) = -\log_{10}(f) \\ \Delta SI &= -\log_{10}\left(e^{\frac{\kappa V_m \sigma}{RTr}}\right) \end{aligned} \tag{5.28}$$

This means effectively that the target saturation must be shifted in the opposite direction than ΔSI to achieve an effective solubility effect, thus the negative sign:

$$SI_T^{eff} = SI_T - \Delta SI \tag{5.29}$$

If an initial target saturation index of zero is assumed, the effect of the effective equilibrium constants is expressed as the exponential term of equation 5.21:

$$SI_T^{eff} = 0 - \Delta SI = \log_{10}\left(e^{\frac{\kappa V_m \sigma}{RTr}}\right) \tag{5.30}$$

In turn, the effective target saturation ratio SR_T^{eff} is expressed as:

$$SR_T^{eff}(r) = 10^{SI_T^{eff}} = e^{\frac{\kappa V_m \sigma}{RTr}} \tag{5.31}$$

Equation 5.31 is written as function of the pore radius r since this is basically the input parameter while all other variables are either material constants, e.g. molar volume V_m and surface tension σ, or fundamental thermodynamic properties assumed to be constant within this scope, e.g. R and T.

Assuming that the number of pores remains constant upon dissolution and precipitation of solids, the equations describe two limiting cases, i.e. either change of length or radius of the cylindrical pores. Both assumptions were made by other authors [Emm07,Liu17]. The axial change mode will cause no change of radius in equation 5.23 and thus the effective solubility will remain the same, independently of porosity change. The radial change assumption incorporates a change in pore radius and therefore can be interpreted as a dynamic effective solubility product. During the process of decreasing radius the effective solubility will increase exponentially. Since in this study the effect of clogging and very low porosities plays an important role, the dependence of the solubility product to changes on the radius of the pores has been included in the pore-scale modeling approach via equation 5.24. All equations depicted are evaluated during each iteration by iPP withing the IPPChemistry module and the resulting target saturation indices are transferred to the chemical solver PhreeqcRM.

In order to convert from porosity to a corresponding radius, the following equation is

used.

$$r(V) = \sqrt{\frac{V}{\pi L}} \tag{5.32}$$

This equation is derived from the volume equation for a cylinder. V corresponds to the volume and L is the length of the cylinder.

5.3.3 Adjustments to the effective solubility equation

For high porosities, the cylindrical pore geometry assumption does not hold anymore. If one assumes all cylindrical pores are perfectly aligned in a lattice and have the same radius, at some porosity value the cylinder walls could overlap, which is the geometrical limiting case of still intact pores to exist. However, this is a simplified view, since the pore network is rather a complex intertwined network than perfectly aligned cylinders, thus the cylinders will overlap even earlier during porosity increase rendering the PCS effect negligible. In order to approximate the limit of such a network, a close packing of equally sized spheres is assumed instead of an aligned cylinder lattice. The closest packing of equally sized spheres is calculated by:

$$\phi_{crit} = \frac{\pi}{3\sqrt{2}} \approx 74\,\% \tag{5.33}$$

The model used in this work is extended in a way, that for simulation cells with porosities above this critical value the effective solubility product is set to the thermodynamic constant of the corresponding phase, i.e. the system behaves like and ordinary bulk equilibrium system. However, if the porosity is lower than this critical value, cylindrical pores are assumed to be co-existing with overlapping cylinders. The lower the porosity, the higher the fraction of intact cylindrical pores. This is modeled with a smooth transition between porosity adjusted solubility and the thermodynamic controlled domain via a linear interpolation factor $t(\phi)$:

$$t(\phi) = \frac{\phi}{\phi_{crit}} \tag{5.34}$$

Combined with equation 5.31 and embedding equation 5.32 this leads to:

$$\tilde{SR}_T^{eff}(\phi) = SR_T^{eff}(r(\phi))(1 - t(\phi)) + t(\phi), \quad \phi \in [0, \phi_{crit}] \tag{5.35}$$

This equation is only valid below the critical porosity ϕ_{crit}. Above the critical value, the function simplifies to:

$$\tilde{SR}_T^{eff} = 1, \quad \phi \in [\phi_{crit}, 1] \tag{5.36}$$

As an example, the resulting target saturation index function is plotted in figure 5.5 as red line in conjunction with the thermodynamic equilibrium and the original data of the effective solubility without adjustment. The data used as input for the models plotted correspond to calcite, while a porosity to pore radius conversion as derived in

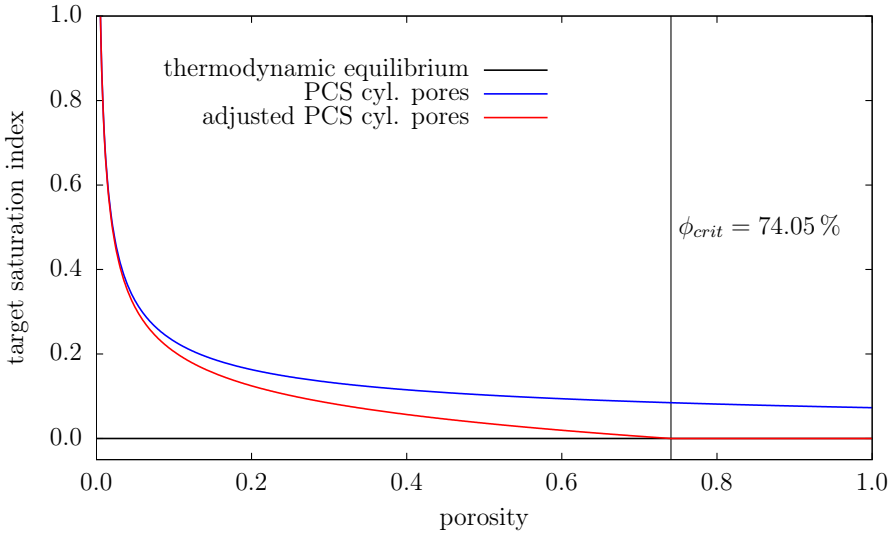

Figure 5.5: Comparison of three different target saturation index functions against porosity: Thermodynamic equilibrium (black curve), original porosity controlled solubility (PCS, blue curve) and adjusted PCS (red curve). The thermodynamic equilibrium function is flat while the PCS approaches converge towards the equilibrium target. The data used correspond to calcite and the porosity is recalculated as radial curvature using the CSH pore radius model described in section 7.6.1. Using the same function with a phase which has a higher surface tension than calcite, the slope towards the low porosity regime would be steeper.

section 7.6.1 was used.

It is clearly observable that the adjusted PCS model (equation 5.35) reaches the equilibrium line at the critical porosity estimated by the closest sphere packing. At lower porosities the SI_T function shows an exponential form. For zero porosity the value converges towards infinity while for porosities close to zero the solubility is significantly increased, i.e. at a porosity of 0.005, a target saturation index of one is exceeded. Thus, under these confining conditions, a tenfold supersaturation (SI > 1) is required to precipitate the solid phase. It is important to note that the curve has a different slope for other solid phases. Although all curves are converging towards the thermodynamic equilibrium saturation (SI $= 0$) at the critical porosity, the effective target saturation index is higher towards lower porosities, if the surface tension and/or molar volume of the solid is higher (compare equation 5.31).

6 Verification, validation and scalability

6.1 Overview

This chapter is dedicated to the benchmarking of different aspects of the implemented Lattice-Boltzmann transport algorithms and iPP. During the development and assessment of algorithmic approaches, different sources and classes of errors were found. Some of them revealed as unacceptable for the further development of reactive transport models to simulate alterations of cementitious materials. On the other hand, there were numerical effects observed which are inherently present due to floating point inaccuracies on current computer architectures. This chapter is about distinguishing between crucial and negligible effects and pointing out potential limitations of the algorithms implemented in iPP.

In section 6.2, different Lattice-Boltzmann schemes and their implementations are tested. As already mentioned, in addition to the SRT scheme, three Lattice-Boltzmann schemes were newly implemented in the framework of iPP to extend Palabos, i.e. PBB, DV-SRT and P-TRT. These four implementations are critically assessed in terms of their applicability to cementitious systems. Cementitious systems have special requirements due to multiple scales and broad diffusivity ranges. In particular, numerical stability effects and oscillations are thoroughly analyzed. For details on the equations implemented, see sections 3.5.8 and 3.5.9. Although the C++ implementations of the extended Lattice-Boltzmann schemes are placed inside iPP, these algorithms are of general purpose for Palabos. Thus, the findings in the corresponding section are independent of whether reactive transport modeling is addressed or not and are hence independent benchmarks.

Section 6.3 deals with the newly developed modeling tool iPP. For once, there is the implementation of the coupling of the transport algorithms to the chemical solver PhreeqC. In addition, there is more code involved dealing with transient porosity changes and implementations of heterogeneous and homogeneous reaction terms (see also section 4.4.1). These implementations are essential to ensure mass conservation and proper implementation of internal boundary conditions. Thus, this section contains selected benchmarks to ensure the validity of the new developments.

In section 6.4, computational scalability benchmarks are presented. In particular, it is shown to what extent different code optimizations have an effect on computational performance characteristics with respect to parallelization. An explanation of the optimizations done within this work is outlined in section 4.4.5. Moreover, a brief comparison of two computer clusters is depicted, in order to show the effect of hardware capabilities

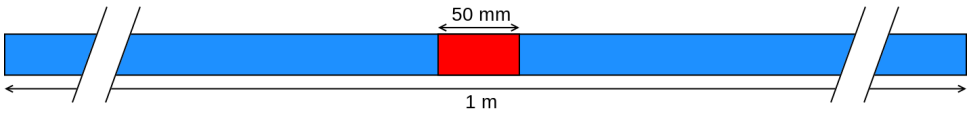

Figure 6.1: Initial conditions of a simple diffusion setup. Red corresponds to a domain with $1\,\mathrm{mol\,L^{-1}}$ solute concentration while blue is initially pure water. The plot's scale is interrupted as indicated with dashed diagonal lines.

on the performance of the algorithms used for implementing various features of iPP.

6.2 General validity of Lattice Boltzmann schemes and stability domains

6.2.1 General correctness of Lattice-Boltzmann schemes

As first test, a simple diffusion model was set up in order to validate the general capabilities of the four selected Lattice-Boltzmann schemes (see table 4.1). The total size of the 1D model was 1 m with a resolution of 5 mm which corresponds to 200 nodes. Assuming a diffusion coefficient of $1 \times 10^{-9}\,\mathrm{m^2\,s^{-1}}$ and a reference relaxation parameter of 1.0, one iteration is equivalent to 4166.66 s. Initially, a zero solute concentration was applied except of a domain in the center with an initial concentration of $1\,\mathrm{mol\,L^{-1}}$. The initial high concentration domain was in the spatial interval of 0.475 and 0.525, thus symmetrical in the center with a total number of 11 nodes (figure 6.1).

The simulations with different LBM schemes were run for 1000 iterations each, which equals to a physical time of 48.23 d. The resulting concentration profiles are shown in figure 6.2 in conjunction with the results of an analytical solution. Since the analytical solution curve is completely covered by the numerical results they are in excellent agreement.

Subsequently, the same setup was modeled with a reduced diffusion coefficient of $1 \times 10^{-10}\,\mathrm{m^2\,s^{-1}}$. For each LBM scheme the corresponding transport scalar was adjusted accordingly while maintaining the same time stepping behavior, i.e. by adjusting the reference relaxation parameter τ for SRT, the bounce-back fraction for PBB, the diffusion velocity correction for DV, and τ_a in the TRT case (see also section 4.2.4). The results are plotted in figure 6.3. Except for the PBB simulation (top right) the results are again in good agreement with the analytical solution.

Obviously, there is a discrepancy in the partial-bounce-back LBM scheme when it comes to adjusting the bounce-back fraction in order to alter diffusivity. This deviation was further analyzed by simulating the same model with a series of varying bounce-back fractions and fitting the analytical solution using the diffusion coefficient as free parameter. This way the corresponding relative diffusion coefficients were obtained, which were actually simulated by the bounce-back scheme. The results are shown in figure 6.4, which reveals a non-linear relation between bounce-back fraction and resulting

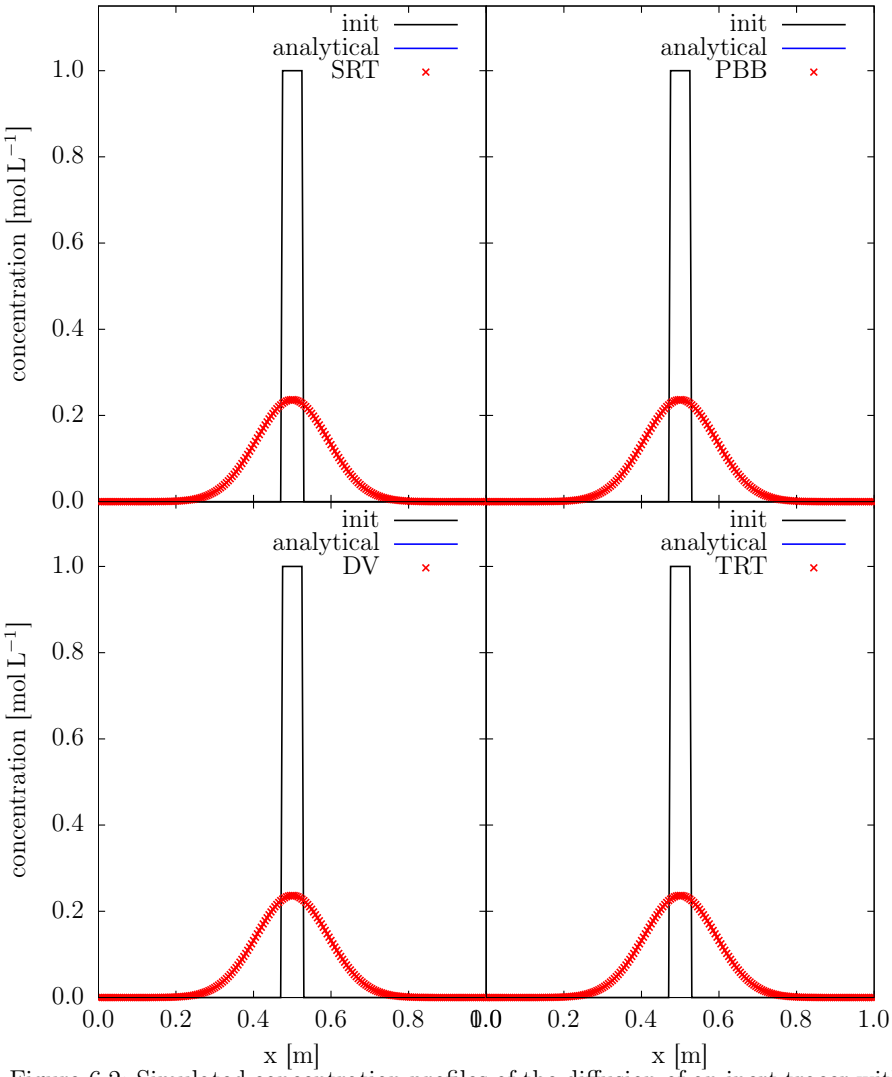

Figure 6.2: Simulated concentration profiles of the diffusion of an inert tracer with diffusion coefficient of $1.0 \times 10^{-9}\,\mathrm{m^2\,s^{-1}}$ after $4.166\,67 \times 10^{6}\,\mathrm{s}$ using different LBM schemes compared to an analytical solution. The results of the analytical solution are completely covered by LBM result points.

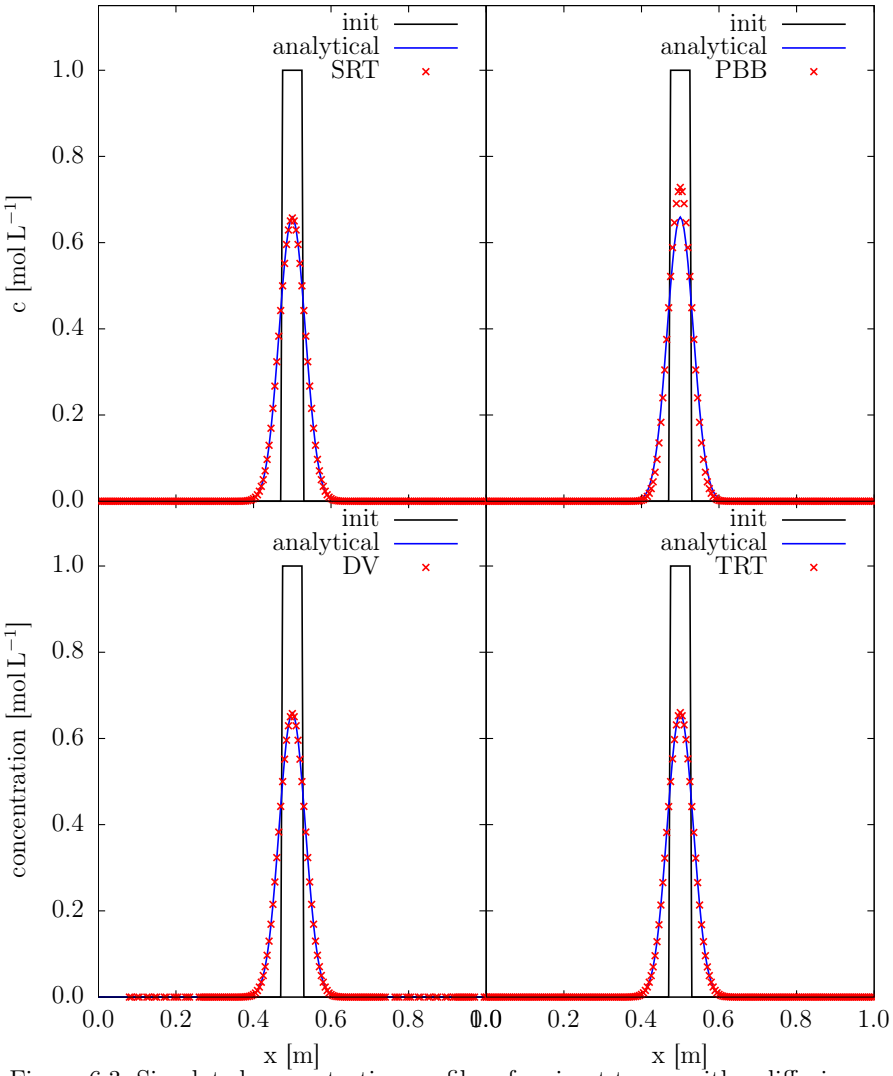

Figure 6.3: Simulated concentration profiles of an inert tracer with a diffusion coefficient of $1.0 \times 10^{-10}\,\mathrm{m^2\,s^{-1}}$ after $4.166\,67 \times 10^6\,\mathrm{s}$ using different LBM schemes compared to an analytical solution.

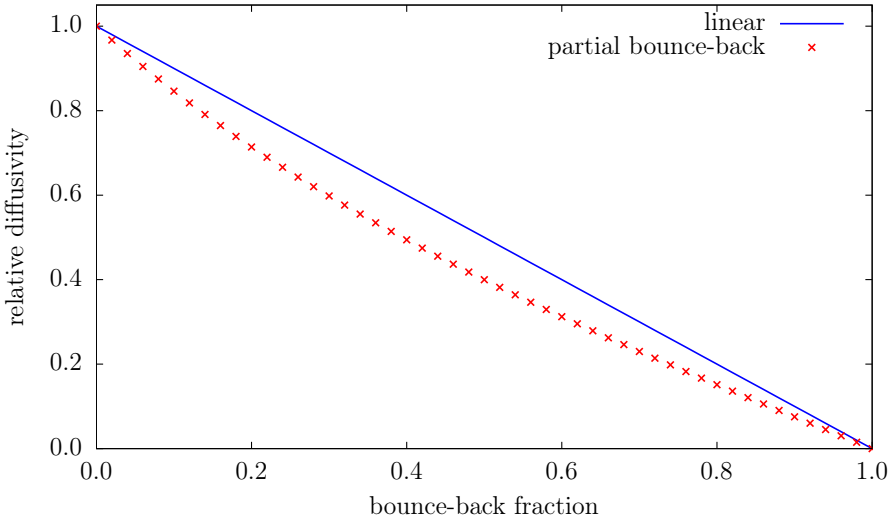

Figure 6.4: Calculated relative diffusion coefficients in dependency of the partial bounce-back fraction used in simulations with the PBB scheme.

diffusion coefficient.

Walsh et al. already reported that the bounce-back fraction n_s is to be regarded as modeling factor and not as physical property by itself and recommended a tortuosity function which has to be fitted [Wal09]. The simple PBB approach without correction gave wrong results and a correction term was not further investigated here, since also other authors also criticized PBB [Gin16]. Moreover, during empirical testing whether very low diffusivities are feasible it turned out that serious oscillations did occur for low diffusivities (not shown here). Therefore, even if correctness issues could be solved, the chance that the stable diffusivity range would be too constrained to a limited range was quite high. Thus, the PBB approach was completely abandoned for this work.

6.2.2 Numerical stability and correctness of LBM schemes

Although the general validity of three LBM schemes (SRT, DV-SRT and P-TRT) was shown in section 6.2.1, there are certain limits of stability for each approach. The tests in this section are intended to show these limits with respect to varying diffusivity values. Therefore, a similar model was set up as in section 6.2.1 with differences in spatial resolution and width of the high concentration domain. Here a spatial discretization of 0.5 mm (i.e. 2000 nodes for the total domain of 1 m) was used, while the high concentration domain was again defined by 11 nodes centered in the model, but due to smaller spatial discretization within the interval between 0.4975 m to 0.5025 m.

As metric to characterize the error during simulation a normalized L2-norm ($\bar{L2}$) was

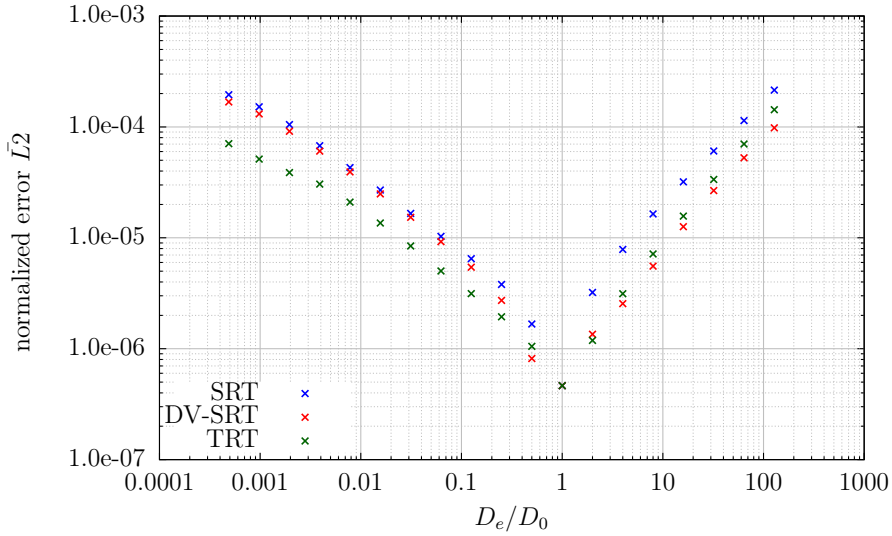

Figure 6.5: L2 errors for different LBM schemes determined over a range of simulated diffusivity ratios (relative diffusivities).

used:

$$\bar{L2} = \frac{\sum_t^{n_t} L2(t)}{n_t n_n} \tag{6.1}$$

Thus, the normalized error is the sum of all L2-norm values of each iteration divided by the number of time steps n_t and the number of spatial nodes n_n. L2 is defined as:

$$L2 = \sqrt{\sum_n^{n_n} (c_a(n) - c_{LBM}(n))^2} \tag{6.2}$$

Here c_a and c_{LBM} are the concentration values of the analytical solution and of the LBM simulation, respectively. The value for $\bar{L2}$ has no direct physical meaning, but the lower the value the lower is the error in the simulation.

A wide range of relative diffusivities (D_e/D_0) from 2^{-11} to 2^7 were tested. Relative diffusivities are referring to the deviation from the reference diffusion coefficient (see also section 4.2.4). The calculated L2 errors of the simulations are presented in figure 6.5. As expected, the lowest error was observed at a diffusivity ratio of 1, at which no adjustments were in effect to alter the diffusion coefficient. Although the L2 error is not zero, the results were in excellent agreement with the analytical solution, i.e. very similar to the results shown in figure 6.2.

Besides, the error increases for all three analyzed LBM schemes when increasing or decreasing the simulated diffusion coefficient. It is clearly visible that the errors in the

relative diffusivity region below 1 are lower for the TRT scheme compared to both SRT schemes. In the domain above 1, the simple SRT approach performs worse than DV and TRT.

In order to evaluate the significance of the errors observed here, the resulting concentration profiles were inspected in more detail to figure out the origin of the errors. A reference volume of free water has virtually the highest diffusivity in saturated porous media, while diffusivity in a porous medium with an obstructing solid matrix experiences certain reductions from this value. Therefore, it is beneficial to define free water as reference diffusivity and scale all other lower diffusive phases accordingly. Thus, of particular interest are the errors occurring in the domain lower than one.

In figure 6.6 two magnified views of the simulated concentration profiles are plotted for the simple SRT scheme. The relative diffusivities used were 1/32 and 1/64, corresponding to a relaxation parameter of 0.516 and 0.508, respectively. Barely visible, but starting with a relative diffusivity of 1/32 small negative concentrations occur at locations where a high concentration gradient prevails. The numerical errors are more significant with lower diffusivities as 1/64. In addition to the negative concentration peak, the bottom figure shows a magnified view of the baseline. Clearly visible is an oscillation of the concentration around zero. These oscillations propagate over the whole simulation domain. Moreover, the results also diverge from the analytical solution by 1×10^{-5} for simulated relative diffusivities higher than approximately 5. These numerical effects are known artifacts of the SRT scheme and obviously already occurring with moderate relaxation parameters.

Based on these analyses, if prevention of oscillations and results within an error bound of 1×10^{-5} are demanded, the SRT approach is limited to relative diffusivities approximately between 1/20 and 5. Thus, the SRT scheme produces results which are valid in a range of a factor of 100.

Similar plots are shown for the DV-SRT approach in figure 6.7. For these simulations, the relaxation parameter τ was unaltered. Instead, the diffusive fraction in the velocity term was adjusted to fit to the corresponding diffusivity (see also equation 3.69). The scheme seems to be more robust with respect to negative concentration issues, since for a relative diffusivity of 1/32 there are apparently no negative concentrations visible in the magnification. However, starting with a relative diffusivity of 1/64, the negative concentration issue emerges as well. Moreover, in the bottom plot there is no baseline oscillation effect over the complete domain. However, close to the location of the high concentration gradient an up-down-up pattern is visible. Thus, there is still oscillation present but limited to a few spatial nodes and, in contrast to the default SRT scheme, which does not propagate into the whole computational domain.

As already mentioned, for the L2 error plot only the diffusive velocity term in the DV-SRT scheme was adjusted and the relaxation parameter was left to 1.0. Still, it is possible to adjust either or both parameters to fit a desired diffusion coefficient. In a further benchmark, both values were varied and the L2 error was sampled. The resulting 2D space of errors is shown in figure 6.8. The data plotted in figure 6.5 are represented as data points on a horizontal line at $\tau = 1.0$. The dark-blue colored region depicts a domain in which the error is low. Clearly, using a relaxation parameter of 1 gives the

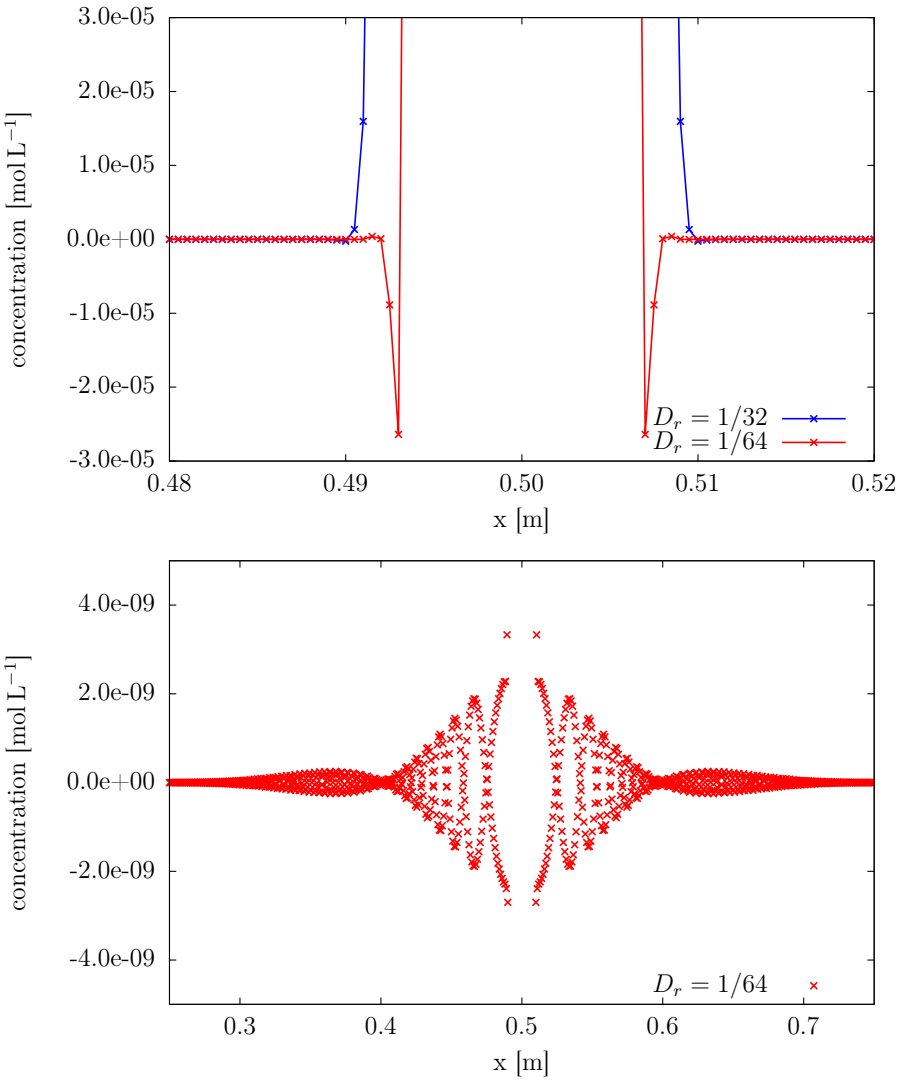

Figure 6.6: Top: Closeup at the high gradient region of the concentration profiles of the simulation conducted by the SRT approach. The data shown were determined by using a diffusivity ratio of 1/32 and 1/64 (blue and red, respectively). Concentrations at the edge between high and low concentrations show significant negative concentration results. The lines serve as guidance to the eye. Bottom: Magnified concentration baseline showing strong oscillations for lower diffusivity values.

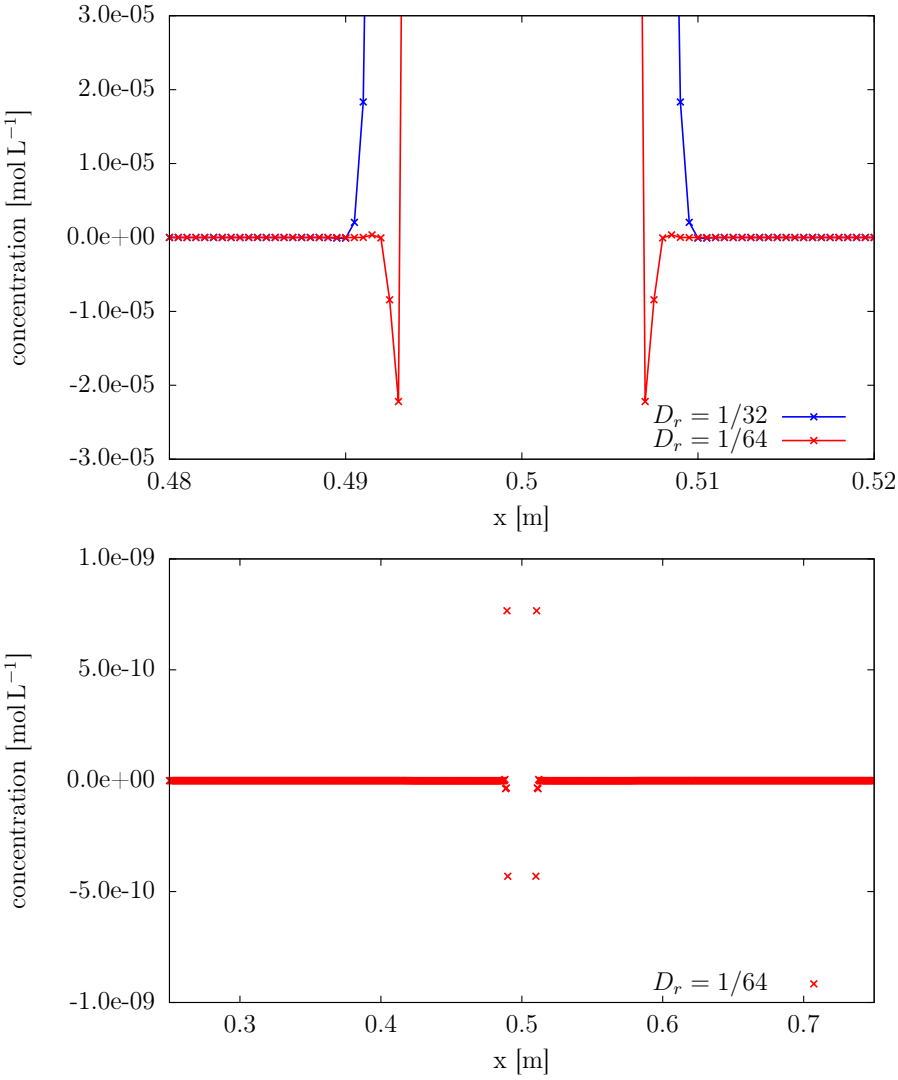

Figure 6.7: Top: Closeup at the high gradient region of the concentration profiles of the simulation conducted by the DV-SRT approach. The data shown were determined by using a diffusivity ratio of 1/32 and 1/64 (blue and red, respectively). Bottom: Magnified concentration baseline showing no oscillations for lower diffusivity values.

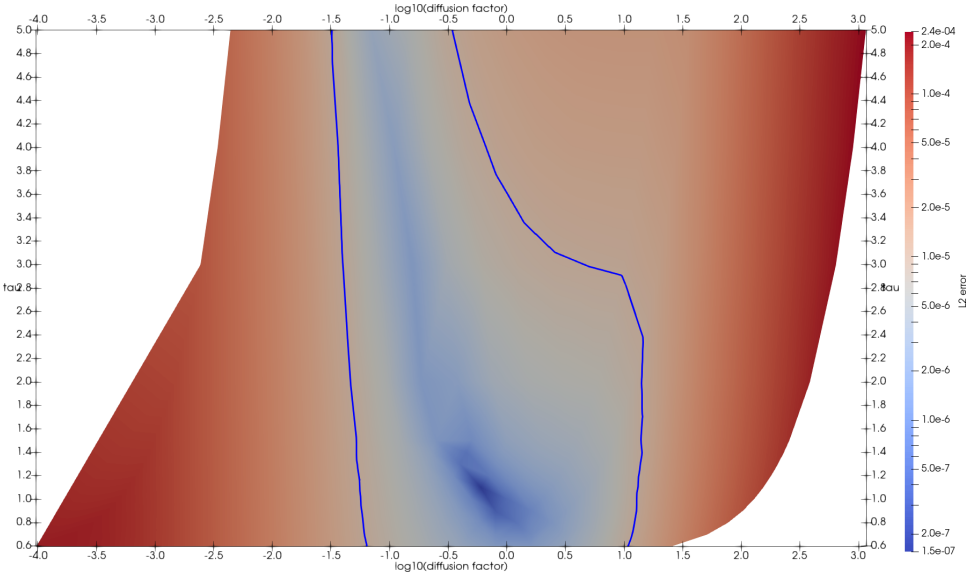

Figure 6.8: L2 error of concentration profiles determined by the DV-SRT approach. The blue colored domain depicts values which were determined as non-oscillating. The values indicated by the blue line are lying on a threshold error of 1.0×10^{-5}.

most stable and accurate results. Within the boundaries of the blue iso-line the error is below 1×10^{-5} which has none or only tiny oscillatory issues. Outside this domain, the results of the simulations were erroneous and not reliable. Thus, it is possible to adjust the relative diffusivity from $10^{-1.3}$ to $10^{1.0}$ when using a τ value between 1.0 and 2.0. Obviously, if negative concentration values and oscillations are to be prevented, the DV-SRT scheme is limited to a diffusivity variance of approximately $\frac{10^{1.0}}{10^{-1.3}} = 200$. Also, by adjusting the relaxation parameter and the diffusive fraction at the same time, the DV-SRT scheme is not capable to gain more flexibility.

The TRT scheme was the third LBM scheme tested. Here, the simulations were performed using a very low diffusivity ratio of 1/2048. The simulation results compared to the analytical solution are shown in figure 6.9. Even for a very low relative diffusivity value, the TRT results are still in good agreement to the analytical solution. The error for this simulation is shown in figure 6.5 on the very left side of the graph and is about 7×10^{-5}. Mainly, this error stems from the flanks of the high concentration domain. The simulation results show no oscillations or negative concentrations at all. Simulations which used a diffusivity ratio of 64 were still stable (not shown here) but with errors emerging in the same magnitude as the DV-SRT scheme. Thus, the stability and correctness range of TRT obeys similar limits to the upper end as DV-SRT. On the other hand, there is no stability limit to the lower end. Thus, it is impossible to express

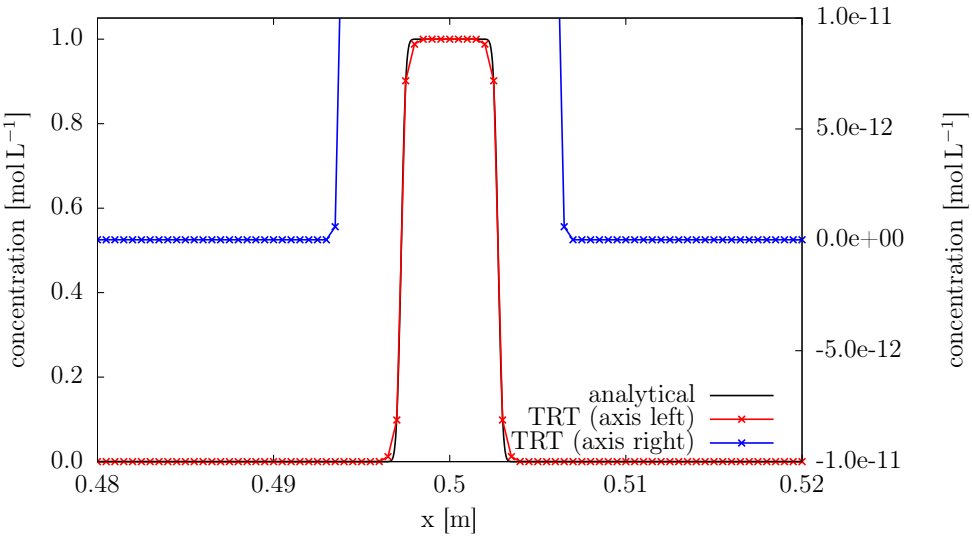

Figure 6.9: Concentration profiles of the simulation conducted by the TRT approach compared to analytical solution (red and black, respectively, scaled to left axis). The data shown were determined by using a diffusivity ratio of 1/2048. The magnified concentration baseline shows no oscillations for lower diffusivity values (blue, scaled to the axis on the right). Lines connecting the numerical data points are a guide to the eye.

it in a range as done before for both SRT schemes.

6.2.3 Conclusions

Four different Lattice-Boltzmann schemes were analyzed regarding their capability of adjusting simulated diffusion coefficients and analytical concentration profiles in a diffusive setup. The used partial-bounce-back scheme does not capture the diffusivity correctly. Obviously, this scheme was developed for simulating variances in permeability instead of diffusivity. However, due to the poor performance in a diffusive framework, the scheme was dropped for further analyses and applications.

Subsequently, the remaining three schemes were tested with regard to their numerical stability. At the lower end of relative diffusivities, the basic SRT approach has shown nonphysical negative concentrations and oscillations even for quite moderate relaxation parameters. While the DV-SRT scheme shows improvement compared to the SRT scheme, it still suffers from negative values. Oscillations are reduced but still occur around regions with high concentration gradients. In contrast, the TRT scheme revealed unconditionally stable, even for very low relative diffusivities and no limit was found in this regard. Still, the correctness was reduced for TRT at very low diffusivities, although

distinctively less than for both SRT schemes. On the upper end of relative diffusivities, increased diffusivity over the reference value, both, TRT and DV-SRT approaches, were more stable and accurate than SRT. However, the limits cannot be pushed indefinitely even by using the TRT scheme.

The limitations regarding applicable ranges for diffusivities were determined for all three schemes. The SRT (BGK) scheme can cope with variations in diffusivity of up to two orders of magnitudes, while the DV-SRT approach expands this limit to a factor of 200. Although, DV-SRT gave better stability results than SRT, it is deemed still too limiting for the demands of simulating cementitious systems with CSH as diffusive continuum. The application range of the TRT technique is difficult to quantify, because there was no limit of stability towards the lower end, just a limit of accuracy. Still, the accuracy for the factor of 1/2048 simulation was quite satisfying compared to the SRT schemes, which were limited at 1/64.

In addition to the wider application range, the TRT scheme used here has the feature to capture transient porosity changes intrinsically, which did not enter the discussion of stability. Both SRT techniques would have still to be extended to capture this effect. All in all, the TRT scheme outperforms all other tested Lattice-Boltzmann diffusive transport schemes and was used subsequently for all further simulations.

6.3 Analytical and numerical benchmarks

6.3.1 Transport only simulations

In this section the capabilities of the implemented algorithms in iPP with respect to transport processes are analyzed. Essentially, this section is distinguished from the reactive transport section in order to separate the effects observed. All the following benchmarks were conducted with the TRT scheme as described in sections 3.5.8.3 and 3.5.9.4.

6.3.1.1 Constant concentration (Dirichlet) boundary condition

In solute transport simulations, constant concentration boundaries are imposed via the Dirichlet boundary conditions. To test iPP regarding correctness and accuracy, a simple 1D model was used. The system was composed of a domain containing pure water with a length of 10 µm with a spatial discretization of 0.1 µm. At the left boundary, a constant concentration of $1\,\mathrm{mmol\,L^{-1}}$ calcium was applied. This concentration was low enough to prevent any solid (e.g. portlandite) to precipitate. Therefore, the whole simulation is regarded as chemically inert. The simulation was run for 300 iterations, which corresponds to 0.5 ms assuming a diffusion coefficient of $1 \times 10^{-9}\,\mathrm{m^2\,s^{-1}}$. The resulting concentration profile is shown in figure 6.10 in comparison to the results of the

analytical solution given as [Cra75]:

$$c(x,t) = c_0 \operatorname{erfc}\left(\frac{x}{2\sqrt{(Dt)}}\right) \tag{6.3}$$

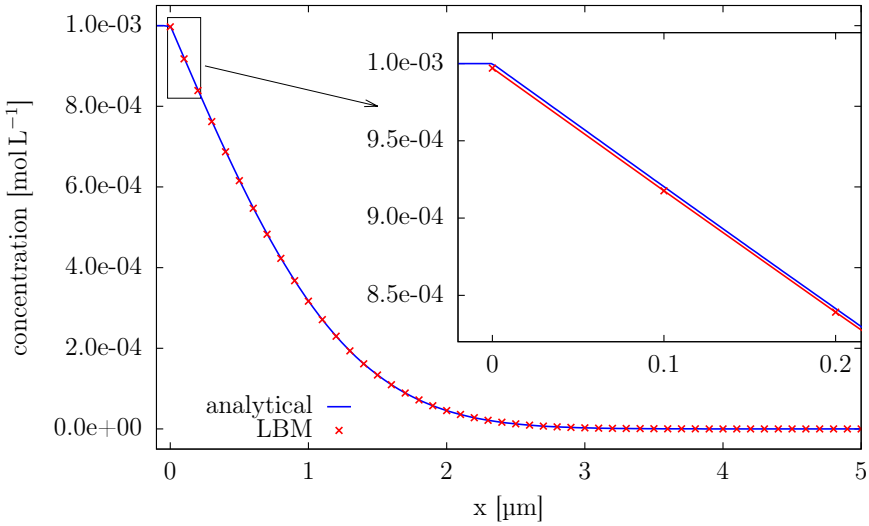

Figure 6.10: Simulated concentration profiles of calcium diffusion into pure water assuming a constant calcium concentration (Dirichlet) boundary condition at $x = 0$ and a diffusion coefficient of $1 \times 10^{-9}\,\mathrm{m^2\,s^{-1}}$. Simulation time is 0.5 ms.

Comparing the numerical results with the analytical solution the reveals an excellent agreement. The only difference visible in the magnification is a small offset towards the boundary. However, this artifact has a minor effect and is negligible.

6.3.1.2 Closed boundary condition and mass conservation

Conservation of mass is a fundamental property of every closed physical system. As a simulation describes a physical system, it has to obey the same rules of conservation. In order to validate iPP in this regard and check for numerical issues, a simple 1D model was set up simulating the diffusive transport of tracers. The simulation results are concentration profiles which are multiplied by the respective volume and the total sum of solute of the complete domain is computed. These values are calculated for subsequent iterations and compared to the initial total solute mass in the system. This way it is deducible if any mass is lost or gained.

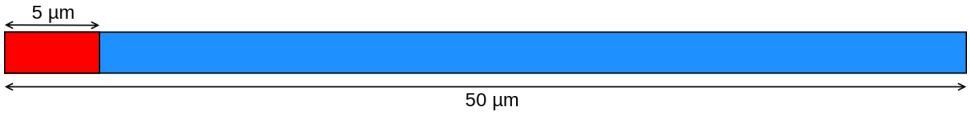

Figure 6.11: Initial conditions of a closed system setup. Red corresponds to a domain with $1\,\mathrm{mmol\,L^{-1}}$ solute concentration (NaCl) while blue is initially pure water.

The selected tracers were Na and Cl ions in low concentrations in order to prevent precipitation of a solid phase. The total length of the model domain was 50 µm with a spatial discretization of 0.1 µm yielding to 500 nodes. The system was closed at both ends, i.e. closed boundary conditions, and split into two domains. Initially, the first 50 nodes contained the tracers with concentrations of $1\,\mathrm{mmol\,L^{-1}}$ each, while the remaining 450 nodes just contained pure water without solute (see figure 6.11). After 100 time steps the amount of the tracers, i.e. amount of Cl and Na, were integrated over the whole system and a relative error was determined. The error is calculated by the sum of amount at a certain time step normalized by the sum of the initial value. This was repeated until 50,000 iterations. Since only the conservation of mass and amount of a substance is of importance in this benchmark, the resulting relative errors for the first 5,000 iterations are plotted against the iteration steps in figure 6.12.

Initially, two different configurations were simulated, one with PhreeqC including its equilibrium calculation (speciation) enabled (green) and one in which the chemical equilibrium calculation was disabled internally in PhreeqC (blue). The latter one still did all floating point arithmetic of the coupling, which is not negligible, and the Lattice-Boltzmann code, but omitted just PhreeqC. This allows to test all coupling and transport algorithms for correctness with respect to mass conservation separate from PhreeqC. Since no solid phase precipitation occurs at these low tracer concentrations, the local chemical equilibrium concentrations shall remain the same and the source/sink term in the transport code is zero. Analytically, the relative error should be zero, but the plot shows a tiny error and an increase in mass even for the configuration where the PhreeqC equilibrium calculation is replaced by a dummy (indicated in green and blue in figure 6.12).

The error of the *no-speciation* setup is likely due to accumulated rounding errors of the floating point arithmetic, which is heavily used during the transport algorithm. The precision of the double precision floating point data format is in the same order of magnitude as the errors obtained here [IEE08].

The simulation involving PhreeqC with double precision arithmetic shows another error which is higher by 5 to 6 orders of magnitude. Although PhreeqC did not necessarily need to adjust the concentrations at all because the solution was undersaturated and equilibrium conditions with respect to solids were already met, it introduces some kind of error. This is likely due to the numerical accuracy involved in solving the algebraic equations internally. Coincidentally, PhreeqC uses a parameter called *convergence_tolerance*, which has a value of 1×10^{-8} in default configuration [Par13], which is in the same order

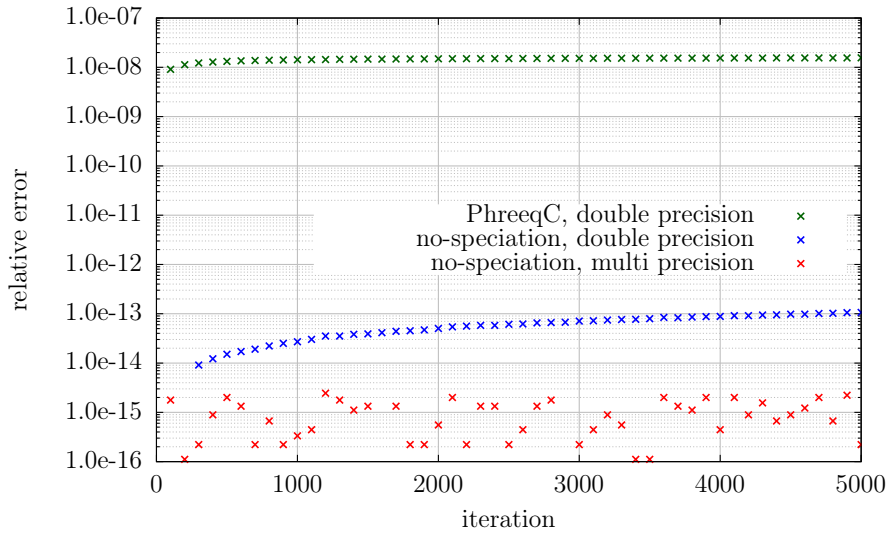

Figure 6.12: Relative errors in mass conservation of three different algorithmic setups. The results indicated by PhreeqC (green) are obtained by running the simulation with full speciation of PhreeqC, while for *no-speciation* the chemical solver PhreeqC was replaced by a dummy implementation without any effect. The results indicated in blue have used double floating point precision (about 16 digits precision), while the red data points refer to a simulation using a multi-precision data type with 50 digits.

of magnitude as the error observed here. For testing purposes, the PhreeqC convergence tolerance parameter was reduced to 1×10^{-14} and the error observed was about 1×10^{-11} However, at the same time the computational performance of the speciation calculation was reduced.

To test the assumption of floating point rounding effects in the simulations without speciation calculation, the transport code was ported to utilize a multi-precision floating point data type defined by the boost C++ library. The particular type used here was *cpp_dec_float_50*, which supports up to 50 digits accuracy [Mad19]. In contrast, the CPU built-in double floating point type has about 16 digits accuracy. Although the transport module and Palabos are written in a manner to relatively easily replace the underlying floating point type, several caveats had to be treated. For the whole porting procedure also program code within Palabos had to be extended in order to support this rather exotic data format, since only data types provided by the C++ standard are supported by Palabos in its original version. In particular, MPI data exchange functions had to be extended.

The resulting error with respect to mass conservation in the simulation is plotted in figure 6.12 as red data points. It is clearly visible that the numerical error drops by

3 orders of magnitude compared to the simulation using double precision (blue data points). However, the performance dropped also significantly, i.e. the simulation took 70 times the runtime of the double precision arithmetic. The reason is that no floating point accelerated CPU instructions can be used with those multi-precision data types and each arithmetic operation is replaced by a pure software based one. Another test was run using single precision floating point format, which has only about 7 digits of precision, and the error increased by 5 orders of magnitude, which supports the same conclusions. The detailed results are not shown here due to the sake of clarity in the plot.

All in all, the errors in mass conservation depicted here need to be viewed in relation to their significance on the simulation results. Even with PhreeqC enabled using the default convergence tolerance, the error is below $1 \times 10^{-5}\,\%$ and can be neglected with respect to the accuracy needed for reactive transport simulations. Benefits in computational performance exceeded the minor accuracy gain in this case. Other errors, like Lattice-Boltzmann truncation errors, and uncertainties with respect to model assumptions have by far more impact on the effective error and uncertainty of the simulation results. Therefore, no further measures were taken to reduce the errors introduced by PhreeqC or any other floating point round-off issues.

6.3.1.3 Steady state transport

In order to test the capabilities of iPP regarding the determination of transport parameters in terms of effective diffusion coefficients, an analytically solvable 3D model was set up. For this, a single spherical obstacle was placed into a cubic box with two dimensions defined as periodic boundaries, which renders the model essentially infinitely repeating (cf. figure 6.13).

At the boundaries of the remaining dimension, constant concentrations were applied (Dirichlet type). Initially, the concentration is initialized by a linear gradient from inlet to outlet. The edge length of the box was varied between 1 m to 0.5 m in order to establish different sphere to box size ratios, thus mimicking different porosities. The radius of the sphere was set to $r = 0.25$. Non-axis aligned geometries have to be approximated by a staircase scheme in LBM, thus the surface of the sphere was approximated in the same manner and thus is not a perfect mathematical description of a spherical body. Only in the limit of an infinite spatial resolution, the sphere could be perfectly represented. However, the spatial resolution was set to 5 mm here.

The outlet flux eventually converges towards a steady state value. At this point, the Fick's first law can be applied to determine the effective diffusion coefficient of the system. Some resulting diffusive stream-lines of the steady state solution in combination to the solid geometry are shown in figure 6.13.

The analytical solution of such a problem as function of porosity is described by a simple Archie's law approach with an exponent of 1.5 [Glo09,Pha00]:

$$D_r = \frac{D_e}{D_w} = \phi^{1.5} \tag{6.4}$$

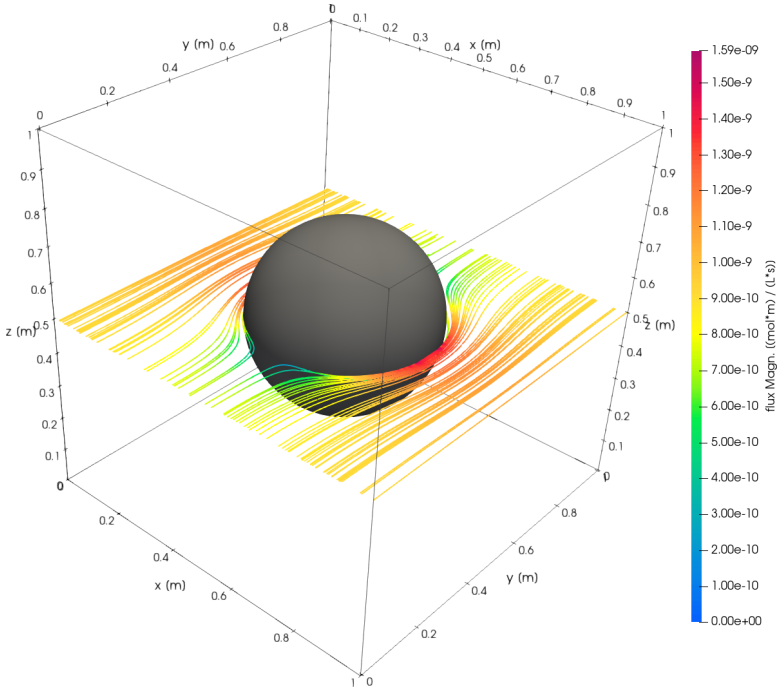

Figure 6.13: Diffusive flux streamlines around a spherical obstacle (radius 0.25 m) embedded in a cubic box (edge length 1 m). The streamlines are only shown in the central XY-plane for illustrative reasons.

In this equation D_w corresponds to the diffusion coefficient of the matrix which embeds the inclusions, which might be water, hence the subscript w. The resulting relative diffusion coefficients D_r and the corresponding analytical solution are shown in figure 6.14.

The results are in good agreement to the analytical solution for higher porosity values but tend to deviate slightly at lower porosities. This is likely due to neighboring effects and due to the staircase approximation of the surface of the sphere, which is getting coarser in relation to the box size with decreasing total porosity. With a higher spatial resolution this effect would decrease (not shown here), because the error due to the staircase effect would be reduced. Essentially, by increasing the spatial resolution the simulated results would converge even more accurately to the analytical solution.

6.3.2 Reactive transport simulations

In section 6.3.1 only the transport module of iPP was tested for solute diffusion, while all benchmarks in this section have the reaction module enabled. This allows to evaluate the validity of the reactive transport simulations described in Part III.

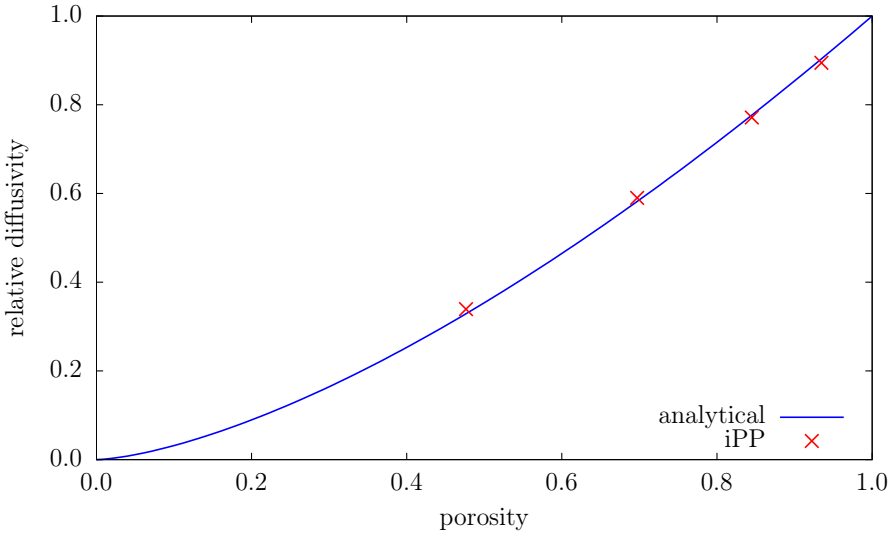

Figure 6.14: Relative diffusivity of a system including a spherical inclusion as obstacle. Comparison between an analytical solution (blue curve) and the numerical results of iPP (red).

6.3.2.1 Internal boundary condition

In order to benchmark the heterogeneous reaction term, a 1D model was used, consisting of a portlandite domain with a length of 0.5 µm and a 9.5 µm domain comprising pure water (see figure 6.15). The spatial discretization was chosen as 0.1 µm and the boundaries were modeled using a closed boundary condition. The diffusion coefficient assumed for dissolved calcium was $1 \times 10^{-9}\,\mathrm{m^2\,s^{-1}}$.

The simulation was run for 0.5 ms physical time and the calcium concentration profile in solution was determined. During this short time, the solid interface node has not been completely depleted of portlandite and can be assumed as constant boundary condition in terms of a source of calcium diffusing into the water-filled domain. The simulation

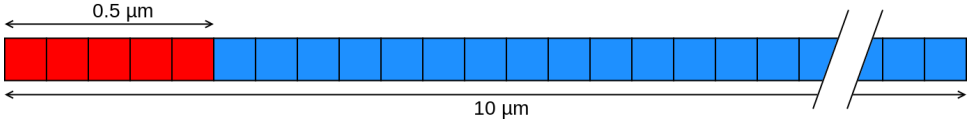

Figure 6.15: Schematics of the initial setup of the internal boundary condition benchmark. Red indicates the domain, with a width of 5 cells, initially filled with portlandite while blue is pure water. The plot's scale is interrupted as indicated with dashed diagonal lines.

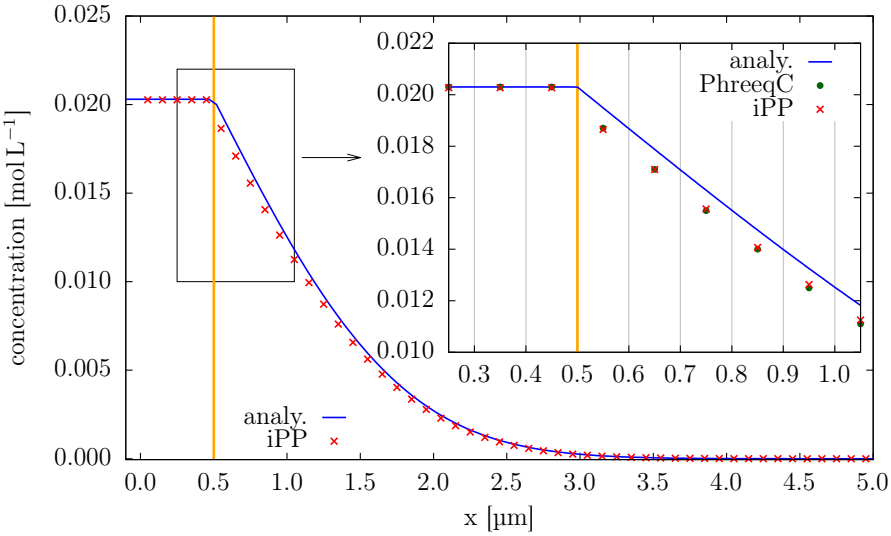

Figure 6.16: Simulated calcium concentration profiles due to portlandite (domain left of orange vertical line) dissolving in pure water after 0.5 ms using iPP in comparison to an analytical solution. The diffusion coefficient assumed was $1 \times 10^{-9}\,\mathrm{m^2\,s^{-1}}$. The magnified area shows the interface domain and compares the iPP result to the analytical solution and the results of a 1D PhreeqC simulation. The cell boundaries are indicated as vertical gray lines. Notice that the PhreeqC results (green dots) are almost covered up by the iPP data points (red crosses).

results are shown as red crosses in figure 6.16 in addition to the analytical solution and the results of a 1D PhreeqC simulation of the same geometry and timescale.

The overview plot shows the analytical solution (blue curve) with respect to the exact interface location compared to the iPP results (red symbols). The numerical results of iPP for the concentrations of dissolved calcium are not perfectly in agreement with the analytical solution, i.e. essentially shifted towards the left.

The close-up in figure 6.16 compares the concentration profile derived by an analytical solution, assuming a constant boundary concentration exactly at the interface at 0.5 µm, and the results from iPP and PhreeqC. Apparently, the results from iPP and PhreeqC are shifted half a discretization step towards the solid portlandite domain. Thus, the magnitude of the error is lower than the accuracy of the spatial discretization, which renders the accuracy sufficient.

As the portlandite starts to dissolve, with this half-step spatial discretization error, the effect on the concentration of the solution is temporarily underestimated. However, during dissolution of portlandite the interface is moving towards lower x coordinates until the solid interface cell would be half filled by solution. At that point in time, the

boundary location is exactly as simulated (cf. figure 6.16).

During further dissolution the physical boundary would even move further to lower x-values and the simulated interface would then be located too far in the fluid domain. The effect is that the concentration imposed on the solution would be temporarily overestimated, i.e. has a half-step spatial discretization error. The effect is the opposite and symmetric to the situation in the beginning, when the interface cell was still filled more than half (see text above). However, on average during the dissolution process, the simulated interface location is positioned correctly in the cell center and thus displays the expected behavior. Interestingly, the 1D reactive transport implementation in PhreeqC behaves similarly (green points in figure 6.16), since the results are in very good agreement to the iPP simulation.

6.3.2.2 Mass conservation during porosity changes in reactive transport simulations with iPP

In order to test iPP for implementation errors with respect to the treatment of volume changes due to porosity changes, an artificial phase with a high molar volume with a chemical composition equal to halite was introduced in the PhreeqC database. The new entry reads:

```
HighVm
        NaCl  =  Cl- + Na+
        log_k     -6
        -Vm 100000
```

According to this definition, the phase has a molar volume of $100\,000\,\mathrm{cm^3\,mol^{-1}}$ and a solubility of approximately $1\,\mathrm{mmol\,L^{-1}}$ in pure water. Thus, one liter of volume would be filled by 10 mmol of this phase, while dissolving rather quickly in contact with undersaturated solution. During development of iPP several bugs were revealed by testing with this artificial phase because this way errors show up more pronounced. The artificial HighVm phase is a suitable fictive solid to demonstrate the correctness of the underlying algorithms and porosity treatments, since errors would show up prominently as artifacts in the results. The results shown here are those of the final implementation of transient porosity change treatments.

To evaluate the accuracy, a 1D HighVm phase dissolution model was set up with a large but closed pure water column. The same geometric model, as already described for the mass conservation benchmark in section 6.3.1.2, was used (see figure 6.11), with the difference that the HighVm phase was placed at the left-hand side domain. Thus, the HighVm phase domain serves as source for Na and Cl. In this model, solid nodes with a porosity lower than 0.5 are treated as heterogeneous source, while switching to a homogeneous source as the porosity evolves higher than the threshold value of 0.5. Thus, the HighVm is regarded as non-diffusive. The errors are calculated the same way and are presented in comparison to the mass conservation behavior of the inert transport-only simulation (see section 6.3.1.2) in figure 6.17.

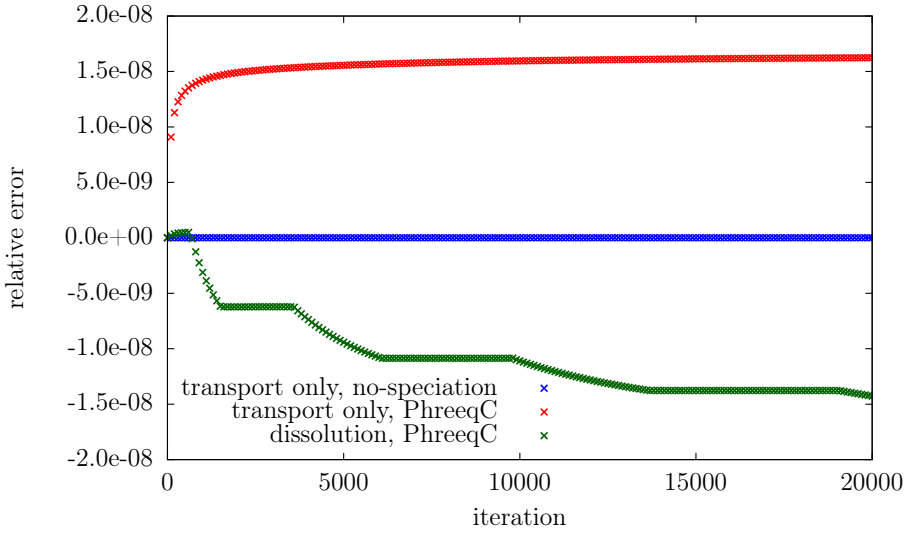

Figure 6.17: Relative error in mass conservation of three different algorithmic setups. Both transport only results (red and blue) are taken from section 6.3.1.2 as comparison to the relative error introduced by dissolution of a fictive HighVm solid (green) with an extremely high molar volume.

Although there is a non-zero mass conservation error in the LBM reactive transport simulation, the order of magnitude is the same as in the inert transport simulation involving PhreeqC. During development and debugging of iPP each tiny implementation error at any involved code location yielded into a huge discrepancy by several orders of magnitude higher than observed here when using the HighVm phase. This supports that the code is treating mass balances for homogeneous and heterogeneous reactions properly, i.e. no additional error is introduced except of the ordinary intrinsic PhreeqC error. The discontinuities are originating from solid to liquid phase changes (at $\phi = 0.5$) subsequently activating new reaction cells in the reaction module and thus within PhreeqC. The simulation of dissolution with iPP shows an insignificant mass loss while inert transport shows a mass gain in the same order of magnitude. The conclusion is that PhreeqC seems to handle floating point numbers with a truncation error internally. As already mentioned in the mass conservation analysis of section 6.3.1.2, the errors and artifacts observed here are below 1×10^{-5} % and only visible due to the HighVm phase, thus deemed negligible for further reactive transport simulations.

6.3.2.3 Evolution of dissolution fronts

During dissolution of solids, the interface between solid and solution is moving. It is important for a reactive transport code, which deals with precipitation and dissolution

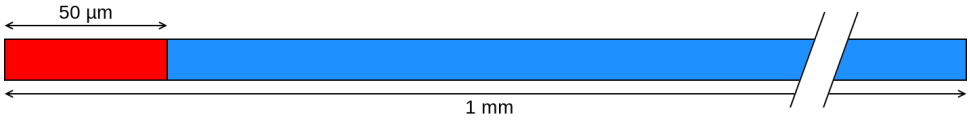

Figure 6.18: Schematic sketch of the initial setup of the dissolution front benchmark. Red indicates a domain initially filled with the HighVm phase while blue is pure water. The plot's scale is interrupted as indicated with dashed diagonal lines.

of solids, to treat this process properly [Noi21]. In this benchmark, the movement of the dissolution front is tested and compared to an analytical solution. Under the assumption of equilibrium conditions at the interface and known initial solid, solute and equilibrium concentration, such a problem is analytically solvable in 1D [Aar70]. The solution itself is given as:

$$x_I - x_0 = 2k\sqrt{Dt} \tag{6.5}$$

x_I is the interface location after time t, x_0 the initial interface position and D the diffusion coefficient of the solute in the medium. k is a constant, which is depending on the equilibrium $_{eq}$ and initial concentrations in solution c_0 and on the concentration of the solid c_m. k has to be determined by a transcendental equation:

$$\sqrt{\pi} k e^{k^2} \operatorname{erfc}(-k) = \frac{c_{eq} - c_0}{c_m - c_{eq}} \tag{6.6}$$

In order to test the agreement between iPP and this analytical solution, a 1D model using the same fictive HighVm phase as in the mass conservation section was employed. Using this HighVm phase stresses the rapid geometrical evolution of the dissolving phase and corresponding errors would be revealed rather prominently. In this benchmark, a 1 mm long column was filled with 50 µm of HighVm phase on the left-hand side (see figure 6.18).

Since the spatial discretization was chosen as 1.0 µm, the system consists of 1000 nodes in total, containing initially 50 nodes of solid phase. The purpose of the long column is to mimic an open system of infinite lengths, which can be directly compared to the analytical solution. By choosing a diffusion coefficient of $1.0 \times 10^{-9}\,\mathrm{m^2\,s^{-1}}$, the resulting time step per iteration is 83.3 µs. During the simulation, the solid-liquid interface moves to the left upon dissolution of the HighVm phase.

The resulting shift of the location of the interface as function of time is shown in figure 6.19 compared to the analytical solution. Even using the stressing high molar volume phase, the numerical result of iPP is in good agreement with the analytical solution. One peculiar effect is the up and down oscillation around the analytical solution. This is due to the half-spatial discretization error of the internal boundary condition as described in section 6.3.2.1. In particular, the oscillation effect is exaggerated by using the artificial HighVm phase. However, on average the location of the dissolution front is properly captured by iPP within the accuracy of the spatial discretization (cf. the gray horizontal

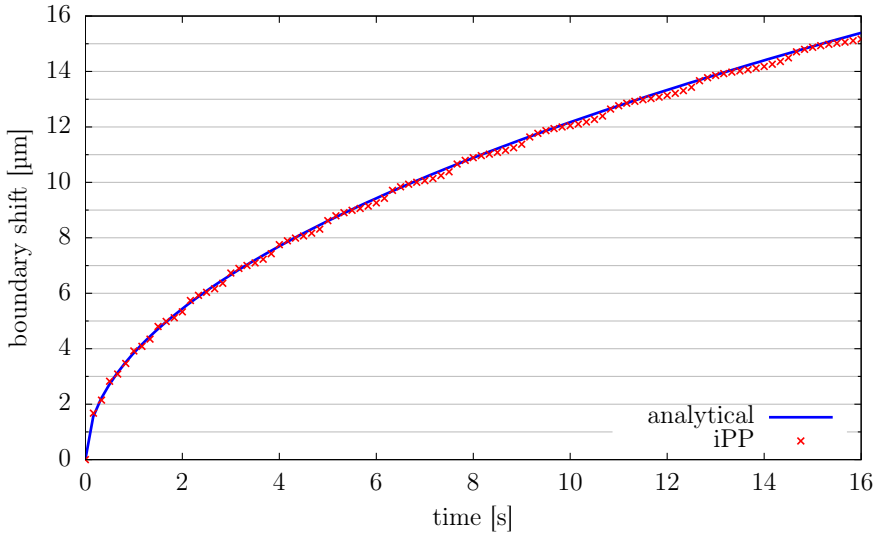

Figure 6.19: Evolution of position of the interface during dissolution of the HighVm phase. The spatial discretization is indicated as gray horizontal lines.

lines, which indicate the spatial discretization).

6.3.3 Conclusions

The reactive transport the benchmarks presented in this section show a good agreement of iPP with analytical solutions. Testing the Dirichlet boundary conditions for constant concentration boundaries shows excellent agreement. Moreover, internal boundary conditions for simulating heterogeneous reaction terms are also in satisfying agreement with respect to discretization errors.

Besides the comparisons with analytical solutions, stress tests with an artificially high molar volume solid phase did not reveal any additional sources of error in terms of mass conservation. Interestingly, there seems to be a truncation error in the algorithms of PhreeqC. However, the errors introduced by that are insignificant and negligible.

Furthermore, with the tests performed in this section, the corrections due to porosity changes in the homogeneous reaction term and the newly developed algorithm addressing the heterogeneous reaction term (see section 4.4.1) were proven to be correct. Moreover, changes within Palabos and PhreeqcRM done within the scope of the performance optimization did not introduce any additional errors (cf. section 4.4.5).

Table 6.1: Hardware specification of IEK-6 octa-core partition and JURECA [Kra18] clusters.

Cluster	IEK-6	JURECA
CPU architecture	AMD FX-8350	Intel Haswell Xeon E5-2680 v3
CPU clock	4 GHz	2.5 GHz
CPU cores (threads)	8(8)	$2 \times 12(24)$
RAM	32 GiB DDR3	128 GiB DDR4
Network connectivity	Ethernet (1 Gbit)	InfiniBand HDR (100 Gbit)

6.4 Scalability and computational performance

Pore-scale reactive transport simulations are computationally very demanding. Therefore, as already mentioned in section 4.4.5, during the development of iPP several optimizations and modifications in iPP and within PhreeqcRM were introduced to improve performance characteristics and multi-processing scalability. Notice that in contrast to multi-threading that multi-processing scalability is more difficult to achieve, as multiple processes are distributed on different compute nodes (cf. section 4.4.4.3). During the development of iPP, two different cluster systems were used to test scalability and to conduct simulations.

On the one hand, a desktop-grade CPU cluster type, which is also called *Beowulf cluster*, was used. The cluster is maintained in-house by the Institute of Energy and Climate Research (IEK-6) at Forschungszentrum Jülich. This kind of cluster consists of ordinary desktop computers which are set up in a way to provide network connectivity and offer MPI software installation. The used cluster consists of several hexa- and octa-core compute nodes which form a partition each. The octa-core nodes, which are specified in table 6.1, were used in this computational scalability benchmark. Although the capabilities of such clusters are outperformed by most setups provided by dedicated institutions offering HPC resources professionally, it is still capable to process smaller and mid-sized reactive transport models. This kind of cluster had also the benefits of be locally available and free for trial and error development iterations, while improving the iPP code without spending CPU hours quota, which would be wasted by using commercial HPC environments.

On the other hand, a general purpose computer cluster named JURECA at the HPC facility of the Jülich Supercomputer Center (JSC) was used. The compute-nodes of JURECA used for this work are specified in table 6.1. Notice that a compute-node of JURECA contains two CPUs and has HyperThread capabilities. Thus, the numbers of CPUs working within one node are 24, while 48 threads are possible to exploit the complete compute capabilities [Kra18]. The intra-node connectivity is realized with an InfiniBand (EDR standard) high-speed network which is much faster than ordinary Gigabit Ethernet, while causing less latency at the same time. Moreover, there are more than 1,500 compute nodes on site, which are exceeding by far the octa-core partition of the IEK-6 cluster, which comprise just 20 nodes.

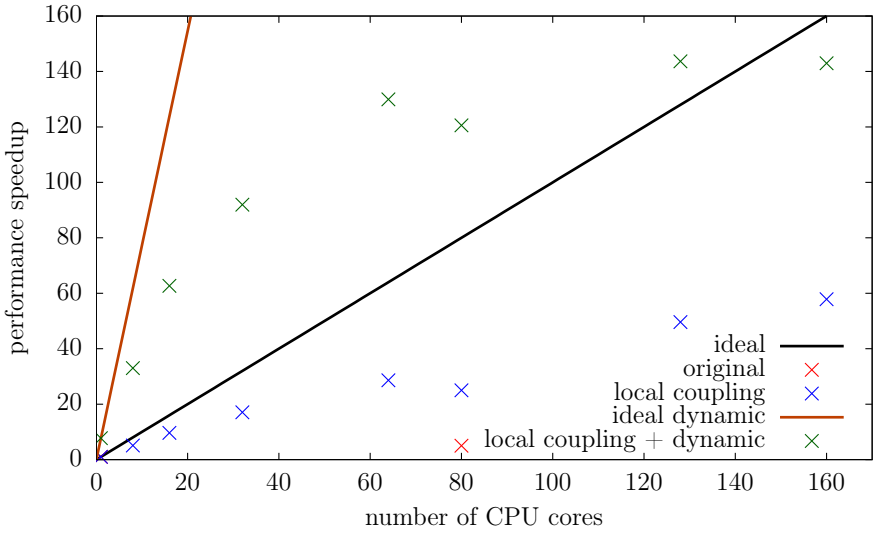

Figure 6.20: Speedup effect due to two different optimizations on the IEK-6 cluster. Improvement in speedup gained due to local coupling by optimizations in PhreeqcRM (blue) and gain in dynamic reaction cell activity optimization within iPP (green). As comparison, the ideal scaling lines are shown in black and orange.

To compare the benefit of the usage of parallelization, a term called speedup has been defined. Speedup S is the normalized time save in relation to a reference calculation:

$$S = \frac{t_{ref}}{t_{calc}} \tag{6.7}$$

Accordingly, a saving in computational time compared to the reference time leads to a higher speedup. An ideal behaving system would provide a reduction of time to half of the reference time, if the computational resources are doubled, achieving thus a speedup of two. However, due to non-ideal behavior, for example due to sequential fractions during calculations which cannot be parallelized, the speedup is usually not doubled. According to Amdahl's law, the sequential fractions are limiting the maximum benefits achievable by utilizing parallelization [Amd67]. Several tools were used to analyze performance bottlenecks, e.g. SCORE-P instrumentation [Knü12] and Ravel [Isa14] for analyzing and visualizing SCORE-P profiling outputs. The engineering work done how to profile, benchmark and optimize different aspects of the simulation codes are addressed only very briefly in the following paragraphs.

For the scalability tests, a 2D reactive transport model setup with a size of 250x250 nodes was used. Essentially, this is a simplified version of the model presented later in section 8.3.2. The model contains only portlandite and CSH as solid phases in equilib-

rium. In total, five solutes need to be transported, namely calcium, silicon, hydrogen, oxygen, water and charge. Moreover, a pure water Dirichlet boundary condition is applied on the left-hand side, while all other boundaries are simulated as closed.

Besides of the performance of a single threaded run, the performance was tested in node chunks, i.e. 8 CPUs per node. The performance data obtained are for 1, 2, 4, 8, 10, 16 and 20 compute nodes, leading to the corresponding eight-fold number of CPUs used. The C++ compiler used to translate iPP, PhreeqcRM and Palabos for the benchmarks was GCC using optimization level 3, while the MPI standard was implemented via OpenMPI [Gab04].

The results of the first optimization step of iPP, i.e. reducing the communication overhead in PhreeqcRM by replacing the blocking global data collection step by using a local coupling, can be seen in figure 6.20 as indicated in blue. For comparison, a data point calculated with iPP using the original PhreeqcRM version is shown in red. The original version of PhreeqcRM has only a speedup of 5 despite using 80 CPU cores. Reducing the network communication overhead by using a local coupling shows a much better scalability. However, the behavior is still not ideal, which can be seen when comparing to the ideal line indicated in black.

The second important optimization deals with the dynamic enabling of reaction cells, only when the concentration change exceeds some threshold (cf. section 4.4.5). Otherwise, the chemical equilibrium calculation is omitted in these cells. The results (green symbols in figure 6.20) are again normalized to the single threaded performance of the static cell activity. The dynamic cell activity feature improves the single threaded performance by about a factor of 7.7, which can be seen from the data point at $nCPU = 1$. Moreover, it is apparent that the saturation of speedup is reached already after 8 nodes (64 CPU cores). One reason for this saturation effect in general is due to imbalances in the load distribution. Except for the reaction cells close to the pure water boundary, the system is quite stable and does not experience significant shifts in solute concentrations and equilibria. Thus, the reaction step is omitted most of the time. The only processing CPU cores which need to re-equilibrate all the time are close to the pure water boundary. Effectively, the CPU cores allocated to the cells where no reactive chemistry has to be calculated finish their calculations almost immediately, while waiting for the few cores, which actually need to compute new equilibria.

Thus, an attempt was made to alter the spatial lattice decomposition to distribute the CPU load more homogeneously to address this imbalance. However, the respective benchmarks have revealed no significant improvement or even a performance degradation due to shifting of imbalances in CPU utilization towards imbalances in communication overhead.

The last scalability test presented here was performed on both clusters, i.e. the IEK-6 and JURECA systems. The input model was the latest evolution of the cementitious system described in section 8.3.4. For details on all features included, the reader is referred to the corresponding section. However, just the differences to the above defined simpler model setup used in the benchmark addressing performance optimization are mentioned here. First, the model contains a much more complicated chemical setup. For example, in total 13 solute components are used in the transport simulation while

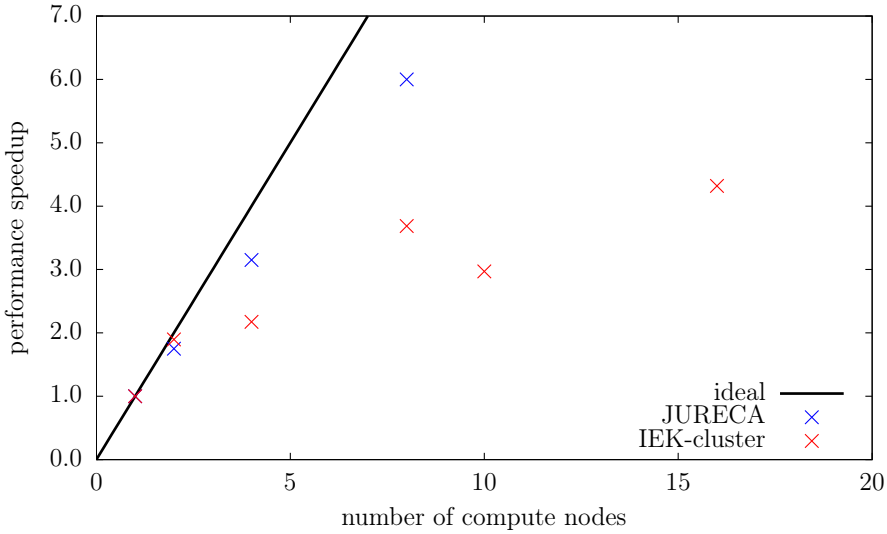

Figure 6.21: Performance speedup gain due to parallelization on JURECA and the IEK-6 cluster.

19 solid phases are considered. Moreover, a much more sophisticated approach is used to control precipitation than the pure equilibrium assumption. On the JURECA cluster the recommended Intel C++ compiler was used with optimization level 3. Moreover, the host specific architecture (Intel Haswell) instructions and advanced vectorization instructions, i.e. AVX2, was enabled. The MPI implementation used was the ParaStation implementation which is according to the JURECA user manual optimized for this specific cluster.

The resulting speedup is shown in figure 6.21. In this plot, the speedups normalized to a single node performance are compared. It has to be noted that the numbers of CPUs per node in the two clusters are not identical. However, the point to be made here is the difference between the saturation level, i.e. the starting point of speedup stagnation. Starting with 8 compute nodes, the IEK-6 cluster reaches a speedup level which seems to be saturated and *noisy*. A similar behavior has been observed in the previous test, since 8 nodes correspond to 64 CPU cores. Deeper analyses have shown that some latency effects in the Ethernet connectivity of the IEK-6 cluster might be the reasons for this. In particular, the decomposition to 80 domains on 10 IEK-6 cluster machines seems to involve more communication overhead.

Regarding the scalability, the JURECA cluster shows still a significant gain in performance by applying more compute nodes and a much closer to ideal behavior. All in all, the low latency InfiniBand connectivity of JURECA seems to mitigate scalability problems with the reactive transport simulator iPP. An even better scalability is expected for larger models encompassing more lattice nodes.

Part III

Application of iPP to cementitious systems

7 Parametrization and preparatory steps for simulating cementitious systems with iPP

Since most of the developments in this work were conducted in the framework of the CEBAMA project [Dur20], exchange among project partners participated in the project was motivated. As the focus of this study is to simulate degradation and alterations of cementitious materials, especially experiments providing data in this scope were of interest. Within the CEBAMA project cementitious material were addressed, which are relevant for nuclear waste disposal concepts. One of these materials was the low-pH CEBAMA reference cement paste (CRP) [Veh17], which was used as study material by several project partners. A similar material was analyzed by project partners at University of Sheffield (USFD). In particular, USFD conducted experiments addressing leaching and degradation of low-pH HCP with different groundwaters [Vas18].

In order to simulate a pore-scale reactive transport model of cementitious systems, several input parameters are required. Most importantly, a representative microstructure of the system is required. This microstructure can be derived for example via numerical modeling (e.g. by using CEMHYD3D [Ben05]) or by segmentation of μ-XCT image data of HCP. Furthermore, the phase assemblage of the constituents and the pore water composition is required. This can be derived from the microstructural information provided by the image data. However, as these data might be insufficiently resolved, a hydration model of the system can help to fill the missing pieces. Both, hydration modeling and reactive transport simulations require thermodynamic data of the components involved. In particular, since CSH is a phase with a continuous C/S ratio, a suitable thermodynamic model must be applied, which reflects the incongruent dissolution of calcium and silicon. This can be treated, either with a solid solution model or with multiple competing discrete CSH phases. Both approaches will be presented and discussed regarding benefits and drawbacks.

Furthermore, for a reactive transport simulation transport properties of the phases in a cementitious system are of importance. In particular, as CSH is regarded as a diffusive phase (cf. section 2.3.4.3), diffusivity values for this material must be assigned. As the nano-structure of CSH is not explicitly resolved the transport simulation conducted in this work, an upscaled diffusivity model for CSH was developed, which takes into account the nano-structural properties of CSH. Depending on modeling assumptions and the resolution of the microstructure, other (non-diffusive) hydration products might be intermixed with the CSH phase. To treat this, a diffusivity model based on

homogenization schemes was developed and is presented in this chapter.

Moreover, depending on the physical effects considered in the reactive transport simulation, more input data are required. For example, if CNT and/or PCS effects are considered, values for surface tension, nucleation rates, and/or representative pore radii must be provided as input. This chapter outlines which specific implementations were included within iPP to treat these effects and how the corresponding input data were derived from experimental data.

7.1 Thermodynamics of CSH and solid solution models

7.1.1 Discrete and continuous CSH solid solution models

There are different models of the thermodynamic properties of CSH. As already outlined in section 2.3.3.1, CSH is a phase with a continuous range of compositions with respect to its C/S ratio. Solubility measurements have revealed that the aqueous calcium and silicon concentrations in equilibrium depend on the composition of CSH and in particular the C/S ratio [Lot15]. Different models have been proposed to describe this dependency. On one hand there are discrete models and on the other hand there are continuous models in the form of solid solution models.

A commonly used discrete phase model representation uses three CSH phases, namely CSH-0.8, CSH-1.1 and CSH-1.6 [Bla10a,Gif14]. The equilibrium constants of these phases are fit to different experimental data from other authors [Bla10a]. This CSH model is also included in the *ThermoChimie* thermodynamic database [Gif14]. The resulting C/S ratio using a discrete model is determined by the C/S ratio of the phase weighted by their mass fractions. For example, a mixture of CSH-1.1 and CSH-1.6 with mass fractions of 80 % and 20 %, respectively, results in a CSH phase with a C/S of 1.2.

On the other hand, there are solid solution models for CSH proposed as binary, tertiary and quaternary models representing the complete compositional variability. A common thermodynamic database for modeling cementitious systems is CEMDATA [Jac09,Lot19]. The earlier released version of 2007 contains a two-step binary CSH solid solution model, thus this model effectively suggests two binary solid solutions of CSH-I ($0 < C/S < 0.833$) and CSH-II ($0.833 < C/S < 1.667$). CSH-I is proposed as an ideal solid solution between the end-members amorphous silica SiO_2am and CSH-0.83, which has a tobermorite-like structure and hence named CSHtob. The CSH-II solid solution consists of an interpolation between CSH-0.83 and CSH-1.67, a jennite-like structure, thus named CSHjen [Kul01].

However, later publications are pointing out a lack of evidence of a CSH phase in the C/S ratio range between 0 and 0.8 [Kul11,Mat07b,Wal16]. This led other authors to the conclusion that the CSH-I part of the model should not be used in benchmarks [Jac09]. Even later versions of the CEMDATA database do only contain the CSH-II part with the same justifications [Lot19]. Thus, with this model there is no stable CSH phase with a C/S ratio lower than 0.833 possible. The full reaction equations for the CSH-II model

are:

$$(CaO)_{0.833}(SiO_2)(H_2O)_{1.333} + 0.5\,H_2O \rightleftharpoons 0.833\,Ca^{2+} + SiO(OH)_3{}^- + 0.667\,OH^- \tag{7.1}$$

$$(CaO)_{1.667}(SiO_2)(H_2O)_{2.1} + 0.567\,H_2O \rightleftharpoons 1.667\,Ca^{2+} + SiO(OH)_3{}^- + 2.333\,OH^- \tag{7.2}$$

Furthermore, non-ideal binary [Wal16], ideal ternary (CSH3T) and quaternary (CSHQ) [Kul11] solid solution models have been proposed for CSH. In addition, there are CNASH and ECSH models, which simulate the incorporation of alkalis and aluminum into the CSH gel. The CNASH model deals with incorporation of Na an Al, hence N and A in the acronym, while the ECSH extends the CSH-I/II model with Na, K and Sr containing end-members. Most of these models are included in the CEMDATA18 database [Lot19].

However, in this work it, the focus is on the CSH-II and CSHQ models. The CSHQ model was developed to address some drawbacks of the CSH-I/II model, i.e. to be more consistent with structural investigations of the CSH phase and removing the unrealistic assumption of ideal mixing between a tobermorite-like and an amorphous silica end-member. The model includes two end-members each for a tobermorite and a jennite-like structures. The reaction equations of each CSHQ end-member are:

$$(CaO)_{0.667}(SiO_2)(H_2O)_{1.5} \rightleftharpoons 0.667\,Ca^{2+} + SiO(OH)_3{}^- + 0.334\,OH^- - 0.167\,H_2O \tag{7.3}$$

$$(CaO)_{0.833}(SiO_2)_{0.667}(H_2O)_{1.833} \rightleftharpoons 0.833\,Ca^{2+} + 0.667\,SiO(OH)_3{}^- + OH^- + 0.333\,H_2O \tag{7.4}$$

$$(CaO)_{1.333}(SiO_2)(H_2O)_{2.167} \rightleftharpoons 1.333\,Ca^{2+} + SiO(OH)_3{}^- + 1.667\,OH^- - 0.167\,H_2O \tag{7.5}$$

$$(CaO)_{1.5}(SiO_2)_{0.667}(H_2O)_{2.5} \rightleftharpoons 1.5\,Ca^{2+} + 0.667\,SiO(OH)_3{}^- + 2.333\,OH^- + 0.333\,H_2O \tag{7.6}$$

The thermodynamic data and molar volumes of the end-members of both solid solution models used in this work are given in table 7.1. Besides of the discrete phase model contained in the ThermoChimie database [Gif14], both solid solution models in their discretized forms will be used later in this work. The discretization process is described in the next section.

7.1.2 Discretization of CSH solid solution models

During some preliminary reactive transport tests, both ideal solid solution models, CSH-II [Jac09,Mat07b] and CSHQ [Kul11], have revealed to be numerically error-prone within PhreeqC calculations. Apparently, for certain numerical corner cases the simulations did not converge and PhreeqC exited with an error. A similar observation is also stated by Blanc et al. [Bla10a]. By manual user interaction with the KNOB section of the PhreeqC input, i.e. tuning the convergence parameters, this could often be circumvented. How-

Table 7.1: Thermodynamic database entries of the end-members of a binary (CSH-II [Jac09,Mat07b]) and a quaternary (CSHQ [Kul11,Lot19]) solid solution model for CSH. Molar volumes V_m are in the units of $[\mathrm{cm}^3\,\mathrm{mol}^{-1}]$ and are referring to dry CSH, i.e. without gel porosity. V_m^{norm} corresponds to the stoichiometric normalized molar volume of the CSH end-member, i.e. normalized to the silicon fraction. Equilibrium constant values K correspond to 25 °C.

model	end-member	n_{Ca}	n_{Si}	$\log_{10} K$	V_m	V_m^{norm}
CSH-II	CSHtob2	0.8333	1	-8.0014	59	59
	CSHjen	1.6667	1	-13.1659	78	78
CSHQ	TobH	0.6667	1	-6.190832	55.30	55.3
	TobD	0.8333	0.6667	-6.8995533	47.95	71.93
	JenH	1.3333	1	-10.96765	75.63	75.63
	JenD	1.5	0.6667	-10.47635	80.58	120.87

ever, this measure was not applicable for an automated recovery for reactive transport simulations, in which millions or even billions of such calculations are performed. Moreover, a significant degradation of computational performance was observed compared to ordinary simulations using only discrete phases. In order to circumvent these issues, a discretized solid solution approach was used. For this, multiple CSH phase compositions were used, reflecting the continuous solid solution model in discrete steps. A similar approach was incorporated into reactive transport simulations by other authors [Lic06].

In order to convert and interpolate the thermodynamic data of the CSH solid solutions to produce a discrete model, the underlying law of mass action equations needs to be applied. The general concept to determine the discrete solid solution equilibrium constants K_{SS} is to calculate the product of all contributions of all end-members E_i [Lic06]:

$$K_{SS} = \prod E_i \tag{7.7}$$

The product form of the equation can be expressed in a sum form by using the logarithms:

$$\log_{10} K_{SS} = \sum \log_{10} E_i \tag{7.8}$$

In an ordinary law of mass action equation without solid solution treatment, the activities of the solid components are equal to unity. However, the activities of the components of an ideal solid solution are by convention equal to the molar fraction X_i of the end-member. Thus, the logarithmic form of the end-member contribution is defined as [Lic06]:

$$\log_{10} E_i = \log_{10} \left(\left(\frac{K_i}{X_i} \right)^{X_i} \right) = X_i \left(\log_{10} K_i - \log_{10} X_i \right) \tag{7.9}$$

In this equation K_i indicates the equilibrium constants of the end-members. Inserting into equation 7.8 yields the sum form to determine the intermediate logarithmic

Table 7.2: Thermodynamic data of the discretized CSH-II solid solution model.

Phase	n_{Ca}	n_{Si}	$\log_{10} K$	$V_m = V_m^{norm}$
CSH_083	0.8333	1	-8.001400	60.09
CSH_092	0.9167	1	-8.659032	62.70
CSH_100	1.0000	1	-9.251622	65.41
CSH_108	1.0833	1	-9.816045	68.25
CSH_117	1.1667	1	-10.359485	71.21
CSH_125	1.2500	1	-10.884680	74.29
CSH_133	1.3333	1	-11.392385	77.51
CSH_142	1.4167	1	-11.881845	80.87
CSH_150	1.5000	1	-12.350322	84.37
CSH_158	1.5833	1	-12.790632	88.03
CSH_167	1.6667	1	-13.165900	91.84

equilibrium constants:

$$\log_{10} K_{SS} = \sum X_i \left(\log_{10} K_i - \log_{10} X_i\right) \tag{7.10}$$

The mole fractions of each end-member combination in the CSH-II model can easily be determined by just using the amounts of the end-members. However, the procedure for a quaternary solid solution, even for an ideal one, is more complicated because there is no unique solution to achieve the end-member fractions of a certain solid solution with respect to the C/S ratio. Thus, PhreeqC calculations were conducted to obtain the mole fraction data for the corresponding intermediate solid solutions. The resulting mole fractions were subsequently used to evaluate the interpolated equilibrium constants using equation 7.10. For both solid solution models, CSH-II and CSHQ, the discretized values of 10 steps, i.e. 11 different phases, were calculated by this approach. The numbers of intermediate phases were kept small in order not to sacrifice too much computational performance.

Additionally, the molar volumes of the discrete phases were interpolated. The molar volume of an interpolated discrete phase was determined by the sum of the product of molar volume and mole fraction of each end-member:

$$V_m = \sum V_m^i X_i \tag{7.11}$$

It is important to notice that the molar volumes depend on the stoichiometry of the respective phases. The D-CSHQ end-members, i.e. TobD and JenD, are not normalized with respect to silicon, while the CSH-II end-members are (cf. table 7.1). Consequently, when interpolating the molar volumes of the solid solutions to produce discretized thermodynamic data, the stoichiometry of CSHQ is not normalized with respect to C/S. Thus, for comparing the molar volumes of the solid solutions in the two different models, one has to normalize by dividing by the C/S-ratio. By this approach, the molar

Table 7.3: Thermodynamic data of the discretized CSHQ solid solution model.

Phase	n_{Ca}	n_{Si}	$\log_{10} K$	V_m	V_m^{norm}
CSH_068	0.67073	0.99352	-6.256263	55.18	55.54
CSH_077	0.72745	0.94532	-6.823269	55.12	58.31
CSH_086	0.78498	0.91391	-7.299891	55.73	60.98
CSH_096	0.84931	0.88632	-7.787626	56.73	64.00
CSH_106	0.91332	0.86374	-8.238824	57.96	67.11
CSH_115	0.97040	0.84649	-8.615374	59.27	70.02
CSH_124	1.03253	0.82955	-8.995874	60.97	73.49
CSH_133	1.08576	0.81483	-9.291822	62.71	76.96
CSH_143	1.14020	0.79770	-9.558515	64.75	81.17
CSH_153	1.18977	0.77982	-9.767260	66.77	85.63
CSH_160	1.22659	0.76546	-9.902454	68.33	89.27

volumes of the solid solutions for the CSHQ model were generated. Based on this, the molar volumes for the CSH-II model were interpolated. For this, an empirical exponential relationship is fitted to the normalized molar volumes of the CSHQ model:

$$V_m(n_{Ca}/n_{Si}) = a\, e^{k\frac{n_{Ca}}{n_{Si}}}, \quad a = 39.32, k = 0.509 \tag{7.12}$$

This relationship was used to determine the molar volumes of the discrete phases of the CSH-II solid solution model. This was necessary to obtain comparable data in terms of volume fractions for both CSH models, which is important to calculate the porosity of a reaction cell. The resulting thermodynamic data and molar volumes are compiled in tables 7.2 and 7.3, for CSH-II and CSHQ, respectively.

In order to illustrate the comparability of the discrete phase approach and the solid solution models, PhreeqC calculations were performed. In the calculations, equilibrium between the CSH phases, amorphous silica and portlandite and the solution was assumed. The results are compared in figure 7.1. The upper plot shows the aqueous calcium concentration in equilibrium, while the bottom plot refers to the silicon concentration. Obviously, the discrete phase model shows a stair-case approximation compared to the continuous curves corresponding to the solid solution models. The difference between the stair-case and the continuous concentrations could be further reduced by introducing more intermediate discretized steps. However, this would sacrifice further computational performance. Thus, it was accepted that the used 11 steps are sufficiently approximating the equilibrium concentrations.

The CSH-II model leads in general to higher calcium concentration in equilibrium compared to the CSHQ model. However, both calculated concentration curves are in agreement with the data published by the authors of the solid solution models [Jac09,Kul11]. Moreover, it is apparent that the CSHQ model infers a broader stability range of CSH with respect to the C/S ratio. The same is visible in the silicon concentration plot, which is smoother towards the lower end of C/S ratios in the CSHQ model. The CSH-II model,

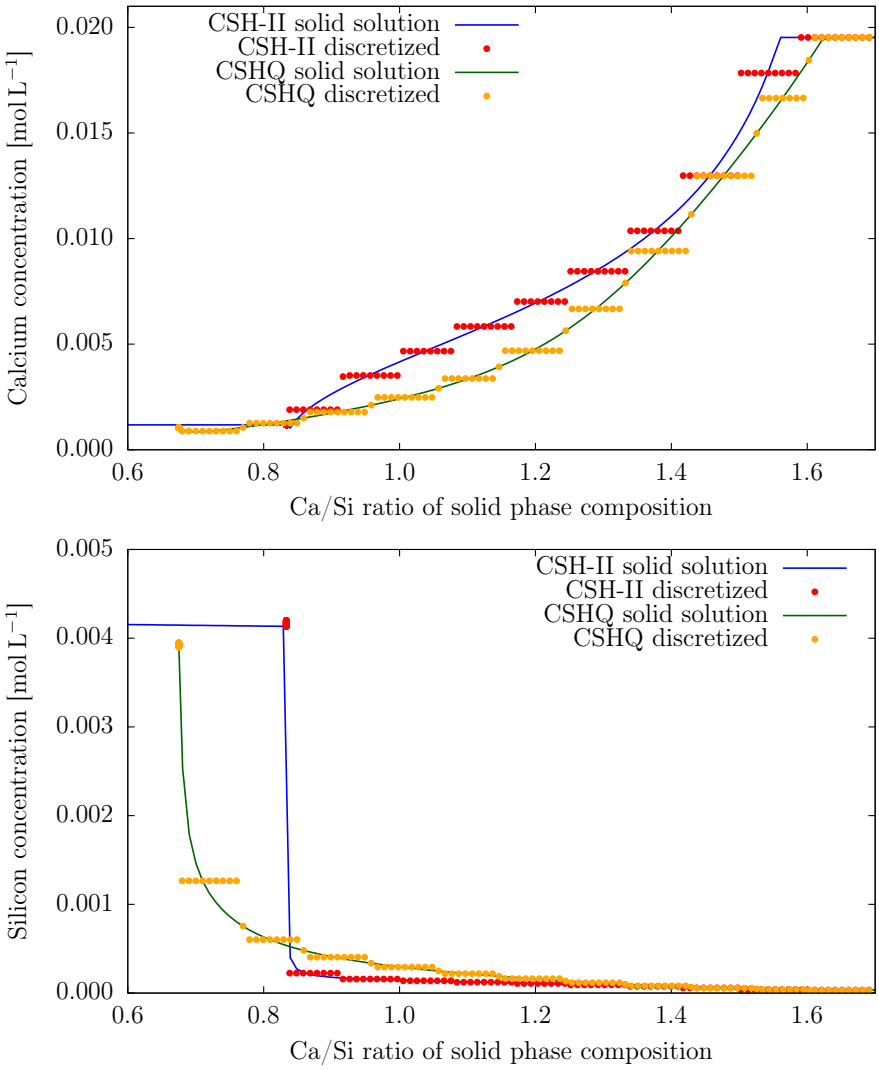

Figure 7.1: Aqueous calcium (top) and silicon (bottom) concentrations in a solution in equilibrium with CSH, amorphous silica and portlandite as function of the C/S ratio in CSH calculated with the CSH-II and CSHQ solid solution models in comparison to the corresponding discrete phase approaches.

on the other hand, shows a quite rapid decomposition of low C/S-CSH into amorphous silica.

It has to be noted that the definition of the high C/S ratio CSH is not perfectly translatable between the different approaches. Already the original continuous solid solution models have some limits. For example, in the CSHQ model, the maximum C/S ratio in CSH is 1.62, while the CSH-II model is limited at C/S = 1.56. At higher C/S ratios the Ca concentrations in solution at equilibrium would exceed the solubility limit of portlandite, thus limiting the achievable C/S ratios. However, this is in line with observations that CSH with a high C/S ratio above 1.45 coexists with portlandite which refers to range what is called CSH(I) [Lot15] [Tay97, pp.132]. Using the discrete phase models, the maximum values are shifting even more. The maximum values for the discrete CSH-II model is CSH_158 (C/S = 1.58), while the discrete CSHQ model has its limit at the CSH_160 phase (C/S = 1.60). This means the CSH_167 phase (C/S = 1.67) of the discrete CSH-II model is not stable when equilibrated with portlandite, i.e. not present in figure 7.1.

7.2 Derivation of microstructure and phase assemblage

The microstructure of porous media might have significant effects on their macroscopic properties. Thus, an important foundation for modeling approaches of cementitious materials at the pore-scale is the definition of the microstructure, which serves as initial geometry for reactive transport simulations.

There are several ways to acquire microstructures of hydrated cements. On the one hand, geometrical descriptions can be obtained from numerical models such as CEMHYD3D [Ben05] or HYMOSTRUC [Bre95]. On the other hand imaging data, for example obtained by SEM/EDX (**s**canning **e**lectron **m**icroscopy / **e**nergy-**d**ispersive **X**-ray spectroscopy), BIB/SEM (**b**road **i**on **b**eam / **s**canning **e**lectron **m**icroscopy) or μ-XCT (**micro-X**-ray **c**omputer **t**omography) techniques can be applied to derive microstructures via segmentation.

7.2.1 Derivation of microstructure with the CEMHYD3D code

CEMHYD3D is a three-dimensional cement hydration and microstructure development modeling package [Ben05]. It contains a code module which transforms particle size distributions of unhydrated cement into representative 3D geometries of the same material, i.e. clinker, SCM and gypsum grains dispersed in water. The code maintains the same volume fractions, size distributions and surface area fractions for each component. Another module uses this 3D geometry as input to simulate the hydration process of the cement. The hydration code uses a cellular automata-based algorithm with specific rules, how the cement components are hydrated and subsequently form hydration products and how chemical shrinkage is applied. The code works in simulation cycles and the output is a new 3D microstructure [Ben95].

Table 7.4: Composition of the unhydrated cement used as input for the CEMHYD3D calculation [Mor04,Pat18b].

component/clinker	mass fraction
C_3S	0.71
C_2S	0.13
C_4A	0.04
C_4AF	0.08
gypsum	0.035

Table 7.5: Hydrated cement composition given as output of the CEMHYD3D calculation.

component	number voxels	fraction
porosity	49976	17.38 %
CSH	164431	57.19 %
portlandite	53036	18.45 %
unhydrated cement (e.g. clinker)	20053	6.98 %
sum	287496	100.00 %

Such a simulated hydration of OPC was performed by other researchers, where the microstructure was reused for a reactive transport simulation [Pat18b]. The oxide composition of the cement used as input is depicted in table 7.4. Although the authors were using different w/c ratios (0.25, 0.4 and 0.5), the focus in this work is on a w/c ratio of 0.4 for the CEMHYD3D generated microstructures. The resulting microstructure of the hydrated cement was provided by Patel et al. [Pat18b].

The geometrical data are represented as 3D array of 66 x 66 x 66 voxels with a size of 1 µm, thus the total cube edge length in this model is 66 µm in each dimension. The output of CEMHYD3D is a complex distribution of various cement hydration products, residual cement phases as clinker, and void voxels, which can be regarded as capillary porosity. This geometrical description is later used as input for several simulations. A rendered image of the microstructure is given in figure 7.2. An assessment of the counts of voxels per phase type is presented in table 7.5.

The total porosity ϕ_T can be estimated with help of Power's model [Han86] (equation 2.7). The equation contains the degree of hydration α. According to an empirical model, the maximum degree of hydration can be estimated by the model of Bejaoui et al. [Bej07] (equation 2.2). Since in this example the w/c equals to 0.4, the maximum degree of hydration is estimated as 83.65 %. Plugging this value into Power's model leads to a total porosity of 35.81 %.

This porosity must be assigned to reaction cells in the CEMHYD3D derived geometry. Obviously, completely empty pore voxels in the microstructure are contributing to this. Counting the number of these voxels and dividing it by the total number of voxels

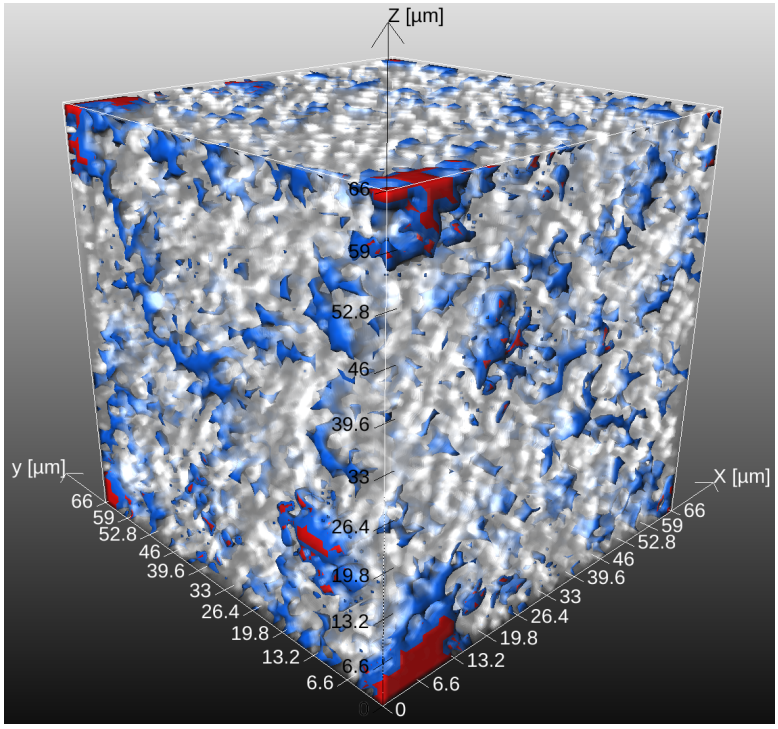

Figure 7.2: Volume rendering image of the CEMHYD3D generated HCP microstructure derived from hydration of OPC. In this image, the porosity is transparent, while voxels corresponding to hydration products, other than portlandite, are indicated in white and semi-transparent. Portlandite and residual clinker phases are rendered as iso-surfaces and depicted in blue and red, respectively.

in the model, in this case $49976/(66 \times 66 \times 66) = 49976/287496$ yields a capillary porosity of $\phi_{cp} = 17.38\,\%$ (cf. table 7.5), which is smaller than the estimated value calculated according to Power's model. It was assumed here that the remaining porosity is embedded as capillary porosity in the voxels representing CSH phases. Accordingly, the total pore volume of the CSH phases voxels V_{ϕ}^{CSH} can be expressed as follows:

$$V_{\phi}^{CSH} = \phi_T - \phi_{cp} \tag{7.13}$$

In this equation ϕ_T corresponds to the total porosity value determined by Power's model, while ϕ_{cp} is the capillary porosity. Effectively, there is $18.42\,\%$ of capillary porosity embedded in the CSH phase voxels. Similar to the process of determination of the capillary pore fraction ϕ_{cp}, the number of CSH voxels were counted and normalized (164431/287496), yielding a CSH volume fraction V_S^{CSH} of $57.19\,\%$ in the complete hardened cement monolith (cf. table 7.5). The resulting total porosity in CSH voxels is

Table 7.6: Composition of the low-pH cement paste mix used as CEBAMA reference paste (CRP) [Veh17] and by USFD [Idi18].

component	density [kg m^{-3}]	CRP m [kg m^{-3}]	CRP volume fraction	USFD m [g/100g solid]	USFD volume fraction
CEM-I	3100	468	0.14	37.5	0.18
silica fume	2300	491	0.20	39.3	0.25
blast furnace slag	2900	290	0.09	23.2	0.12
quartz filler	2320	517	0.21	0	0
superplasticizer	1200	75	0.06	6.0	0.07
water	1000	312	0.29	25	0.37

then determined by:

$$\phi_{CSH} = \frac{V_{\phi}^{CSH}}{V_{S}^{CSH}} \tag{7.14}$$

All in all, the porosity of the CSH voxels is calculated as 32.21 % which includes capillary and gel porosity. In other words, the CSH voxels contain 67.79 % CSH solid volume, without gel porosity included. Moreover, since the OPC still contains portlandite, it is assumed that the CSH phase in the model is non-degraded.The CSHQ model predicts, a maximum C/S ratio of 1.62 and a molar volume of 68.7 cm^3 mol^{-1} for non-degraded CSH. Note that his molar volume corresponds to dried CSH phase and does not contain any gel porosity. Accordingly, on average the CSH voxels contain a CSH solid phase concentration of 9.86 mol L^{-1} per voxel volume.

7.2.2 Derivation of microstructures from μ-XCT image data

In addition to microstructural inputs from a numerical hydration model, microstructural data derived from μ-XCT measurements were used. Within the CEBAMA project, University of Sheffield (USFD) have conducted experiments dedicated to quantify compositional and microstructural changes in low-pH cement pastes due to leaching with different types of groundwaters [Vas18]. The mixture of the cement paste is similar to the one provided as reference cement mixture within the CEBAMA project [Veh17], with the exception that quartz filler is not added to the mix (see also [Idi18]). The resulting component and oxide compositions are given in tables 7.6 and 7.7, respectively.

For obtaining data of the initial microstructure, cylindrical cement monoliths were cast with a diameter of 2 mm and a height of 5 mm and cured for 28 d in an oven at 40 °C and 95 % relative humidity. For selected samples μ-XCT imaging data were obtained. This section deals with the segmentation of the image data to derive microstructural information and the phase distribution.

Table 7.7: Oxide composition of the components of the low-pH cement paste mix used by USFD [Idi18].

oxide	CEM I	SF	BFS
CaO	64	1.46	41.5
SiO_2	21	91.1	32.8
Al_2O_3	3.5	1.44	10.6
SO_3	2.2	0.47	1.4
MgO	0.7	0.88	8.29
Fe_2O_3	4.6	0.91	0.81
K_2O	0.62	1.73	0.62
Na_2O	0.07	0	0.62
CO_2	2.2	0	0

7.2.2.1 Initial analysis and segmentation

μ-XCT data taken on samples from the CEBAMA reference paste were provided by USFD. The cylindrical sample was measured by μ-XCT with a resolution of 3 µm per voxel, resulting into a gray value data set of 671 x 742 x 1449 = 721 431 018 voxels. The data were provided in a raw volume image data format. In this section it will be described which insights could be gained from the image data and how a segmentation of different phases was achieved.

The image data resolved six different gray values of unhydrated clinker (C_2S/C_3S and C_3A/C_4AF), blast furnace slag (BFS), silica fume, voids (air) and hydration products (mainly C-S-H). Different hydration products could not be further distinguished and separated due to the similar X-ray attenuation effects (see figure 7.3).

Additional insights about the phases present in the HCP can be retrieved from the histogram corresponding to the μ-XCT image data in figure 7.4. The histogram shows the distribution of the gray values of the complete data set. The histogram reveals the limited dynamic in gray value differences, which renders the segmentation by just gray values difficult.

First, noise removal was attempted to improve the situation, by applying different filters on the image data such as Gaussian blur, convolution or diffusion filter. The convolution filter results are depicted as red line in figure 7.4. In particular interesting is the small bump at a gray channel of about 6000 within the range assigned to voids, which emerges after convolution filtering. Deeper analyses showed that the void actually has two different gray value domains. The larger count and lower gray values correspond to the domain outside of the volume of the HCP cylinder, while the gray values around 6000 represent voids inside the specimen. The higher gray values in the voids inside the specimen might be either an artifact due to X-ray attenuation or due to presence of pore water (vapor), which would indicate that the specimen had not been dried completely. The specimen was immersed in acetone and water should have been replaced [Vas20]. From the gray image slice shown in figure 7.3 there are beam hardening artifacts visible.

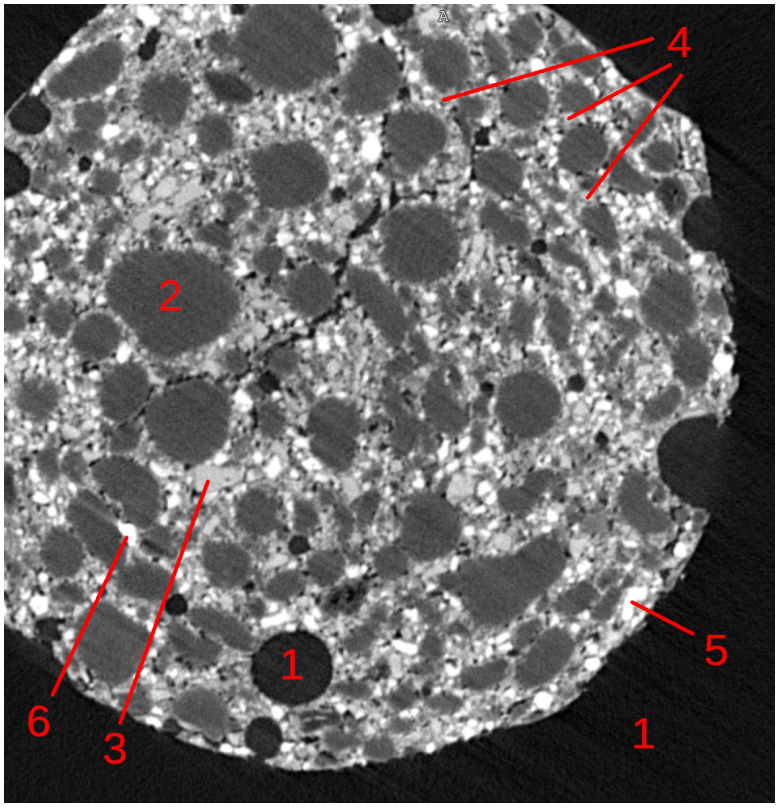

Figure 7.3: Gray image slice of the original μ-XCT data. Different phases / zones are indicated with numbers: Void (1), silica fume (2), blast furnace slag (3), hydration products (4), calcium silicate clinker (5), ferrite clinker (6).

In particular this artifact is apparent at the spot indicated with 6, which is a region with high X-ray attenuation due to the presence of ferrite clinker. Accordingly, the gray value shift for the voids within the specimen is likely caused by this effect. Moreover, in an adjusted brightness and contrast view of the same image (not shown here), ring artifacts were visible as well.

For initial segmentation, the six gray value ranges depicted in figure 7.4 were used to separate the different phases in the HCP specimen to reconstruct its microstructure. Unfortunately, in this way major artifacts of wrongly assigned voxels occurred. An example of this effect is depicted in figure 7.5a, where the voxels of the gray value range corresponding to the unreacted silica fume were extracted. It is clearly visible that between hydration products and voids erroneously voxels were assigned to silica fume. This effect is visible in particular at the outer rim of the specimen and at the boundaries of macro pores (compare pore depicted with 1 in figure 7.3).

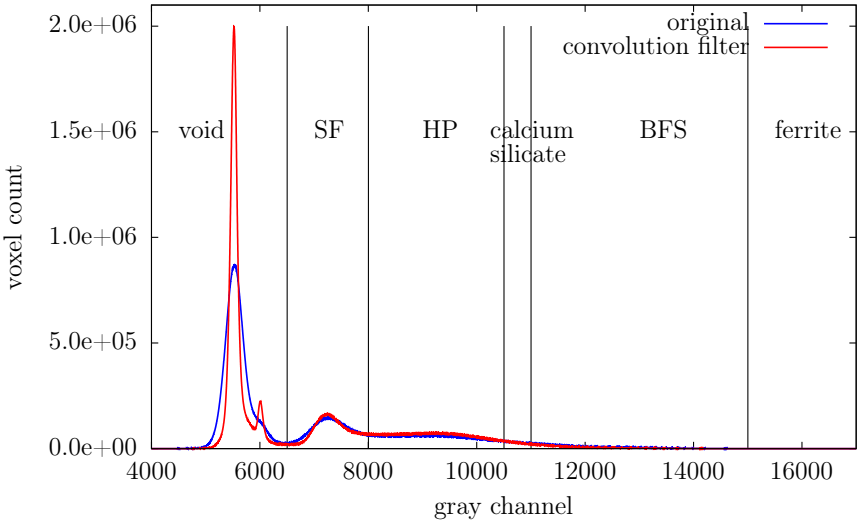

Figure 7.4: Histogram of the gray values of the original μ-XCT image file and phases assigned to different gray channels compared to a histogram obtained using a convolution filter. Channels from left to right: void, silica fume (SP), hydration products (HP), calcium silicate clinker, blast furnace slag (BFS) and ferrite clinker. Although filtering with a convolution filter does blur the image data, the resulting histogram indicates a better phase separation due to a reduction of noise.

This kind of artifact is common in CT measurements, known as so-called *partial volume effect*, also referred to as volume averaging artifact. It occurs when a single voxel contains more than one phase, leading to an intermediate X-ray attenuation value between all materials present in the voxel's volume [Ket01]. In this example, the gray value range of silica fume is between hydration products and void (compare figure 7.4), thus voxels containing both phases, express a gray value corresponding to silica fume. The effect is that silica fume is wrongly assigned to the respective voxels.

As a consequence, separating the different phases by a simple gray value threshold algorithm would actually lead into false positive assignments for voxels corresponding to phase mixtures. In general, these artifacts, noise and low gray value dynamics revealed to be challenging to segment the image data appropriately. Thus, a more sophisticated segmentation algorithm was developed to mitigate the partial volume effect.

7.2.2.2 Segmentation with partial volume effect mitigation

The segmentation algorithm for mitigation of the partial volume effect developed in this work comprised 5 steps (see figure 7.5b). These first step is a semi-manual process

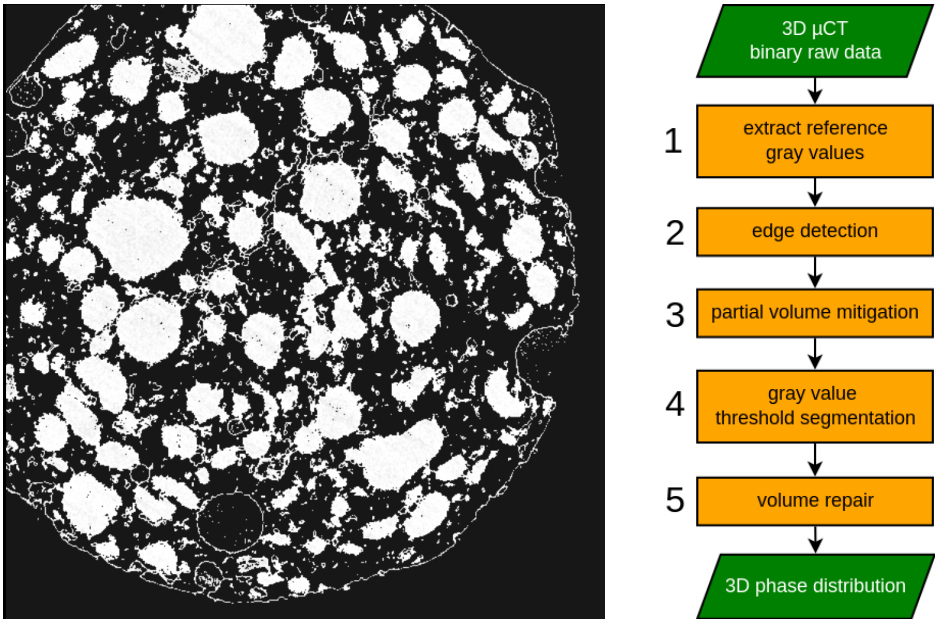

(a) (b)

Figure 7.5: (a) 2D slice of segmented voxels corresponding to silica fume. White refers to voxels assigned to silica fume. While the spherical shaped particles within the specimen are correctly assigned (cf. regions indicated with 2 in figure 7.3), wrongly assigned voxels due to the partial volume effect are visible, for example as rim at the surface of the specimen. (b) Different steps of the newly developed algorithm to allow segmentation of the phases of the μ-XCT image data, including partial volume effect mitigation. Green refers to input and output data, while orange boxes are algorithms.

and depends on the input data, while the other steps are algorithmic entities, which were solved as software solution. The first step, referred to as *extract reference gray values*, is explained in section 7.2.2.1. The *edge detection* (2) and the final *gray value threshold segmentation* (4) steps in the pipeline need the gray value thresholds as input. In general, step 2 and 3 are removing the partial volume artifacts from the image data by omitting the voxels which are suspected to suffer from this effect. This introduces gaps which need to be treated later. In turn, step 4 is a classical threshold segmentation, but the output does not suffer from the artifacts anymore, because they were removed in the prior step. Resulting from the voxel removal procedure before, the gaps must be filled again. The assumption is that the gaps must be again filled symmetrically by the neighboring phases. For this, a new iterative algorithm was developed, which is based on region grow and subsequent masking.

Table 7.8: Gray value ranges and volume fractions of the phases distinguishable in μ-XCT image data of the hydrated USFD cement paste specimen. The gray value ranges are also depicted in figure 7.4. The voxel count and volume fraction data were determined by the newly developed segmentation algorithm.

phase	gray values	n voxel	vol. fraction	frac. w/o air
air / void	< 6500	4.05E+08	56.09 %	0.00 %
silica Fume	6500 - 7999	1.29E+08	17.89 %	40.76 %
hydration products	8000 -10499	1.67E+08	23.20 %	52.83 %
C2S / C3S	10500 - 10999	2.49E+06	0.34 %	0.78 %
BFS	11000 - 14999	1.73E+07	2.40 %	5.46 %
ferrite	>= 15000	5.27E+05	0.07 %	0.17 %

Steps on to four of the segmentation algorithm were prototyped with MeVisLab [Rit11]. MeVisLab is a visual programming software, which uses a pipeline approach to process image data. It allows quick trial and error adjustments of input parameters and direct visual assessment of the resulting image output. The algorithm in the MeVisLab view is shown in figures 7.6 and 7.7. In the algorithmic overview, six channels are depicted, one for each gray value range corresponding each to a single phase.

The results from the first step of the algorithm are applied to the data as shown in the sketch in figure 7.6 at the bottom. It is depicted as a combination of "Threshold >= value_low" and "Threshold < value_high". For each phase, the corresponding voxels of a gray value range were extracted by a simple threshold discrimination. The gray value ranges used are listed in table 7.8. The resulting image contains the artifacts as visible in figure 7.5a.

As second step a canny edge detection filter [Can86] was applied. This filter uses information of partial derivatives of the gray values with respect to space to extract regions that have high gradients in terms of gray value, which in turn is proportional to the probability of edges. Thus, the result of the edge detection is the contour of the initially extracted gray value voxels. This contour does also overlap with the artifact voxels. By finding all contours of each extracted phase, all artifact voxels can be masked and subsequently removed from the original image data in the third step (cf. "Mask" in figure 7.6 at the top). Obviously, in this step are also voxels removed which correspond to correctly assigned phases, i.e. there are gaps between the different gray value regions. However, this will be addressed in the last volume repair step.

Within the fourth step, the stripped image data of the second step were used as input for a simple threshold discrimination. Here the same ranges were used as in the first step (cf. table 7.8). The difference now is that the retrieved output has almost no partial volume artifacts left. However, for silica fume, calcium silicate clinker and blast furnace slag there were still tiny and thin artifacts left. This was mitigated by applying a Gaussian blur convolution filter and subsequently discriminating at a threshold value of 0.5 (cf. second, fourth and fifth channel in figure 7.7). By this technique, small and

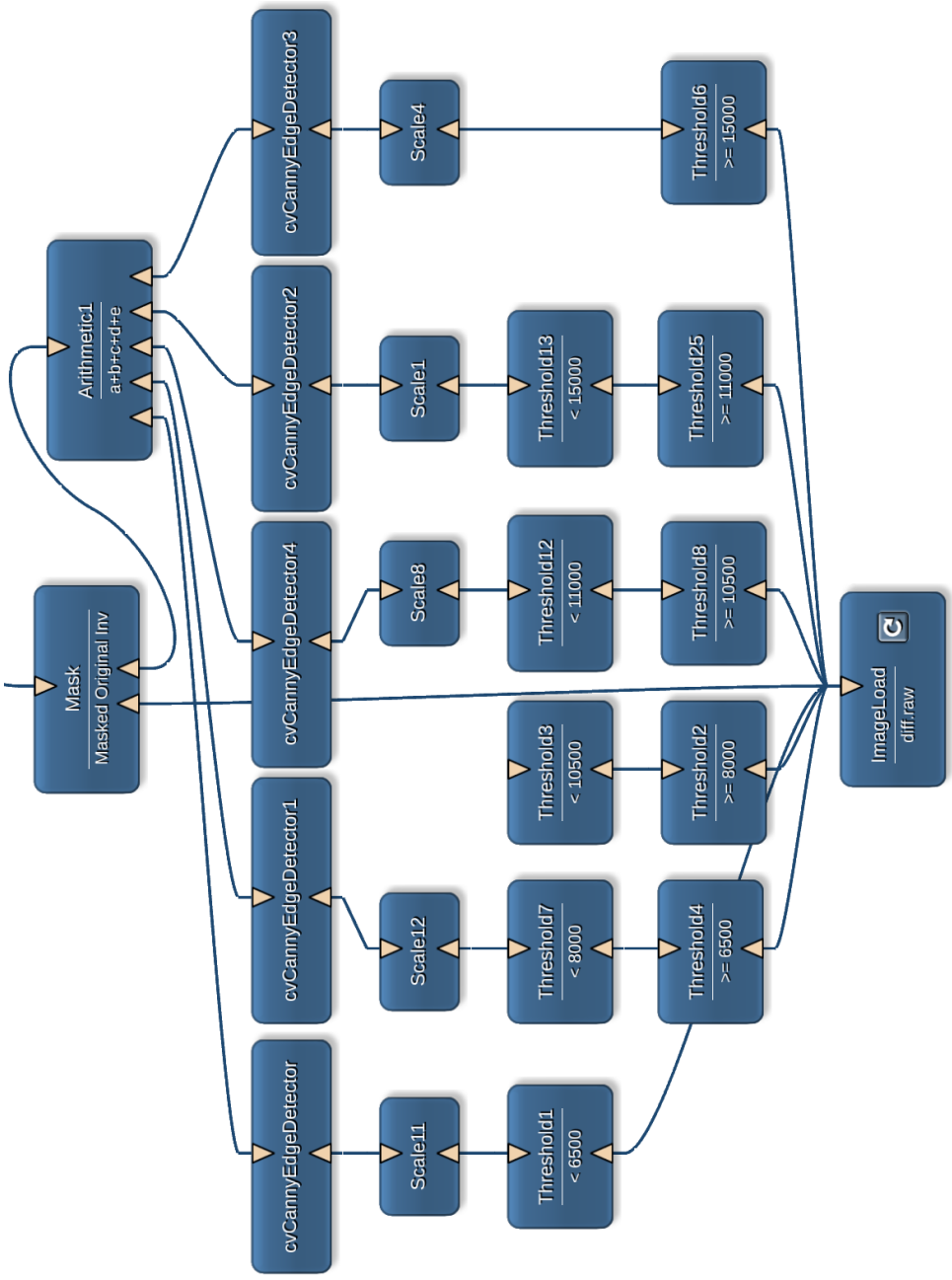

Figure 7.6: Algorithm for removing artifacts due to the partial volume effect implemented in MeVisLab. Input are raw μ-XCT image data in gray scale at the bottom while the cleaned output is located at the top.

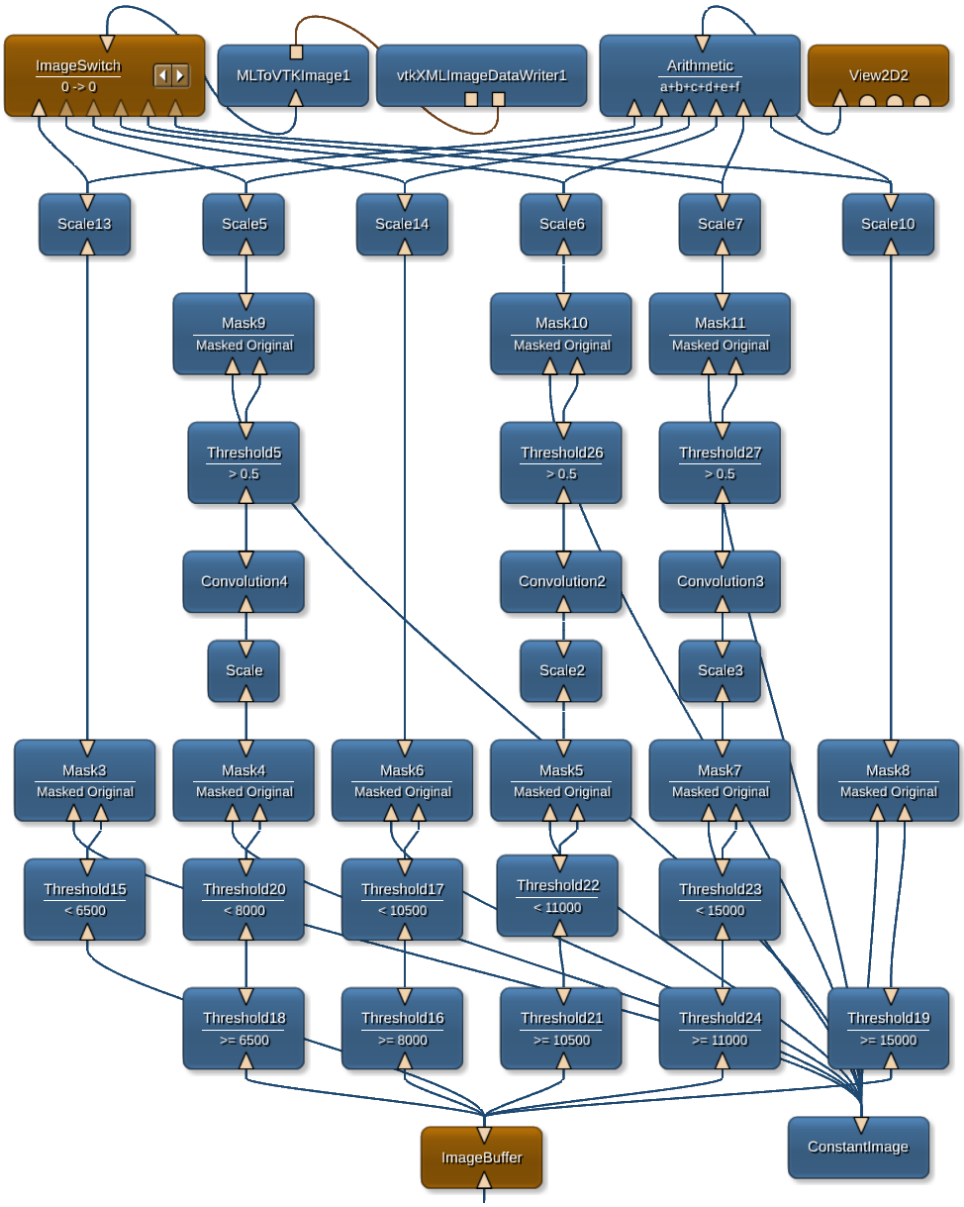

Figure 7.7: Algorithm for separating gray scale voxels of the μ-XCT image data via thresholds implemented in MeVisLab. Input at the bottom is the cleaned up data set from the algorithm shown in figure 7.6.

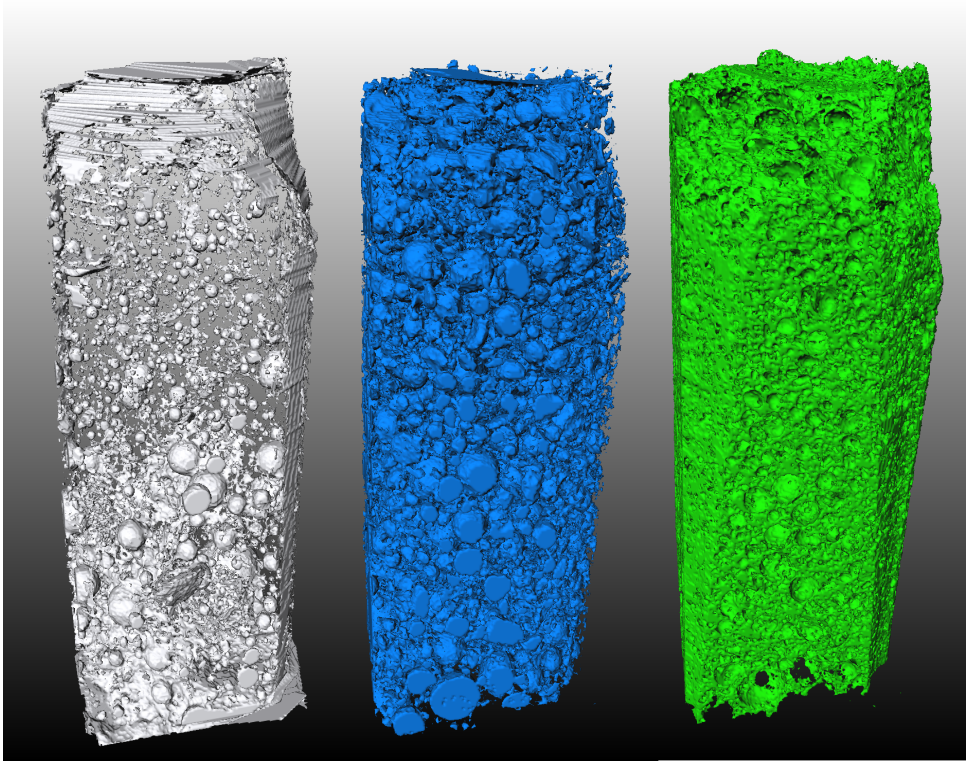

Figure 7.8: Segmentation results of the μ-XCT volume data of the hydrated low-pH cement paste specimen. The diameter of the cylinder was 2 mm with a height of 4 mm. In this figure the following phases are depicted (left to right): Air/void, silica fume and hydration products. Further separated phases are not shown here for clarity.

thin artifacts are blurred out, while rigid structures are still present.

Although there are almost no falsely assigned voxels in the resulting image, there are gaps between different domains of phases, which were removed in the third step by masking with the edge detection filter. Furthermore, by removing further tiny structures within step four, the gaps have even grown. To fill the gap volumes, a fifth step was necessary, which was a volume repair algorithm implemented in C++ code, thus this is not contained in the MeVisLab based implementation. The general idea of the volume fill algorithm is to grow the volume of each phase symmetrically, until the gaps are closed again. For this, a Gaussian blur filter is applied, but the blurred output is masked by the sum of all single phase images. The latter is important, to prevent growth into the volumes of other phases.

Using this algorithm, a three-dimensional phase distribution of the cement paste spec-

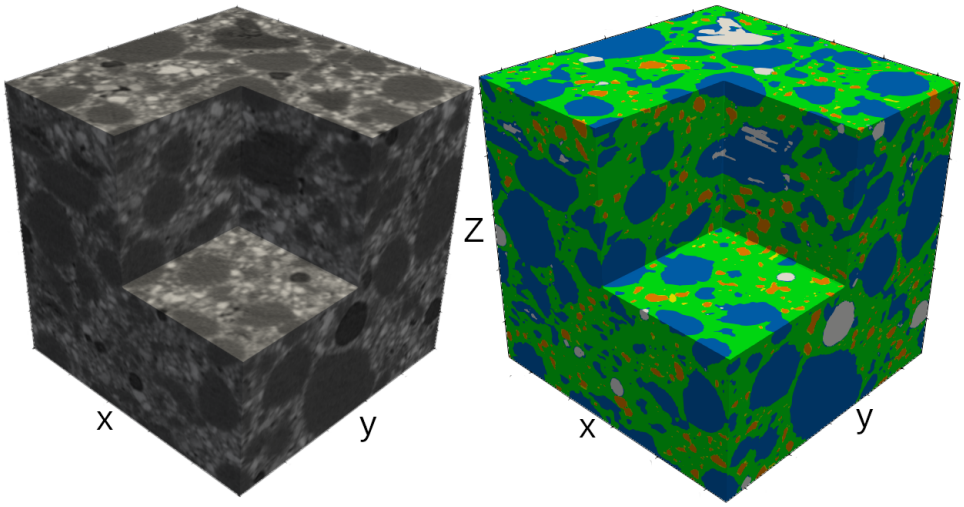

Figure 7.9: Plot of the original μ-XCT raw gray image data corresponding to the extracted cube (left) and microstructure of CEBAMA reference paste from segmented μ-XCT data used as input geometry for the calculation of effective diffusion coefficients (right). A box was clipped from the cube for illustrative purposes. Phases: Air (white), silica fume (blue), alite/belite (yellow), blast furnace slag (orange), ferrite (red) and hydration products (green). Total model size is 750x750x750 µm with a resolution of 3 µm.

imen could be derived, in which air, silica fume, calcium silicate clinker, blast furnace slag, ferrite clinker and hydration products could be distinguished. Unfortunately, further separating of the cement hydration phases was not possible with the resolution delivered by the μ-XCT image data. Thus, it is assumed within this work that the hydration products in the USFD HCP are mixed homogeneously. Applying this method, the microstructure of the hydrated low-pH cement paste was reconstructed and used as input geometry in reactive transport simulations (cf. figures 7.8 and 7.9). The relative volume fractions of the different phased determined by this way are depicted in table 7.8.

The homogeneous mixture of the hydration products has implications on the choice of modeling approach used in this work. The hydration products need to be regarded as continuous phase with different components. Essentially, this leads to the development of an effective medium approach as detailed in section 7.4.4. By using a better resolved image data set, it might be possible to extract explicit distributions of the distinct hydration products.

Moreover, a rather high volume fraction of voids/air was detected in the HCP. When subtracting the voxels corresponding to air which are outside of the cylinder, a volume fraction of 11.2 % corresponding to air is found inside the specimen. Since the specimen

was produced in a thin 2 mm mold, air was embedded within the paste during that process. Thus, for further phase composition treatment it is assumed that this volume does not correspond to typical capillary porosity.

7.2.2.3 Size distribution of silica fume particles

During hydration of composite cements, silica fume serves as an additional source of silicon. The reaction between high pH water, including a high concentration of calcium ions, and silica is called pozzolanic reaction. Since this reaction is kinetically controlled, the specific surface area of the silica fume particles is important. In order to gain more insights into the hydration process, the distribution and size of silica fume particles in the hardened cement paste were analyzed in more detail.

For this purpose, the silica fume volume data were treated with a newly developed algorithm to separate each particle from one another. This is not straightforward, since almost all particles are in contact with another one at some point. Thus, the application of a region grow algorithm led to a connection of almost all particles. However, this newly developed algorithm is based on the *signed distance field* [Jon06] of the original silica fume volume data and a region grow algorithm [Gon08, pp.763]. The algorithm does find big particles first and then consecutively searches for smaller particles.

The idea of the separation algorithm is to calculate the signed distance function of the whole domain. The distance field is defined, such that the particle surface has a distance of zero, while everything outside of the solid volume has a positive distance value assigned and vice versa. Then the most negative value in the signed distance field is searched for. This means, the location of the center of the largest particle is found. As next step, a region grow algorithm is applied on the distance field. The region grow algorithm starts at a seed location and subsequently conquers all connected voxels iteratively, until no more voxels can be captured. The condition to capture a voxel might be, for example, that growth is only allowed until a threshold value. In contrast to the simple approach using the volume data directly, a non-zero negative threshold value of -5 was used for the signed distance field. This means that the particle will not be captured completely by the region grow algorithm in the first place, but also does not connect to adjacent particles if the diameter of the junction is narrower than 10 voxels. The choice of this threshold was determined empirically. To expand the region to the residual particle volume, a Gaussian blur is applied with a binary mask of the silica fume voxel volumes. Using the mask helps to only track the true silica fume volume and not falsely assign voxels from other phases to the particle.

Subsequently, the determined volume is masked as particle with an index and the volume is removed from the silica fume volume, in order to prevent double tracking of the same volume. The algorithmic procedure is repeated at the generation of the distance field and the search for the most negative value in the field. In this way, iteratively all silica fume particles are removed from larger to smaller ones. If no more regions can be successfully determined with the region grow algorithm, the threshold is reduced by a factor of 2 and the search is repeated. The algorithm runs until no more negative values are found in the distance transformation field.

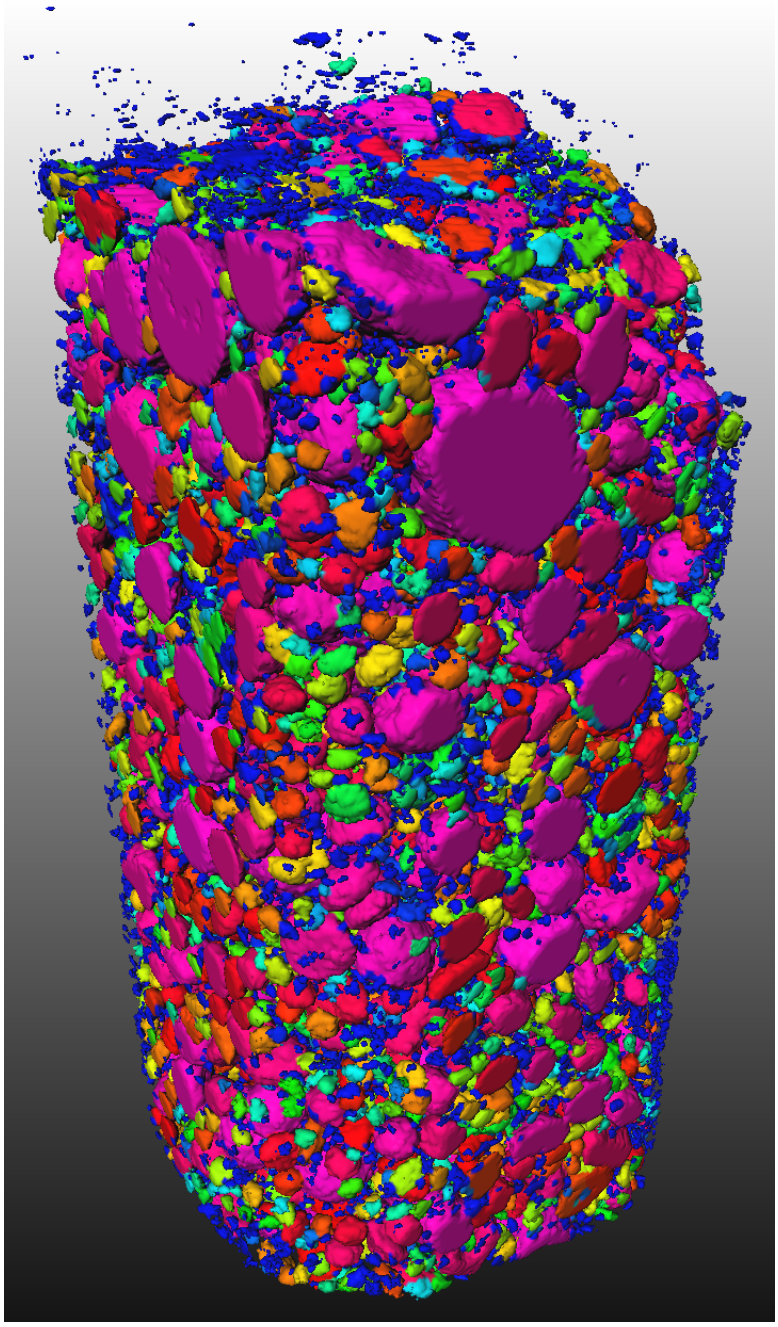

Figure 7.10: Separated silica fume particles in hydrated low-pH cement paste derived from μ-XCT image data. Each particle has an index assigned, while the particle index is indicated out of a continuous color spectrum. Since the indices are correlating with the particle size, the color approximates the order in size.

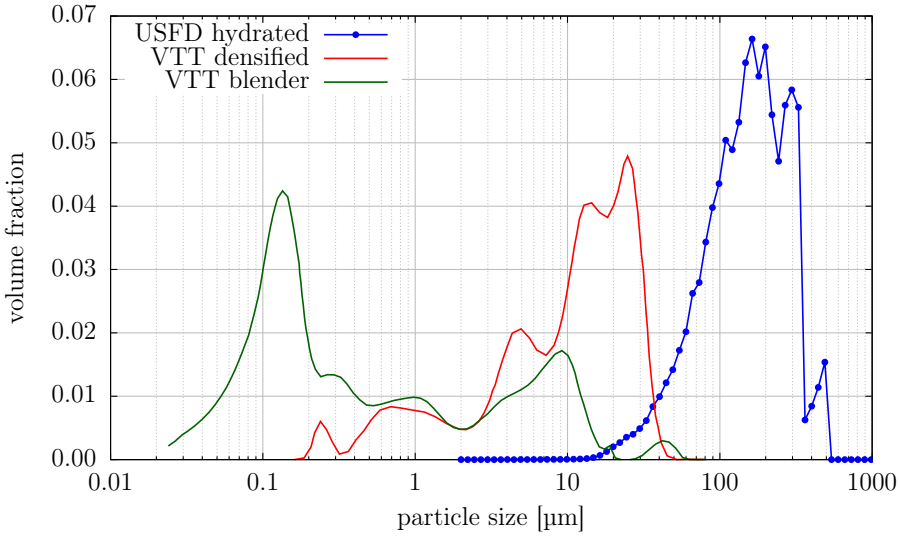

Figure 7.11: Size distribution of silica fume particles determined by particle detection within the segmented μ-XCT volume data in hydrated low-pH cement paste provided by USFD (blue). The lines are only a guide to the eye. For comparison, particle size distributions of densified raw (red) and finely blender dispersed (green) silica fume as used in the VTT reference cement paste are shown. The values provided by VTT were experimentally determined by laser diffraction [Veh17].

Figure 7.10 shows the separated silica fume particles in the hardened low-pH cement paste in different colors. Initially found particles are colored in purple, while particles found later by the algorithm are depicted in a continuous color spectrum from purple to dark blue. Since the algorithm sorts the particles by size to some extent, larger particles are colored purple while smaller ones are colored blue. It is clearly visible that the smaller particles fill the gaps between the larger ones.

For a non-spherical body, the definition of diameter is ambiguous. However, visible inspection of the single particles revealed a quasi-spherical shape in particular for larger silica fume particles. Therefore, in order to determine the size of the particles, a spherical geometry was assumed. This way an equivalent diameter was calculated respecting the volume of each particle. The resulting particle size distribution of the silica fume particles in the hardened low-pH cement paste is depicted in figure 7.11 in blue. For comparison, the same figure contains the particle size distributions of the CEBAMA reference cement mixture produced by VTT with (green) and without (red) application of a high-speed blender [Veh17].

Although the number of small particles is vastly higher than the number of larger ones, the volume fraction of the small particles is rather small, i.e. particles with a diameter

smaller than 40 µm do only contribute 5 % to the volume found as silica fume particles within the USFD data set. The main volume fraction of the silica fume is constituted by particles with diameters between 30 µm and 300 µm. It has to be noted that the used μ-XCT imaging method provided only a spatial resolution of 3 µm. Additionally, it is possible that particles in the size close to the image's resolution will not be reconstructed completely during the segmentation algorithm. However, the particle distribution shows that there is almost no volume fraction stemming from particles around 20 µm which should be still included and survived the segmentation. Additionally, it is important to mention that these data were obtained after hydration. Hydration would more likely consume smaller particles faster because of the higher specific surface area. A similar conclusion can be drawn from comparison of the determined particle size distribution published within the design of the VTT cement mixture [Veh17]. Accordingly, the particle size of the raw densified silica fume is between 3 µm to 30 µm. The application of a high speed blender to disperse the silica fume in a better way than the densified silica fume, yielded a size distribution between 0.02 µm to 0.2 µm [Veh17]. High quality silica as produced as by-product by silicon production has a typical particle size of 0.1 µm [Tay97, p. 284]. Although there was a high-shear mixer applied during the preparation of the USFD mixture [Vas18], the particle dispersion seems to be poorer compared to the reference mix. Effectively, this might have an effect on the phase assemblage of the hydration products and subsequently on derived diffusion coefficients. Thus, the results of experiments and simulations regarding the USFD mix will likely differ from experiments conducted with the CRP.

7.3 Hydration modeling and composition of the low-pH HCP

Since it was not possible to determine the amounts of the different hydration products in the hardened low-pH cement by evaluation of the μ-XCT-imaging, this information was obtained via a hydration model using PhreeqC. Other authors have developed such modeling approaches which incorporate various kinetic reaction terms and assumptions regarding reactive surface areas (e.g. [Lot06]). These thermodynamic models assume a homogenized system in a perfect mix reactor. In the model used for this work, the consumption of clinker, slag and silica fume during hydration is governed by empirical kinetic laws. Other phases are assumed to be in equilibrium with the pore water at 40 °C. The superplasticizer is regarded as chemically inert (cf. table 7.6). The thermodynamic database used for the hydration modeling was *ThermoChimie_eDH_v9b0* [Gif14]. The CSH model included in ThermoChimie uses three distinct CSH phases. Furthermore, this hydration model includes the effect of relative humidity of the curing chamber [Idi18].

Silica fume is an additional source for silica in the low-pH cement blend and affects the composition of the hydration products. Thus, the kinetic reaction parameters of silica fume were adjusted in the hydration model to meet the volume fraction determined from

Table 7.9: Simulated phase concentrations of hydration products in USFD low-pH cement paste after 28 days of hydration in the reference volume and volume fractions obtained by thermodynamic modeling. The inert component originates from superplasticizer, which is regarded as inert in the thermodynamic model. These data define the hydration products phase of table 7.8 in more detail.

Phase	c $[\mathrm{mol\,L^{-1}}]$	volume fraction (without Ferrihydrite)
Calcite	0.08	0.28 %
CSH 0.8	1.54	9.12 %
CSH 1.2	6.78	48.76 %
CSH 1.6	0.00	0.00 %
Ettringite	0.05	3.33 %
Ferrihydrite(am)	0.44	-
Hydrotalcite	0.18	3.87 %
Portlandite	0.00	0.00 %
Strätlingite	0.34	7.38 %
inert	-	2.83 %
Hydrates total porosity ($\phi_g + \phi_c$)	-	24.41 %
Hydrates gel porosity (ϕ_g)	-	18.55 %
Hydrates capillary porosity (ϕ_c)	-	5.87 %

the μ-XCT imaging (i.e. 17.89 %, see also table 7.8) after 28 days of hydration.

The resulting amounts and volume fractions of the hydration product phases are given in table 7.9. Interesting to notice is the absence of CSH-1.6 and portlandite, which is a result from the hydration of silica fume and slag, effectively reducing the C/S ratio of the CSH. From the residual clinker phases, a degree of hydration of 85 % was determined (not reproduced here, taken from the raw data of the publication [Idi18]). The composition of the pore water of the low-pH cement paste was determined by equilibration with the hydration products during the hydration modeling. The resulting pore water composition at 40 °C is depicted in table 7.10.

The hydration model contains also iron species and predicts the formation of minor amounts of iron containing phases (e.g. amorphous ferrihydrite). However, iron species and iron containing solid phases were not included in the reactive transport simulations presented in chapter 8.3, because of chemical stability problems due to redox effects.

For all leaching simulations of the hardened low-pH cement paste in this work, the same thermodynamic database as in the cement hydration model was used. Since this database does not contain molar volumes in general, the missing data were calculated using density data from Balonis and Glasser [Bal09] and subsequently added as database extension.

Table 7.10: Simulated pore water composition in hydrated USFD low-pH cement paste after 28 days of hydration at a temperature of 40 °C. The resulting pH at 40 °C is 12.05.

Element	c [mmol L^{-1}]
Al	0.773
C	0.7
Ca	0.691
Fe	2.83E-3
K	741
Mg	3.25E-06
Na	212
S	444
Si	4.62

7.4 Diffusivity models for CSH and hydration products

7.4.1 Overview

Since CSH incorporates an intrinsic gel porosity it can be regarded as a diffusive medium. At the nano-scale, however, CSH consists of different building blocks and interlayer water (cf. section 2.3.4.3). For several reasons it is challenging to conduct experiments to determine the diffusion coefficients of CSH directly. One of the reasons is that CSH is in confined spaces embedded within other hydration products and sensitive to mechanical stress. In fact, CSH is thought to be at the origin of creep of concrete [Pig16]. This renders it difficult to extract intact specimens of CSH to investigate it in a diffusion chamber. The formation of CSH under higher fractions of water in the cement mixture, i.e. to relax the confinement level to ease the process of obtaining a representative sample, will change the compactness and thus porosity. Hydration of C_3S or C_2S produces a mixture of LD- and HD-CSH, whose ratio depends on the w/c ratio and degree of hydration, too [Ten00]. Furthermore, drying of CSH would change the gel pore structure and hence alter the diffusivity. This excludes techniques and preparations for which a vacuum is needed, e.g. focused ion beam (FIB) treatment.

All in all, to the author's knowledge, due to these complications so far no diffusion experiments have been conducted on separated CSH. Usually, more often the opposite approach is described in which the macroscopic diffusivity of the hydrated cement paste is determined by experiments and with knowledge of the microstructure and introducing some assumptions the diffusivity of CSH phase is deduced (e.g. [Phu19]). On the other hand, macroscopic continuum scale simulations often treat the diffusivity of hydrated cement as input property from experimental data.

However, in this work the microscopic effect on this macroscopic property is in focus.

In fact, a sound representation of the diffusivity of the CSH phase is paramount for modeling the macroscopic (phase averaged) diffusivity of hydrated cementitious materials. Keeping in mind that this work seeks to determine the macroscopic diffusivity of hydrated cement paste starting from simulations at a lower scale, bottom-up approaches need to be developed, to assign realistic diffusion coefficients to the CSH phases. However, this is still an open research field, in which the effects of morphology and the adequacy of different modeling approaches describing the transport properties of CSH are still under debate (e.g. [Pat18c,Sto08]). Although, there are different approaches to derive the theoretical diffusivity of CSH, there are always assumptions made about the nano-scale structure of the material. Moreover, embedding non-diffusive hydration products in the model is needed for this work.

7.4.2 Archie's law diffusivity model of CSH

An apparently simple model to describe the diffusivity of CSH as a function of its porosity is the well-known Archie's law [Pat18b]. Researchers have fitted the cementation factor / exponent of Archie's law (see also equation 3.13) to more sophisticated micro-mechanical models. With this approach an exponent of 7.23 was determined. Thus, the effective diffusivity of the CSH phase can be written in terms of porosity as [Pat18b]:

$$D_e^{CSH} = \phi D_p = \phi D_w \phi^{7.23} \tag{7.15}$$

Here, ϕ corresponds to the total porosity, i.e. sum of capillary and gel porosity. This relation will later be used in certain simulations. However, this simplified model does take into account non-diffusive inclusions in the CSH medium, since it is fitted to a micro-mechanical model which assumes that CSH is only being dissolved and degraded but not replaced by another phase.

7.4.3 Multi-scale diffusivity models and homogenization schemes

The microstructural model of hardened low-pH cement paste developed in section 7.2.2.2 considers explicitly different phases: Voids, unreacted clinker phases, SCMs (i.e. blast furnace slag and silica fume) and a homogeneous continuum of hydration products. In this work unreacted clinker and SCMs are considered as non-diffusive as other authors have done before (e.g. [Pat18b]). Voids are interpreted as water saturated pores. Based on the hydration model, more than 50 % of the volume of the continuum of hydration products corresponds to CSH (cf. table 7.9). Since CSH is a diffusive medium, it is assumed that besides of the water saturated pores, the hydration product phase contributes to the effective diffusivity of the hardened cement paste.

Since the hydration products could not be separated from the given μ-XCT image data, a homogeneous mixture of the hydration products was assumed. The diffusion coefficient and porosity of the hydration products in the hardened cement paste depend on the volume fraction of CSH and other hydration products. To this end, a multiscale homogenization model (effective medium approach) was implemented.

In general, homogenization schemes are used in the field of modeling mechanical and diffusivity properties of cementitious materials (e.g. [Bar14,Bej07,Pat16b,Sto08]). Homogenization schemes are based on effective medium approximations. The general idea is to use morphological information of the microstructure of a composite material and identify shape and volume fraction of inclusions embedded into a matrix to determine effective properties of the combination of both. Inclusions refer to another phase which is embedded into a matrix with different properties. In some cases, hardened cement paste is regarded as composite material (e.g. [Bar14,Sto08]).

Effective medium approximations assume that there are separate scales. The microscopical scale is intended to resolve the heterogeneity, while the macroscopic scale must be large enough to average out the heterogeneity [Cha10]. Although initial developments in the field of effective medium techniques were focusing on effective mechanical properties (e.g. [Hil65]), it was consequently extended for the purpose of diffusive transport properties as well (e.g. [Bar08], [Tor02, pp.459]).

7.4.3.1 Maxwell / Mori-Tanaka scheme

The Mori-Tanaka effective medium method is based on the generalized Maxwell approximation [Mor73]. The basic idea is to embed small spherical particles (inclusions) into a larger sphere with different diffusive properties. The larger sphere is immersed in an infinite matrix of the same phase as the larger sphere, i.e. to define an unbounded system [Sev19]. The volume fraction of the small particles should be small enough to neglect interactions among each other, i.e. a diluted particle assumption [Tor02, pp.460]. The original derivation from Maxwell [Max73, pp.435] is solving thermal conductivity and electric field problems but can be translated to a heat diffusion transport problem.

With the assumption that particles do not interact with each other, the contribution to conductivity of each particle can be solved by its own. Additionally, to the embedded sphere system a temperature gradient is assumed, thus, this problem can be tackled by solving the Laplace equation. The intermediate result is an equation for describing the temperature field. Furthermore, at radial distances far away from the larger sphere, it can be assumed that each particle contributes linearly to the result, i.e. the so-called superposition principle can be applied [Das08, pp.169].

Solving the differential equations for a binary system, i.e. two different phases, leads to the following explicit equation for the effective diffusivity:

$$D_e = D_M \frac{1 + 2\beta_i V_i^f}{1 - \beta_i V_i^f} \tag{7.16}$$

D_M refers to the matrix diffusion coefficient, V_i^f is the volume fraction of the inclusions while β_i is called *polarizability*. It is defined as:

$$\beta_i = \frac{D_i - D_M}{D_i + 2D_M} \tag{7.17}$$

D_i is the diffusion coefficient of the inclusion phase. There are limiting cases, i.e. per-

fectly insulating or superconducting inclusions, which have simplified expressions. Thus, for the purpose of including a non-diffusive phase ($D_i = 0$) into a diffusive matrix, the following equation is obtained:

$$D_e = D_M \frac{2\left(1 - V_i^f\right)}{2 + V_i^f} \tag{7.18}$$

This equation can be rewritten in terms of porosity $\phi = 1 - V_i^f$:

$$D_e = D_M \frac{2\phi}{3 - \phi} \tag{7.19}$$

Equation 7.16 can be extended to support multiple inclusion types to:

$$D_e = D_M \frac{1 + 2\sum_i \beta_i V_i^f}{1 - \sum_i \beta_i V_i^f} \tag{7.20}$$

Because of the diluted particle assumption introduced in the Maxwell derivation, the resulting equations are strictly speaking only valid in the case of a low volume fraction of inclusions. However, the Maxwell approach has the benefit of resulting in a directly usable explicit equation, which is not always the case for other homogenization methods shown later.

7.4.3.2 Differential scheme

The basic idea behind the differential scheme is to replace incrementally matrix volume by inclusion phase until the desired volume fraction is reached. The process starts at a known composite diffusivity value corresponding to a certain composition. This is usually the pure matrix phase only. During the process of adding inclusions, the homogenized diffusivity is determined at each step. This can for example be done with a *dilute approximation* with spherical [Tor02, p. 489] or with spheroidal [Pha00] shaped inclusions. The evolution of the diffusion coefficient is done in infinitesimal steps, resulting into a differential equation. The differential equation is then either solved analytically or numerically. By an analytical approach, closed-form solutions might be found for interesting cases.

For spheroidal inclusions, a differential scheme based solution has been derived [Pha00]. The resulting equations still need to be solved numerically for the general case, i.e. treating an arbitrary number of phases. However, the following equations for a binary system with insulating inclusions was reported [Pha00]:

$$D_e = D_M \phi^{1/(B-A-C)} \tag{7.21}$$

The variables A, B and C are defined as:

$$A = 3\frac{R - R^2}{1 + 3R} \tag{7.22}$$

$$B = 3\frac{9R^2 - 2R + 1}{(1 + 3R)^2} \tag{7.23}$$

$$C = 3\frac{4 - 24R + 36R^2 + 3R^3 - 9A^4}{(5 + 3R)(1 + 3R)^2} \tag{7.24}$$

R corresponds to a shape factor, for which two different solutions for prolate and oblate shapes are found. Prolates and oblates are spheroid geometries representing either a thinned or a flatted sphere geometry, respectively. For prolates, the following shape factor was reported [Pha00]:

$$R = \frac{1 - e^2}{2e^3}\left(\ln\left(\frac{1 + e}{1 - e}\right) - 2e\right) \tag{7.25}$$

On the other hand, the solution for oblates is [Pha00]:

$$R = \frac{1 + e^2}{e^3}\left(e - \tan^{-1} e\right) \tag{7.26}$$

In both equations, e is the eccentricity and is defined as:

$$e = \sqrt{1 - k^2} \tag{7.27}$$

k is the aspect ratio of the spheroid, namely the ratio between equatorial radius and distance from center of the spheroid to the pole. Thus, for oblates k is lower than unity, while for prolates the parameter is greater than unity. For the special case of a sphere, the ratio is exactly unity. Unfortunately, the equations above yield a singularity if the eccentricity of unity corresponding to a sphere is used. Similar issues occur for the limiting cases of flat oblates (disks) and prolates (fibers). However, with an analysis of the limits of the functions, the following equations with constant exponents emerge as simplification of equation 7.21:

$$\frac{D_e}{D_M} = \begin{cases} \phi^{3/2} & \text{(spheres)} \\ \phi^{5/3} & \text{(fibres)} \\ \phi^{16/9} & \text{(disks)} \end{cases} \tag{7.28}$$

For the non-insulating binary system case, also a more general solution was found [Pha00]:

$$\phi = \left(\frac{D_M}{D_e}\right)^A \left(\frac{D_i - D_e}{D_i - D_M}\right)^B \left(\frac{D_M(5 - 3R) + D_i(1 + 3R)}{D_e(5 - 3R) + D_i(1 + 3R)}\right)^C \tag{7.29}$$

Under the assumption of spherical inclusions, this equation simplifies to:

$$\phi = \left(\frac{D_M}{D_e}\right)^{1/3} \left(\frac{D_i - D_e}{D_i - D_M}\right) \tag{7.30}$$

Equation 7.30 is an implicit function, which means it is not explicitly solvable for D_e. Thus, in order to determine D_e, a numerical solution step is required. However, the derivation for the insulating case leads to an explicit solution, which is computationally beneficial. Moreover, the differential scheme does recover Archie's law. This is due to the assumption that the matrix volume is always connected and percolating [Tor02, p.468]. From that perspective, the differential scheme is superior to the Maxwell approximation in cases of a high volume fraction of the inclusion, i.e. low porosity in the case of a water matrix.

7.4.3.3 Others schemes and concluding remarks

There are other homogenization schemes, for example the self-consistent scheme. However, the self-consistent approximation results in negative diffusivities for porosities below 0.3 [Dor07, p. 97]. Thus, it is not applicable to reactive transport modeling of a low porosity medium, e.g. cementitious materials, and therefore not presented here. Nevertheless, the Maxwell and differential scheme are valuable techniques for approximation of the diffusivity of the hydration product continuum.

7.4.4 Diffusivity model for hydration product phase of low-pH cement

Figure 7.12 depicts schematically different scales of heterogeneity of a cementitious material. This illustration is focused on the model which will be developed here, to determine the diffusivity of the hydration product phase. To assign a diffusivity value to the hydration product continuum, a bottom-up upscaling approach was developed. At the very bottom are the CSH globules, which themselves are composed of *basic building blocks* shown as black layers. Since it is assumed that the interstitial water is electrochemically bound and rather structural water [All07b,Ulm04], it is assumed in this work that it does not contribute to diffusive transport. Hence, in this scheme a CSH globule is assumed as the smallest entity relevant for the determination of diffusivity of CSH.

CSH consists of at least two different sub-types: LD- and HD-CSH, which have different intrinsic gel porosities (see section 2.3.4.3 and "Level 1" in figure 7.12) and thus different diffusive transport properties. The relative fractions of both CSH variants can be separated with an empirical relation from Tennis and Jennings [Ten00] (see also equation 2.9). This model relation requires the w/c ratio and the degree of hydration as input data.

The w/c ratio for the low-pH cement paste is defined by the mix design, which is given as 0.25 [Vas18,Idi18] (cf. section 7.2.2). The empirical equations derived by Parrot and Killoh and the correspondingly determined parameters [Lot08], which allow to estimate

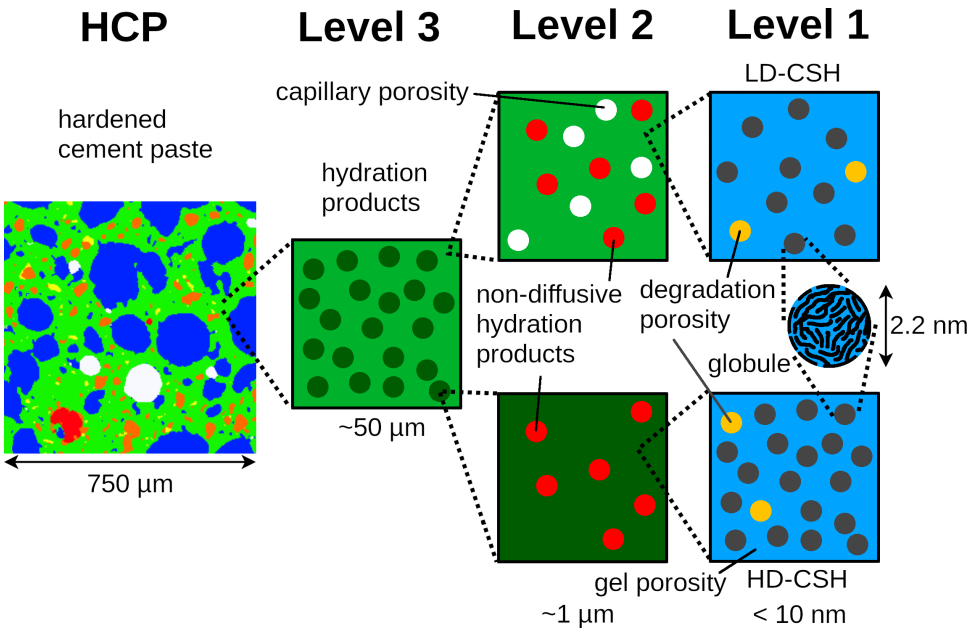

Figure 7.12: Different scales of the homogenization scheme used to determine the diffusivity of hydration products. Magnification is increasing from left to right.

the degree of hydration, usually correspond to hydration of OPC. In the case of a low-pH cement it is likely more accurate to determine the resulting degree of hydration by the residual amount of clinker phases. Thus, a degree of hydration of 85 % is used, which was estimated by the cement hydration model with PhreeqC (cf. section 7.3). However, neglecting the restrictions, the estimated degree of hydration with the Parrot and Killoh approach yields a value of almost 80 %.

Originally, the Tennis-Jennings CSH model were derived for Portland cement. Although there is no proof that the correlation is directly applicable to other cementitious materials, due to lack of data available in literature, the model was applied in this study to determine the fractions of LD- and HD-CSH in the hydrated low-pH cement paste. By this way, different gel porosities can be assigned to each phase. In the right part on figure 7.12, the gel porosity itself is shown as blue background while the different gel porosities of the CSH variants are illustrated in differing numbers of the globules.

Furthermore, it is assumed that only the nitrogen accessible porosity of the gel porosity in the CSH phase contributes to diffusive transport, which was determined to 17.8 % and 0 % for LD- and HD-CSH, respectively, rendering HD-CSH as a non-diffusive phase [Ten00]. According to Stora et al. the assumption of HD-CSH being non-diffusive does not alter the resulting effective diffusivity of the medium significantly [Sto08]. However, in the case of a low-pH cement paste with a low w/c, the volume fraction of HD-CSH in the CSH phase is quite high. Applying the CSH separation model of Tennis and

Jennings [Ten00], the HD-CSH volume fraction is about 96 %. Assuming such a high volume fraction of a non-diffusive HD-CSH phase, the hydration product matrix would be almost completely inaccessible for diffusive transport, since in this model capillary porosity is regarded as non-connected and thus not percolating [Sto07]. This conclusion would be quite unexpected and contradictory from experimental experiences [CEB19].

While some researchers have actually assumed for their modeling work that HD-CSH has no accessible porosity for solute transport [Pat18c], other researchers have stated that the accessible porosity is increased upon degradation of both CSH variants by 6.5 % [Sto09]. Nanoindentation measurements suggest that mechanical properties of LD-CSH degrade at a higher rate than HD-CSH, i.e. a residual elastic modulus of 14 % and 41 % were obtained for LD- and HD-CSH, respectively, after calcium leaching conducted with OPC (w/c = 0.5) [Con04]. This suggests that there is a simultaneous effect on both types of CSH. For the sake of simplification, however, the same rate of additional porosity is assumed and therefore in this work the same assumption is made as Stora et al. [Sto09], assuming a linear relationship of the *degradation porosity* ϕ_d for both CSH variants in dependency of the C/S ratio. This introduces an additional porosity of maximum $\phi_{dm} = 6.5\,\%$ when reaching a C/S ratio of 0.8 and no additional degradation porosity at C/S ratio of 1.667. The function reads:

$$\phi_d(C/S) = (C/S - 1.667)\frac{\phi_{dm}}{0.8 - 1.667} \tag{7.31}$$

Moreover, in this work it is assumed that the degradation of CSH would increase the nitrogen accessible gel porosity. This additional porosity generated due to degradation is indicated in yellow in the HD and LD-CSH scheme on the right-hand side in figure 7.12.

Since the effective porosity contributing to diffusion is quite low in LD- and HD-CSH, the diluted inclusion argument of the Maxwell/Mori-Tanaka scheme is strictly speaking no more valid. Note that the CSH solid is embedded into a gel pore matrix and not vice versa. Hence, the effective diffusion coefficients of the LD- and HD-CSH phases are determined by the differential scheme explained in section 7.4.3.2. Since there is no consensus among authors about the shape of the globules forming the in gel pore space [Pat18c], in this study a spherical shape was assumed. Thus, the simplified equation for sphere morphology (7.30) was used to derive the diffusion coefficients of both CSH variants. In addition, there is a constrictivity effect reported affecting the gel porosity. Accordingly, the connectivity of the gel pores is limited. A factor of about 0.1 was determined from data obtained experimentally [Phu19,Sto07]. Thus, the gel water diffusion coefficient in CSH was reduced by a factor of 10 compared to the diffusion coefficient applied to capillary water.

As next upscaling step (cf. "Level 2" in figure 7.12), the non-diffusive hydration products other than CSH and capillary pores are inserted into the CSH medium. For capillary porosity (illustrated in white in figure 7.12), this is done separately in each CSH type, since it is assumed only to be incorporated in the LD-CSH medium [Bar06]. On the other hand, the hydration products other than CSH are linearly split between

Table 7.11: Effective medium schemes used in the corresponding homogenization levels. The input data required by the equations are depicted (molecular diffusivity D_w, nitrogen accessible porosity ϕ_{N_2}, degree of hydration α, capillary porosity ϕ_{cp}).

Level	homogenization method	equations	input data
Level 1	differential scheme	7.21, 7.31	D_w, ϕ_{N_2}, C/S
Level 2	Maxwell scheme	7.20, 2.9	w/c, α, ϕ_{cp}, volume fractions of non-diffusive phases
Level 3	Maxwell scheme	7.20, 2.9	volume fractions of LD/HD-CSH

HD- and LD-CSH with respect to the corresponding volume fraction of each CSH type [Bar06]. Non-diffusive hydration products are indicated as red spherical particles in the CSH medium in figure 7.12.

With the data available, it was not possible to determine the size, shape and morphology of the non-diffusive inclusions in the CSH medium. Therefore, the other hydration product defined as non-diffusive components are assumed as spherical particles dispersed in the diffusive CSH medium. Because the composite is no more a simple binary system, neither equation 7.21 nor 7.30 can be applied. Since the general solution must be solved by a computationally intensive numerical integration, this approach was rejected. However, the volume fraction of CSH gel (including gel porosity) accounts for about 67 % of the initial hydrates in the low-pH cement paste (cf. table 7.9), i.e. the fraction of inclusions is about 33 %. Thus, the diluted particles condition of the Maxwell approach (Mori-Tanaka scheme) is satisfied. Hence, the estimation of the diffusion coefficients at this level was based on the Mori-Tanaka homogenization scheme, which previously proved to provide satisfactory results (e.g. [Bar14,Sto09]).

As last step, both CSH media (which include other hydration products and capillary porosity) need to be combined (cf. "Level 3" in figure 7.12). Although this is a binary system, the use of the differential scheme is problematic, due to the missing explicit solutions for equation 7.30. Thus, the Mori-Tanaka scheme is used again by respecting the new volume fractions including all other phases. Here the assumption is made that the HD-CSH is embedded as spherical inclusion in LD-CSH (cf. figure 7.12). As a summary, in table 7.11 the homogenization levels and their corresponding effective medium methods are listed.

As validation of the homogenization code implemented in iPP, two simplified scenarios of the resulting diffusion coefficients determined by the developed effective medium scheme were modeled. The first setup consists of a CSH phase, which only contains LD-CSH. That was done by tweaking the w/c ratio and the degree of hydration dh to only obtain LD-CSH ($w/c = 0.6077$, $dh = 0.95$). That allows neglecting of the HD-CSH fraction in the effective medium. Subsequently, a series of effective diffusion coefficients were calculated using different capillary porosity fractions, which are embedded as spherical inclusions in the CSH phase. The molecular diffusivity was assumed

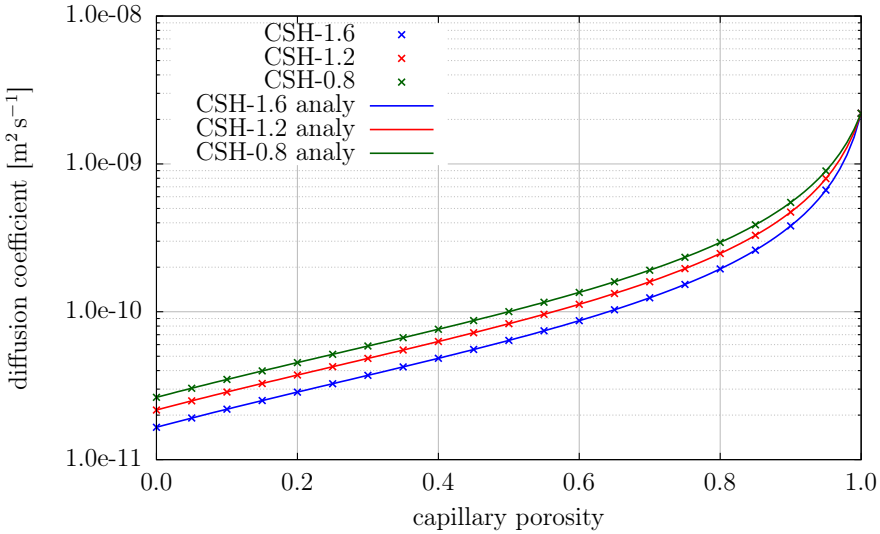

Figure 7.13: Effective diffusion coefficients for LD-CSH determined by the effective diffusion approach. The results from the implementation of iPP are compared to the analytical solution (cf. equations 7.20, 7.21 and 7.31).

to be $2.2 \times 10^{-9}\,\mathrm{m^2\,s^{-1}}$. Moreover, three different degradation states were assumed, i.e. CSH-1.666, CSH-1.2 and CSH-0.8. The resulting diffusion coefficients are compared to the analytical solutions (cf. equations 7.20, 7.21 and 7.31) in figure 7.13. As expected, the CSH-1.6 phase has the lowest diffusivity because it does not contain the additionally introduced degradation porosity. All in all, the results are in good agreement with the analytical solution.

Another test was implemented, which assumes a CSH-1.6 matrix, which is replaced by a non-diffusive phase, i.e. the phase is embedded as inclusions in the LD-CSH matrix. The resulting effective diffusion coefficients are compared to the analytical solution of the Maxwell scheme and an Archie's law approach using a cementation factor of 1.5 (cf. figure 7.14). As already expected, the Mori-Tanaka/Maxwell scheme does not replicate Archie's law perfectly. However, the error is small in the diluted domain, which is the more relevant scenario, since the cell will turn in to a heterogeneous reaction node, when the porosity becomes lower than a certain threshold (cf. section 4.4.1.3). Thus, the mentioned benefits prevail and this scheme is used anyway.

For the calculation of the effective diffusion coefficient of the continuum of hydration products of the low-pH HCP, a free water diffusion coefficient of $2.2 \times 10^{-9}\,\mathrm{m^2\,s^{-1}}$ was assumed for all dissolved species, corresponding to the value of Ca as a major solute in cement pore waters. When applying all the steps described above, the initial diffusion coefficient of the hydration products continuum in the low-pH HCP was determined as $8.26 \times 10^{-12}\,\mathrm{m^2\,s^{-1}}$. Since during a reactive transport simulation of the HCP the

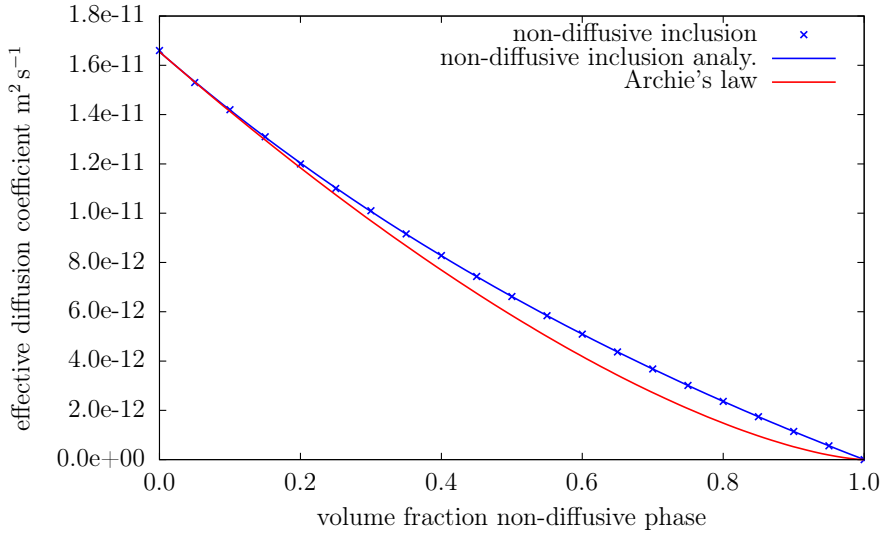

Figure 7.14: Effective diffusion coefficients of CSH-1.6 with embedded spherical inclusions of a non-diffusive phase using the effective medium approach. The resulting diffusion coefficients by the software implementation are compared to the analytical solution (cf. equations 7.20, 7.21 and 7.19) and to the results from an Archie's law approach with an exponent of 1.5.

phase composition can change, the diffusion coefficient calculated as described above will change accordingly. Thus, this effective medium calculation is performed at each time step and for each lattice node during the simulation.

7.4.5 Software implementation

Based on the derivations above, multiple models had to be implemented into iPP, including two groups of porosity models and diffusivity models, respectively (cf. table 7.11). The implementation in iPP was done using an abstract C++ interface. Several classes were implemented for serving the purpose of simulating transport and degradation processes in hydrated cement pastes:

- TennisJenningsCSHPorosityCalc
- DegradedCSHDiffusionCalc
- CSHGelDiffusionCoefCalc
- MoriTanakaDiffusionCalc

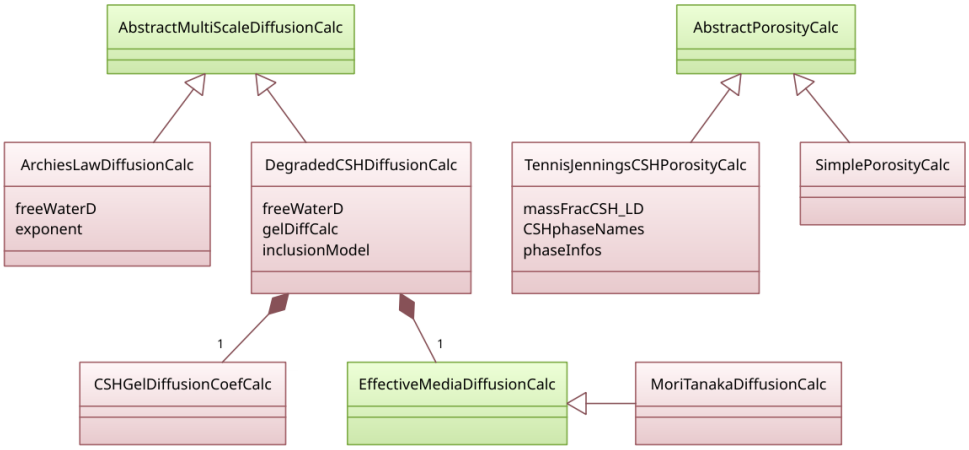

Figure 7.15: UML diagram of the C++ class interface design for the porosity and diffusivity models. Abstract interfaces are colored in green while specific implementations are depicted in red.

The corresponding unified modeling language (UML) class diagram is shown in figure 7.15. The iPP client algorithms use the abstract interface *AbstractPorosityCalc* to retrieve porosity information from the phase composition passed into the algorithm. There are two concrete (in terms of specific) implementations depicted in the figure. *SimplePorosityCalc* just converts the molar amounts per phase to volumes with help of the molar volume and sums up all phase entries. On the other hand, *TennisJenningsCSHPorosityCalc* distinguishes between HD- and LD-CSH via the Tennis-Jennings CSH model [Ten00]. For this purpose, the class needs the w/c ratio and the degree of hydration as input. When calculating the porosity, it respects the gel porosity effects of the different CSH types and treats capillary and gel porosity in a separate way. This class implements a form of equation 2.9 and uses data from table 2.3.

DegradedCSHDiffusionCalc implements a concrete algorithm of the type *AbstractMultiScaleDiffusionCalc*, which refers to the diffusivity law to apply (see equations 7.31 and 7.15). Another example implemented is *ArchiesLawDiffusionCalc* (eqation 3.13). The *DegradedCSHDiffusionCalc* implementation communicates with the *inclusion model* of type *EffectiveMediaDiffusionCalc*. The concrete implementation used for the low-pH model is defined in *MoriTanakaDiffusionCalc* (equation 7.20). Additionally, to retrieve the gel diffusion coefficient of CSH, *DegradedCSHDiffusionCalc* uses the *CSHGelDiffusionCoefCalc* implementation (equation 7.21).

The introduction of abstract interfaces easily allows to exchange and to extend the algorithmic implementations of both, the porosity and diffusivity calculations. Another feature of the used abstract interfaces is to compose different levels and steps of porosity and diffusivity models. For example, it is quite easy to add another effective media diffusion algorithm, if, for instance, the Mori-Tanaka scheme does not suit the purpose

of the end-user.

7.5 Parameters for simulating calcite nucleation

Calcite is an important solid phase commonly occurring in degraded HCP due to carbonation. In fact, calcite will become relevant for leaching simulations later in this work. Thus, here data are derived, which are needed for simulating nucleation of calcite. In the following sections experimental data providing surface energies are reviewed and subsequently the number of nucleation sites will be determined. This value is important for the determination of the probability of HEN. Afterwards an example of nucleation controlled precipitation of calcite in a counter diffusion setup will be presented.

7.5.1 Literature review of surface tension values determined for calcite

Several authors have conducted measurements of nucleation rates of calcite and subsequently determined surface energy values based on this (e.g. [Li14], [Lio07], [Söh82a], [Söh82b], [Spa98], [Ver92]). For this purpose, induction time measurements for different supersaturated solutions were performed. A first group of experiments conducted were intended to observation of a homogeneous nucleation process. Depending on the experimental set-up, homogeneous nucleation rates of $85\,\mathrm{mJ\,m^{-2}}$ (conductivity measurements) and $98\,\mathrm{mJ\,m^{-2}}$ (optical microscope) were obtained [Söh82a,Söh82b]. In both cases, cubic nuclei were assumed. Using equation 5.5, inserting the definitions of the cubic (β_c) and spherical (β_s) shape factors and subsequently compare both equations by division, the comparison yields:

$$\frac{\beta_s}{\beta_c} = \left(\frac{\sigma_c}{\sigma_s}\right)^3 \tag{7.32}$$

Using equation 7.32 to convert the $98\,\mathrm{mJ\,m^{-2}}$ value to spherical nuclei, a value of $122\,\mathrm{mJ\,m^{-2}}$ for the surface tension of calcite is obtained.

Other authors determined a value of $64\,\mathrm{mJ\,m^{-2}}$ [Lio07]. Unfortunately, in the publication of Lioliou et al. the shape factor β, which were used to determine the value, is not explicitly stated. However, recalculations of the determined value, done in the scope of this work, suggest that a shape factor corresponding to spherical nuclei was assumed. Thus, the value reported seems quite low compared to Söhnel et al. [Söh82a], i.e. the values differ by a factor of two.

Furthermore, the pH dependency was analyzed by other authors [Spa98]. The reported values are $25\,\mathrm{mJ\,m^{-2}}$ and $45\,\mathrm{mJ\,m^{-2}}$ for pH values of 10 and 9, respectively. The nuclei were assumed to be spherical. Although the experimental setup was intended to measure HON, the authors stated that due to the determined very low values it is more likely that HEN was observed, which probably stems from impurities in the used water [Spa98]. Similarly, other experimentalists determined values as $37\,\mathrm{mJ\,m^{-2}}$ for HON, which they again interpreted as HEN, due to possible impurities in the system [Ver92].

The second group of experiments deals with the voluntary observation and analysis of the heterogeneous nucleation (HEN) process. Both data sets assessed in this work deal with precipitation of calcite on quartz as substrate. The first experiment used online pH monitoring to capture the change in pH, when the precipitation commences. The value reported for the surface tension of HEN of calcite on quartz is $31.1\,\mathrm{mJ\,m^{-2}}$ [Lio07]. The second experimental setup used **g**razing **i**ncidence **s**mall-**a**ngle **X**-ray **s**cattering (GISAXS) measurements to track the number of nuclei. In this way, a surface tension of $47\,\mathrm{mJ\,m^{-2}}$ was determined [Li14]. The same value was applied as surface tension value for general foreign nucleation sites in a reactive transport model. The foreign nucleation site in this particular case was a Teflon liner in the reactor of the modeled system [Li17].

The most reliable source of HON surface tension data are those from Söhnel and Mullin [Söh82a] ($98\,\mathrm{mJ\,m^{-2}}$), since all other authors mentioned here have already stated that their values are too small to be related to HON only. The most accurate measurement technique for surface tensions of calcite in a HEN process with a value of $47\,\mathrm{mJ\,m^{-2}}$ was already used by Li for modeling heterogeneous nucleation in another system. Nevertheless, there was no specific surface tension value stated for calcite-calcite HEN. Usually, the nucleation rate of a phase on itself should be much higher than on foreign substrates, i.e. the value must be lower than the $47\,\mathrm{mJ\,m^{-2}}$ corresponding to HEN on quartz. It has even been reported from calcite seed experiments that there is no induction time at all but rather poly-nuclear growths [Lio07], corresponding to a surface tension of $0\,\mathrm{mJ\,m^{-2}}$. In order to capture the calcite-calcite nucleation effect, the value was estimated to $20\,\mathrm{mJ\,m^{-2}}$ within this work, which is significantly lower than $47\,\mathrm{mJ\,m^{-2}}$ but deliberately not zero. A value of $0\,\mathrm{mJ\,m^{-2}}$ was rejected, since still a geometric effect should play some role. In particular, in the scope of pore-scale models the geometry of concave corners and flat surfaces should impose a different effect on adjacent reaction nodes. The envisaged effect here is that the nucleation starts at a concave corner with a higher probability, which would be due to the higher neighboring surface area.

7.5.2 Derivation of the number of nucleation sites for calcite

Since equation 5.16 requires the monomer concentration N_1 and surface tension σ as input, experimentally quantified values for these data are needed. An experiment dealing with surface tension properties of calcite on a quartz substrate was reported by Li and Jun [Li18]. In the experiment, the saturation of calcite was subsequently increased by simultaneously feeding $CaCl_2$ and $NaHCO_3$ into the reaction chamber. The calcium concentration was reported to be 4 times higher than the carbonate one. However, unfortunately the authors have not calculated the aqueous monomer concentrations N_1 nor the number of nucleation sites N_0 on the quartz substrate.

To fill this gap, in this work, a similar setup was modeled with PhreeqC to obtain the resulting monomer concentrations. PhreeqC provides the concentrations of aqueous species including $CaCO_3$(aq), which corresponds to the monomer concentration. The resulting dependency of the monomer concentration on the saturation index is plotted in figure 7.16.

As already expected, the monomer concentration increases exponentially with increas-

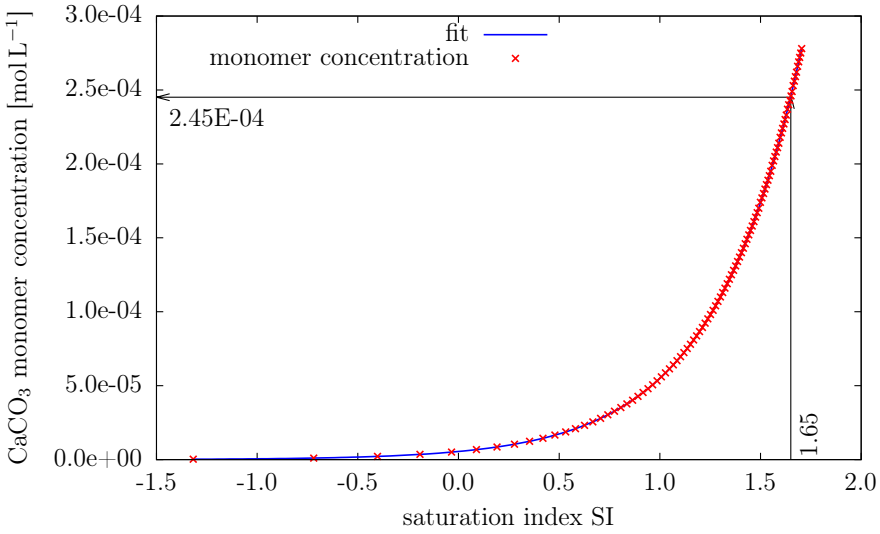

Figure 7.16: Calculated $CaCO_3$(aq) monomer concentration as function of the saturation index of calcite using PhreeqC corresponding to the experiments of Li and Jun [Li18].

ing supersaturation. For further evaluation, the monomer concentration C_m were fitted to an empirical equation in the form of:

$$c_m(SI) = a\, b^{k\, SI} \tag{7.33}$$

The least square fit of the function to the output data of PhreeqC revealed coefficients of $a = 5.497 \times 10^{-6}$, $b = 4.272$ and $k = 1.586$. These coefficients do not have necessarily any physical meaning, but allow to estimate the monomer concentration, which was present in the experiment of Li and Jun [Li18]. The saturation index reported by experiments was 1.65 [Li18]. Thus, and the resulting monomer concentration determined with PhreeqC is $2.45 \times 10^{-4}\,\mathrm{mol\,L^{-1}}$, which is later used as input for equation 5.16. Additionally, the calculated pH value corresponding to the interpolated SI value was about 7.64, which is in the same order of magnitude reported from the experiments (7.8 - 8.0 [Li18]).

Using equation 5.16 and assuming a surface tension of $47\,\mathrm{mJ\,m^{-2}}$ [Li14] (corresponding to calcite nucleation on quartz), a pre-exponential factor J_0 of $2.06 \times 10^{14}\,\mathrm{m^{-2}\,s^{-1}}$ [Li18] and a diffusion coefficient of $9.30 \times 10^{-9}\,\mathrm{m^2\,s^{-1}}$ [Poo16a,Pri14], the number of nucleation sites for calcite on quartz in the experimental setup given, was determined as $1.331 \times 10^{8}\,\mathrm{m^{-2}}$.

In principle, this value is only valid for nucleation of calcite on a quartz surface with the surface roughness and properties used in the experiment of Li and Jun. However,

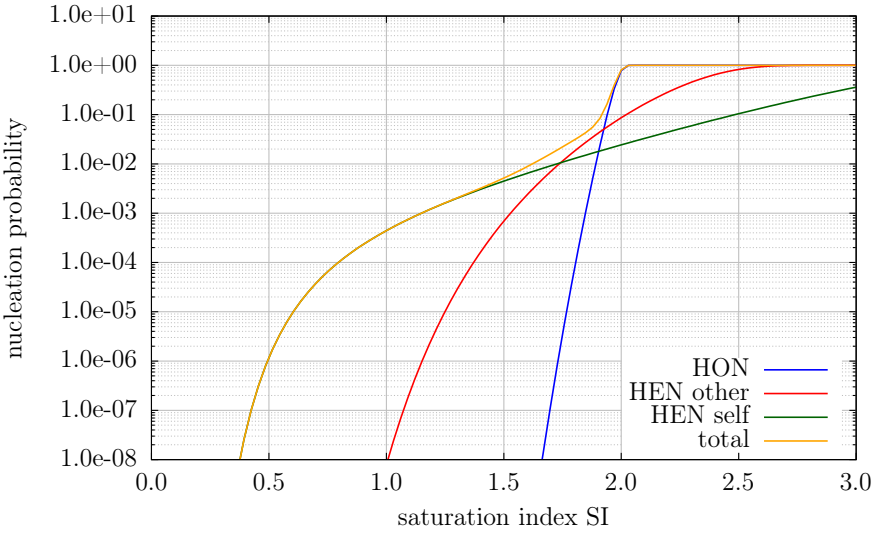

Figure 7.17: Nucleation probabilities as function of saturation index of calcite in a $CaCl_2$-$NaHCO_3$ system. The values were determined assuming a spatial discretization of 3 µm and a temporal discretization of 0.45 ms. Note that the total probability (orange) corresponds to the combined probability according to the union law depicted in equation 5.17.

the surface tension value, which is an input to the derivation shown here, was also used for the determination of nucleation rates on other materials (including inert Teflon) in reactive transport models [Li17]. Moreover, there is a lack of experimental data for all cementitious mineral phases as substrate. Thus, in this work it was assumed that this value is still representative and was subsequently used for the calculation of heterogeneous nucleation rates on all substrate phases.

7.5.3 Nucleation probability at microscopic scale

In order to sketch the nucleation probability of calcite against the supersaturation, the same monomer concentration behavior as for the $CaCl_2$-$NaHCO_3$ system as in section 7.5.2 was assumed. For illustrative purposes, all three single nucleation probabilities (i.e. HON, HENo on another substrate, and HENs on itself) are plotted separately in figure 7.17. For these calculations, a reaction cell size corresponding to the 2D reactive transport simulations to be performed was chosen, i.e. a cell volume of 9 nL and a neighboring cell interface area of 3 µm^2. Neighboring volume fractions of other substrates were set to 1 %, while the content of calcite was assumed to be 3×10^{-3} %. These low fractions were chosen for illustrative reasons. The surface tensions used were 98 mJ m^{-2}, 47 mJ m^{-2} and 20 mJ m^{-2} for HON, HENo and HENs, respectively.

The nucleation probability of calcite on a calcite substrate is by far the most significant one at a saturation index lower than 1.8. Even tiny amounts of calcite in the neighboring cells are leading to a huge nucleation rate, compared to HENo or HON. Although not visible due to the scale in the plot, even the HON nucleation probability at SI = 1.5 is tiny at 1×10^{-14}. Thus, statistically this needs 100 trillion iterations of 0.45 ms in a time marching simulation as the Lattice-Boltzmann method to form one single nucleating reaction cell via HON. On the other hand, even the tiniest solid impurity would cause a nucleation event rather quickly via HEN.

7.5.4 Example of calcite nucleation in a counter diffusion setup

As a test of the implementation of the nucleation algorithm, a 2D simulation of calcite precipitation due to counter diffusion of solutes was used. This modeled 2D system has a size of 3 µm in both dimensions with a resolution of 30 nm. According to the spatial discretization and the selected diffusion coefficient of $1 \times 10^{-9}\,\mathrm{m^2\,s^{-1}}$, each iteration is worth a time step of 30 ns. Constant boundary conditions of Na_2CO_3 and $CaCl_2$ solutions were applied on the left and right boundaries, respectively, while the top and bottom boundaries were periodic. Each side of the system contained initially the solution corresponding to their respective boundary. Two different setups with solution concentrations of 4 mmol and 6 mmol were simulated to address different supersaturations. Theoretically, the mixtures of the initial solutions have saturation indices of 2.54 and 2.76 for the low and high concentration cases, respectively. However, this is not achieved because the solutes are separated initially.

The simulation addressing the higher supersaturation, i.e. with higher solute concentration boundaries, was run for 10 million iterations yielding a physical time of 300 ms. The resulting distribution of precipitated calcite is presented in figure 7.18 (right). A calcite concentration of $26.8\,\mathrm{mol\,L^{-1}}$ corresponds to a completely filled reaction cell which is depicted in red color. For comparison, figure 7.18 (left) shows the resulting calcite distribution of the lower concentration case, which achieves a lower supersaturation. To account for the lower precipitation rate, the simulation was run for a longer physical time (540 ms) to precipitate the same total amount of calcite.

The nuclei are formed initially via HON. Almost all initial nuclei are formed within the first iterations because the highest supersaturation is achieved on initial contact of both diffusing solutes. Due to diffusion, the mixing process is not instantaneous and only $SI_{low} = 2.1$ and $SI_{high} = 2.3$ are reached within the first 100 iterations at the center line between both domains. After the first events of HON and subsequent onset of HEN, the supersaturation decreases quite fast, because the formation of calcite imposes a concentration sink for Ca^{2+} and $CO_3{}^{2-}$ within the system.

At higher supersaturation, a higher number of new nuclei are created although the precipitated calcite crystals are smaller compared to the case with lower supersaturation. This is in agreement with empirical experiences during precipitation of crystals out of supersaturated solutions [Mer89].

Although the factor in concentration difference is only 1.5, the simulation time required to precipitate the same amount of calcite was longer by a factor of 1.8 for the

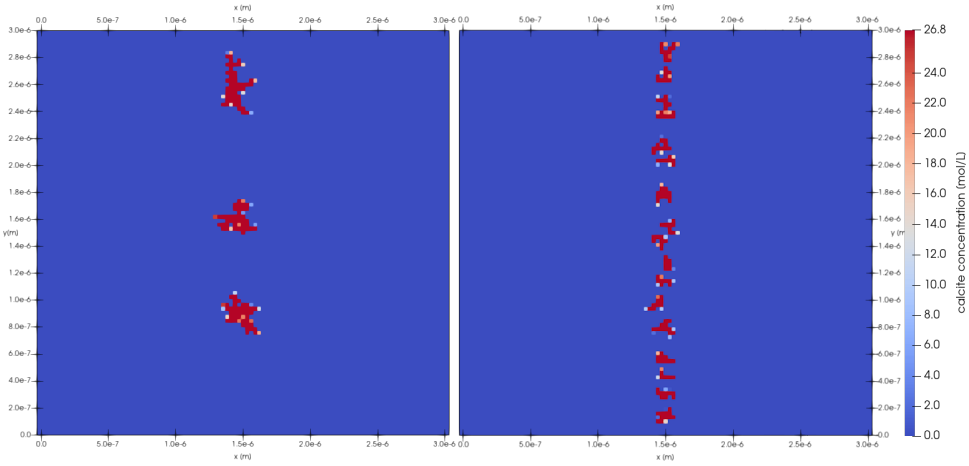

Figure 7.18: Simulated calcite distributions originating from precipitation at low (left, SI = 2.54) and high (right, SI = 2.76) super saturation using CNT. The results are tuned to show a similar amount of total precipitated material. Thus, the plot on the left is obtained after 540 ms while the plot on the right is already achieved after 300 ms (cf. text for further explanations).

lower concentrated simulation. Although in a simplified view, the concentration gradient should differ by a factor 1.5, too, there is another effect present. In both cases the initially precipitated nuclei act as a point sink. However, in the higher supersaturation case more nuclei emerge rather quickly than in the lower supersaturation case. Essentially, many vertically aligned points merge towards a vertical rim in the high supersaturation case rather quickly. Thus, the concentration gradient is more pronounced in the x-direction for the high supersaturation case. On the other hand, the y-component in the gradient effectively reduces the concentrations between the nuclei and therefore reduces the nucleation rate, preventing precipitation of calcite in between. Effectively, the resulting concentration gradient is lower than the factor of 1.5 in the low supersaturation case and therefore the flux and precipitation rate are lower, too.

The simulation for the solutions with lower supersaturation was run further to 70 million iterations. The distribution of calcite at selected time steps is shown in figure 7.19. At a time of approximately 2 s the system is clogged by a vertical barrier. Interestingly, the barrier is not a flat layer which would emerge if a pure equilibrium or kinetic precipitation model is employed. Thus, for capturing surface roughness and layer thickness, the incorporation of nucleation theory in a simulation is a powerful tool to explain such experimental observations. However, it is important to notice that the simulation presented here is a 2D simulation. Thus, the reaction cell size in z-axis is assumed as 1 m. This has implications on the probability function of the nucleation events. In order to retrieve more physically meaningful values, e.g. to measure the resulting barrier thickness or crystal size, 3D simulations have to be conducted.

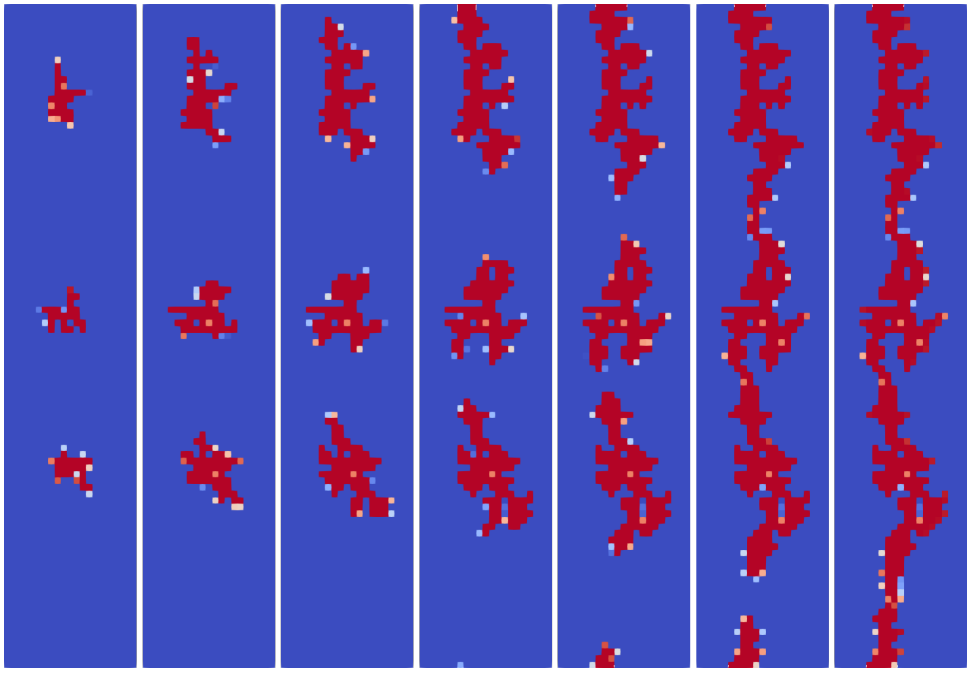

Figure 7.19: Calcite concentrations obtained in a simulated counter diffusion experiment after different times. From left to right: 300, 600, 900, 1200 1500, 1800 and 2100 ms. Clogging happens at approximately 2 s.

7.6 Derivation of parameters for PCS

7.6.1 Estimating pore radii in CSH

Microscopically, the CSH phase is described in the modeling approaches in this work as a porous medium. However, the nano-scale pore structure is of importance if the PCS approach is to be applied. In this section it is assumed that the pore network within CSH consists of cylindrical shaped pores.

With help of knowledge about the specific surface area of CSH and an assumption about the pore geometry, pore radii of CSH can be derived. However, reported values of the specific surface area of CSH and hardened cement paste are in a broad range (e.g. [Jen00,Tho99,Mik66]). Obviously, the total surface area of the paste mixture is a combination of all constituents. The major contribution, however, is originating from CSH, due to the typical high volume fraction of CSH in hardened cement pastes and high specific surface area [Mik64]. A selection of data on the specific surface area of young and mature CSH is given in tables 7.12, 7.13 and 7.14.

A distinct variation can be observed due to differences in drying procedures and experimental methods used. The determined surface areas seem to increase when performing

Table 7.12: Specific surface area [$m^2\,g^{-1}$] data of young CSH and hardened cement pastes [Jen00].

Technique	12h	24h	conditions and comments
SAXS	620	800	wet cement paste
NMR	700	1000	sealed cement paste
SANS	390	280	wet C_3S paste
sorption N_2		200	careful dry, C_3S paste
		100	D-dried
		55	oven dry
sorption H_2O	500	450	

the drying more carefully, in the case of BET sorption experiments. Water vapor BET measurements lead to higher values than BET using N_2 as sorption agent, while NMR, SANS and SAXS methods reveal even higher specific surface areas. The surface area of hardened cement pastes measured by water vapor BET is almost independently of the w/c ratio and approximately $200\,m^2\,g^{-1}$. However, the nitrogen accessible porosity has a surface area which depends on the w/c ratio and is always lower than the one derived by water vapor BET (cf. table 7.14) [Mik64,Tho99]. The interpretation of this effect is that nitrogen is excluded from certain parts of the pore structure which, however, is accessible for water vapor [Mik64] and detectable by NMR, SANS and SAXS techniques. Interestingly, the values derived by N_2 sorption on carefully dried young C_3S paste samples (see table 7.12) and mature pastes (see table 7.13 [Jen00,Lit76]) are about $200\,m^2\,g^{-1}$. Carefully drying the specimens to prevent a collapse of the CSH pore structure has apparently a significant impact on the determined surface areas.

Since the nitrogen accessible porosity of intact CSH is used as basis for the transport model (see section 7.4.4), these values have the highest importance to this work, thus, a value of $200\,m^2\,g^{-1}$ for intact CSH is assumed here. Furthermore, in order to estimate the pore radius of CSH, it is assumed that all pores are cylindrical. To derive average corresponding cylinder radii, all cylinders are assumed to have the same radius and the surface of the ending caps is neglected. With these assumptions, it is possible to determine the radius and a fictitious length of all cylindrical pores per unit volume of CSH. As first step to determine the pore radii, the mass specific surface area A_s is converted to a volume normalized value A_v:

$$A_v = \frac{A_s M}{V_m} = 9.71 \times 10^7\,m^2\,m^{-3} \tag{7.34}$$

Since the surface values determined in the experiments are corresponding to undegraded samples, here also the values for unleached CSH were used in terms of molar volume V_m and molar mass M, which correspond to CSH-1.6 ($M = 191\,g\,mol^{-1}$, $V_m = 78\,cm^3\,mol^{-1}$).

Eliminating the cylinder length from the volume and the outer surface area equations

Table 7.13: Specific surface area (SSA) $[m^2\,g^{-1}]$ of mature CSH and hardened cement pastes. If not stated otherwise, data are from compilations in [Jen00].

Technique	SSA	conditions and comments
SAXS	1000	wet
	425	11 % RH
	320	D-dried
	195	oven dried
	350	
NMR	1000	at 3 days
	700	at 28 days
SANS	230	
sorption N_2	230	very careful dry
	110	solvent exchange
	55	oven dry
sorption isopropanol	60	
sorption H_2O	320	
	200	HCP, vacuum drying [Mik64]

of a cylinder, while neglecting the cylinder cap area gives:

$$r_0 = \frac{2V_0}{A_0} \tag{7.35}$$

The nitrogen accessible porosity of non-degraded CSH is about 17.8 % (see also section 2.3.4.3). Inserting the surface and porosity volume values in equation 7.35 yields a radius of 3.67 nm and a length of $L_{pores} = 4.2 \times 10^{15}$ m. The radius value is in the same order of magnitude as the thickness of the CSH intra-layer of 4.1 nm obtained by NMR measurements [McD10]. Moreover, other analysis of NMR data revealed open gel pore radii in the range of 2.5 nm to 4.0 nm for hardened cement pastes [Hal94], which is in good agreement with the value determined here.

Table 7.14: Specific surface area (SSA) $[m^2\,g^{-1}]$ of mature hardened cement pastes determined by N_2 BET for various w/c ratios. All samples were vacuum dried before BET measurements [Mik64].

w/c	SSA
0.35	56.7
0.40	79.4
0.50	97.3
0.57	132.2
0.70	139.6

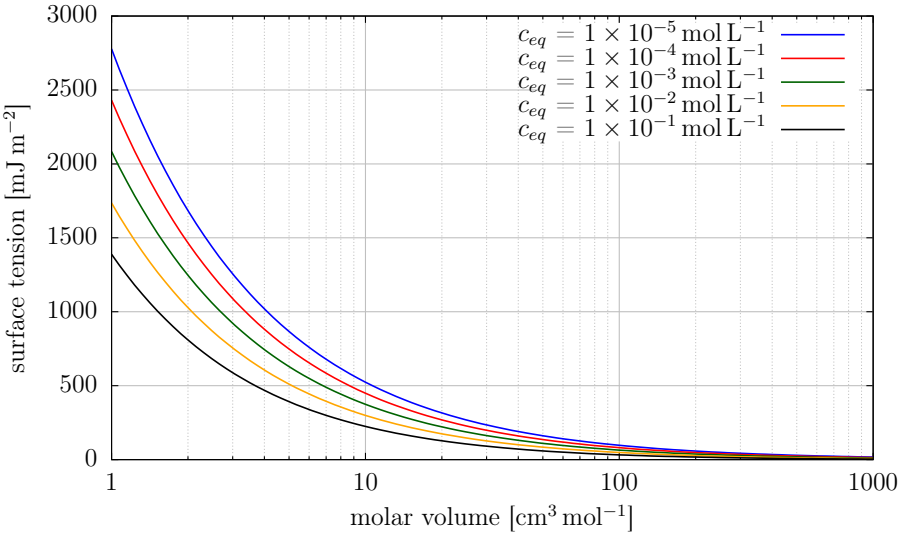

Figure 7.20: Surface tensions for a series of equilibrium concentration in dependency of molar volume calculated by the Stefan-Skapski-Turnbull (SST) equation.

On the other hand, the length is in the order of magnitude of peta meter, which seems like a huge number. Nevertheless, the value corresponds to the sum of the length of all pores in total within 1 m^3 of CSH. Unfortunately, without knowledge about the average pore length there is no possibility to further validate this value for example by comparing to the number of pores in CSH. However, with the help of the sum of the lengths of all pores and using equation 5.32, it is possible to recalculate the pore radius in case the porosity changes:

$$r(\phi) = \sqrt{\frac{\phi}{\pi L_{pores}}} \tag{7.36}$$

7.6.2 Surface tension values input for PCS calculations

In order to apply equation 5.24, in addition to the molar volumes of each solid phase corresponding values of surface tension are needed. The surface tension data available for phases relevant for cement paste is quite scarce [Liu17]. Surface tensions of tobermorite and portlandite of about 386 mJ m^{-2} and 1180 mJ m^{-2}, respectively, were reported [Bru59]. Both values are quite high compared to other values reported, e.g. for portlandite (66 mJ m^{-2} [Las98, p.499]), calcite (98 mJ m^{-2}, see also section 7.5.1), hydrotalcite (26 mJ m^{-2} [Li94]), or barite (135 mJ m^{-2} [Nie71]).

The same observation led other researchers to reject the high value for portlandite [Liu17] and used a lower value of 66 mJ m^{-2} [Las98, p.499] instead. However, Liu and Jacques [Liu17] still accepted the high tobermorite value as surface tension for CSH. As

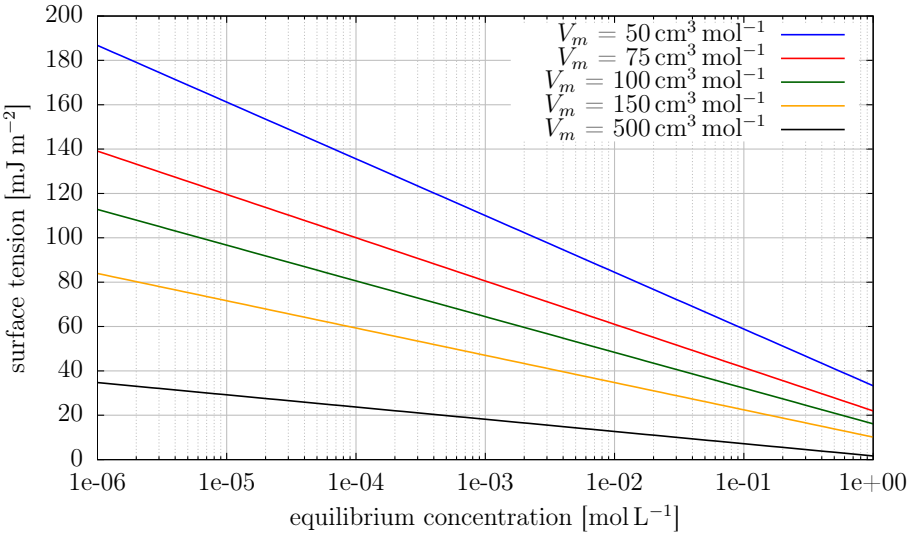

Figure 7.21: Surface tensions calculated by the Stefan-Skapski-Turnbull equation for a series of molar volumes in dependency of equilibrium concentration.

an example, following the PCS approach and applying the high value for CSH leads to high possible supersaturation ratios of about 10 at a porosity of 0.25, i.e. applying such a high surface tension will artificially dissolve CSH in a reactive transport simulation even for moderately confined pore spaces. Moreover, the terms *surface tension*, *interfacial tension* or *surface energy* are ambiguous and values obtained by contact angle measurements have a different meaning than those derived by nucleation kinetics [Pri14]. The length scale relevant for the PCS approach is more similar to the scale of nucleation, i.e. both processes are microscopic effects, while contact angle measurements are macroscopic observations. Thus, since the resulting supersaturations are not reasonable, the higher values were also rejected in this work. In order to fill the gap of needed data for application of the PCS approach, the Stefan-Skapski-Turnbull (SST) equation (7.37) [Kas03] was applied to approximate the missing surface tensions.

$$\sigma = \frac{\beta k_b T}{(V_m/N_A)^{\frac{2}{3}}} \ln \frac{1}{V_m c_{eq}} \tag{7.37}$$

Within the SST equation, the molar volume V_m comes to act in an exponential factor and within an inverse logarithmic form, while the aqueous equilibrium concentration c_{eq} of the phase is only present in the logarithmic term. Additionally, surface tension depends on the Boltzmann constant k_b, Avogadro constant N_A, the absolute temperature T and a constant geometrical fitting factor β. β is intended to incorporate the geometrical shape of the nucleation clusters of the respective solid. The term clusters

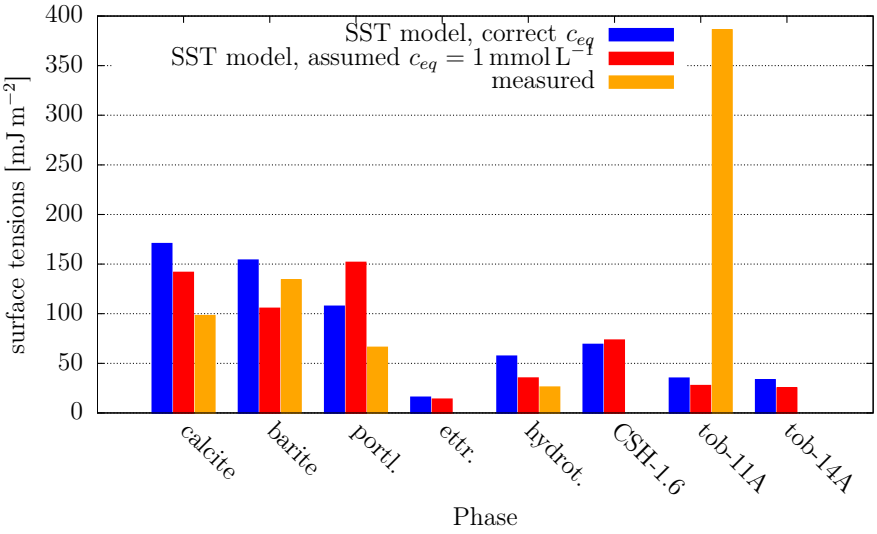

Figure 7.22: Comparison of calculated and experimentally determined surface tensions. While experimental data were available in literature for calcite [Söh82a], barite [Nie71], portlandite [Las98, p.499] and tobermorite-11A [Bru59], for ettringite, CSH and tobermorite-14A no experimental data were available.

refer in this context to nucleation clusters, since this equation is originating from the domain of nucleation theory. While for cubic clusters a value of 0.414 was determined for β, it has to be corrected for spherical clusters to 0.514 [Kas03].

Results from different combinations of V_m and solubility are plotted in figure 7.20 and 7.21. It is important to note that, although according to the SST equation there is a direct effect caused by both, the molar volume V_m of the phase and the corresponding equilibrium solubility, to the surface tension, the result is more sensitive to variances in molar volumes than to solubilities (compare figures 7.21 and 7.20). This effect of insensitivity is more pronounced for phases with higher molar volumes (see bottom curve in figure 7.21). Unfortunately, since the equilibrium solubility of a solid phase depends on the whole solution chemistry, i.e. the presence of other solutes or concurrent reactions, there is no unique estimation possible for the solubility value, which can be fed into the SST equation. Thus, an assumption was made here to define the solubility for each phase as 1 mmol L^{-1} as input for the SST equation.

To test this assumption, figure 7.22 plots the surface tension of various phases from different origins: measured, estimated with correct, and fixed solubility (1 mmol L^{-1}). Generally, the SST model predicts surface tensions within the right order of magnitude. Although the equilibrium concentration of 1 mmol L^{-1} is just a rough estimation for most of the phases, using this solubility is still in the right order of magnitude to the measured values. As already mentioned, the measured surface tension value for tobermorite-11A

Table 7.15: Surface tension values [$\mathrm{mJ\,m^{-2}}$] for different phases used in reactive transport simulations incorporating the PCS model. Values are determined by the Stefan-Skapski-Turnbull (SST) approximation and compared to measured data.

Phase	SST	measured
Brucite	189	
C3AH6	47	
C4AH13	29	
CSH0.8	97	
CSH1.2	83	
CSH1.6	73	
Calcite	142	98 [Söh82a]
Ettringite	14	
Friedel-salt	29	
Gypsum	81	
Hemicarboaluminate	28	
Hydrotalcite	35	26 [Li94]
Hydrotalcite-CO3	33	
Monocarboaluminate	30	
Monosulfoaluminate	27	
Portlandite	152	66 [Las98, p.499]
Stratlingite	35	
Thernardite	105	

seems to be off by an order of magnitude and most likely due to an unsuitable measurement technique. Moreover, it is remarkable how close the values for ettringite are, which results from the high molar volume. Thus, for all PCS model based simulations, the Stefan-Skapski-Turnbull equation with fixed solubility at $1\,\mathrm{mmol\,L^{-1}}$ was used to fill the gap of unknown surface tensions values. The measured surface tension values and those estimated by SST are listed in table 7.15.

8 Application cases

In the following sections several application cases of iPP are presented. The implementation of the reactive transport code iPP are applied to simulate the transient behavior of leaching and degradation of different cementitious materials, e.g. OPC and low-pH HCP. Different microstructures generated by different methods, i.e. obtained by numerical modeling or μ-XCT image data, are used as input for the simulations. The simulations consider different thermodynamic models and physical effects relevant in confined pores, thus comprise different complexities. For example, these simulations deal with different thermodynamic descriptions of CSH (cf. section 7.1.1) and diffusivity models (cf. section 7.4). Furthermore, a pure equilibrium assumption is compared to models taking into account nucleation theory and/or porosity-controlled solubility effects (cf. sections 5, 7.5 and 7.6). Moreover, the resulting effect of these modeling parameters on the effective diffusivity of the system is analyzed.

8.1 Degradation of hardened OPC paste

8.1.1 Overview, model setup and computation

The purpose of this chapter is to show how numerically generated microstructural data can be used to simulate degradation processes in HCP and how to determine the effective diffusion coefficients of the pristine and degraded material. The setup is intended to simulate leaching and decalcification of hardened OPC paste with deionized water. As basis, a microstructure numerically generated with CEMHYD3D from Patel et al. [Pat18b] was used. The microstructure and the composition of the CSH phase is described in section 7.2.1. The cubic 3D geometry is $66\,\mu m \times 66\,\mu m \times 66\,\mu m$ in size (cf. figure 7.2).

In this simulation, a simplified chemical model was used, i.e. the mineralogical model was reduced to contain only CSH and portlandite. In this setup, all other hydration products were assumed to be CSH. In this way, the chemical system was reduced to contain only calcium, silicon and water (H and O). All phases except of CSH are assumed as non-diffusive. Unhydrated clinker does not react further in this model and is assumed as inert and non-diffusive. In order to model the CSH diffusivity the same Archie's law approach as in the original publication [Pat18b] was implemented in iPP (cf. section 7.4.2).

Patel et al. [Pat18b] used look-up tables for the chemical equilibrium calculations, i.e. no calculations with a chemical solver such as PhreeqC were involved during the reactive transport simulation. The benefit was not only in enhanced computational performance

but also to work around several convergence issues encountered during the PhreeqC calculation. The quaternary ideal solid solution model CSHQ [Kul11,Lot19] (cf. section 7.1) was the basis for pre-calculating the equilibrium look-up table in the work of Patel et al. [Pat18b].

In contrast, in this work no look-up tables were used, but the geochemical system was solved explicitly using PhreeqcRM, i.e. full reactive transport calculations were attempted. To avoid problems with the numerical stability, the discretized solid solution models of CSH-II and CSHQ were used (cf. section 7.1.2). The thermodynamic database used here is the PhreeqC formatted database derived from CEMDATA07 [Jac12] applied also in [Pat18b]. However, CEMDATA07 contains only the end-members of the CSH-II solid solution, thus it was extended by the CSHQ solid solution [Pat18b]. Accordingly, here the CEMDATA07 database was extended with the discrete solid solution models of CSH-II and CSHQ (cf. section 7.1.2). In order to define the initial CSH composition, the respective remarks about additional portlandite content as described in section 7.1.2 were taken into consideration. Therefore, to express a CSH with high calcium content, for example CSH-1.62, this implies that a certain amount of portlandite has to be placed additionally in companion to the CSH content in the same reaction cell.

A deionized water boundary condition was applied to one side of the cube (x = 0 µm), while the opposite boundary was set as closed boundary (x = 67 µm), i.e. zero flux. Since the CEMHYD3D microstructure represents a self-repeating geometry, the boundaries in the other two dimensions are assumed as periodic (cf. section 3.5.10.2). Since the simulation only comprised dissolution of cement hydrates due to leaching by deionized water, there are no clogging effects expected. Therefore, similar as in the original publication [Pat18b], none of the more sophisticated approaches developed in this work to control precipitation processes, such as nucleation theory and/or porosity controlled solubility, were applied.

In order to analyze the effects of the different solid solution models, both discretized models of CSH-II and CSHQ were used in distinct simulations. The simulations were carried out on the JURECA cluster of the Jülich Supercomputing Center (JSC) [Kra18]. For the simulation of the models 8 compute nodes were used, corresponding to 192 CPU cores and 384 threads, respectively. One iteration took about 240 ms for solute transport, chemical equilibration and data synchronization. The average time for solute transport alone was just about 3.3 ms, which corresponds to only 1.4 % of the total time. The rest of the time is spent either within PhreeqcRM calculations or accounting to preparations mandatory for the reactive steps. The latter comprised for example updating of solute concentrations within PhreeqcRM, collective operations for preparation for the heterogeneous source terms and updating of diffusivity properties in the transport code. To obtain the reactive transport results, up to 840000 iterations, corresponding to 56 s simulated time, were carried out for the CSH-II model. Thus, an equivalent of more than 10000 CPU hours were spent on JURECA in the case of the CSH-II model. Additional time was spent for the CSHQ based simulation, however, less than for the CSH-II based simulation as only the comparison of solid solution models were of interest. More information of the model setup are given in table 8.1.

Table 8.1: Essential information about the modeling setup of the leaching simulation of the CEMHYD3D generated HCP microstructure. The degrees of freedom correspond to the product of the number of nodes, transported solutes and treated solid phases.

property	value
LBM scheme	P-TRT
lattice stencil	D3Q7
LBM nodes	$66 \times 66 \times 66 = 287496$
D_{ref}	$5 \times 10^{-10}\,\mathrm{m^2\,s^{-1}}$
ϕ_{min}	0.2
ϕ_{ref}	1.0
Δx	$1\,\mu\mathrm{m}$
Δt	$66.67\,\mu\mathrm{s}$
number of transported solutes	5 + charge
thermodynamic database	CEMDATA07 + discrete CSH-II / CSHQ
CSH model	11 discrete phases emulating CSH-II / CSHQ
degrees of freedom	20699712

8.1.2 Results and analyses

The simulations addressed the leaching of hardened OPC with pure water. Consequently, during the simulation the phases close to the water interface dissolved first. In particular, portlandite dissolved while buffering the calcium concentration and pH in the solution. When the portlandite has been dissolved completely close to the interface the CSH is decalcified. In this subsection the degree and depth of degradation is analyzed. In this context, the heterogeneity of the resulting degradation depth is assessed. Furthermore, the results obtained in this work are compared to the results from the original publication [Pat18b]. Moreover, the resulting effect on the effective diffusion coefficients after degradation are determined.

Most of the 2D plots in this section show either averaged values or statistical information per slice in the YZ-plane and are plotted perpendicular to the leaching interface. Therefore, the interface in contact with pure water is located on the x-axis at $0\,\mu\mathrm{m}$. Focus is made on the residual portlandite content and the distribution of the CSH phase stable with the highest C/S ratio when using this discrete solid solution model, i.e. CSH-1.58 (cf. section 7.1.2). As long as portlandite buffers the calcium concentration in the solution, the CSH does not degrade. Moreover, time dependent properties are shown as degradation depth and resulting diffusion coefficients as function of leaching time.

8.1.2.1 Effect of CSH model on the simulation results

To evaluate the effect of the different CSH thermodynamic solid solution models on the leaching depth, the average portlandite concentration after 10 s leaching time is plotted

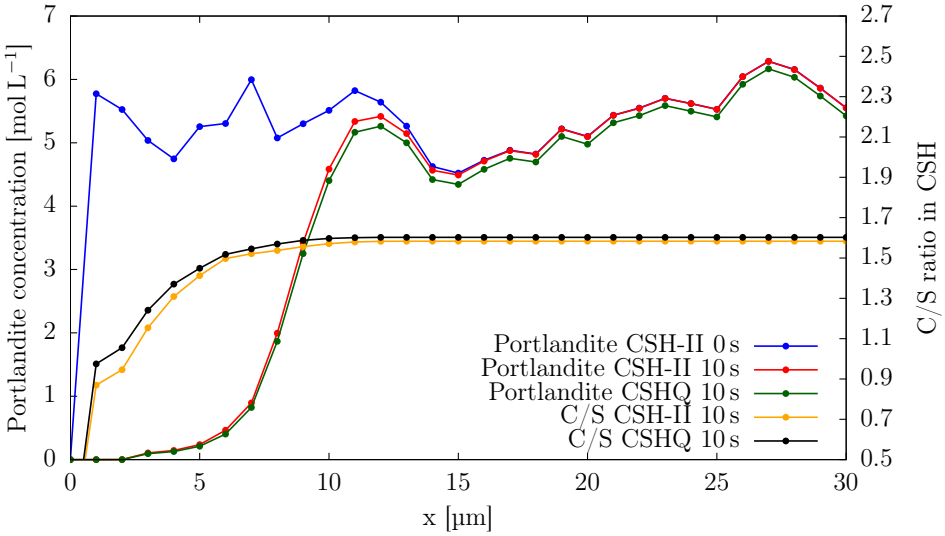

Figure 8.1: Average portlandite concentrations in the initial (blue) and leached OPC paste perpendicular to the leaching surface using the discretized CSH-II (red) and CSHQ (green) solid solution models after 10 s simulated with iPP. Only the first 30 µm of the 66 µm monolith size are shown for illustrative purposes. Notice that the slight difference in the portlandite concentration and C/S ratio in the intact zone on (x > 20) is due to the differences in the CSH solid solution models (see section 7.1.2). The lines serve as guidance to the eye.

in figure 8.1 for both CSH models. Up to the first 10 µm from the interface, the material has been degraded with respect to portlandite. In comparison, the CSH-II and CSHQ results are virtually identical except for a small offset, originating from the additional amount of portlandite present in CSH-II compared to CSHQ in order to render the same initial calcium content in the CSH (see section 7.1.2). However, it is remarkable that the results are very close, despite the equilibrium calcium concentrations in solution of the CSH-II model are higher compared to the CSHQ model (cf. figure 7.1). A higher equilibrium concentration suggests a higher diffusive gradient and thus an accelerated calcium leaching rate. However, this effect seems not to cause a significant change in the transient behavior of the portlandite concentrations in the short time scales analyzed in this simulation.

Moreover, the resulting C/S ratio of the CSH after leaching is plotted as function of depth using the different CSH solid solution models (orange and black, respectively). Interestingly, the application of the CSH-II model leads to a slightly higher decalcification of the CSH phase close to the interface than using the CSHQ model. This is in line with the statements above, since a higher calcium concentration gradient leads to a higher diffusion rate and thus decalcification rate.

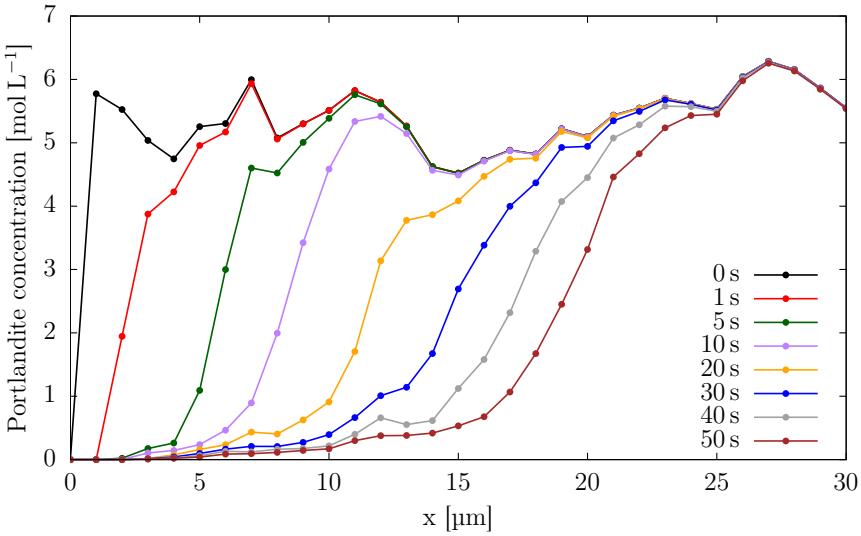

Figure 8.2: Average portlandite concentrations in the leached OPC paste perpendicular to the surface for selected steps in time simulated with iPP using a discretized solid solution model (CSH-II). The lines serve as guidance to the eye.

8.1.2.2 Transient leaching depth

The simulation using the CSH-II model was carried out further until 56 s of physical leaching time. The resulting portlandite profiles for selected time steps up to 50 s and up to the initial 30 µm from at the interface are shown in figure 8.2. The portlandite has experienced some alteration within the first 25 µm after 50 s leaching time, but was completely leached only within the first 1 µm. The C/S ratio of the CSH, however, is only affected within the first 10 µm to 25 µm (not shown here), since the portlandite buffers the calcium concentration at a high level effectively stabilizing the high C/S CSH. Comparing the leaching depths of adjacent time steps with the same duration, e.g. 0 to 10 or 10 to 20 seconds, it is apparent that the progress of the degradation depth decreases with time. This behavior is originating from the fact that the distance to the interface is increasing and thus the concentration gradient consequently decreases. Several authors have shown that leaching by pure water shows a leaching kinetics which is proportional to the square root of time passed for a diffusive scenario (e.g. [Mor04]). A similar transient behavior is observed in the simulation results presented here.

Figure 8.3 shows the resulting distribution of CSH-1.58 (left), which is the discrete CSH phase with the highest C/S ratio in this setup, and portlandite (right) for the initial conditions (top) and after 56 s leaching (bottom). The phase concentrations are depicted in blue to red for low and high values, respectively. To emphasize the leaching depth, the volume rendering images are superimposed by the maximum degradation depth of the

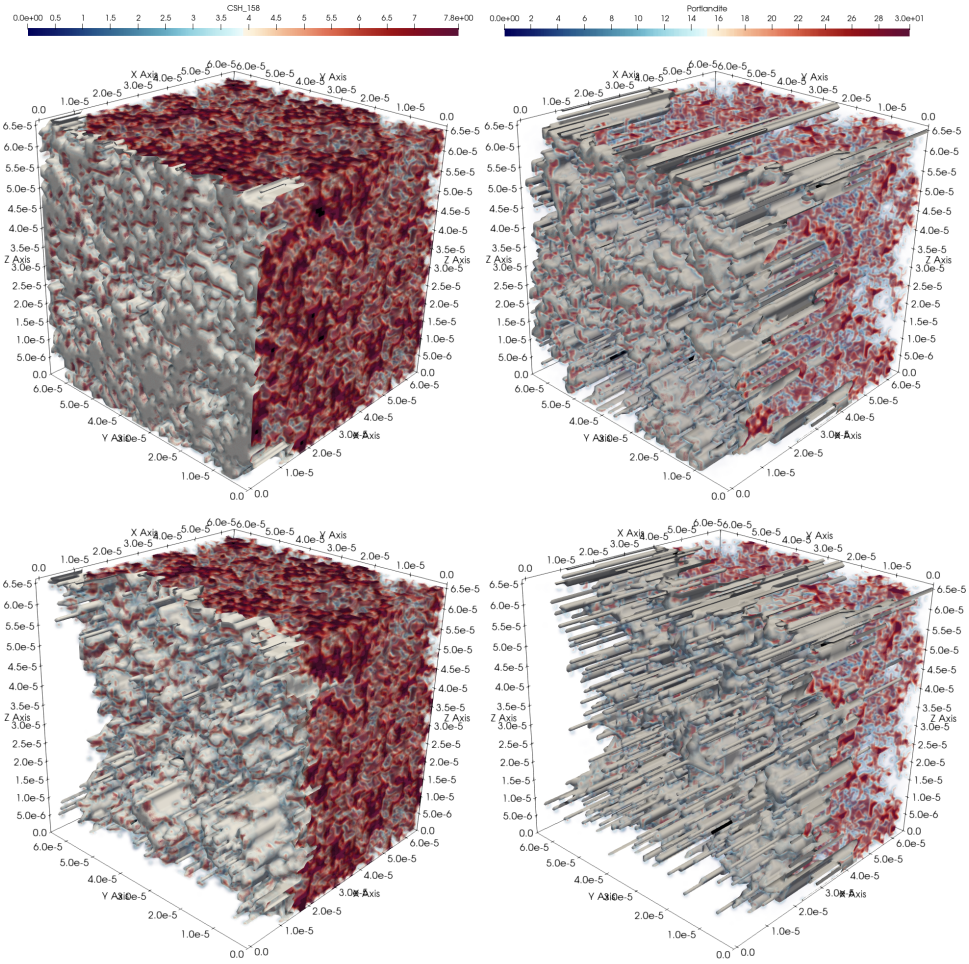

Figure 8.3: Simulated CSH-1.58 (left) and portlandite (right) concentrations of the initial time step (top) and after 56 s leaching (bottom). The volume rendering images are superimposed with an iso-surface depicting the corresponding leaching depth.

respective phase as gray colored surfaces. The surfaces are produced by using a threshold value of $7.79\,\mathrm{mol\,L^{-1}}$ and $0.5\,\mathrm{mol\,L^{-1}}$ for CSH-1.58 and portlandite, respectively. Since the initial concentration of the CSH-1.58 is approximately $7.8\,\mathrm{mol\,L^{-1}}$, the value for the CSH surface corresponds to voxels that just started to be degraded. On the other hand, the value corresponding to the portlandite surface indicates an almost complete degradation of the voxel. A threshold value of zero for portlandite could not be applied, since the CSH solid solution model uses portlandite in conjunction to CSH to express CSH phases with a high C/S ratio such as CSH-1.62 (cf. section 7.1.2).

Initially the CSH is completely intact in the whole monolith (top left), while the material degrades during leaching, the CSH-1.58 is replaced by a CSH with a lower C/S ratio. Thus, invisible in the image at the bottom left, at the same time the CSH-1.58 surface is moved towards deeper domains with respect to the leaching direction (x-axis). The portlandite distribution (right) is apparently more heterogeneous than the CSH distribution already in the initial state, which is the output of the CEMHYD3D calculation. In particular, the iso-surface shows already tunnels through the complete monolith for the initial condition. Thus, the CSH medium is rather well-connected and percolated. After degradation, the portlandite degradation depth (bottom left) is even more heterogeneous. It turned out that some voxels filled with portlandite are shielded by inert material. Thus, they are either never dissolved if they are completely embedded in inert material, or it takes significantly longer for the leaching water to dissolve the portlandite. A delayed dissolution occurs, for example, when the access to the portlandite voxel is limited to a single surface side, which is facing in the opposite direction than the leaching direction.

In order to analyze the heterogeneity of the resulting microstructure, the minimum, maximum and average degradation depths of CSH-1.58 and portlandite in the monolith as function of leaching time are plotted in figure 8.4. In particular, in the portlandite case, again the broad concentration range distribution is observable, i.e. the minimum (purple) and maximum (green) curves are close to zero and maximum monolith size (66 µm), respectively, during the complete simulation. On the other hand, the maximum degradation depth of the CSH is limited to 23 µm in the beginning and increases to 35 µm after 56 s time of leaching. For both phases the minimum depth remains close to the leaching water interface (orange and purple), because for both phases single voxels are isolated by inert material (see paragraph above). Furthermore, the average leaching depth as function of time for both phases show approximately a square root dependency with respect to time, which is in line with analytical solutions for diffusivity controlled systems. Moreover, the standard deviation of the leaching depth of CSH-1.58 is plotted as gray shaded area around the average depth, which is an indicator for the statistical spread of the leaching depths. Apparently, the standard deviation increases with time, thus the heterogeneity of the average degradation depth increases during the process of leaching. This is in line with visual observation of the leaching depth (see paragraph above).

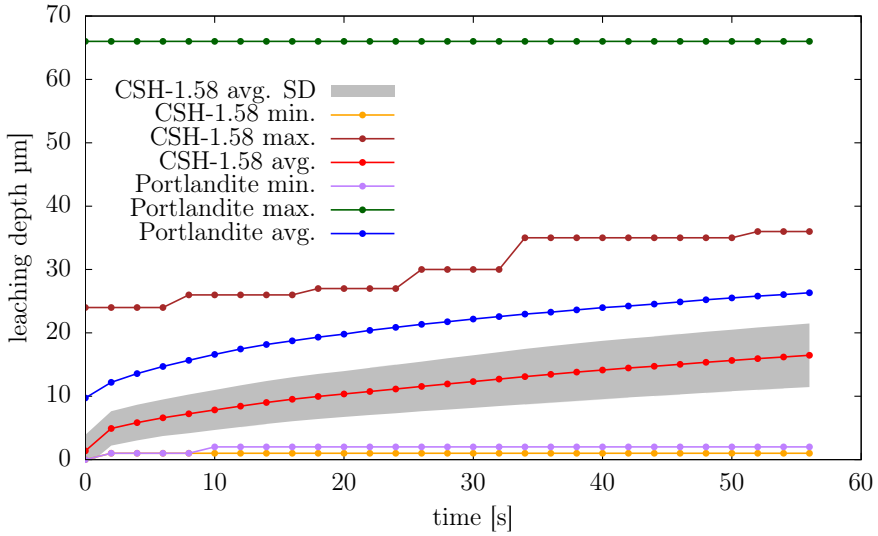

Figure 8.4: Calculated leaching depths of portlandite and CSH-1.58 as function of leaching time. For both phases the average, minimum and maximum leaching depths are given. Additionally, the one σ standard deviation interval for the average leaching depth of CSH-158 is indicated as gray shaded region. The lines serve as guidance to the eye.

8.1.2.3 Comparison to results from Yantra LBM code

The resulting portlandite concentrations of the simulations conducted in this work are compared to the results from the original publication [Pat18b] in figure 8.5. Although the results are in good agreement for early time steps as 1 s, results corresponding to steps later in the simulation performed with iPP show a significantly higher degree of decalcification of the OPC. Essentially, the simulated leaching rate is twice as high although using a comparable chemical model and the same Archie's law type for the diffusive solute transport as Patel et al. [Pat18b].

In order to investigate the origins of this discrepancy, a simplified 1D column setup was prepared. For comparison, simulations by four different reactive transport codes were carried out, i.e. iCP [Nar14], iPP, PhreeqC (using the 1D transport feature) [Par13] and Yantra [Pat18a] and compared to an analytical solution.

This geometrical setup comprises a 1D column filled with water with a length of 10 µm. The spatial discretization chosen was 0.1 µm. The 1D column contains 5 cells filled with CSH on the left-hand side, corresponding to 0.5 µm. In fact, the geometrical setup is identical as previously presented in the benchmark section to test internal boundary conditions (cf. figure 6.15), except that the portlandite is replaced by CSH. The amount of CSH is chosen so that a porosity of 0.3 is achieved, which is comparable to the

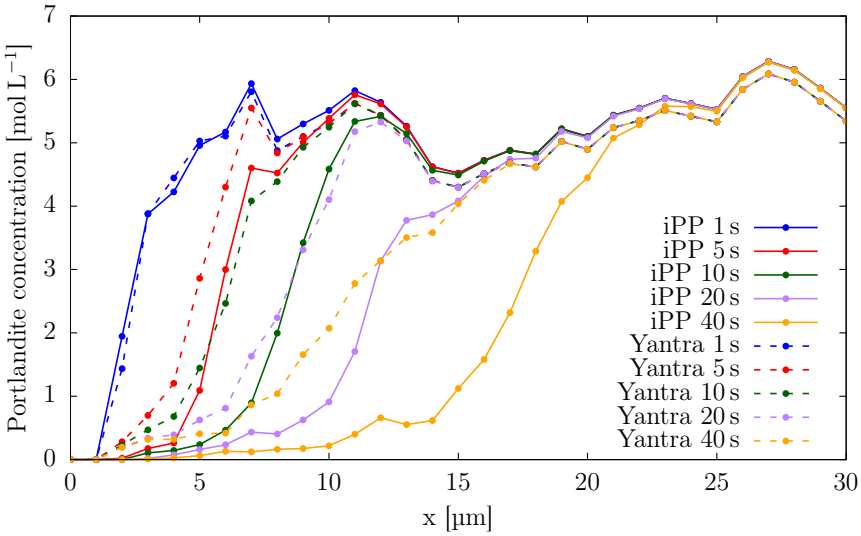

Figure 8.5: Average portlandite concentrations in the leached OPC paste perpendicular to the surface for selected steps in time simulated with iPP using a discretized solid solution model (solid lines) in comparison to results obtained by Yantra using a pre-computed CSHQ solid solution model (dashed lines). The lines serve as guidance to the eye.

porosity of the CEMHYD3D model (0.32). No porosity model is applied, i.e. the CSH is regarded as dry without gel porosity, which corresponds to the setup of the leaching simulations of the 3D geometry. Furthermore, in this setup the CSH equilibrium chemistry is determined with the CSHQ solid solution model. Further details on the setup used for the simulation with iPP are listed in table 8.2.

In order to analyze the effect of the description of the diffusivity of the medium, two different cementation factors in Archie's law were applied, i.e. 2 and 7.23. The latter corresponds to the value used in the 3D leaching simulation. Based on these values and using a water diffusion coefficient of $2.2 \times 10^{-9}\,\mathrm{m^2\,s^{-1}}$ effective diffusion coefficients of $5.94 \times 10^{-11}\,\mathrm{m^2\,s^{-1}}$ and $1.09 \times 10^{-13}\,\mathrm{m^2\,s^{-1}}$ are obtained by applying Archie's law (cf. equation 7.15). The simulations were run for 0.1 ms physical time and the resulting calcium concentration profiles are shown in figure 8.6.

The concentration profile determined by iPP show again the shift of half of a discretization step compared to the analytical solution. The effect was already discussed in the reactive transport benchmark section 6.3.2. However, except of this shift, the results are in excellent agreement with the analytical solution for both simulations, simulating different cementation factors. This is because there is an interface treatment for variances in diffusion coefficients implemented in iPP (cf. section 4.4.1.6).

One has to notice, that the analytical solution shown here slightly overestimates the

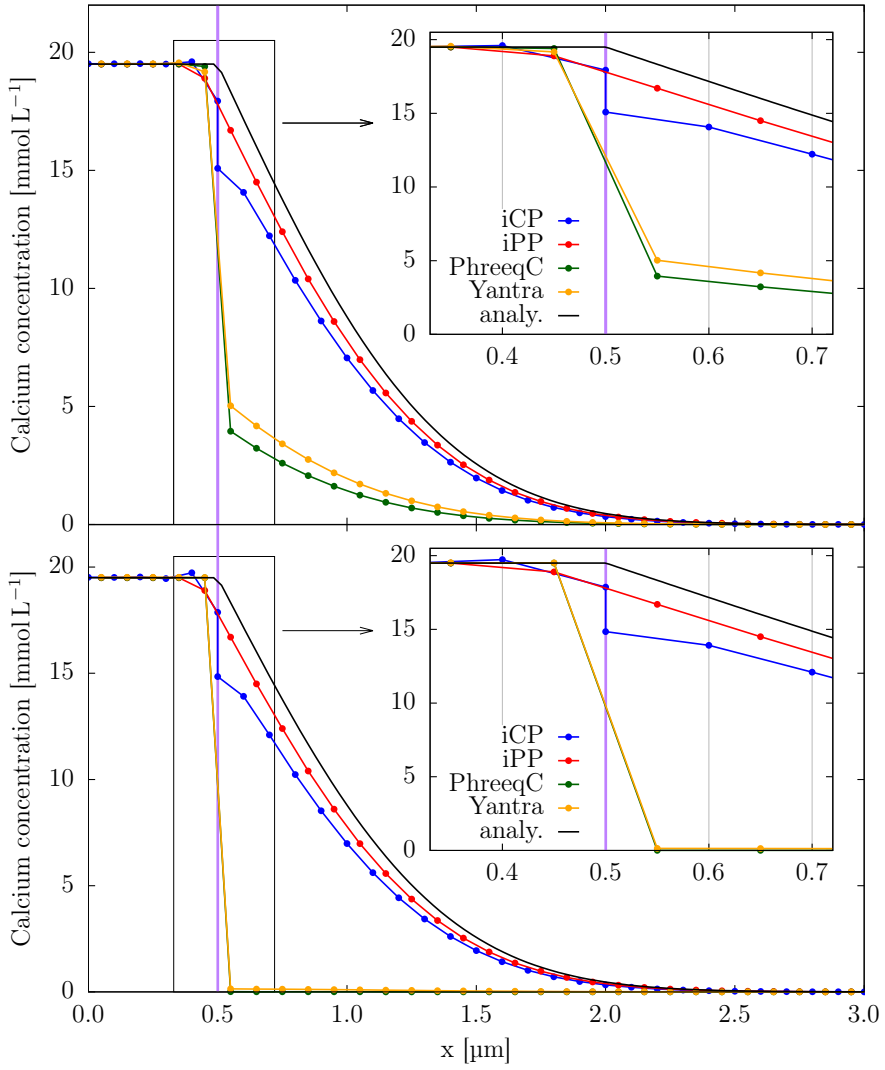

Figure 8.6: Simulated calcium concentration profiles due to CSH dissolving in contact with water after 0.1 ms using iCP, iPP, PhreeqC and Yantra, in comparison to an analytical solution assuming a constant calcium concentration at the CSH/water interface. The assumed cementation factors m in Archie's law used for the CSH phase were 2 (top) and 7.23 (bottom). The water diffusion coefficient assumed was $2.2 \times 10^{-9}\,\mathrm{m^2\,s^{-1}}$. The inserts show the interface domain in more detail with cell boundaries of the LBM codes and PhreeqC indicated as vertical gray lines. The vertical purple line indicates the initial interface between the CSH and water. The lines connecting the points serve as guidance to the eye.

Table 8.2: Essential information about the modeling setup used for the dissolution simulation of CSH. The degrees of freedom correspond to the product of the number of nodes, transported solutes and treated solid phases.

property	value
LBM scheme	P-TRT
lattice stencil	D2Q5
LBM nodes	$100 \times 3 = 300$
D_{ref}	$2.2 \times 10^{-9}\,\mathrm{m^2\,s^{-1}}$
ϕ_{min}	0.264
ϕ_{ref}	1.0
Δx	0.1 µm
Δt	200 µs
number transported solutes	5 + charge
thermodynamic database	CEMDATA07 + CSHQ
CSH model	CSHQ solid solution model
degrees of freedom	9000

concentration profile since the equilibrium calcium concentration of the CSH at the boundary drops slightly during the simulation. This is due to the changes in the solid phase assemblage caused by decalcification of the CSH at the interface, i.e. the C/S ratio drops to 1.61 from the initial 1.62. However, as results from iCP and iPP have shown, the effect on the calcium concentration was less than 3 % for the short run time and limited decalcification of the CSH. Thus, the effect is neglected in the analysis presented here.

The resulting concentration profiles from the iCP calculations underestimate the expected values close to the interface. However, it has to be considered that iCP uses COMSOL, which is a continuum transport code. The abrupt changes in diffusivity can cause oscillations at the interface. Furthermore, the chosen discretization was the same as for the other codes just for comparison purposes. A better spatial resolution at the interface will likely reduce these errors. Moreover, iCP determines results at the cell boundaries instead at the cell center node. This is fundamentally different to the Lattice-Boltzmann approaches used here and the technique how PhreeqC solves the diffusion equation. Still the results of iCP are in the right order of magnitude and insensitive to the high cementation factor of 7.23, i.e. iCP solves both inputs with a comparable quality. This is likely a result of the interface treatment that iCP has implemented. This technique treats domain interface nodes in a special way, such that the chemical reaction term is calculated for both domains and subsequently the concentrations are averaged with an arithmetic mean approach. Moreover, COMSOL treats chemically dependent properties as porosities with a linear interpolation [Nar14]. Apparently this treatment helps to overcome discontinuities in the simulation.

The intrinsic capabilities of the 1D transport feature of PhreeqC are quite limited, e.g.

it is impossible to define a porosity feedback to the transport model out of the box. For this simple test presented here, this was neglected since the porosity change was only minor due to the small changes on the CSH phase at the interface due to decalcification. However, in the PhreeqC input used here, no averaging rule at the interface nodes has been implemented either. It is impossible to control the diffusion coefficient explicitly via the PhreeqC input, rather it is only possible to define a porosity, which is used with an Archie's law approach to determine the pore diffusion coefficient [Par13]. During a test by tweaking the diffusion coefficient at the interface via the porosity, i.e. setting it to one, it was possible to retrieve the results given by iPP with PhreeqC as well.

The results produced with Yantra are apparently more in agreement to the simple PhreeqC results than to the results of the other codes or the analytical solution. The discrepancy of Yantra to the analytical solution and the results of iPP and iCP are even more pronounced than expected. This suggest that there is no interface rule in work. The original publication of Patel et al. claims that version 0.5 of Yantra was used for the simulations [Pat18b]. During a more thorough audit of the Yantra source code [Pat18a], no logic for an interface treatment could be found in the published code, neither within version 0.5 nor more recent ones. Benchmarks of Yantra reported dealing with dissolution of CSH, were carried out with a moderate cementation factor of $m = 1/3$ [Pat16a]. By using a moderate cementation factor it is expected that the discrepancy between results from Yantra and the analytical solution is much smaller. All in all, this suggests that the results of Yantra might be flawed due to this effect.

8.1.2.4 Effective diffusion coefficients of leached HCP

The resulting microstructures of the HPC monolith after different leaching times were reused as microstructural input for calculating steady state effective diffusion coefficients of the leached HPC. According to Fick's first law, at steady state the diffusion coefficient can be calculated as the quotient of the diffusive flux and the concentration gradient in a through-diffusion setup:

$$D_e = \frac{-J}{\nabla c} \tag{8.1}$$

The flux J can be obtained via numerical simulation of the diffusive transport. This is achieved by imposing a concentration gradient to the porous medium, while measuring the diffusive outlet flux by using equation 3.46. For this, a constant concentration (Dirichlet) boundary condition of an inert tracer is imposed. The boundary conditions applied consist of a high concentration boundary (e.g. $1\,\mathrm{mol\,L^{-1}}$) and a low concentration boundary at the opposite side (e.g. $0\,\mathrm{mol\,L^{-1}}$).

The initial concentration profile is initialized by linearly interpolating the concentration gradient along the sample length in order to speed-up convergence of the simulation. Subsequently, during the simulation the diffusive flux is tracked at the outlet. The simulation is run until the outlet flux at the lower concentration boundary converges to steady state. Using equation 8.1 and with help of the outlet flux and the length of the specimen, the effective diffusion coefficient can be calculated.

To determine the effective diffusion coefficient of the leached HPC monolith, the con-

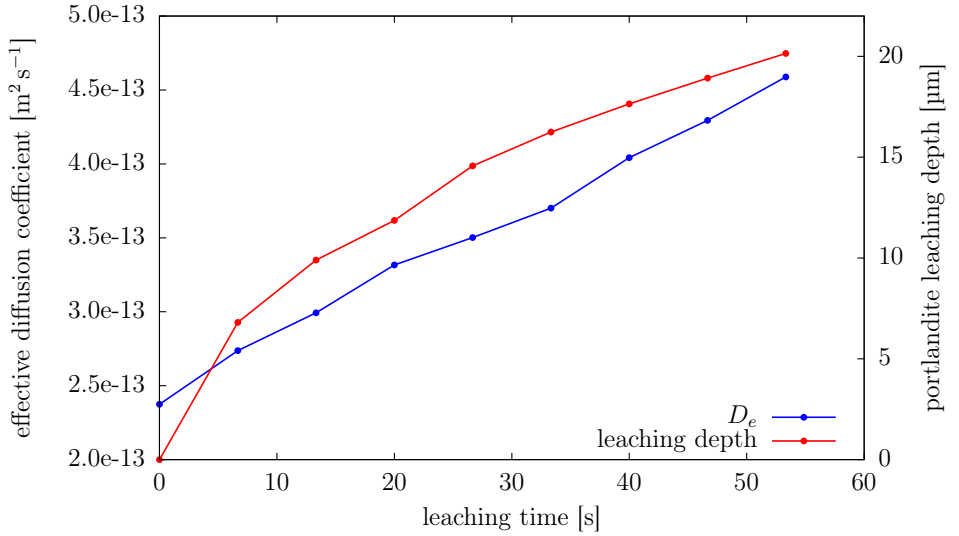

Figure 8.7: Simulated effective diffusion coefficients (blue) and leaching depth (red) of a HCP monolith obtained from OPC after leaching. Notice that the leaching depth corresponds to the right axis. The cubic monolith size was 66 µm and almost a third of the monolith was degraded after 53 s of leaching. The lines connecting the points serve as guidance to the eye.

centration gradient is applied on opposite boundaries, i.e. perpendicular to the x-axis. In this simulation the same diffusivity law for CSH was applied as during the simulation of the leaching process, i.e. an Archie's law approach with an exponential factor of 7.23 (cf. section 7.4.2).

The obtained effective diffusion coefficients for different leaching times in comparison to the degradation depths with respect to portlandite are plotted in figure 8.7. After approximately 53 s of leaching, an increase of the diffusivity of the HPC of almost a factor two can be observed. The degradation depth here is defined as the x-value at which 50 % of the portlandite in that yz-slice has dissolved, e.g. 17.6 µm at 40 s (cf. figure 8.2). The degradation depth reaches 20 µm at after 53 s leaching time. Although the leaching depth follows a square root behavior, the diffusivity of the HPC apparently increases linearly with respect to leaching time.

Further analyses were conducted in order to analyze the apparent discrepancy between the transient behavior of the leaching depth and the effective diffusion coefficient. As first attempt, the initial monolith was split into two domains, corresponding to the resulting leaching depths after a certain leaching time, e.g. 20 µm and 46 µm (complement to the total monolith size of 66 µm), which corresponds to the leaching depth after 53 s leaching time (cf. figure 8.7). For each subdomain the effective diffusion coefficients were determined separately using the same numerical modeling approach as described

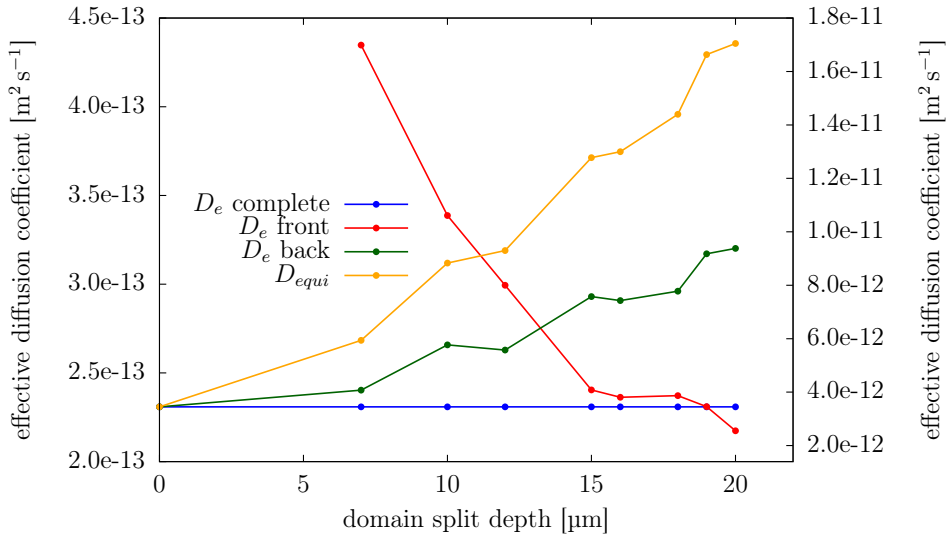

Figure 8.8: Simulated effective diffusion coefficients of subdomains of a HCP monolith obtained from OPC compared to the value obtained by the full sized monolith (blue). Notice that the values of front domain correspond to the axis on the right. The lines connecting the points serve as guidance to the eye.

before.

The equivalent diffusion coefficient D_{equi} of a series of layers, with a thickness of L_i and intrinsic diffusion coefficient of D_i, is given as [Cus09, p.580]:

$$D_{equi} = \frac{\sum_i L_i}{\sum_i \frac{L_i}{D_i}} \tag{8.2}$$

This equation corresponds to a weighted harmonic mean of each subdomain. Using this equation, it should be possible to combine the two diffusion coefficients of the subdomains, in order to recover the diffusion coefficient of the complete domain. The simulation results and the equivalent diffusion coefficients according to equation 8.2 are shown in figure 8.8.

According to the values obtained by numerical modeling of the subdomains, the diffusivity of the front domain is higher by one order of magnitude than the complete domain, while the diffusivity of back domain (green) increases the smaller the fraction becomes. Moreover, the equivalent (harmonic mean) of the diffusivity of the combined values here is always higher, up to a factor of about 1.9, than the numerical results obtained by using the complete domain. This is surprising as the harmonic mean is a well known approach to determine the equivalent diffusivity of a series of layers. However, the series model using the harmonic mean is only valid if the layers are intrinsically homogeneous.

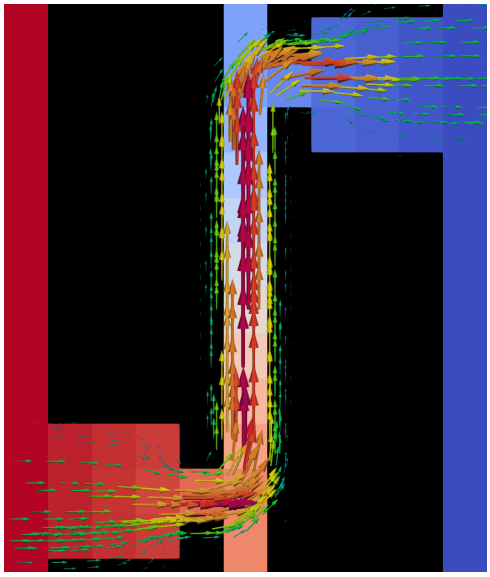

Figure 8.9: Illustration of a diffusion chamber containing a mirror symmetric geometry with shifted pinholes. The flux is converged to steady-state. Black color corresponds to a non-diffusive structure, while the blue to red color corresponds to the concentration of the diffusive solute in water. The diffusive flux is depicted by arrows aligned to the flux direction. The size and color of the arrows are proportional to the flux magnitude, i.e. a green color depicts a low and red a high flux.

To illustrate the effect observed in the pore-scale model, figure 8.9 is presented. The model comprises a diffusion chamber which contains a geometry of two mirror symmetric domains, each having a pinhole leading to the corresponding boundary. The pinholes are shifted to each other to force the solute through a vertical slit. The solute diffuses from left to the right boundary while in the center the flux turns vertical.

If each domain were calculated individually in a diffusion setup, the vertical flux component would not be contained in the results. Moreover, the vertical slit would serve as constant concentration boundary for the simulation using the right-hand structure, thus always be refilled with solute. Thus, the effective diffusivity obtained separately is higher than in combination.

A similar effect can be observed by applying the separated domain approach on the HCP microstructure. Figure 8.10a shows the concentration profile of an inert tracer of a slice in the height of 33 µm after convergence of the diffusion chamber simulation. Figure 8.10b shows the same slice in an inclined 3D view in companion to diffusive flux streamlines. The streamlines originate from seeds within the sphere depicted as green circle in figure 8.10a.

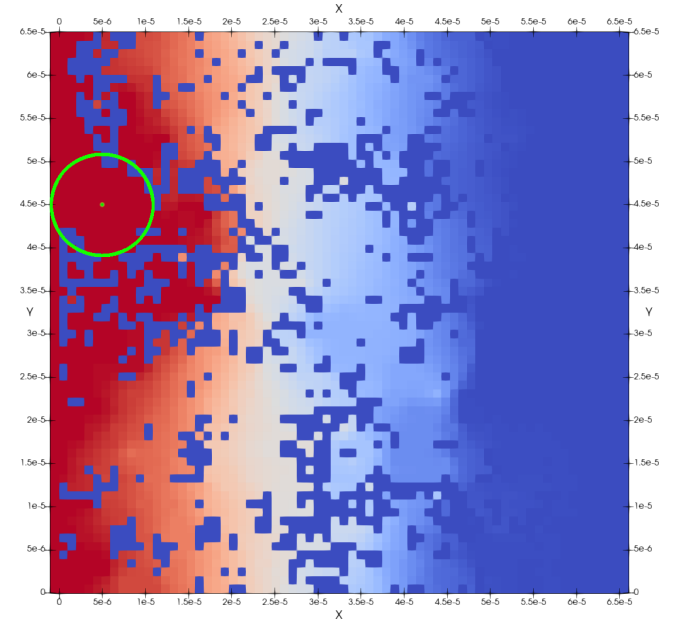

(a)

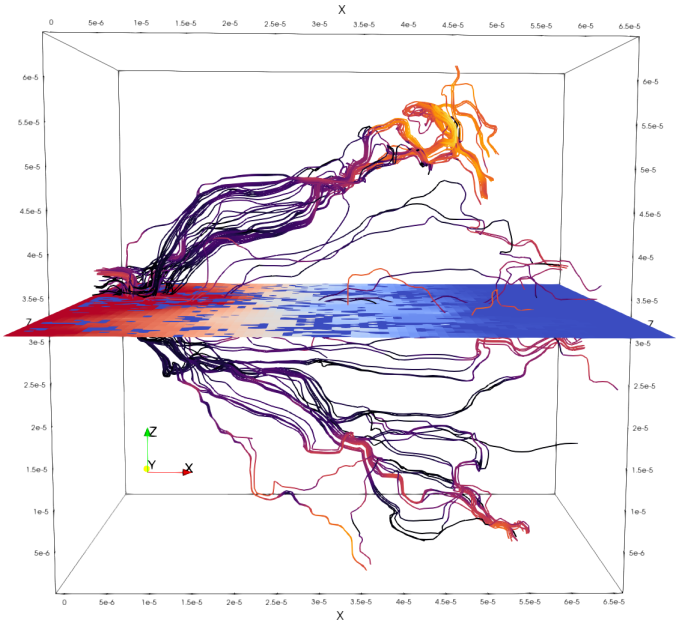

(b)

Figure 8.10: (a) A slice of the concentration profile of a flux converged diffusion chamber simulation of the initial HCP monolith microstructure. The green circle depicts the region of the source seeds used for the streamlines of image (b). (b) Inclined view on the slice of the concentration profile and diffusive flux streamlines. The diffusive flux is diverted by an obstacle and thus spread towards the z-axis.

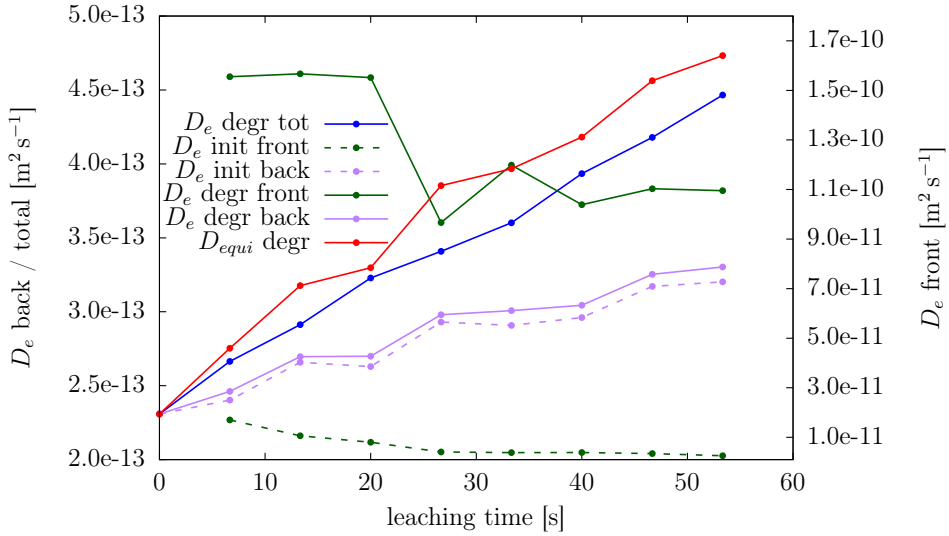

Figure 8.11: Simulated effective diffusion coefficients of subdomains (front and back) of a HCP monolith obtained from OPC compared to the value obtained by the full sized monolith (blue, indicated as "tot"). Values determined by using the degraded ("degr") microstructure are indicated with solid lines, while dashed lines correspond to the initial values ("init", cf. figure 8.8). Notice that the scale of the values of the front domain (green) correspond to the axis on the right. The lines connecting the points serve as guidance to the eye.

Apparently, the concentration is not a smooth gradient in the region of the green circle as the flux is obstructed by non-diffusive obstacles consisting of unreacted clinker and in particular undissolved portlandite. Resulting from the hindrance, the diffusive flux is forced to bypass the obstacles in the y and z direction. This leads to a reduced concentration behind the obstacle and subsequently entry pores of the residual domain are not saturated completely. Basically, the same effect is present as illustrated in the artificial example shown in the pinhole example (cf. figure 8.9). Thus, flux components in the y and z directions are required for the solute to reach these entry pores, effectively leading to a lower diffusive flux within the residual domain.

Although the effect here is less pronounced than in the pinhole example, the mechanism is not negligible as been observable in the resulting effective diffusion coefficient of separated domains (cf. figure 8.8). Note that this effect is only observed for heterogeneous media as simulated here. In particular the artificial pinhole example was designed to illustrate this pore-scale effect. Moreover, the magnitude of this effect depends on the degree of valid representation of the sample to the system to be analyzed.

In order to be able to better compare the diffusivities of the degraded to the initial HCP

microstructure, the microstructures of the front and back subdomains of the degraded HCP were used in the same diffusion chamber setup as previously described for the pristine HCP. The resulting effective diffusion coefficients are plotted in figure 8.11.

The degraded front domain (green, solid) has an increased diffusivity by factor 9 to 42 compared to the initial values (green, dashed). The resulting diffusivity of the degraded domain is about $(1.26 \pm 0.26) \times 10^{-10}\,\mathrm{m^2\,s^{-1}}$. The diffusivity of the domain in the back of the monolith is increased by only up to 3 % (purple). This is in line with the visual analysis of the phase and microstructure alterations, as the domain at the backside of the monolith is virtually unaltered. On other hand, the front domain experienced significant decalcification leading to the dissolution of the portlandite here. The dissolution of portlandite results in an increase of porosity in the front domain and therefore allows the diffusive solute for a better access to the back-sided domain.

The equivalent diffusivities (red) are still higher by about 10 % than the actual numerically determined values by simulations (blue). However, the difference is not as pronounced as observed for the non-degraded microstructure (cf. blue and orange curves in figure 8.8), which was about a factor of 1.9. The reason for that is that the degraded front domain resembles to a more homogeneous medium than the intact microstructure, i.e. as the portlandite has been dissolved, only porosity and CSH is left.

To support this analysis, the lateral fluxes are compared to the flux component aligned to the concentration gradient applied to the monolith. For this, the integral sum of the magnitudes of the lateral flux components $\vec{j_{yz}}$ are divided by the integral flux towards the x direction (j_x):

$$t = \frac{\sum \|\vec{j_{yz}}\|}{\sum j_x} \tag{8.3}$$

In this equation t is a quantity which is related to the tortuosity. This calculation was done for the degraded front and non-degraded back domains separately for the different degradation times. To get a qualitative figure of the change of tortuosity, the values determined for the pristine and degraded material, t_p and t_d, respectively, are divided to yield the ratio t_r:

$$t_r = \frac{t_d}{t_p} \tag{8.4}$$

The resulting values are determined for the front and back domains separately. Resulting from degradation, the tortuosity determined by this formalism was reduced by 17 % to 39 % for the degraded domain. On the other hand, the t_r value for the non-degraded back sided domain has been changed by less than 1 %. The values obtained here are lower than 1 as the degradation reduces the tortuosity. The reduction in tortuosity is more pronounced in the degraded zone. This is qualitatively in line with the analysis conducted with respect to the evolution of the diffusivity.

The observations made in this section underlines that the microstructural connectivity of the pore network is an important property to determine transport parameters. As a series model assumes homogeneous media it cannot be applied directly to heterogeneous media if the specimen is not macroscopically representative. In the analysis conducted here it has been shown, that pore-scale effects play a significant role in models resolving

the pore structure explicitly.

8.2 Derivation of the effective diffusivity of the pristine low-pH cement paste

8.2.1 Model setup

In this chapter the application of iPP to derive the effective diffusion coefficient of a hydrated low-pH cement paste is illustrated. The 3D model used for this purpose is based on the microstructure derived from μ-XCT measurements performed on a HPC sample by USFD (cf. section 7.2.2). To derive transport properties of the hydration product phase, the corresponding phase composition derived by hydration modeling was used (cf. section 7.3). A 3D model (figure 7.9) was applied to determine the effective diffusion coefficient in the x, y, and z directions to determine possible anisotropic diffusivity. It has to be noted that the chemical equilibrium calculation in this simulation was only used to initialize the composition of each individual cell, but no calculations of chemical reactions were carried out during the transport simulation.

The same methodology as given in section 8.1.2.4 was used for the simulations. While constant concentration boundary conditions are imposed to the two faces corresponding to the direction for which diffusivity is to be obtained, closed (slip) boundary conditions are imposed on all other boundaries. Furthermore, the diffusivity model of the hydration products phase was implemented using the multi-scale homogenization model described in section 7.4.4. The assumed hydration products continuum has a diffusion coefficient of about $8.26 \times 10^{-12}\,\mathrm{m^2\,s^{-1}}$, while for free water the diffusion coefficient corresponding to calcium ions was assumed ($2.2 \times 10^{-9}\,\mathrm{m^2\,s^{-1}}$). More information about the model setup is given in table 8.3.

8.2.2 Results

8.2.2.1 Effective diffusivity derived by numerical modeling with iPP

After steady-state was reached, the simulations were stopped and the results were evaluated. The resulting concentration profile and flux streamlines at steady state for the z-direction test are presented in figure 8.12 as an example. From the outlet fluxes, the effective diffusion coefficients for each direction were calculated, as shown in table 8.4. The values for all directions are quite similar ($(3.47 \pm 0.26) \times 10^{-12}\,\mathrm{m^2\,s^{-1}}$), suggesting that the diffusivity is quasi-isotropic for the depicted sub-geometry of the low-pH HCP, although, the results show a slightly lower diffusion coefficient for the z axis. Further analysis of the geometry has shown that a rather big and flat silica fume particle is obstructing the pathway in the z direction, effectively reducing the solute flux.

For comparison, the effective diffusion coefficient of the cement paste was estimated by homogenizing the geometry used in the pore-scale model using the Mori-Tanaka (MT)

Table 8.3: Essential information about the modeling setup used for the determination of the effective diffusion coefficient of the low-pH HCP microstructure derived from μ-XCT image data. The degrees of freedom correspond to the product of the number of nodes and transported solutes.

property	value
LBM scheme	P-TRT
lattice stencil	D3Q7
LBM nodes	$250 \times 250 \times 250 = 15625000$
D_{ref}	$5 \times 10^{-10}\,\mathrm{m^2\,s^{-1}}$
ϕ_{min}	0.24
ϕ_{ref}	1.0
Δx	3 µm
Δt	720 µs
number transported solutes	1 for each direction, i.e. 3 in total
thermodynamic database	ThermoChimie_eDH_v9b0 (for initialization only)
CSH model	3 discrete phases
degrees of freedom	46875000 (no phases)

Table 8.4: Results of the effective diffusion coefficient calculations for each spatial axis and average value.

direction	D_e $[\mathrm{m^2\,s^{-1}}]$
x	3.55×10^{-12}
y	3.69×10^{-12}
z	3.19×10^{-12}
average	3.47×10^{-12}

scheme (cf. equation 7.20). To this end, the volume fractions of hydration phases, inert solids and voids given in table 8.5 were used.

The resulting diffusion coefficient obtained by the homogenization is $4.18 \times 10^{-12}\,\mathrm{m^2\,s^{-1}}$, i.e. the MT technique yields a 20 % higher diffusion coefficient compared to the average value derived from the pore-scale model for this geometrical setup. This may suggest that some inaccessible porosity and geometrical effects can play a non-negligible role here. In this line, it is important to evaluate the accuracy needed for an upscaled model, i.e. whether the MT technique is sufficient for providing reliable values of diffusivities, or if complex numerical simulations are needed instead.

It should be noted that the effective diffusion coefficients determined here correspond to a microstructure that was obtained after 28 d of hydration. Thus, long-term degradation processes should be assessed with diffusion coefficients obtained for well-hydrated systems, which in low w/c ratio mixes of blended cements may take substantially longer than 28 d. It is known that the apparent diffusion coefficient for chloride ingress decreases

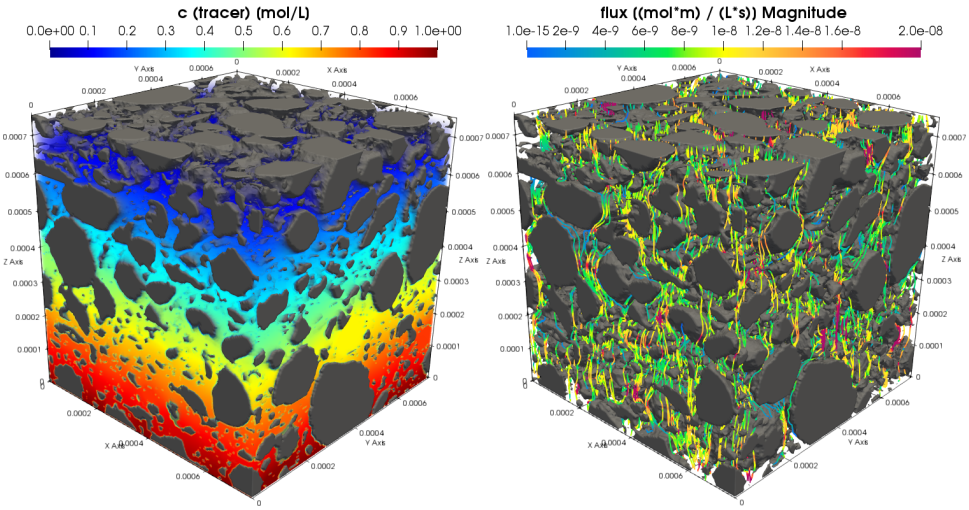

Figure 8.12: Concentration profile (left) and diffusive flux streamlines (right) of an inert tracer after convergence of the diffusion coefficient simulation in z direction. Non-permeable phases are indicated in gray while hydration products and voids are transparent.

Table 8.5: Voxel count, corresponding volume fractions and diffusion coefficients of different phase types in the low-pH HCP cube.

phase	voxel count	volume fraction	D_e [$m^2\,s^{-1}$]
void / porosity	482755	0.031	2.2×10^{-9}
solid / non diffusive	7117164	0.455	0×10^{-9}
hydration products	8025081	0.514	8.26×10^{-12}

as a function of time much more rapidly in cement mixes with a high substitution by SCMs than in OPC [Rid13]. HCPs hydrated from mixtures using a low w/c ratio, the primary pathway for solute transport tends to be via the CSH phase, i.e. the contribution of capillary porosity to diffusive transport is less pronounced. Moreover, addition of SF decreases the portlandite content in the hardened cement paste, which can increase the relative diffusivity due to replacement of portlandite by CSH [Tay97, p. 291]. In the low-pH HPC addressed here, no portlandite is present, thus this process has already been completed.

8.2.2.2 Comparison to experimental data

In the following, the diffusion coefficients derived by numerical modeling are compared to experimentally derived values, which were determined using chloride ions or HTO as

Table 8.6: Comparison of experimentally derived diffusion coefficients of the CEBAMA low-pH reference cement paste [CEB19] with values derived by iPP simulations. The values for iPP are derived with help of equation 7.21 and the results from iPP transport simulations (cf. table 8.4). Using equation 8.5 and assuming the corresponding free water diffusion coefficients of the tracers D_w yields the normalized diffusivities D_n. The units of the absolute diffusion coefficients (D_e and D_w) and the standard deviation are in $[m^2\,s^{-1}]$.

data set	tracer	D_w	D_e	std. dev.	D_n
Cl CTU	Cl^-	2.03E-09	< 1.00E-13	-	< 4.92E-05
Cl KIT	Cl^-	2.03E-09	1.55E-12	6.74E-12	7.63E-04
HTO KIT	HTO	2.24E-09	2.25E-12	2.20E-13	1.01E-03
HTO Subatech	HTO	2.24E-09	3.94E-13	4.00E-14	1.76E-04
iPP sphere	Ca^{2+}	2.20E-09	2.44E-12	1.81E-13	1.11E-03
iPP disk	Ca^{2+}	2.20E-09	2.28E-12	1.70E-13	1.04E-03

tracers. For a meaningful comparison a few steps are needed. The composition of the CRP was not the same as the mixture used by USFD to cast the investigated specimens, i.e. the quartz filler was missing in this mix (cf. table 7.6). To correct the diffusivity obtained via iPP for the presences of a quartz filler, a differential scheme is used (cf. equation 7.21). Since the morphology of the quartz filler particles is not known, two extreme cases are considered, which yield the lowest and highest effect on tortuosity, i.e. spherical and disk shaped inclusions. According to the mix design of the CRP, the volume fraction of the quartz filler was 21 % [Veh17]. Here it is assumed that the volume fraction of the quartz filler remains the same during hydration. Using the data and the differential scheme equation yields to effective diffusion coefficients of $2.44 \times 10^{-12}\,m^2\,s^{-1}$ and $2.28 \times 10^{-12}\,m^2\,s^{-1}$ for spherical and disk shaped inclusions, respectively.

Note that the molecular diffusivities of the used tracers are different. To eliminate this effect and to be able to compare the experimentally derived effective diffusion coefficients, the results of the simulations presented here and those of the experiments must be normalized to the tracer used in the experiments. Thus, the effective diffusion coefficient D_e obtained is divided by the diffusion coefficient of the tracer in free water D_w which yields the normalized effective diffusion coefficient D_n:

$$D_n = \frac{D_e}{D_w} \tag{8.5}$$

The corresponding diffusion coefficient in water D_w are assumed as $2.03 \times 10^{-9}\,m^2\,s^{-1}$ [Hay17, p.5-75] and $2.24 \times 10^{-9}\,m^2\,s^{-1}$ [Eas89] for Cl^- and HTO, respectively. For the simulation case, the value of $2.2 \times 10^{-9}\,m^2\,s^{-1}$ is used, which corresponds to the diffusion coefficient of calcium in the pore water of cement, which was used in the simulations. Both sets of values are determined and presented in table 8.6 and compared in figure 8.13.

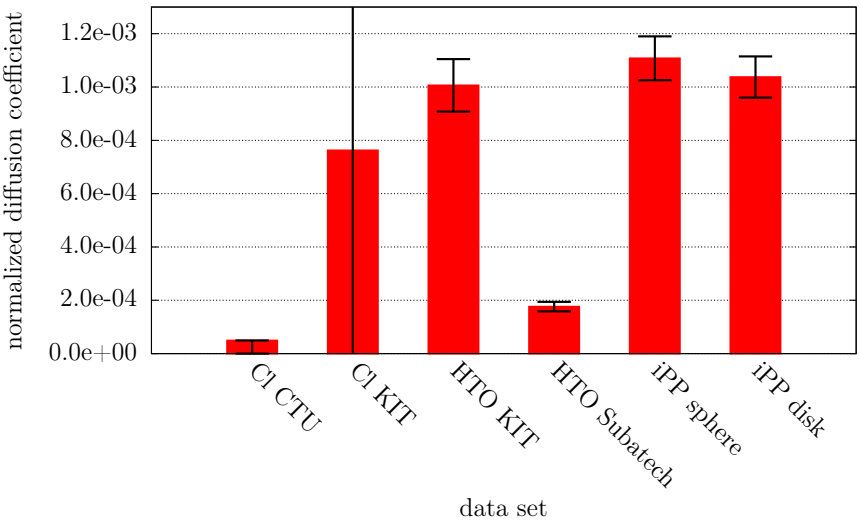

Figure 8.13: Comparison of normalized diffusion coefficients of the CEBAMA low-pH reference paste derived from experiments and numerical modeling with iPP. The values for iPP are corrected for non-diffusive quartz filler inclusions. The experimental data are normalized to the diffusion coefficient the corresponding tracer diffusivity, i.e. D_w values for Cl^- and HTO. The error bars show one sigma confidence interval reported by the authors of the experiments. The confidence interval of CTU is indicated as a range starting from zero, since only an upper limit was reported. The error bars of the iPP results are estimated with the standard deviation of the three different results in table 8.4. The experimental data are taken from a CEBAMA project report [CEB19].

The experimentally derived values revealed a large scatter. Experimentalist from KIT reported a more than 4 times higher standard deviation value than the value itself for the experiments using chloride diffusion (cf. the error bar in figure 8.13, which exceeds the plotted range). The values determined by iPP, and the application of another effective medium step for incorporating the quartz filler, are at the upper end of the range of the values obtained via experiments. At least the values derived via iPP overlap with the confidence interval of the results from KIT dealing with HTO diffusion. Experiments from Subatech using HTO as tracer suggest a 6 times lower diffusivity than the values obtained with the methods in this work. However, it is difficult to compare both results, since the cement mixture design was different. Moreover, as shown in section 7.2.2.3, the size of the residual silica fume particles are quite high compared to the particle's size reported by analysis gained from the initial reference mix design [Veh17]. This suggests that the phase composition and microstructure obtained via μ-XCT, and subsequently

used for the modeling approaches, is different from the one of the CRP material used in the diffusion experiments. Nevertheless, the results obtained here are within one order of magnitude or even closer to the experimental results.

8.3 Degradation of low-pH cement due to leaching

8.3.1 General model setup and considerations

In this chapter, simulations in the line with experiments conducted by USFD are presented. For the leaching experiments at USFD, cylindrical samples with a diameter and height of 15 mm were prepared. The cement composition and curing conditions were the same as for the 2 mm samples used for μ-XCT imaging. After curing, the top and bottom ends of the cylinders were sealed with resin in order to prevent axial diffusion between the monoliths and the surrounding groundwater. Prior to the experiments, the hardened cement pastes were characterized inter alia by XRD, SEM, TGA and μ-XCT.

The 15 mm samples were placed into 60 mL vessels and submerged in 50 mL leaching solution in oxygen and CO_2 free atmosphere at 40 °C, while allowing equilibration for several months. The experiments were performed with different synthetic solutions, namely granitic groundwater, clay water, and saline (sea) water. Every two months the solutions were replaced by fresh leaching solution. The sampled solutions were analyzed with respect to Ca, Si, Al, K, S and Mg concentrations, pH, etc. The experiments addressing the leaching of the CEBAMA reference paste in granitic water were chosen as input for the simulations in this work dealing with pore-scale effects resulting from cement paste degradation and alteration. The granitic groundwater used in the leaching experiments is referred to as *Allard water* [All07a]. The composition of the water used in the experiments is depicted in table 8.7 in column c_{init}.

The granite water as reported was supersaturated with respect to calcite. During the experimental setup, this fact was neglected and likely a small amount of calcite precipitation overlooked during the preparations of the solution. Thus, during the experiment the solution was assumed to be stable and in equilibrium. However, this assumption is insufficient for a modeling approach assuming thermodynamic equilibrium, as calcite would consequently precipitate at the inlet of the system, irrespective of any contained material or solution.

For adjusting the carbonate concentration of the granite water, calcite and hydration products were allowed to precipitate in a PhreeqC calculation. Due to supersaturation, calcite precipitated in the initially reported solution. However, to find a stable solution and maintain the calcium concentration at the same time, carbonate was removed until no more calcite precipitated. In order to compensate for charge imbalance, chloride was added to the solution. Both, the reported solution composition by USFD [Vas18] (c_{init}) and the adjusted concentrations (c_{sim}) are depicted in table 8.7. Essentially, the carbonate concentration (indicated as carbon) was reduced by more than a factor of two, while the chloride concentration increased by approximately one third (cf. columns c_{sim} and c_{init} in table 8.7). The resulting composition of the solution in column c_{sim}

Table 8.7: Granite leaching water composition at 40 °C. c_{init} refers to the composition used in the experiments, which needed some corrections in order to be suitable for simulations (see text). The adapted values are indicated as c_{sim}. In addition, the initial pore water composition of the low-pH cement (c_{pore}) is depicted for comparison. All concentrations are given in units of mmol L^{-1}.

Element	c_{init}	c_{sim}	c_{pore}
Al	0	0	0.773
C	2.02	0.86	0.7
Ca	0.5	0.5	0.691
Cl	2.18	3.227	0
K	0.1	0.1	741
Mg	0.2	0.2	3.25×10^{-6}
Na	2.8	2.8	212
S	0.1	0.1	444
Si	0.2	0.2	4.62

is saturated with calcite and was subsequently used for all leaching simulations with granitic water.

Several simulations of the leaching process were performed with increasing complexity. The simplest approach is assuming all cement hydration phases are in equilibrium with the pore water. Subsequently, the model is extended to include classical nucleation theory and porosity controlled solubility effects.

All simulations are based on a 2D domain, which is a slice of the segmented μ-XCT image of the low-pH HCP as outlined in section 7.2.2 (cf. figure 8.14). The HCP slice in this model is defined by a 250x250 cells domain with a resolution of 3 µm per pixel, i.e. a total area of 750 µm × 750 µm. Clinker, blast furnace slag and silica fume were assumed to be inert, while the composition of the hydration product phase is defined as in table 7.9 and the macro pores were filled with pore water in equilibrium with the hydration products (cf. table 7.10).

Since the initial hydration model to derive the hydration products composition made use of the *ThermoChimie_eDH_v9b0* [Gif14] database, this database was used subsequently for the simulations conducted. As already outlined in section 7.1.1, this database contains a CSH model with three discrete phases instead of a solid solution model. To adapt to the experimental conditions, the thermodynamic equilibrium calculations were carried out for 40 °C. The ThermoChimie database contains data for the relevant phases to correct for the non-standard temperature. Moreover, the diffusivity and porosity models applied were based on the Tennis and Jennings CSH model [Ten00] (cf. equation 2.9) and the multi-scale approach as defined in section 7.4.4, respectively.

The left-hand side of the modeled domain was assumed to be in contact with a constant concentration boundary, which simulates an infinite reservoir with a fixed concentration of the leaching solution. Unless else stated, the cells at $x = 0$ are adjacent to the

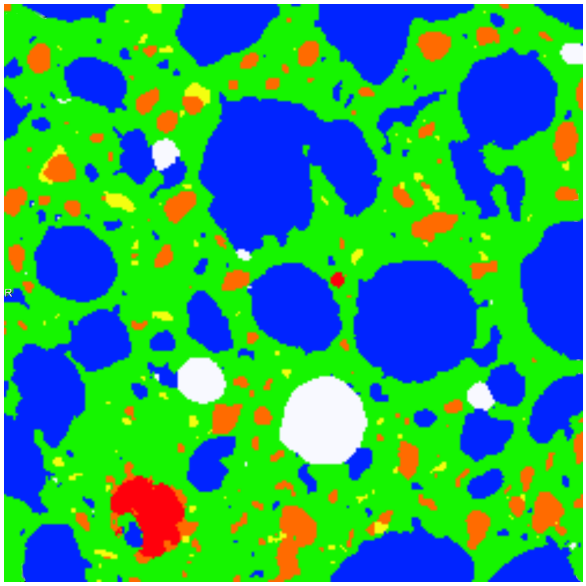

Figure 8.14: 2D slice of the segmented HCP microstructure. The colors are analogous to figure 7.9.

HCP monolith surface. Since the spatial discretization is 3 µm, the interface between the HCP domain and the granite water is at 1.5 µm. Therefore, the domain $x \leq 1.5$ implies initially a non-solid phase containing pore space occupied by leaching water only, containing the granitic water depicted in table 8.7. All other boundaries are assumed to be closed by imposing a slip boundary condition.

Due to numerical stability implications of the P-TRT Lattice-Boltzmann scheme, the lowest possible diffusive porosity (threshold) was set to 0.15. According to equation 4.10 and using the data above, one iteration equals to a physical time step of 0.45 ms for all simulations described in this chapter, unless stated otherwise. If a porosity below this threshold is encountered, the corresponding node is switched from a mixed heterogeneous and homogeneous reaction cell to a heterogeneous reaction term only (cf. section 4.4.1.2 and 4.4.1.3). Note that this porosity threshold is not the lowest achievable porosity in the simulations. Due to the treatment of the heterogeneous term, lower porosities can be reached. However, the reactive minimum porosity was limited to 0.1 %, unless stated otherwise, in order to maintain a safety distance to negative porosities and prevent numerical issues (cf. section 4.4.1.4 about negative porosity treatment). More details about the model setup of the simulations carried out are given in table 8.8.

Table 8.8: Essential information about the modeling setup of the leaching simulation of the low-pH HCP monolith with granite water. The degrees of freedom correspond to the product of the number of nodes, transported solutes and treated solid phases.

property	value
LBM scheme	P-TRT
lattice stencil	D2Q5
LBM nodes	$250 \times 250 = 62500$
D_{ref}	$5 \times 10^{-10}\,\mathrm{m^2\,s^{-1}}$
ϕ_{min}	0.15
ϕ_{ref}	1.0
Δx	3 µm
Δt	450 µs
number transported solutes	12 + charge
thermodynamic database	ThermoChimie_eDH_v9b0
CSH model	3 discrete phases
degrees of freedom	15437500

8.3.2 Pure equilibrium conditions

8.3.2.1 Model setup

Within this simulation, the local equilibrium approach was applied to control the dissolution and precipitation processes (see also section 4.4.2). This means effectively the chemical equilibrium is achieved instantaneously in each cell, irrespective of geometry or absence of surfaces serving as nucleation sites.

In order to simulate the interface between granitic water inlet and hardened cement paste, a small reservoir initially empty of solids filled with granitic water was applied on the left-hand side. When granite water comes into contact with the high pH cement pore water, calcite forms instantaneously under assumption of a local equilibrium. A larger reservoir would represent the free water domain better with respect to possible crystal grows on top of the surface of the HPC monolith. Preliminary simulations have shown that the highest supersaturation with respect to calcite occurs directly at the model boundary (x = 0). Thus, as first attempt by applying a larger reservoir led to an unrealistic calcite precipitation always at the granitic water inlet (x = 0) rather than in the reservoir space between HPC and boundary or on the surface of the cementitious material.

This effect revealed already one of the flaws of the pure equilibrium model regarding the precipitation of solids, especially at the pore-scale. However, this simulation was conducted anyway as a baseline for comparison with more sophisticated approaches. For this purpose, the smallest possible reservoir of only a single column of cells was added, which corresponds to the size of one spatial discretization step. This reservoir

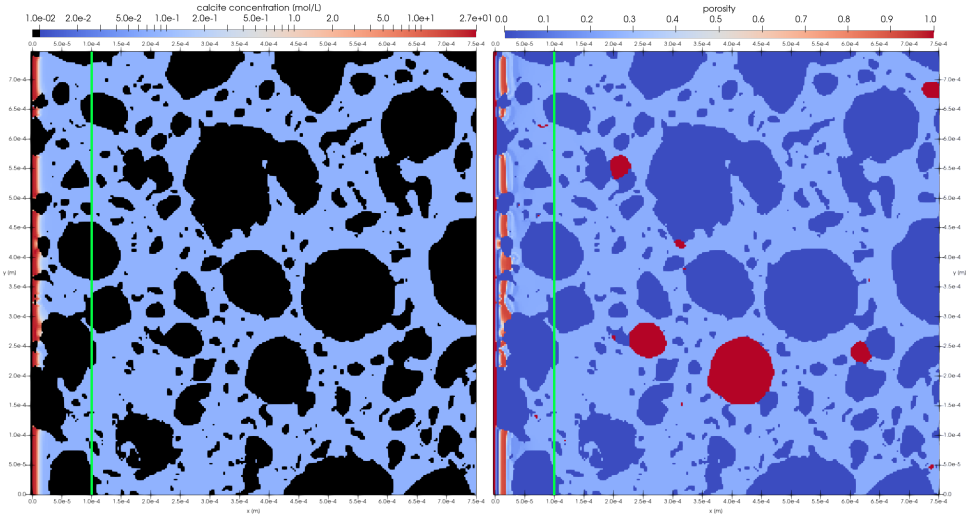

Figure 8.15: Simulated calcite concentration (left) and porosity (right) after leaching of the low-pH cement paste with granitic water for 40 min. Note that the hydration product phase of the hardened cement monolith contains some amount of calcite already initially (cf. table 7.9). The size of the plot is 753 µm × 750 µm. The green vertical line indicates a depth of 100 µm.

was initially filled with leaching water only. Thus, the total model size was 251 × 250 nodes or 753 µm × 750 µm.

8.3.2.2 Results

The 2D model was run for 5.4 million iterations, equivalent to a physical leaching time of 40 min. Some of the results are presented in figures 8.15 through 8.18. The resulting calcite and porosity distribution after 40 min is shown in figure 8.15. It can clearly be seen that calcite is already precipitating as a passivating crust on the surface of the HCP on the left-hand side. At the same time, the porosity in the cement paste close to the interface decreases. In the time frame of the simulation, only the first 20 µm of the HCP are affected by the carbonation.

Figure 8.16 shows the average phase assemblage perpendicular to the leaching front. For better visibility of the effects, only the first 100 µm are plotted. This average is calculated by summing up all phase concentrations along the y-axis and dividing by the number of cells (n = 250). As indication for the depth addressed in figure 8.16, a vertical green line is shown in figure 8.15 (left) at this depth.

In addition, with a similar averaging approach, in figure 8.17 the average porosity of the HCP is compared to the maximum porosity achievable due to leaching effects. This means, the maximum achievable porosity is not unity because of the volume of phases

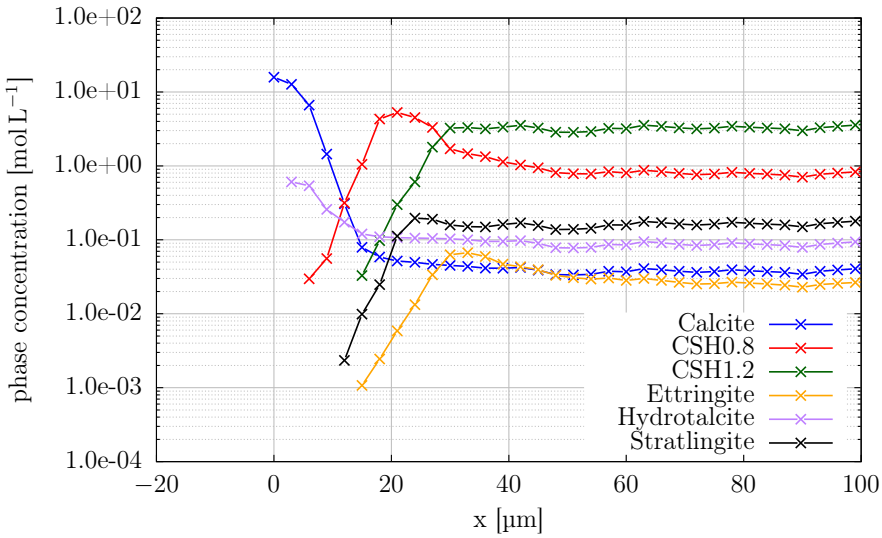

Figure 8.16: Average solid phase concentrations at the interface after leaching of the low-pH HCP with granite water for 40 min. All phases assumed to be in local equilibrium. Lines in this plot are only a guide to the eye.

(e.g. clinker, SF and BFS) assumed as inert in the simulation. In the same plot, the corresponding C/S ratios of the CSH phase are shown.

The concentrations of hydration phases (figure 8.16) at depths greater than 60 µm correspond to the initial composition of the HCP and are not altered due to leaching. It is visible that the right-hand parts of the curves are not perfectly constant with respect to x. This is due to heterogeneous distribution of the assumed inert phases (clinker, BFS and silica fume) and capillary porosity in the HCP. CSH is only degraded in the first 30 µm of the sample in the simulation. In figure 8.17 a significant decrease of the C/S ratio of the CSH phase in the leached zone is indicated. In this zone, the CSH is mainly replaced by calcite and hydrotalcite. It can be deduced that initially the leaching leads to a decalcification of the CSH and a decrease in the C/S ratio. Later on the decalcified CSH is subsequently replaced by calcite and hydrotalcite. The formation of hydrotalcite is triggered by the ingress of magnesium, which is contained in the granitic water.

Furthermore, the amount of ettringite increases slightly close to the leaching front while being depleted in the leached layer. This effect is indirectly triggered by decomposition of strätlingite when in contact with the granite water rather than addition of sulfate, since the sulfate concentration in the leaching water is lower than in the equilibrated pore solution (compare also tables 8.7 and 7.10). Here strätlingite serves as supply for aluminum in solution, which causes more ettringite to form.

Moreover, in figure 8.17 the porosity shows a down-up-down shape. At about 10 µm the porosity reaches more than 85 % of the achievable porosity, while at the interface

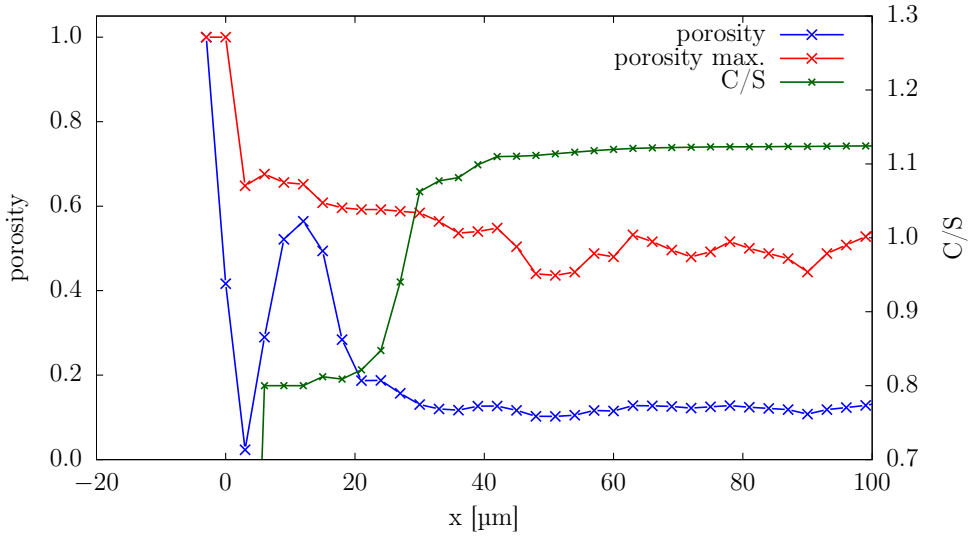

Figure 8.17: Average porosity (blue, left axis), maximum achievable porosity (red, left axis) and Ca/Si ratio of CSH phase (green, axis right) at the cement paste interface after leaching with granite water for 40 min. Lines in this plot are only a guide to the eye.

the value is decreased to 3.5 % due to calcite and hydrotalcite precipitation. This effect has also been reported from imaging data of carbonation experiments of cement pastes and is termed as carbonated and dissolution zone, respectively [Šav16]. This dissolution zone with a higher porosity mediates between the carbonated zone and the intact HPC domain.

Since calcite was assumed as non-diffusive, calcite precipitation at the surface of the HCP reduces the diffusivity of the domain close to the interface rather fast. This causes the leaching and alteration rate to decrease at the same time. Thus, the dissolution rate of the hydrates is rather limited after an equilibration time of about 10 minutes, which can be observed in figure 8.18. However, due to the treatment of heterogeneous reaction terms within iPP (cf. section 4.4.1.3), there is no equilibrium reached by clogging only a single column of cells. More accurate analyses of the porosity distribution at different time steps during the simulation have shown that there was an alternation of clogging and calcite redissolution, which contributes to a non-zero transport effect.

Simulating the leaching of the low-pH paste on the pore-scale using the simplified approach of assuming each phase in equilibrium with the adjacent pore solution has revealed some limitations. First, the location of calcite and hydrotalcite precipitation was always adjacent to the boundary imposing an inlet of granitic water. Even with a distance of the boundary to the HPC monolith, the supersaturation was the highest at the system boundary in the free pore space. Although the supersaturation might be the

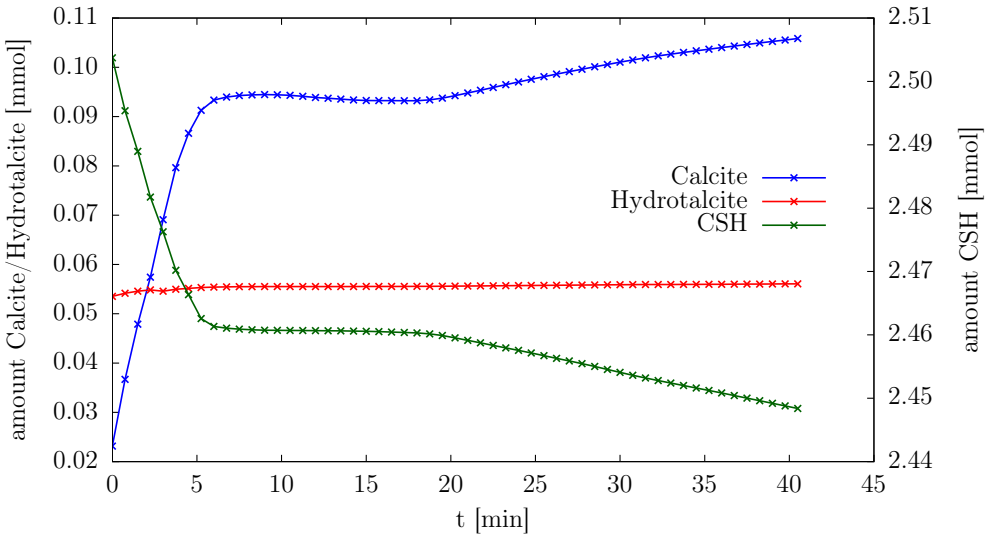

Figure 8.18: Simulated total amounts of calcite (blue, left axis), hydrotalcite (red, left axis) and CSH (green, right axis) in the complete modeled domain as function of contact time with granitic water. Lines in this plot serve as guide to the eye.

highest at the boundary, from empirical experiences the location of precipitation would be rather on the cement monolith surface than in free pore space. In particular the CSH imposes a high reactive surface area which should be preferable as precipitation site compared to the free pore space. Preliminary simulations, not presented here in detail, have shown that clogging would occur directly at the inlet without any contact to the HPC surface. Just neglecting the effect and increasing the size of the reservoir would lead to an unreasonable build-up of a calcite crust in the reservoir directly at the inlet without contact to the HPC surface. To work around this effect, the reservoir was constrained to the smallest possible size of one spatial discretization step.

After some time of simulation, calcium has been partly leached in the first 30 µm and the CSH phase has been replaced by calcite and hydrotalcite. Effectively, the thin layer of calcite led to clogging close to the surface limiting further exchange of granite and pore water solutes. The leaching rate significantly decreases within 10 min, which might be rather quick since only a thin layer of calcite has formed. This is also caused by an oversimplification of the precipitation front which is thin, smooth and almost without heterogeneity. Both effects are caused by neglecting the presence of surfaces during precipitation.

8.3.3 Incorporating classical nucleation theory

8.3.3.1 Model setup

The simulations described in this section comprise a model which extends the classical thermodynamic equilibrium approach for all species and phases by nucleation theory. The theoretical background, derivation of surface tension values and other parameters for the nucleation probabilities, as well as the implementation details for iPP are described in section 5.2. The simulations of the system with pure equilibrium assumptions revealed several drawbacks. Indeed, calcite precipitated preferably in free water instead on surfaces of the cement monolith and in addition a formation of a thin layer of calcite led to a rapid clogging of the system. For example, the instantaneous precipitation in free pore space can be regarded as a limiting case in which an infinite homogeneous nucleation rate is considered. This section is intended to show the effect of reduced homogeneous nucleation and preferred heterogeneous nucleation, i.e. depending on surfaces, on the calcite formation patterns. To this end, in the simulation the location of the precipitation front during leaching and carbonation by calcite saturated granite water is controlled. This model extension regards calcite as governing phase whose precipitation is controlled by nucleation theory. All other phases are not treated with a nucleation probability and are only allowed to precipitate once a calcite nucleus emerged in a reaction cell. This is justified by having the highest supersaturation present for calcite within these simulations of leaching of HCP with granite water.

First, a simulation with simplified geometrical assumptions was implemented. This simulation was conducted to demonstrate the effect of the incorporation of nucleation theory in the pore-scale model. This model contains the same hydration product phase composition as the hydrated low-pH cement paste (see also table 7.9), but disregards the presence of the inert phases and large pores in the geometrical description. Thus, this 2D simulation consists of a monolith of hydration products in contact with granite water on the left. The applied porosity and diffusivity models are identical to the other simulations performed in this context. Furthermore, the spatial resolution of the 3 µm sized system was enhanced to 30 nm, in order to magnify the achieved effects. In order to leave space for newly forming solids, on the left-hand side a reservoir of 10 cells, or expressed in physical units 300 nm, was left free of hydration products and just filled with leaching solution.

In contrast to the test depicted in section 7.5.4, the solutions coming into contact are the pore solution of the low-pH HCP hydration products and granite water. This corresponds to the conditions present during the simulations of leaching of the low-pH HCP, but just with simplified geometry. Moreover, the hydration products are altered during the process, while the $CaCl_2/Na_2CO_3$ system just precipitated calcite without dissolution of any other phase at the same time.

While the free water diffusivity of the solutes was set to $2.2 \times 10^{-9}\,m^2\,s^{-1}$, the numerically Lattice-Boltzmann reference diffusivity was set to $0.5 \times 10^{-9}\,m^2\,s^{-1}$ to speed up the simulation (cf. section 4.2.4). According to equation 4.10 and using a minimum transport porosity of 0.15, one iteration is worth a time step of 45 ns. The simulation

was run for more than 65 million iterations which corresponds to approximately 2.9 s physical time.

In addition, the simulation approach including nucleation theory is applied to the leaching of the low-pH HCP by granitic water. In this model setup, a reservoir of 10 nodes width, corresponding to 30 µm, which is initially filled with granite water is applied at the left of the HCP domain. As for the other simulations, a constant concentration boundary condition of granite water is applied at the left boundary of the system.

8.3.3.2 Results of simulated leaching of hydration products by granitic water

For the initial 1.5 s of the simulation containing only the hydration phases in contact with the granite water, the vertical cells containing hydration products close to the interface to the granite water are degraded. Since these cells have not been completely filled yet with solids, heterogeneous nucleation for the neighboring cells is suppressed by the technique outlined in section 5.2.4.2. After 1.5 s the cells at the interface are filled completely with solids and HEN takes place for the first time next to the interface in the liquid domain. This gradually occupies the complete surface of the material but with a statistical pattern. The simulation was run until 2.9 s and the simulated calcite concentrations and the porosity distribution of the system is shown in figure 8.19. Similar to the simulations using the local equilibrium approach, there is a decrease of porosity close to the surface followed by an increased porosity and a zone where CSH is degraded.

Similar to the definition in section 8.3.1, the distance statements here are defined from the monolith interface to the granite water. On average, CSH is degraded almost completely to a depth of 2.4 µm, i.e. only traces of CSH are left. A C/S ratio of 0.8 is maintained up to 3.9 µm depth. Beyond 4.5 µm the CSH phase is intact with a C/S ratio of about 1.12. In turn, the calcite concentration is increased in the range of −1.2 µm to 2 µm. Thus, calcite has formed on top of the surface and replaced the CSH close to the interface, too. At the same time, the porosity is significantly increased in the range 0.9 µm to 3 µm.

In similarity with the results of the $CaCl_2/Na_2CO_3$ system (see section 7.5.4), there is also a non-homogeneous and uneven layer of calcite formed. The maximum supersaturation with respect to calcite observed, was a saturation index of about 1.1. Compared to the $CaCl_2/Na_2CO_3$ systems ($SI_{low} = 2.54$ and $SI_{low} = 2.76$), in the current example the supersaturation is rather moderate. The unrealistic preferred precipitation on the granite water inlet boundary, as resulted from simulations in section 8.3.2, is now absent, due to statistical hindrance of precipitation in free pore space by homogeneous nucleation. No homogeneous nucleation event happened even after 65 million iterations in the 10 x 100 = 1000 reservoir cells, which are free pore space in the beginning. This underlines how low the probability of HON is in this small volume under moderate supersaturation.

Moreover, an interesting effect is that the degradation depth, which corresponds loosely to the zone of increased porosity in this simulation, is slightly higher in the center of the interface (y = 0.8 µm to 2 µm). Coincidentally, the coarseness of the formed calcite is higher in this range. An obvious conclusion is that a coarse surface leaves diffusive pathways for solute transport open, while a dense rim clogs and passivates the surface

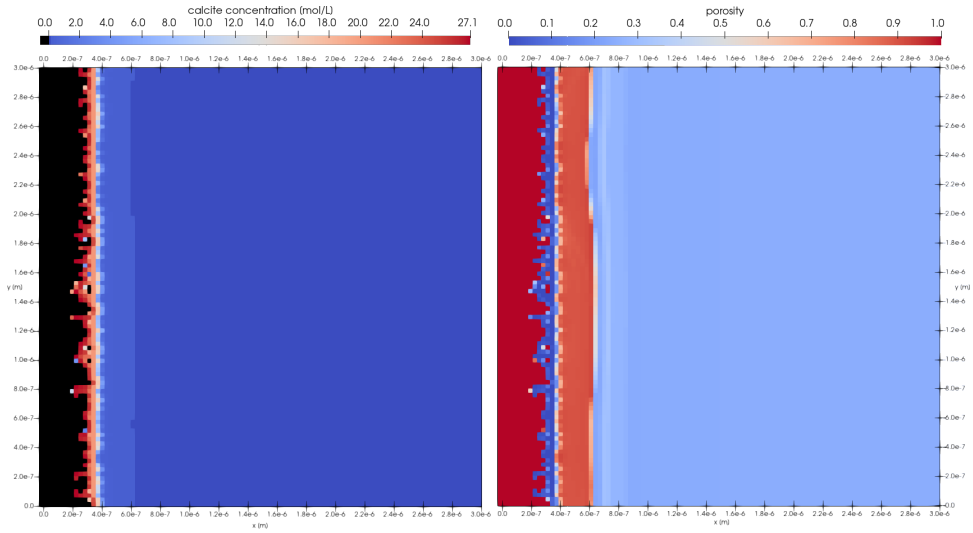

Figure 8.19: Simulated growth of calcite crystals on the surface of cement hydration products. The resolution is 30 nm and system size is 3 µm in both dimensions. The results shown here are after 2.9 s in contact with granite water. The initial interface of hydration products was at x = 300 nm, which is approximately at the vertical baseline of the coarse calcite layer.

earlier. This yields into more possibilities for calcium to diffuse from the monolith into the solution. The calcium either escapes via the constant concentration boundary or precipitates as calcite. The location and the presence of rather dense or coarse calcite rims on the other hand are random. A re-run of the same setup will not yield exactly the same phase distribution in the image. The statistical distribution, however, is controlled by nucleation parameters as surface tension, nucleation sites and magnitude of supersaturation. Thus, the conclusion drawn here are still the same.

With help of this kind of simulations, it might be possible to estimate for example surface roughness data of precipitated materials on another substrate, given the right parametrization with respect to nucleation. The simulations here were carried out in 2D space, while for proper surface roughness information at the interface the simulation must be modeled in 3D. However, this process was not in the scope of this work. Nevertheless, the possibilities of such a modeling approach and tool are shown to be diverse, and the implemented framework is a powerful tool for the assessment of such processes.

8.3.3.3 Results of simulated leaching of low-pH HCP with granite water

The simulated calcite and porosity distributions after a physical simulation time of 2.48 h of leaching of the low-pH HCP are presented in figure 8.20. Again, a calcite crust forms on top of the monolith surface. However, compared to the pure equilibrium simulation

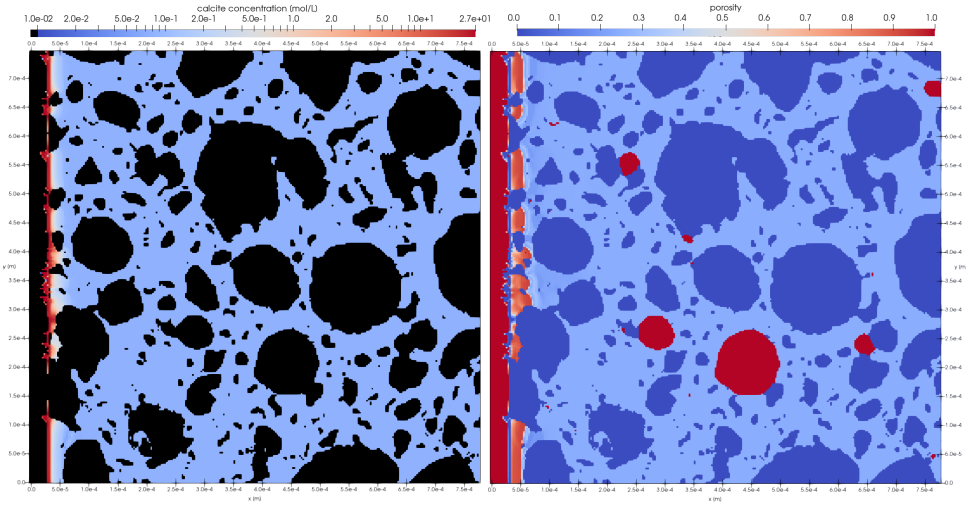

Figure 8.20: Calcite crystal growth on the surface of the low-pH cement paste (left) and resulting porosity (right) after 2.48 h in contact with granite water. The domain size is 780 µm × 750 µm.

in section 8.3.2, this surface layer is less homogeneous. Essentially, the crust formed is rather coarse and rough. For the same simulation time of 75 min, the calcite zone is significantly broader here, compared to the pure equilibrium model. The comparison of the results is outlined below in section 8.3.5. With respect to clogging, however, the result is comparable to the pure equilibrium simulation, i.e. there are no completely open pathways for solute transport along the x direction.

The average solid phase composition perpendicular to the x-axis is shown in figure 8.21, indicating calcite and hydrotalcite are precipitating in particular on the surface of the HCP monolith, growing into the free solution. This is in line with experimental observations analyzing the healing process of fractures with carbonates, which suggests that calcium carbonate phases precipitate on top of pore surfaces [Har98, pp.119]. Leaching of CSH within the first 40 µm and replacement of hydration products by calcite and hydrotalcite within the first 20 µm can be observed. Moreover, the down-up-down shape in porosity distribution in the leached region occurs (visible at the right-hand plot in figure 8.20). Further comparison to the simpler pure equilibrium model can be found in the comparison section 8.3.5.

The main outcome of this model extension is that the unrealistic preferred precipitation on the granite water inlet boundary, as seen in the simulations in section 8.3.2, is now absent. Preliminary analyses have shown that a maximum saturation index of approximately 1.2 with respect to calcite is achieved. This supersaturation present in the pore space in combination with a small spatial and temporal discretization renders it very unlikely that a HON event takes place in the free pore space. Since the probability

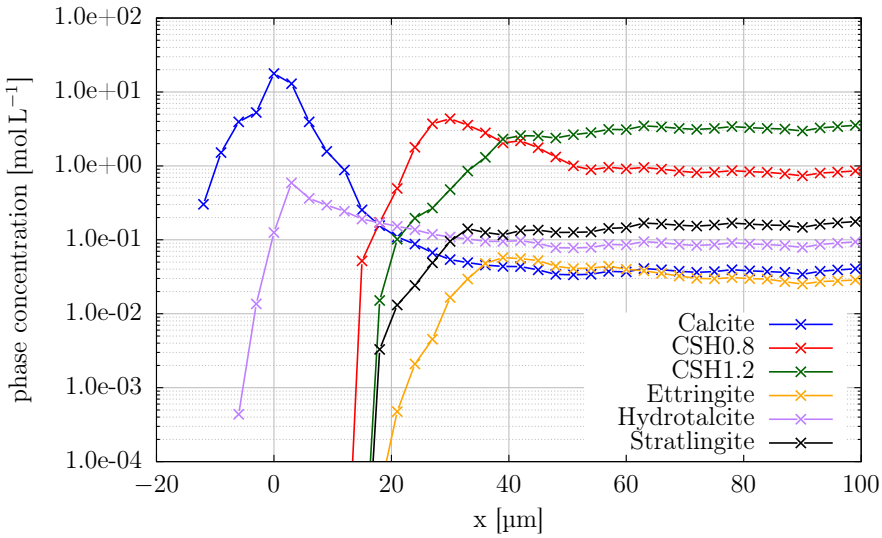

Figure 8.21: Average solid phase concentrations at the interface after leaching of low-pH HCP with granite water for 2.48 h. Phase precipitation was limited by nucleation. Lines in this plot serve as guide to the eye.

for HEN at the monolith surface is much higher, the precipitation preferably takes place at the surface of the HCP monolith.

Moreover, a broader calcite zone also leads to a deeper decalcification of the hydration products. It is expected that the resulting effective diffusivity is also changed by this. However, still a modeling assumption about a minimum reactive porosity is needed to be applied (cf. section 8.3.1). To further tackle this, the HPC leaching model will be extended by incorporating porosity controlled solubility effects.

8.3.4 Incorporating porosity controlled solubility

8.3.4.1 Model setup

To illustrate the effect of pore size distribution on the simulation results, simulations of the leaching of the low-pH HCP by granitic water using iPP and including nucleation theory and porosity controlled solubility were performed. Similar to section 8.3.3, only calcite is treated with a nucleation probability. The PCS effect, however, is applied to all phases at the same time. The methodology and parametrization of the used porosity controlled solubility mechanism is outlined in section 5.3. The same model set-up as in the previous section using a reservoir of 10 cells, which contain granitic water was used to capture possible surface roughness effects due to nucleation. The simulations were run for 10 million iterations, which corresponds to 80 min of physical time.

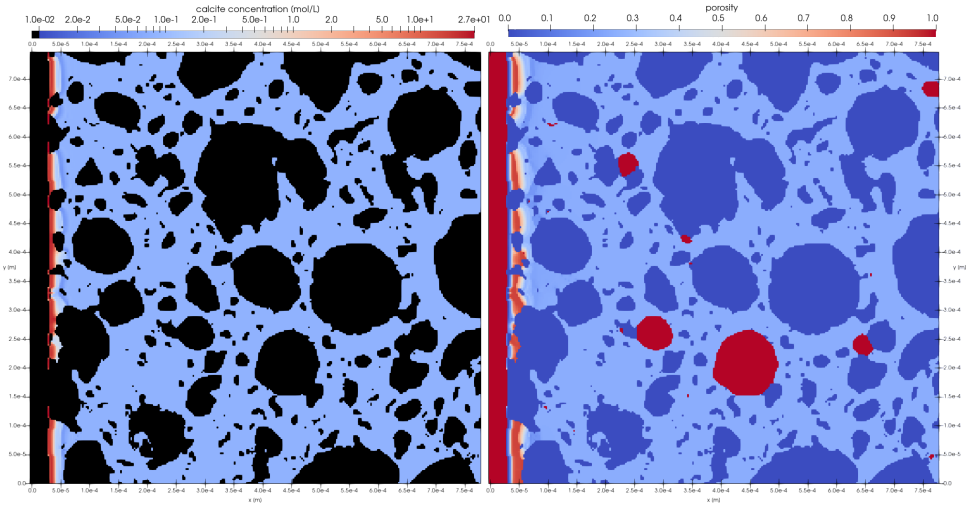

Figure 8.22: Simulated distribution of calcite and porosity in the low-pH HCP in a simulation considering CNT and PCS. The results plotted are obtained after 80 min leaching with granitic water.

8.3.4.2 Results

The simulated calcite and porosity distributions in the HCP monolith after leaching are presented in figure 8.22. As expected, calcite precipitates at or close to the interface, which effectively lowers the porosity. As in the other simulations, the porosity distribution shows a down-up-down pattern along the x-axis. The precipitation rim containing calcite and hydrotalcite seems much less rough compared to the simulations including nucleation theory only. The results suggest that nucleation plays a minor role compared to PCS effects, since here the precipitate growth on top of the monolith is less pronounced. However, although the calcite front is still present, the lowest porosity obtained is limited to 0.3 %. This porosity threshold was not explicitly limited in the simulation to prevent numerical issues, but is an actual outcome of the model, while 0.1 % was explicitly set as limiting value in the simpler models. Essentially, this seems to be the minimum porosity achievable with the supersaturation levels reached upon contacting the hardened low-pH paste with the granitic water. However, this result is based on the assumptions regarding pore geometry as outlined in section 5.3, e.g. cylindrical pore geometry in CSH, and usage of surface tensions estimated by the Stefan-Skapski-Turnbull equation.

The averaged solid phase assemblage of the HCP perpendicular to the x-axis is plotted in figure 8.23. Qualitatively, the plot shows similar features as the other simulations, although the timescale presented here is not the same, thus, leaching depths are not directly comparable. However, for example, calcite and hydrotalcite replaced the hydration products within the first 20 µm, while decalcification of CSH is predicted up to 30 µm. As already visible in figure 8.22, there is almost no calcite growth on top of

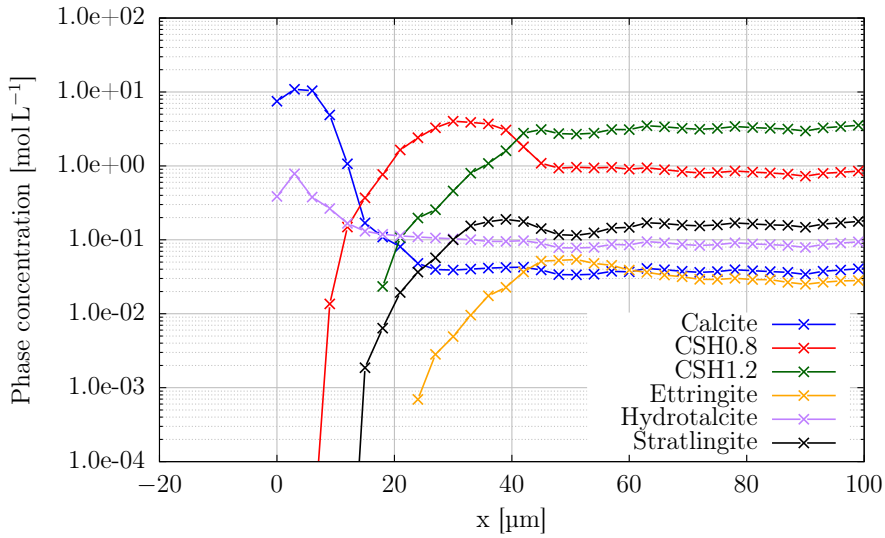

Figure 8.23: Average solid phase concentrations in the HCP at the interface after leaching with granite water for 80 min. The precipitation of solids was controlled by nucleation and porosity controlled solubility effects. Lines in this plot serve as guide to the eye.

the surface of the HCP, i.e. the calcite and hydrotalcite zone is quite limited in width. Further comparisons of the different simulations are presented in section 8.3.5.

The PCS apparently seems to smooth out numerical artifacts, which might cause for example non-physical negative porosities due to excessive precipitation of solids. The most important outcome of this model extension was that the minimum porosity does not need any artificial threshold, as typically used in reactive transport models, at least with the chosen boundary conditions and initial phase composition. Essentially, the porosity never undershot 0.3 % during the simulated leaching of low-pH HCP with granite water. Thus, with porosity controlled solubility, the lowest porosity was limited by some physical effect rather than by a preset numerical threshold. However, the minimum value achieved is specific for this kind of setup, i.e. the achieved supersaturation, the assumptions made with respect to CSH pore geometry and estimation of surface tension of precipitating solids. On the other hand, not all known nano-porous properties of hardened cement paste might be transferable directly into this concept. In this context it was assumed that the pore structure of hydration products mainly stems from the nitrogen accessible porosity of the CSH phase. Hence, the minimum achieved porosity might change if other assumptions are made.

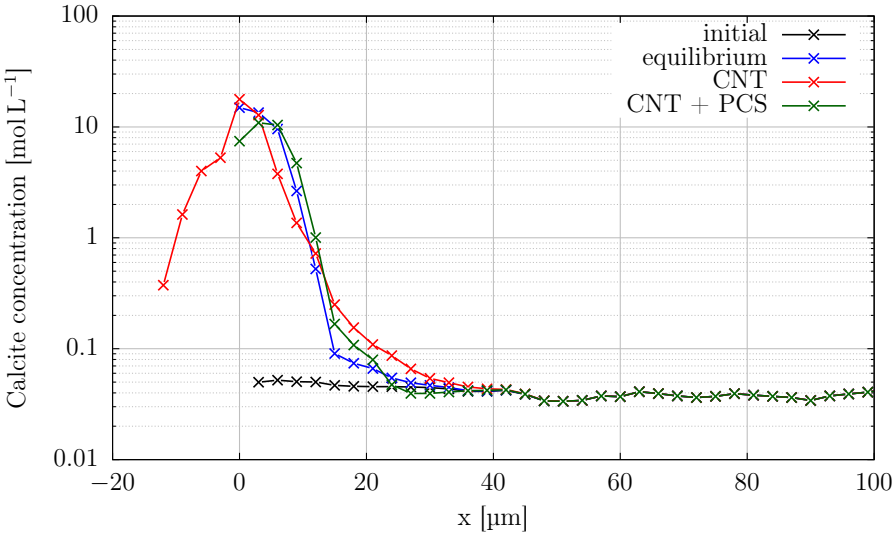

Figure 8.24: Comparison of simulated calcite concentrations close to the interface of the low-pH HCP monolith after leaching with granite water for 75 minutes for simulation cases using different approaches regarding mineral precipitation (CNT: classical nucleation theory, PCS: porosity controlled solubility). Lines in this plot serve as guide to the eye.

8.3.5 Comparison of the calculation cases

In this section all three simulation cases are compared to each other with respect to calcite precipitation, porosity and C/S ratios of the CSH phases after leaching. For this purpose, the simulation results after 75 min of leaching of the low-pH HCP with granitic water are used and compared to the initial conditions.

Figure 8.24 depicts the most obvious mineralogical change of the system, i.e. the precipitation of calcite at and close to the interface of the cement monolith in contact with the granite water. Apparently, the pure equilibrium approach shows the smallest zone with precipitated calcite compared to the other simulations. Furthermore, the precipitation outside of the monolith was limited in this case, because the boundary distance was modeled with one cell column reservoir only (at x = 0). As already mentioned, this was done to avoid the non-physical preferred precipitation of calcite in the reservoir volume.

After the inclusion of precipitation control by nucleation, it was possible to increase the reservoir without having this non-physical behavior, because homogeneous nucleation imposes a barrier. HON seems quite unlikely in such a small volume in the short time span at the moderate supersaturation with respect to calcite. Since precipitation is controlled by nucleation and the reservoir is large enough, crystallization does also occur on the surface of the monolith, developing some kind of coarse structure growing into

the initially free pore space reservoir (cf. figure 8.20). However, the highest amount of calcite is also present close to the initial interface (x = 0) and is even a bit higher than in the simulation with the pure equilibrium model. In general, the predicted calcite precipitation zone is broader, although the initial decrease in the first 15 µm of the monolith is slightly steeper than in the pure equilibrium model.

With the additional extension of the model by PCS, the calcite precipitation zone is slightly narrower again, compared to the approach including only nucleation theory. At the interface the amount of precipitated calcite has dropped already after 75 min to lower values, meaning the maximum is lower compared to the other simulations. In fact, the calcite content at the interface for the nucleation case is shifted by 3 µm to 6 µm, corresponding to one to two spatial discretization units. It seems that the complete zone is shifted by that distance towards the inside of the monolith. Moreover, after approximately 17 µm the PCS curve lies between the other two simpler models. All in all, after the simulated 75 min, the thickness of the calcite zone is between 20 µm for the equilibrium and PCS models, and 30 µm for the CNT model.

As comparison, carbonation experiments of C_3S pastes produced with a w/c ratio of 0.47 have shown a densely formed calcite crust of 5 µm to 10 µm on the surface of the sample after one week of submerging in carbonated water [Sei17]. Additionally, the authors conducted a pore-scale modeling study of a similar setup as the experiment. Accordingly, already after two hours of simulation, the surface was clogged while the calcite thickness was on average about 6.3 µm. In this experiment and the corresponding modeling study, portlandite was initially present. Moreover, the leaching water composition was different from the granite water, i.e. the carbonate concentration was higher while other solutes were not present. This leads to a higher supersaturation with respect to calcite at the interface at the HCP surface. Subsequently, an even more confined calcite rim can be formed. At the same time this causes a stronger passivating effect due to a decrease in diffusivity. Moreover, the presence of portlandite limits the diffusivity as well [Tay97, p. 291], while buffering the calcium concentration on a higher level than CSH. In particular, the CSH in the low-pH cement has a lower C/S ratio. Thus, the calcium concentration in equilibrium is lower than for the CSH within hardened C_3S pastes. Following this rationale, the reason for a broader calcite zone in the current study is explainable.

Moreover, the modeling results of Seigneur et al. suggest that 80 % of the calcite precipitated on the surface of the HCP material (cf. bottom part of table 8.9) [Sei17]. However, in their modeling study calcite was only allowed to precipitate in *macro* pores (>1.15 µm in their definition), thus preventing precipitation of calcite as embedded material within CSH. Some numerical experiments by increasing the diffusivity of CSH and/or the fraction of macro porosity reduced the amount of calcite precipitated on top, while increased the amount precipitated inside if the HCP material. The achieved fraction outside of the material was 30 % when increasing both parameters. However, the resulting effect of an increment of the macro porosity was more significant [Sei17].

In this study, using the CNT model within the leaching simulations lead to the highest fraction of calcite precipitated on the surface of the HCP monolith, while the lowest fraction is observed for the PCS model (cf. top part of table 8.9). At the same time,

Table 8.9: Fractions of calcite precipitated during leaching simulations outside of the initial HCP material of low-pH cement paste of the three different modeling approaches presented in this work (top). In comparison, precipitated calcite fraction of different simulations dealing with different C_3S pastes and diffusivity assumptions for CSH (bottom). The D_e^{ref} value was reported as $2.5 \times 10^{-11}\,m^2\,s^{-1}$ [Sei17], while in this work a diffusion coefficient of $8.26 \times 10^{-12}\,m^2\,s^{-1}$ was used for initial the hydration product phase (cf. section 7.4.4).

	model	macro porosity [%]	D_e^{CSH}	total calcite precipitate [µmol]	fraction outside [%]
this work	equilibrium			92	36
	CNT			108	61
	CNT + PCS			78	22
[Sei17]	reference	3	D_e^{ref}		80
	high / high	30	10 D_e^{ref}		32
	high / low	23	D_e^{ref}		30
	low / high	3	10 D_e^{ref}		53
	high / very low	23	D_e^{ref} / 10		53

the CNT model yields the highest total amount of precipitated calcite, while the results using the PCS model suggests a reduction of the total amount. Since no precipitation within the CSH was allowed in the model used by Seigneur et al., it is obvious that the formation spreads into the macro pores and into the outside volume. In the model of this work it is still allowed to precipitate calcite as embedded material within the CSH pore structure, which is also supported by observations [Šav16]. However, this comparison underlines the importance of a proper model to control precipitation.

Figure 8.25 shows the differences in predicted porosities close to the interface of the hardened cement paste and the granitic water. First, all three models agree that the lowest porosity developed close to the interface with the granite water. Additionally, all models show the down-up-down shaped porosity distribution, which was also reported by authors conducting carbonation experiments [Šav16]. The first domain is called carbonated zone while the domain with elevated porosity is called leached zone. Essentially, in the leached zone the CSH phase is decalcified and degraded, while in the carbonated zone the hydration products are replaced by calcite. In the simulated case, the granite water contains magnesium which leads to the precipitation of additional hydrotalcite in companion with the calcite, which also contributes to the reduction of porosity in the carbonated zone.

Compared to the more sophisticated models, the simulation results of the pure chemical equilibrium model suggest a narrower width of the degraded zone than in the other simulation cases. A more intense degradation is in agreement with the predicted distribution of newly formed calcite. This suggests that the predicted progress of degradation

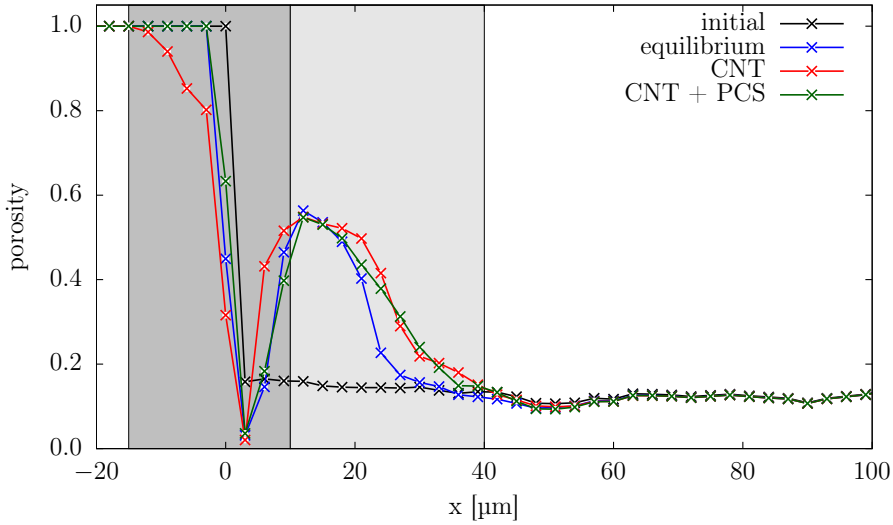

Figure 8.25: Comparison of the predicted porosity of the hardened cement paste close to the interface after leaching with granite water for 75 minutes for the three different simulation approaches (CNT: classical nucleation theory, PCS: porosity controlled solubility). The carbonated and degraded zones are indicated in gray (left) and lighter gray (right), respectively. Lines in this plot serve as guide to the eye.

with respect to porosity increase and carbonation is lower for the pure equilibrium approach compared to the more sophisticated simulations. This is due to the fact that with the pure equilibrium model pore clogging occurs earlier than in the other simulations. In particular, in the case of the simulations incorporating nucleation, calcite crystals grow on top of the surface, essentially imposing a sink term for carbonate such that the carbonate is no more able to ingress deeper into the monolith. Prevention of early clogging at the interface by including PCS and/or CNT thus retaining open pathways and reducing the effect of passivation leads to an increase in the predicted leaching and degradation kinetics.

In the nucleation and PCS simulations, the leaching front with increased porosity is shifted towards the inside of the monolith, which is in line with the observations done already for the calcite distribution. However, at a depth of 20 µm the porosity drops again comparable to the nucleation model, rendering the leached zone width smaller than for the nucleation model. Again, a similar observation was already made for the calcite distribution.

In figure 8.26 the C/S ratio in the CSH phase after leaching is depicted. All three models show a rapid drop of the C/S ratio from 1.13 to 0.8 close to the interface, which is the lowest stable CSH phase in the thermodynamic model used. It has to be noted that

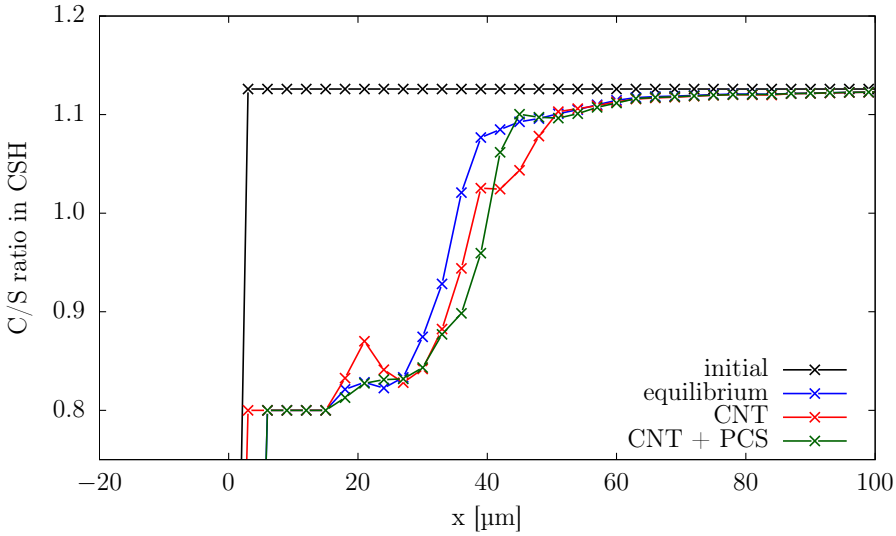

Figure 8.26: Comparison of the C/S ratio in the CSH phase close to the interface after leaching of low-pH HCP with granite water after 75 minutes for the three different simulation approaches (CNT: classical nucleation theory, PCS: porosity controlled solubility). Lines in this plot serve as guide to the eye.

the plot up to a depth of 17 µm from the interface is probably misleading, because CSH is only present in traces. However, starting from a depth of 30 µm it can be observed that the progress of decalcification of CSH is lower in the pure equilibrium modeling approach. This is again in line with earlier observations and deductions that earlier clogging at the interface reduces the leaching rate. Moreover, all three models are in agreement with respect to maximum CSH decalcification depth, i.e. after approximately 60 µm, there is only a slight CSH degradation observed and all models yield similar results. However, 60 µm is deeper than the degradation visible in the porosity plot which would suggest a leaching depth of approximately 50 µm (cf. figure 8.25).

In figure 8.27 the relative mass balances of calcite and hydrotalcite (top), CSH-0.8 and CSH-1.2 (bottom) are plotted. Obviously, for all three modeling approaches the CSH-0.8 content increases during leaching (dashed lines) on expense of CSH-1.2 (solid lines), due to the decalcification of the CSH phase. At the same time, all three models predict an increase in calcite content. As already indicated in figure 8.24, the simulation including nucleation effects has the highest build-up of calcite. The lowest increase in calcite is observed for the PCS approach, resulting from a hindrance of calcite precipitation. On the other hand, the amount of precipitated hydrotalcite is the highest applying the PCS effect in the simulation (dashed lines). This is likely because hydrotalcite has a significantly lower surface tension value than calcite, i.e. $26\,\mathrm{mJ\,m^{-2}}$ compared to

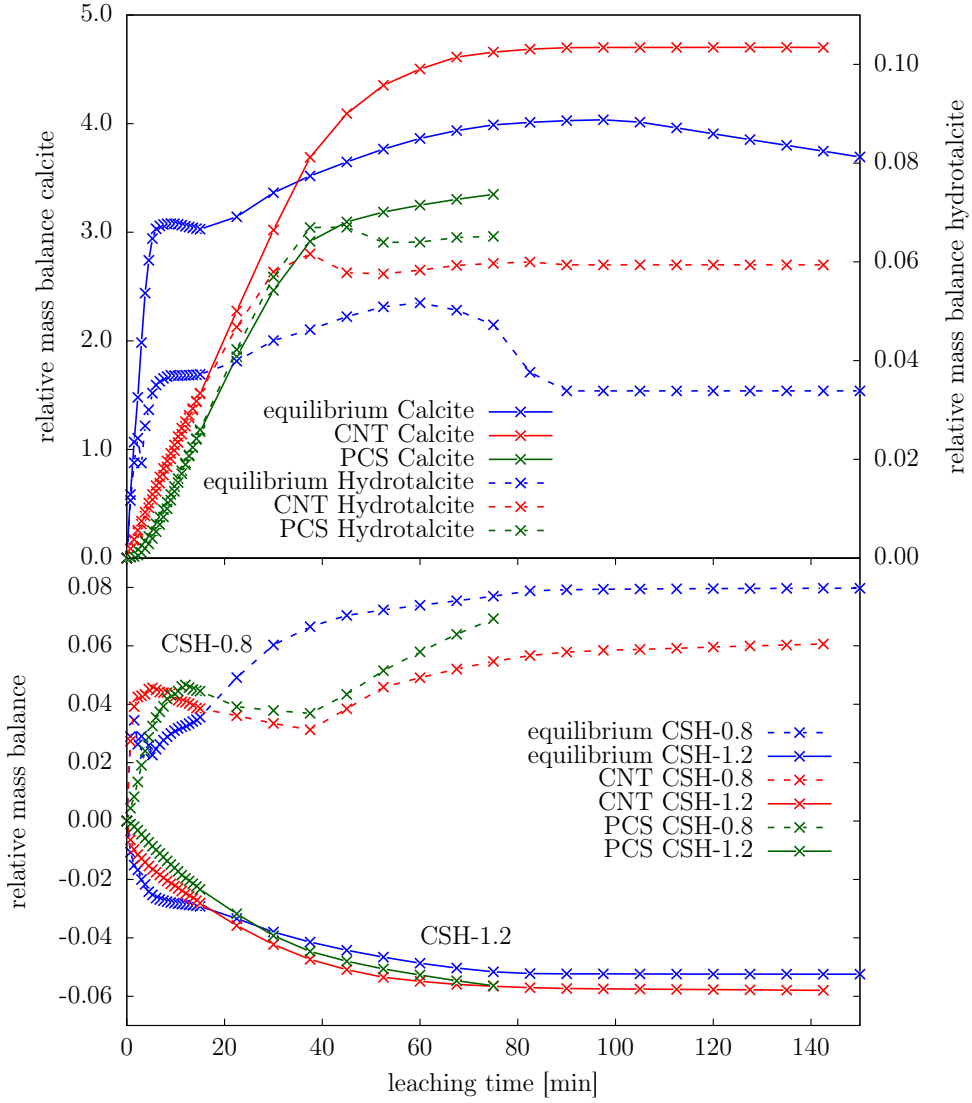

Figure 8.27: Comparison of the relative mass balances of calcite and hydrotalcite (top) and the two occurring CSH phases (bottom), i.e. CSH-0.8 and CSH-1.2, as function of leaching time. Note that the hydrotalcite data correspond to the axis on the right. The data were generated using the three different simulation approaches. Lines in this plot serve as guide to the eye.

$98\,\mathrm{mJ\,m^{-2}}$, respectively (cf. table 7.15). Thus, in confined pores the energy barrier to precipitate hydrotalcite is lower than for calcite, i.e. the required supersaturation to initiate precipitation is lower. This suggests that not only the microstructure is affected by the PCS mechanism but also the resulting phase assemblage.

Although the numerical values used as inputs for determination of the nucleation rates and porosity controlled thermodynamic shift might not be perfectly accurate and based on various assumptions, the results still show a trend. A general output of this analysis is that both physical effects, CNT and PCS, in addition to local thermodynamic equilibrium assumptions, have non-negligible effects on the leaching rate, phase distribution and resulting porosities in particular at the interface to the leaching water. Although the simulations carried out in this study were limited in time scales due to computational restrictions, it is to be expected that the effects will turn out to be more pronounced on longer time scales.

It has to be pointed out that all simulations performed are neglecting mechanical stress on the HCP microstructure. It is still under debate to which extent the formation of solids induces pressure [Fla02,Sch04,Ste05b]. Furthermore, it is thinkable that the precipitation of calcite in confined pores during carbonation of cementitious materials induces to some extent stress. However, there is still debate in the scientific community, if precipitation of solids in confined pores causes pressure or if the precipitation is prevented by this effect. By using the PCS model in this study, which is derived from the Kelvin equation as well as crystallization pressure, it is assumed that precipitation is prevented if the super saturation is moderate. If mechanical stress by pressure plays a role in the process, the formation of cracks is possible, while subsequently increasing diffusivity. On the other hand, precipitation of solids in the structure of CSH might also compress the material and reduce its diffusivity.

8.3.6 Computational performance

Within this section, the restrictions with respect to simulated leaching time will be analyzed. Obviously, the simulated leaching times in the range of 1 h to 2 h physical time are not suitable to be compared to long term leaching experiments. In the following paragraphs the limiting factors and possible treatments within iPP are outlined. Moreover, an estimation for the range of simulation times which would be feasible if the treatments would be successful is given.

The simulations were run either on an in-house cluster of the IEK-6 and/or on the JURECA cluster of the Jülich Supercomputing center (JSC) of the research center Jülich. The capabilities of the clusters were briefly described in previous performance scalability section 6.4. Depending on the cluster, the number of used compute nodes and performance characteristics differ. For example, one iteration on the IEK-6 cluster took about 300 ms using 8 compute nodes corresponding to 64 CPU cores, while the performance improved to 230 ms per iteration using 16 compute nodes (128 CPU cores). The speedup is only moderate on this cluster, which was already reported in more detail in section 6.4. On the other hand, on the JURECA cluster one complete iteration took 180 ms by using 8 compute nodes, which corresponds to 384 threads and 192 CPU cores, respectively.

JURECA was in particular used to simulate the PCS model while the other simulations of HPC leaching by granitic water were carried out on the IEK-6 cluster.

Deeper analysis and performance profiling of the JURECA runtime characteristics have revealed that less than 1 % of the runtime is actually spent during the LBM transport step. The pure runtime of the *PhreeqcRM::runCells()* function calls of the PhreeqC chemical equilibrium calculation accounts for 45 %. A rather large fraction of about 10 % is spent in the collective operation for preparing of the heterogeneous reaction terms as described in section 4.4.1.3. Moreover, another large chunk of 39 % of the time was used to update the post-reaction state in the transport code. This part of the coupling code includes the update of all source terms, porosities, diffusion coefficients, geometries, etc. All this can be regarded as auxiliary computation either to treat heterogeneous reaction terms or to feed-back information to the transport code. It has to be noted that these large fractions only occur when using a high parallelized setup of a simulation. Running iPP with a few CPU cores only yields that the PhreeqC calculations consume more than 90 % of the runtime.

Both code branches, the collective operation for the heterogeneous reaction term and the updates of the transport properties, were already optimized with respect to runtime performance to some extent. However, the residual bottlenecks are in the treatment of the lattice data structures within Palabos. In particular, the implementation within Palabos invokes data exchange via synchronous MPI calls. With regard to end-user usage simplicity this is meaningful but causes bottlenecks with respect to parallel computing scalability, if multiple lattices are in use at the same time. Within this work a commonly used technique was applied, which uses one lattice for each solute. Thus, an increasing number of transported components causes an increase of the bottleneck there as well. Implementing a potentially better performing asynchronous approach would mean that the caller of some Palabos functions must take care of explicit synchronizations at particular points in the code path. Although it was not evaluated to implement an asynchronous approach within Palabos, it is expected that the issues of both bottlenecks would improve significantly.

Following this, it can be deduced that the 49 % fraction of auxiliary computation time can be improved with reasonable efforts. However, the geochemical solver PhreeqC uses still a significant amount of computational overhead. Improving the other parts, the fraction of runtime spend in PhreeqC even increases. One conclusion drawn here is that either in depth improvements within PhreeqC must be done, the chemical solver must be replaced by another better performing one, a lookup table approach or other surrogate model approaches need to be applied. However, the lookup table approach might be quite complicated and memory demanding as well, e.g. when treating a high number of chemical species, various phases, solid solutions and kinetic laws. Recent developments in the field of geochemical solvers show promising results, e.g. usage of machine learning in the framework of the solver Reaktoro. Reaktoro is claimed to improve the performance of the chemical calculations by two orders of magnitudes compared to conventional approaches [Lea17]. Using such a solver might mitigate the computational barriers faced in this work, although Reaktoro might not yet support all features required by iPP, e.g. to implement nucleation theory and porosity controlled solubility effects.

All in all, the pure equilibrium simulation was carried out spending 23,000 CPU-hours, with a runtime of 15 d, the nucleation theory extended model took 55 d run time and 85,000 CPU-hours. The most sophisticated model, the PCS simulation, was run on the JURECA cluster [Kra18] and took almost 30 d, while spending 130,000 CPU-hours. The magnitude of simulated leaching times, i.e. in the range of 1 h to 2 h physical time, were not deliberately chosen, but rather limited due to current computational performance constraints as outlined above.

Removing the mentioned bottlenecks of 45 % (chemistry calculations within PhreeqC) and 49 % (explicit MPI synchronization within Palabos) completely, would uplift the performance by a factor of 50. Effectively, this would allow simulating about 62.5 h of leaching time using cluster computers as JURECA by spending 130,000 CPU-hours within one month of time. Since the scalability would have improved, it would be justified to use more than 8 compute nodes. Assuming to use 24 compute nodes instead (i.e. 576 CPU cores, 1152 threads), within a runtime of about one month, about one week of simulated leaching time might be achievable. One week of leaching is more realistic for an experimental setup as the degradation and connected effects should be more pronounced. However, since the exchange of the geochemical solver and subsequent evaluation, and the further MPI extension of Palabos is out of the scope of this work, it was not tested, and these values are based on a rough estimation only and should be regarded as potential outlook for applications of iPP. Still it is prudent to advance developments in these directions, because the fundamental problems cannot be completely compensated nor solved with a future hardware generation. The issues observed and discussed here address bottlenecks in the parallelization and super computers rely on a good parallelization of the underlying algorithms to perform and scale well.

It has to be noted here that the time and length scales required for simulating processes relevant in nuclear waste repositories, e.g. cement waste interactions and simulation of clay cement interfaces, are much higher. Thus, simulations of repositories using a pore-scale resolution are out of reach for foreseeable future. Accordingly, more sophisticated methods must be found, which will hopefully allow an upscaling of reactive transport simulations towards longer spatial and temporal scales.

8.4 Effective diffusivity of leached low-pH HCP

8.4.1 Model setup

8.4.1.1 Overview

In the previous chapter, three different approaches for simulating the leaching process of low-pH cement paste with granite water on the pore-scale were presented. Beginning with the basic assumption of strict equilibrium chemistry, incorporating classical nucleation theory for calcite precipitation and at last the extension of the model with porosity controlled solubility effects. The alteration of hardened cement paste caused by chemical agents leads to changed transport properties. Microstructural changes of different kinds can be observed. One major effect was the dissolution of CSH and subsequently

Table 8.10: Essential information about the modeling setup of the simulation for determination of the effective diffusion coefficient of the degraded low-pH HCP after leaching with granite water. The value for ϕ_{ref} was dynamically set and subsequently the temporal step Δt (cf. section 8.4.1.3). The degrees of freedom correspond to the product of the number of nodes and transported solutes.

property	value
LBM scheme	P-TRT
lattice stencil	D2Q5
LBM nodes	$250 \times 250 = 62500$
D_{ref}	$5 \times 10^{-10}\,\mathrm{m^2\,s^{-1}}$
ϕ_{min}	0.001
ϕ_{ref}	dynamic, starts with 0.0001
Δx	3 µm
Δt	dynamic, 0.3 µs for $\phi_{ref} = 1$
number transported solutes	1
thermodynamic database	ThermoChimie_eDH_v9b0 (for initialization only)
CSH model	3 discrete phases
degrees of freedom	62500 (no phases)

replacing its space by calcite and hydrotalcite, consequently reducing the porosity in the outer carbonated zone of the HCP monolith. An observation already made was that the outer surface of the HCP was either almost or completely clogged due to calcite and hydrotalcite precipitation. Although the hydration products in the inside of the monolith are degraded and thus have an increased diffusivity, the clogged outer shell results in a significant reduction of overall diffusivity.

Although the simulated timescale of the leaching process was limited by the computational performance of the geochemical solver PhreeqC, in this chapter the effect of these microstructural changes on the effective diffusivity of the low-pH HCP are presented. The effective diffusion coefficients of the 2D HCP monolith perpendicular to the leaching front are estimated in dependency of the leaching time. For this, the approach described in section 8.1.2.4 was applied to the microstructures simulated at different time steps. The input data are originating from the results obtained by the simulations of leaching of the low-pH HCP with granite water. More modeling setup parameters are given in table 8.10.

8.4.1.2 Diffusivity law for calcite

In simulations detailed in the previous chapter, the CSH phase was the primary diffusive phase constituting the whole pore network. A total porosity lower than 15 % at a certain Lattice-Boltzmann node was considered as non-diffusive, although this is a simplified assumption. At porosities below this threshold, the node is switched to a heterogeneous

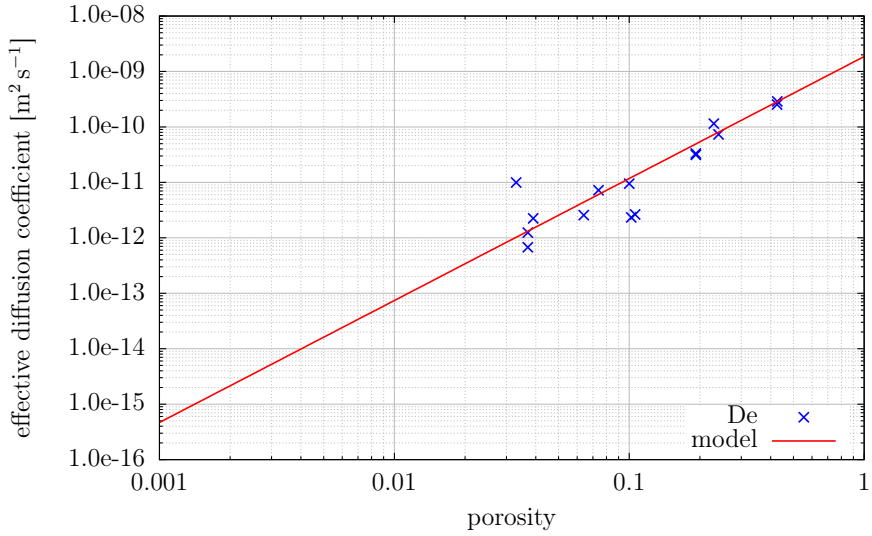

Figure 8.28: Experimentally determined effective diffusion coefficients of limestone samples using iodide as tracer. Free water diffusion coefficient of iodide was assumed as $1.86 \times 10^{-9}\,\mathrm{m^2\,s^{-1}}$ [Bov01]. The fit uses an Archie's law approach with an exponent of 2.2.

reaction term (cf. section 8.3.1). On the other hand, it is known that limestone, which is mainly calcium carbonate, is still diffusive at low porosities down to a few percent [Bov01]. Nevertheless, the diffusion coefficients are quite small and the assumption, to regard nodes with a porosity lower than 15 % as non-diffusive, during reactive transport simulation was regarded as acceptable.

However, for the determination of effective diffusion coefficients of carbonated cement paste, the diffusivity of the calcite layer is expected to play a rather crucial role. In order to apply a diffusivity-porosity relationship for the calcite layer, a model was developed based on the CSH effective medium diffusivity and experimentally obtained data for limestone. The derived diffusivity law applicable to limestone is based on Archie's law (see equation 8.6) fitted to experimental data obtained from through-diffusion experiments [Bov01]. The effective diffusivity data are plotted in figure 8.28 in conjunction with the fitted exponential law. The exponent m used to fit the model to the data points was determined to be 2.2 [Bov01].

$$D_e^a = D_w \phi^m \tag{8.6}$$

The desired formulation of the diffusivity relationship needs to be consistent with the previously used formulation during the reactive transport simulations. To this end, an extension is required rather than a replacement. Since all reactive transport simulations

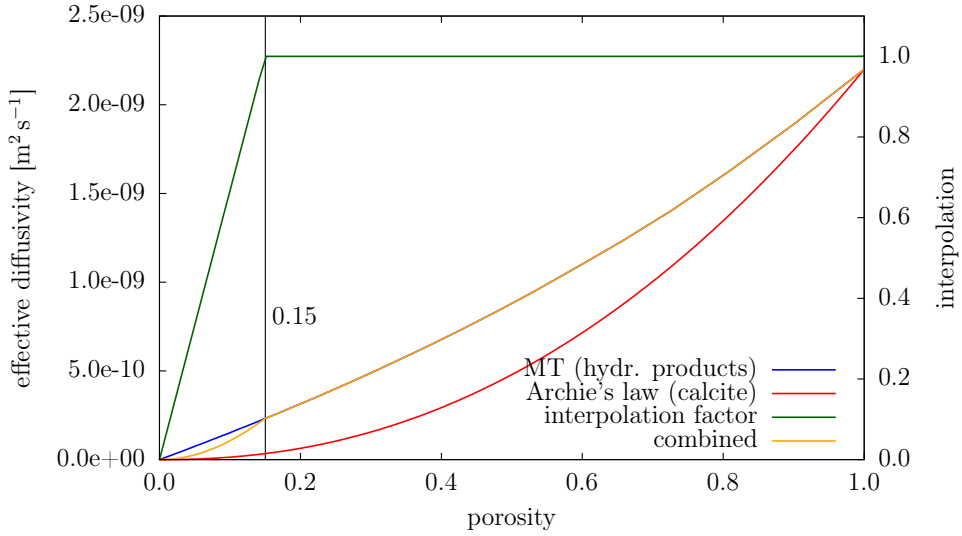

Figure 8.29: Effective diffusion coefficients of hydration products according to the homogenization scheme, of calcite (based on Archie's law) and their linear combination in the low porosity regime. The values of the diffusion coefficients correspond to the left axis while the interpolation curve corresponds to the axis right.

before used a porosity threshold value of 15 % (cf. section 8.3.1), the diffusivity law valid for porosities above this threshold are considered purely governed by the homogenization model used for the hydration products as described in section 7.4.4. Consequently, the Archie's law approach was used only for porosities less than the 15 % threshold. However, directly applying Archie's law would lead to a non-continuous function. Therefore, a smooth interpolation was introduced:

$$t = \begin{cases} \frac{\phi}{\phi_t} & \text{if } \phi \leq \phi_t \\ 1 & \text{if } \phi > \phi_t \end{cases} \tag{8.7}$$

The resulting interpolation value is plotted in figure 8.29 as green line. Subsequently, this interpolation value is used in a linear interpolation function:

$$D_e = D_e^{MT} t + (1 - t)\, D_e^a \tag{8.8}$$

Basically the interpolation value t dictates a linear relationship between a porosity of zero and 15 % and clamping to the Mori-Tanaka approach above that threshold value. An example of a Mori-Tanaka based hydration product diffusivity law without inclusions (cf. section 7.4.4) and the Archie's law based calcite diffusivity relationship in combination

with the resulting interpolated curve is shown in figure 8.29.

As already mentioned, the effect does only come into play below the porosity threshold of 15 %. A rather low diffusivity reduction effect corresponding to the calcite diffusivity law is present down to 10 %, since the combined function takes the Archie's law approach for calcite into account only for one third. However, the effect then subsequently becomes more pronounced towards zero porosity, i.e at a porosity of 1.4 % the resulting diffusivity is one order of magnitude lower than the one from the original effective medium approach alone (cf. respective blue and orange curves in figure 8.29 at the bottom-left).

Moreover, the porosity of non-inert nodes during the reactive transport simulations were limited to a minimum porosity, i.e. 0.1 %. This was done to prevent negative porosities and subsequently numerical issues. However, it is assumed that reaction cells with porosities equal or lower than this value are completely filled with solid material and are non-diffusive at all for the through-diffusion simulations in this chapter. The minimum diffusivity according to this combined model at a porosity slightly higher than the threshold value of 0.1 % is $1.09 \times 10^{-14}\,\mathrm{m^2\,s^{-1}}$. Subsequently, this value will be assigned to the cells containing calcite which formed the low porosity rim at the interface.

8.4.1.3 Convergence optimization

In contrast to the reactive transport simulations for the degradation and carbonation of hardened cement paste (see chapter 8.3), the lowest porosity to be treated by the transport step is in this case much smaller. While the reactive transport simulations used a porosity threshold of 15 % to determine c_ϕ of the Lattice-Boltzmann P-TRT scheme, here a value of 0.1 % was needed. This in turn degrades the computational performance of the whole simulation by reducing the physical time step per iteration (cf. equation 4.10). Using a threshold porosity of 15 %, as used in the reactive transport simulations (cf. chapter 8.3), one iteration corresponded to 0.45 ms. However, a reduction of the minimum treatable porosity to 0.1 % yields a time step of 0.3 µs. Obviously, limited by such small time steps, the simulation of the through-diffusion setup would take too many iterations and much computational time to reach steady-state. Thus, an approach to overcome this limitation had to be developed and applied.

Since only the final steady-state flux result of the through-diffusion simulation is of interest to determine the effective diffusion coefficient, the intermediate values towards the converged value are not of direct relevance. On the other hand, during reactive transport simulations, small errors can easily show self-amplifying oscillations due to the chemical feedback and thus need to be prevented. In contrast to the reactive transport simulation, it is possible to determine roughly estimated intermediate diffusive flux results for the though-diffusion simulations.

To achieve an optimization for reaching the steady-state solution, a reference porosity variable ϕ_{ref} was introduced into equations 3.73 and 4.10:

$$D_e^{LB} = \frac{c_\phi}{\phi_{ref}} \left(\tau_a - \frac{1}{2} \right) \tag{8.9}$$

$$\Delta t = T_c = \frac{L_c^2}{D} \frac{c_\phi}{\phi_{ref}} \left(\tau_a - \frac{1}{2} \right) \tag{8.10}$$

This is a linear factor which alters the effect of c_ϕ in the system of equations and is of purely numerical nature, i.e. has no direct physical meaning for the simulated setup. A reduction of ϕ_{ref} can be regarded as a corresponding increase of c_ϕ and thus Δt. As stated in section 3.5.9.4, the factor c_ϕ cannot be altered arbitrarily without causing numerical oscillations and hurting stability in case of presence of porosities in the computational domain, which are lower than ϕ_{min}. Choosing a very low reference porosity leads therefore to an exaggerated time step. It is very likely that intermediate oscillations and inaccuracies would stem from this. However, this is sufficient to get a first approximated steady-state solution.

When the convergence criterion is reached with this fast-forward configuration, the reference porosity ϕ_{ref} is increased by a factor of two. Subsequently, the procedure of satisfying convergence is repeated, and again the reference porosity is increased. This routine is repeated until the final reference porosity of one is reached, and the convergence criterion is met. Although the convergence must be found several times, the simulation converges to the steady-state solution several orders of magnitude faster than running directly with the final reference porosity of one.

8.4.2 Results

The resulting effective diffusion coefficients of the degraded HCP in dependency of leaching time are depicted in figure 8.30. The effective diffusivity corresponds to the complete 2D monolith perpendicular to the leaching front. Apparently, with the chosen diffusivity model (cf. section 8.4.1.2) for low porous calcite ($\phi < 1\,\%$), the tiny rim has only limited absolute effect on the diffusivity. However, this is likely only a matter of the limited leaching time addressed in the underlying simulations.

After 30 min the calcite/hydrotalcite crust is almost completely covering the surface of the monolith and thus clog the pores close to the interface. However, due to clogging the solutes are getting separated and essentially to some extent the calcite is redissolving again. This effect opens pinholes from time to time which are pathways for the through-diffusion resulting in an increased effective diffusion coefficient of the monolith. The pinholes work as some kind of binary switches which are adding discrete flux terms. This is the main reason for the fluctuations apparent for the pure equilibrium and nucleation models. However, the PCS approach shows a smooth transient behavior. In that case, no complete clogging did occur, since the calcite rim has never reached porosities of less than 0.3 %, which is still diffusive in the applied calcite diffusivity model.

Again, it has to be noted that no mechanical stress is taken into consideration within this study. On the other hand, there are some experimental indications that carbonation triggers such effects with complex mechanisms (see [Šav16] and the references within). Possible formation of cracks could render the diffusivity much higher because of opening pathways. Furthermore, the initial conditions are likely playing a major role. For instance, OPC contains initially portlandite, which is replaced by calcite during carbon-

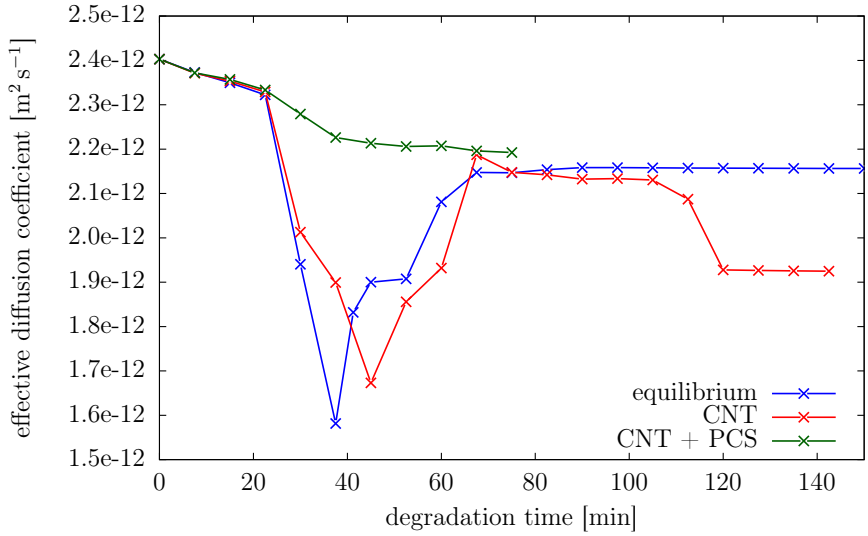

Figure 8.30: Effective diffusion coefficients for degraded cement paste based on reactive transport simulations with different complexities. The connecting lines are only guidance to the eye.

ation. Since the molar volume of calcite is higher than that of portlandite, the porosity is reduced, which may cause mechanical stress. In the case of a low-pH cement paste, which is analyzed in this work, however, there is no portlandite present and the calcium source for calcite formation is mainly the CSH phase. Since CSH has a higher molar volume than calcite, a general porosity increase is an obvious macroscopic effect when such a hardened cement paste is carbonated. A simplified view on the matter would suggest that in this case no mechanical stress would occur due to carbonation and the diffusivity is expected to increase. Under consideration of a more detailed analysis the process revealed to be more complex. In particular, it was shown in this study that the locality of the precipitated calcite plays a role with respect to clogging and possibly mechanical stress, i.e. the stress would rather be introduced in the carbonation zone than in the CSH leaching zone. At the same time the diffusivity has been reduced because the calcite mainly precipitated in a confined zone only.

9 Conclusions and outlook

9.1 Summary and conclusions

Cementitious materials are widely used in repository systems for the final disposal of radioactive wastes, e.g. as construction material, as buffer/backfill material, in some waste containers, or for solidification of wastes. The macro-scale transport properties of concretes and mortars and the chemical conditions in cementitious materials strongly depend on the evolution of pore structure and phase assemblage during hydration and long-term alteration. Although cementitious materials are ubiquitous, the long-term evolution of several material properties, such as the relation between the microscopic pore structure and macroscopic properties, are not well understood. In this work the microscopic degradation mechanisms in cementitious materials were investigated by pore-scale reactive transport modeling techniques, which deal with resolutions in the micro-meter scale. Cementitious materials are complex composites of various phases and hydration products and with multi-scale heterogeneity, rendering it a challenging system for reactive transport modeling approaches.

By using the Lattice-Boltzmann method (LBM) and a geochemical solver, a reactive transport code named iPP was developed, which can perform reactive transport simulations on the pore-scale. This tool was used to address the chemical evolution of porous media and associated changes of transport parameters, using an explicit coupling between the geochemical reactions and the transport simulation, i.e. without using pre-calculated geochemical conditions in the form of look-up tables.

The code iPP has been developed in particular with the aim of efficient high performance computing capabilities, e.g. by an algorithmic implementation with parallelization for distributed memory architectures (i.e. MPI), which allows for the utilization of thousands of CPU cores. This capability is obviously beneficial in contrast to a shared memory model such as OpenMP, which can only utilize one single compute node, i.e. a maximum of 64 CPU cores for recent CPU architectures. Moreover, due to the employed C++ template meta-programming techniques for implementing iPP, sophisticated compiler optimizations can be utilized, e.g. allowing the compiler's optimizer to perform loop unrolling, SIMD vectorizations and other sophisticated high level code transformation.

Although the groundwork for the solute transport module was already available by using the LBM code Palabos, various extensions had to be implemented to provide a proper foundation for a reactive transport simulator. The transport code required to support high contrasts in diffusion coefficients among model domains, which was mandatory since the gel porosity of the CSH phase in nano-meter scale cannot be spatially resolved at the same time as the capillary porosity of the HCP, which is in the scale of micro-meters.

Thus, the gel porosity was not resolved explicitly, rather a multi-scale homogenization model for the diffusion coefficient of the CSH phase was applied. The P-TRT scheme [Vik14] revealed as satisfying technique for this requirement, which needed to be implemented as extension to Palabos in the framework of iPP. Furthermore, a new internal boundary condition scheme for LBM was developed in order to simulate heterogeneous chemical reactions.

The Lattice-Boltzmann transport code was coupled to PhreeqcRM, which is a reaction module implementation for the well-established geochemical solver PhreeqC. Although in this work focus was on PhreeqC, couplings to other potentially more efficient geochemical reaction solvers are easily feasible in the future, due to the modular programming techniques employed within iPP. In addition, the abstract C++ programming interfaces allow for the easy extension of several algorithmic details (e.g. data input/output, definitions of boundary conditions, CSH gel porosity model, diffusivity laws, etc.) without changing implementation details extensively.

Several benchmarks were conducted to proof the validity of the transport and reactive transport features of iPP. The results of these simulation benchmarks were compared to analytical and/or numerical solutions of other reactive transport codes. As a further comprehensive test, a model using a numerically generated 3D microstructure of a cementitious system was simulated. The microstructure was generated by a numerical cement hydration code (CEMHY3D) using a composition of Ordinary Portland Cement (OPC) as input. Within this simulation, a cubic monolith of fresh HCP was leached by deionized water. The typical phenomena of portlandite dissolution and decalcification of the CSH at the interface were observed, which consequently lead to the well-known porosity and diffusivity increases.

Furthermore, a new segmentation technique was developed and subsequently applied to derive microstructural properties from μ-XCT image data of a low-pH HCP sample. Unfortunately, the spatial resolution and noise did not allow to distinguish between separate hydration products. However, by application of a thermodynamic hydration model the composition of the hydration phase could be estimated. A representative 2D slice of the derived microstructure was subsequently used as geometrical input for calculations simulating the ingress of solutes originating from granite water into the hydrated low-pH cement paste.

Besides the expected results as decalcification of CSH and the resulting porosity increase within the HCP monolith, the carbonate content of the granite water led to rather quick formation of a calcite crust on the surface of the monolith. This led to a clogging and passivation of the HCP. From experiences, it is unlikely that a dense 3 µm thick rim of carbonates would be formed on the surface of the material stopping further carbonation (e.g. [Šav16,Sei17]). Moreover, in order to prevent non-physical negative porosities, in this simulation a limiting pre-selected minimum porosity of 0.1 % was required.

In order to analyze various pore-scale effects, for once the locality of precipitation and possible clogging limiting effects, the classical nucleation theory (CNT) was implemented in iPP and subsequently incorporated into the model. Values of kinetic properties such as surface tension and number of nucleation sites were required for the simulations. Values for surface tension were taken from experimental data compiled by other authors,

while the number of nucleation sites was derived in this work. In consequence, the simulations using the extended model showed that calcite now precipitated preferentially on the surface of the HCP monolith, however, compared to the pure equilibrium model, in a broader and more heterogeneous pattern. Although leaching with nucleation effects included left open pathways for a longer time, clogging was only delayed and not prevented completely. Still, similar to the pure equilibrium model, also a pre-selected minimum porosity was required, to prevent negative porosities.

In order to mitigate the artificial modeling assumption of a minimum porosity, in a following development iteration the PCS (pore size controlled solubility) effect was implemented in iPP. To apply the PCS theory, some derivations and assumptions about the CSH phase were made, e.g. the curvature of assumed cylindrical pores were estimated with help of specific surface area data taken from literature. The new feature was applied to the leaching model, too, resulting in a smoother carbonated zone. Moreover, the minimum porosity achieved was no more limited artificially by a pre-selected assumption. Under the assumptions about the CSH microstructure and the moderate supersaturation of the leaching solution with respect to calcite, the limiting minimum porosity of the low-pH HCP is about 0.3 %.

The outputs of the leaching simulations of the low-pH HCP were used as input for steady-state through diffusion simulations. By these simulations the effective diffusion coefficients of the degraded cement paste were determined. Here, an Archie's law-based diffusivity model for the precipitated calcite was applied. Although this diffusivity model was based on rough estimations, it turned out that the leaching simulations taking into account the PCS effects yield to the smoothest transition of the effective diffusion coefficients. On the other hand, the results of the pure equilibrium and CNT models showed temporarily an almost clogged state. However, compared to the pure equilibrium model, the CNT model retarded and reduced the clogging effect slightly. The limited leaching rates and passivation effects due to calcite formation are qualitatively in agreement with the experiments performed with the CEBAMA reference cement paste as well as observations published in literature [Dei21,Nee22].

Although several optimization steps were conducted within PhreeqcRM in the scope of this work, the geochemical solver revealed as the limiting factor with regard to computational performance for the pore-scale reactive transport simulations of the degradation of cementitious materials using iPP. Almost 50 % of the simulation time was spent within the chemical equilibrium calculations when applying a rather highly parallelized computing setup. In single threaded mode, this fraction is even higher ($> 90\,\%$). On the other hand, the simulations also revealed some parallelization bottlenecks in the decomposed data synchronization within Palabos, thus the difference between a low and high parallelized setup. Although PhreeqcRM was optimized within this work, optimization measures within Palabos were out the scope due to development time constraints. Thus, the timescale possible to be simulated by the applied method and the third party software modules (PhreeqcRM and Palabos) used within iPP is limited to a few hours of physical time, when dealing with resolutions in the micrometer scale for models in the millimeter scale.

However, iPP turned out to be a valuable tool to analyze microscopic effects and with

its help it is possible to derive constitutive relations for transport properties of cementitious materials. In particular, the implementation of CNT and PCS and subsequent application on cementitious materials is innovative. Besides the already outlined bottlenecks, which are located in the third party codes, the computational runtime behavior of iPP itself has a low overhead, due to the efficient usage of modern C++ design and programming paradigms as template meta-programming. Moreover, the efficient algorithmic implementation and usage of the distributed memory architecture MPI allows for computational scalability on supercomputers in HPC facilities.

Pore-scale reactive transport models such as iPP provide the means to enhance the understanding of the impact of the long-term alteration processes (e.g. leaching by groundwater, carbonation, reactions at clay/cement interfaces, etc.) on the transport properties of cementitious barrier materials, e.g. with respect to solute transport/radionuclide migration. Thus, it can be employed as process models in support of the safety case. Moreover, an enhanced understanding of the evolution of transport properties on the pore-scale might facilitate the selection of optimized cementitious materials for specific purposes in repository design.

9.2 Outlook

The development of meaningful pore-scale models for simulating the alteration of (low-pH) cementitious materials revealed several shortcomings in the understanding of the processes involved. Although high-resolution imaging techniques were used to describe the microstructure of the porous medium, the provided μ-XCT image data could not fully resolve the pore structure and hydration products in the cementitious material. Consequently, the homogenization approach used for the derivation of the modeling input introduces more uncertainty and does not follow a pure pore-scale modeling approach. Imaging techniques with a higher resolution and signal-noise-ratio are required to resolve the required geometrical information.

Besides the phase assemblage and capillary porosity distribution, it is not completely understood how the nano structure of the CSH gel affects the diffusivity of the CSH phase mechanistically. Some authors reported a constrictivity effect within the pore space of CSH [Phu19], which was taken as given factor in this work and not derived mechanistically.

Furthermore, to apply the CNT model to control the precipitation of calcite, parameters were derived from experiments dealing with homogeneous nucleation of calcite in water and heterogeneous nucleation on quartz. The data required are values for surface tension in free water and on substrates (contact angle), and the number of nucleation sites on substrates. The literature is scarce with respect to data required for application of a nucleation theory model, even for common cement hydration products, for both, substrates and nucleating phases.

Moreover, the evolving intrinsic structure of secondary phases such as calcite, in particular in the context of cementitious systems, is not fully understood. For the setup of the PCS simulations conducted in this work, simplified assumptions about the inter-

nal CSH pore structure and about the surface tensions of secondary phases were made. So-called *lab-on-chip* experiments are a promising approach to analyze the evolving microstructures and phase formations in an in-situ setup [Poo22b]. The outcome of such experiments might help to parameterize properties of the forming secondary phases in a better way, in order to reduce the uncertainties of a pore-scale reactive transport model.

In addition, it was assumed in the simulations that clinker grains were chemically inert, because no kinetic rate laws were available from experiments to describe the rates of the hydration reactions at the microscopic scale, although leaching experiments suggest ongoing clinker hydration in the CEBAMA reference paste for prolonged times. To reduce these uncertainties, further data on the hydration kinetics of the clinker phases on the microscopic scale must be obtained. Moreover, a pore-scale hydration model would involve water transport within the pore structure.

With regard to computational performance, the simulations revealed as computational demanding and required long program execution times even on multi-processor computer clusters. The geochemical simulator PhreeqC has shown significant limitations here. There are several promising possibilities how the boundary might be pushed towards longer simulated time scales by either exchanging the algorithmic approach or optimizing further the currently used third party software packages. For example, a common approach in the field of reactive transport simulations is to use look-up tables, which have their own downsides, e.g. restrictions to specific geochemical systems. Another promising approach to relax this bottleneck might be to replace PhreeqC with a better scaling implementation, e.g. with the machine learning based code *Reaktoro* [Lea17] or other neural network based approaches [Lal21]. In this context, as an alternative to explicit chemical calculations, multidimensional pre-calculated look-up tables adequate for the complexity of the chemical systems might be used, but requiring further developments of highly efficient data science algorithms and machine learning techniques.

However, even with an optimistic estimation on the performance improvements, a nuclear waste repository cannot be simulated using a pore-scale resolution in the foreseeable future. Thus, efficient upscaling approaches, both on the spatial and on the temporal scale, are required to transfer the results from the pore-scale simulations to the continuum scale, taking into account the spatial extensions and time scales relevant for the description of long term experiments or repository system evolution.

References

[Aar70] H. B. Aaron, D. Fainstein, and G. R. Kotler. "Diffusion-limited phase transformations: A comparison and critical evaluation of the mathematical approximations". In: *Journal of Applied Physics* 41.11 (1970), pp. 4404–4410.

[Ahr05] J. Ahrens, B. Geveci, and C. Law. *ParaView: An End-User Tool for Large Data Visualization, Visualization Handbook*. Elsevier, 2005. ISBN: 978-0123875822.

[Ale01] A. Alexandrescu. *Modern C++ Design: Generic Programming and Design Patterns Applied*. Addison-Wesley Professional, 2001, p. 352.

[All07a] B. Allard. "Minerals and precipitates in fractures and their effects on the retention of radionuclides in crystalline rocks". In: *Journal of Experimental Psychology: General* 136.1 (2007), pp. 23–42.

[All07b] A. J. Allen, J. J. Thomas, and H. M. Jennings. "Composition and density of nanoscale calcium-silicate-hydrate in cement". In: *Nature Materials* 6.4 (2007), pp. 311–316.

[All16] E. Alligand and J. Falcou. *Practical C++ Metaprogramming*. Ed. by N. Barber and B. Foster. Sebastopol, CA: O'Reilly Media, 2016. ISBN: 978-1-491-95504-8.

[Amd67] G. M. Amdahl. "Validity of the single processor approach to achieving large scale computing capabilities". In: *Proceedings of the April 18-20, 1967, spring joint computer conference on - AFIPS '67 (Spring)*. New York, New York, USA: ACM Press, 1967, p. 483.

[AND05] ANDRA. *The Geological Disposal of High-Level Long-Lived Radioactive Waste*. Tech. rep. June. 2005, p. 40.

[App17] C. Appelo. "Solute transport solved with the Nernst-Planck equation for concrete pores with 'free' water and a double layer". In: *Cement and Concrete Research* 101 (2017), pp. 102–113.

[Atk92] M. Atkins and F. Glasser. "Application of portland cement-based materials to radioactive waste immobilization". In: *Waste Management* 12.2-3 (1992), pp. 105–131.

[Bal09] M. Balonis and F. Glasser. "The density of cement phases". In: *Cement and Concrete Research* 39.9 (2009), pp. 733–739.

[Bar06] B. Bary and S. Béjaoui. "Assessment of diffusive and mechanical properties of hardened cement pastes using a multi-coated sphere assemblage model". In: *Cement and Concrete Research* 36.2 (2006), pp. 245–258.

[Bar08] B. Bary. “Simplified coupled chemo-mechanical modeling of cement pastes behavior subjected to combined leaching and external sulfate attack”. In: *International Journal for Numerical and Analytical Methods in Geomechanics* 32.14 (2008), pp. 1791–1816.

[Bar14] B. Bary, N. Leterrier, E. Deville, and P. Le Bescop. “Coupled chemo-transport-mechanical modelling and numerical simulation of external sulfate attack in mortar”. In: *Cement and Concrete Composites* 49 (2014), pp. 70–83.

[Bej07] S. Bejaoui and B. Bary. “Modeling of the link between microstructure and effective diffusivity of cement pastes using a simplified composite model”. In: *Cement and Concrete Research* 37.3 (2007), pp. 469–480.

[Bel06] J. J. Bel, S. M. Wickham, and R. M. Gens. “Development of the Supercontainer Design for Deep Geological Disposal of High-Level Heat Emitting Radioactive Waste in Belgium”. In: *MRS Proceedings* 932.1 (2006), p. 122.1.

[Ben05] D. P. Bentz. *CEMHYD3D: A three-dimensional cement hydration and microstructure development modeling package. Version 3.0.* 2005.

[Ben92] D. P. Bentz and E. J. Garboczi. “Modelling the leaching of calcium hydroxide from cement paste: effects on pore space percolation and diffusivity”. In: *Materials and Structures* 25.9 (1992), pp. 523–533.

[Ben95] D. P. Bentz. *A Three-Dimensional Cement Hydration and Microstructure Program. I. Hydration Rate, Heat of Hydration, and Chemical Shrinkage.* Tech. rep. National Institute of Standards and Technology, 1995, p. 60.

[Bha54] P. L. Bhatnagar, E. P. Gross, and M. Krook. “A model for collision processes in gases. I. small amplitude processes in charged and neutral one-component systems”. In: *Physical Review* 94.3 (May 1954), pp. 511–525.

[Bla10a] P. Blanc, X. Bourbon, A. Lassin, and E. C. Gaucher. “Chemical model for cement-based materials: Temperature dependence of thermodynamic functions for nanocrystalline and crystalline C-S-H phases”. In: *Cement and Concrete Research* 40.6 (2010), pp. 851–866.

[Bla10b] P. Blanc, X. Bourbon, A. Lassin, and E. C. Gaucher. “Chemical model for cement-based materials: Thermodynamic data assessment for phases other than C–S–H”. In: *Cement and Concrete Research* 40.9 (2010), pp. 1360–1374.

[Bou01] M. Bouzidi, M. Firdaouss, and P. Lallemand. “Momentum transfer of a Boltzmann-lattice fluid with boundaries”. In: *Physics of Fluids* 13.11 (2001), pp. 3452–3459.

[Bov01] T. B. Boving and P. Grathwohl. “Tracer diffusion coefficients in sedimentary rocks: correlation to porosity and hydraulic conductivity”. In: *Journal of Contaminant Hydrology* 53.1-2 (2001), pp. 85–100.

[Bra08] T. Bray, J. Paoli, C. M. Sperberg-McQueen, E. Maler, and F. Yergeau. *Extensible Markup Language (XML) 1.0.* 2008.

[Bra15] C. Brandel and J. H. ter Horst. "Measuring induction times and crystal nucleation rates". In: *Faraday Discuss.* 179.January (2015), pp. 199–214.

[Bre71] R. P. Brent. "An algorithm with guaranteed convergence for finding a zero of a function". In: *The Computer Journal* 14.4 (1971), pp. 422–425.

[Bre95] K. van Breugel. "Numerical simulation of hydration and microstructural development in hardening cement-based materials (I) Theory". In: *Cement and Concrete Research* 25.2 (Feb. 1995), pp. 319–331.

[Bru59] S. Brunauer, D. L. Kantro, and C. H. Weise. "The surface energy of tobermorite". In: *Canadian Journal of Chemistry* 37.4 (1959), pp. 714–724.

[Can86] J. Canny. "A computational approach to edge detection". In: *IEE Transaction on pattern aanlysis* 6 (1986), pp. 3958–3962.

[CEB19] CEBAMA. "Deliverable D4.19: Draft of the 4th Annual Project Workshop Proceedings". In: 2019.

[Cha10] R. Chamrova. *Modelling and Measurement of Elastic Properties of Hydrating Cement Paste*. Vol. 4606. 2010, p. 128. ISBN: 2005019283.

[Cha11] S. R. Charlton and D. L. Parkhurst. "Modules based on the geochemical model PHREEQC for use in scripting and programming languages". In: *Computers and Geosciences* 37.10 (2011), pp. 1653–1663.

[Cha70] S. Chapman and T. G. Cowling. *The Mathematical Theory of Non-Uniform Gases*. Ed. by T. Edition. 3rd. Cambridge: Cambridge University Press, 1970, p. 423. ISBN: 0-521-40844-X.

[Cha92] K. C. Chang and V. J. Payne. "Numerical treatment of diffusion coefficients at interfaces". In: *Numerical Heat Transfer; Part A: Applications* 21.3 (1992), pp. 363–376.

[Che14] L. Chen, Q. Kang, Y. Mu, Y. L. He, and W. Q. Tao. "A critical review of the pseudopotential multiphase lattice Boltzmann model: Methods and applications". In: *International Journal of Heat and Mass Transfer* 76 (2014), pp. 210–236.

[Che98] S. Chen and G. D. Doolen. "Lattice Boltzmann method for fluid flows". In: *Annual Review of Fluid Mechanics* 30.1 (1998), pp. 329–364.

[Con04] G. Constantinides and F. J. Ulm. "The effect of two types of C-S-H on the elasticity of cement-based materials: Results from nanoindentation and micromechanical modeling". In: *Cement and Concrete Research* 34.1 (2004), pp. 67–80.

[Cra75] J. Crank. *The mathematics of diffusion*. Second Edi. Oxford: Clarendon Press, 1975. ISBN: 0198534116.

[Cus09] E. L. Cussler. *Fundamentals of Mass Transfer*. 3rd. Cambridge: Cambridge University Press, Jan. 2009, p. 631. ISBN: 9780521871211.

[Dam11] D. Damidot, B. Lothenbach, D. Herfort, and F. P. Glasser. "Thermodynamics and cement science". In: *Cement and Concrete Research* 41.7 (2011), pp. 679–695.

[Dam94] D. Damidot, S. Stronach, A. Kindness, M. Atkins, and F. P. Glasser. "Thermodynamic investigation of the CaOAl2O3CaCO3H2O closed system at 25°C and the influence of Na2O". In: *Cement and Concrete Research* 24.3 (1994), pp. 563–572.

[Das08] S. K. Das, S. U. S. Choi, W. Yu, and T. Pradeep. *Nanofluids*. Hoboken, New Jersey: John Wiley & Sons, 2008. ISBN: 978-0-470-07473-2.

[Dei21] G. Deissmann, N. Ait Mouheb, C. Martin, M. Turrero, E. Torres, B. Kursten, E. Weetjens, D. Jacques, J. Cuevas, J. Samper, L. Montenegro, M. Leivo, M. Somervuori, and L. Carpen. *Experiments and numerical model studies on interfaces. Final version as of 12.05.2021 of deliverable D2.5 of the HORIZON 2020 project EURAD. EC Grant agreement no: 847593. Disclaimer*. Tech. rep. 2021.

[Dor07] L. Dormieux, F. J. Ulm, and D. Kondo. *Applied Micromechanics of Porous Materials*. Ed. by L. Dormieux and F.-J. Ulm. CISM International Centre for Mechanical Sciences. Wien: Springer Vienna, 2007. ISBN: 9783211380468.

[Dur20] L. Duro, M. Altmaier, E. Holt, U. Mäder, F. Claret, B. Grambow, A. Idiart, A. Valls, and V. Montoya. "Contribution of the results of the CEBAMA project to decrease uncertainties in the Safety Case and Performance Assessment of radioactive waste repositories". In: *Applied Geochemistry* 112 (2020), p. 104479.

[Eas89] A. J. Easteal, W. E. Price, and L. A. Woolf. "Diaphragm cell for high-temperature diffusion measurements. Tracer diffusion coefficients for water to 363 K". In: *Journal of the Chemical Society, Faraday Transactions 1: Physical Chemistry in Condensed Phases* 85.5 (1989), pp. 1091–1097.

[Emi17] L. Emilio and R. D. Diaz. *Concrete Durability*. Ed. by L. E. Rendon Diaz Miron and D. A. Koleva. Cham: Springer International Publishing, 2017. ISBN: 978-3-319-55461-7.

[Emm07] S. Emmanuel and B. Berkowitz. "Effects of pore-size controlled solubility on reactive transport in heterogeneous rock". In: *Geophysical Research Letters* 34.6 (2007), pp. 1–5.

[Fla02] R. J. Flatt. "Salt damage in porous materials: How high supersaturations are generated". In: *Journal of Crystal Growth* 242.3-4 (2002), pp. 435–454.

[Fle93] E. G. Flekkøy. "Lattice Bhatnagar-Gross-Krook models for miscible fluids". In: *Physical Review E* 47.6 (1993), pp. 4247–4257.

[Flo11] FlowKit. *Palabos user guide*. 2011.

[Fri86] U. Frisch, B. Hasslacher, and Y. Pomeau. "Lattice-Gas Automata for the Navier-Stokes Equation". In: *Physical Review Letters* 56.14 (1986), pp. 1505–1508.

[Gab04] E. Gabriel, G. E. Fagg, G. Bosilca, T. Angskun, J. J. Dongarra, J. M. Squyres, V. Sahay, P. Kambadur, B. Barrett, A. Lumsdaine, R. H. Castain, D. J. Daniel, R. L. Graham, and T. S. Woodall. "Open MPI: Goals, Concept, and Design of a Next Generation MPI Implementation". In: *11th European PVM/MPI Users' Group Meeting*. Budapest, 2004, pp. 97–104.

[Gal10] J. M. Galíndez and J. Molinero. "On the relevance of electrochemical diffusion for the modeling of degradation of cementitious materials". In: *Cement and Concrete Composites* 32.5 (2010), pp. 351–359.

[Gar04] K. Garbev. "Struktur, Eigenschaften und quantitative Rietveldanalyse von hydrothermal kristallisierten Calciumsilikathydraten (C-S-H-Phasen)". PhD thesis. Forschungszentrum Karlsruhe, 2004, p. 241. ISBN: 0947-8620.

[Gif14] E. Giffaut, M. Grivé, P. Blanc, P. Vieillard, E. Colàs, H. Gailhanou, S. Gaboreau, N. Marty, B. Madé, and L. Duro. "Andra thermodynamic database for performance assessment: ThermoChimie". In: *Applied Geochemistry* 49.May (2014), pp. 225–236.

[Gin05a] I. Ginzburg. "Equilibrium-type and link-type lattice Boltzmann models for generic advection and anisotropic-dispersion equation". In: *Advances in Water Resources* 28.11 (2005), pp. 1171–1195.

[Gin05b] I. Ginzburg. "Generic boundary conditions for lattice Boltzmann models and their application to advection and anisotropic dispersion equations". In: *Advances in Water Resources* 28.11 (2005), pp. 1196–1216.

[Gin08] I. Ginzburg, F. Verhaeghe, and D. D'Humieres. "Two-Relaxation-Time Lattice Boltzmann Scheme: About Parametrization,Velocity, Pressure and Mixed Boundary Conditions". In: *Communications in Computational Physics* 3.2 (2008), pp. 427–478.

[Gin10] I. Ginzburg, D. D'Humières, and A. Kuzmin. "Optimal stability of advection-diffusion lattice boltzmann models with two relaxation times for positive/negative equilibrium". In: *Journal of Statistical Physics* 139.6 (2010), pp. 1090–1143.

[Gin16] I. Ginzburg. "Comment on "An improved gray Lattice Boltzmann model for simulating fluid flow in multi-scale porous media": Intrinsic links between LBE Brinkman schemes". In: *Advances in Water Resources* 88 (2016), pp. 241–249.

[Gla08] F. P. Glasser, J. Marchand, and E. Samson. "Durability of concrete - Degradation phenomena involving detrimental chemical reactions". In: *Cement and Concrete Research* 38.2 (2008), pp. 226–246.

[Glo09] P. Glover. “What is the cementation exponent? A new interpretation”. In: *The Leading Edge* 28.1 (2009), pp. 82–85.

[Goh10] L. Goh, K. Chen, V. Bhamidi, G. He, N. C. Kee, P. J. Kenis, C. F. Zukoski, and R. D. Braatz. “A stochastic model for nucleation kinetics determination in droplet-based microfluidic systems”. In: *Crystal Growth and Design* 10.6 (2010), pp. 2515–2521.

[Gon08] R. C. Gonzalez and R. E. Woods. *Digital image processing*. 3rd editio. Upper Saddle River, N.J.: Prentice Hall, 2008. ISBN: 9780131687288.

[Gra20] B. Grambow, M. López-García, J. Olmeda, M. Grivé, N. C. Marty, S. Grangeon, F. Claret, S. Lange, G. Deissmann, M. Klinkenberg, D. Bosbach, C. Bucur, I. Florea, R. Dobrin, M. Isaacs, D. Read, J. Kittnerová, B. Drtinová, D. Vopálka, N. Cevirim-Papaioannou, N. Ait-Mouheb, X. Gaona, M. Altmaier, L. Nedyalkova, B. Lothenbach, J. Tits, C. Landesman, S. Rasamimanana, and S. Ribet. “Retention and diffusion of radioactive and toxic species on cementitious systems: Main outcome of the CEBAMA project”. In: *Applied Geochemistry* 112 (2020).

[Gre97] I. Grenthe, A. V. Plyasunov, and S. Kastriot. “Estimations of medium effects on thermodynamic data”. In: Paris: OECD Nuclear Energy Agency, 1997. Chap. iX. ISBN: 9264155694.

[Hag05] K. Haga, S. Sutou, M. Hironaga, S. Tanaka, and S. Nagasaki. “Effects of porosity on leaching of Ca from hardened ordinary Portland cement paste”. In: *Cement and Concrete Research* 35.9 (2005), pp. 1764–1775.

[Hal94] W. Halperin, J.-Y. Jehng, and Y.-Q. Song. “Application of spin-spin relaxation to measurement of surface area and pore size distributions in a hydrating cement paste”. In: *Magnetic Resonance Imaging* 12.2 (1994), pp. 169–173.

[Han86] T. C. Hansen. “Physical Structure of Hardened Cement Paste”. In: *Materials and Structures* 19.6 (1986), pp. 423–436.

[Har98] A. W. Harris, A. Atkinson, V. Balek, K. Brodersen, G. B. Cole, A. Haworth, Z. Malek, A. K. Nickerson, K. Nilsson, and A. C. Smith. *The performance of cementitious barriers in repositories*. Luxembourg: Publications Office, 1998, pp. 1–2. ISBN: 92-828-2152-8.

[Hay17] W. M. Haynes, D. R. Lide, and T. J. Bruno. *CRC Handbook of Chemistry and Physics*. 97th Editi. CRC Press, 2017. ISBN: 978-1-4987-5429-3.

[Heu10] D. Heubes. “Lattice Boltzmann Method in Theory and in Application to Coupled Problems”. PhD thesis. 2010.

[Hil65] R. Hill. “Continuum micro-mechanics of elastoplastic polycrystals”. In: *Journal of the Mechanics and Physics of Solids* 13.2 (1965), pp. 89–101.

[Hio13] A. Hiorth, E. Jettestuen, L. M. Cathles, and M. V. Madland. "Precipitation, dissolution, and ion exchange processes coupled with a lattice Boltzmann advection diffusion solver". In: *Geochimica et Cosmochimica Acta* 104 (2013), pp. 99–110.

[Hub11] C. Huber, J. Dufek, and B. Chopard. "A Simple Algorithm To Enforce Dirichlet Boundary Conditions in Complex Geometries". In: *International Journal of Modern Physics C* 22.10 (2011), pp. 1093–1105.

[Idi18] A. Idiart, M. Laviña, and J. Olmeda. "Towards coupling of thermodynamic modelling of cement hydration with moisture transfer. Application to low-pH cement systems". In: *ConMOD2018 Symposium on Concrete Modelling*. 1. Delft, The Netherlands, 2018.

[Idi20] A. Idiart, M. Laviña, G. Kosakowski, B. Cochepin, J. C. Meeussen, J. Samper, A. Mon, V. Montoya, I. Munier, J. Poonoosamy, L. Montenegro, G. Deissmann, S. Rohmen, L. H. Damiani, E. Coene, and A. Nieves. "Reactive transport modelling of a low-pH concrete / clay interface". In: *Applied Geochemistry* 115.July 2019 (2020).

[IEE08] IEEE Computer Society. *IEEE Std 754™-2008 (Revision of IEEE Std 754-1985), IEEE Standard for Floating-Point Arithmetic*. Tech. rep. August. 2008, pp. 1–58.

[Int17] International Organization for Standardization. *The JSON data interchange syntax (ISO/IEC 21778:2017)*. Tech. rep. 2017.

[Isa14] K. E. Isaacs, P. T. Bremer, I. Jusufi, T. Gamblin, A. Bhatele, M. Schulz, and B. Hamann. "Combing the communication hairball: Visualizing parallel execution traces using logical time". In: *IEEE Transactions on Visualization and Computer Graphics* 20.12 (2014), pp. 2349–2358.

[Jac05] D. Jacques and J. Simunek. *User Manual of the Multicomponent Variably-Saturated Flow and Transport Model HP1*. Tech. rep. Mol: SCK/CEN - Waste & Disposal Department, 2005.

[Jac09] D. Jacques. *Benchmarking of the cement model and detrimental chemical reactions including temperature dependent parameters*. Tech. rep. Mol: SCK/CEN - Waste & Disposal Department, 2009.

[Jac12] D. Jacques, L. Wang, E. Martens, and D. Mallants. "Benchmarking the cemdata07 database to model chemical degradation of concrete using GEMS and PHREEQC". In: *Cementitious materials in safety cases for geological repositories for radioactive waste: role, evolution and interaction*. January. 2012, pp. 285–288.

[Jan14] M. Januszewski and M. Kostur. "Sailfish: A flexible multi-GPU implementation of the lattice Boltzmann method". In: *Computer Physics Communications* 185.9 (2014), pp. 2350–2368.

[Jen00] H. M. Jennings. “A Model for the microstructure of calcium silicate hydrate in cement paste”. In: *Cement and Concrete Research* 30.1 (2000), pp. 101–116.

[Jen04] H. M. Jennings. “Colloid model of C-S-H and implications to the problem of creep and shrinkage”. In: *Materials and Structures* 37.1 (2004), pp. 59–70.

[Jen08] H. M. Jennings, J. W. Bullard, J. J. Thomas, J. E. Andrade, J. J. Chen, and G. W. Scherer. “Characterization and Modeling of Pores and Surfaces in Cement Paste”. In: *Journal of Advanced Concrete Technology* 6.1 (2008), pp. 5–29.

[Jen94] H. M. Jennings and P. D. Tennis. “Model for the developing microstructure in Portland cement pastes”. In: *Journal of the American Ceramic Society* 77 (1994), pp. 3161–3172.

[Jon06] M. W. Jones, J. A. Bærentzen, and M. Sramek. “3D distance fields: A survey of techniques and applications”. In: *IEEE Transactions on Visualization and Computer Graphics* 12.4 (2006), pp. 581–599.

[Kan02] Q. Kang, D. Zhang, S. Chen, and X. He. “Lattice Boltzmann simulation of chemical dissolution in porous media”. In: *Physical Review E* 65.3 (2002), p. 036318.

[Kan04] Q. Kang, D. Zhang, P. C. Lichtner, and I. N. Tsimpanogiannis. “Lattice Boltzmann model for crystal growth from supersaturated solution”. In: *Geophysical Research Letters* 31.21 (2004), pp. 1–5.

[Kan06] Q. Kang, P. C. Lichtner, and D. Zhang. “Lattice Boltzmann pore-scale model for multicomponent reactive transport in porous media”. In: *Journal of Geophysical Research: Solid Earth* 111.B5 (2006).

[Kas00] D. Kashchiev. *Nucleation: basic theory with applications*. Oxford: Butterworth Heinemann, 2000, p. 529. ISBN: 0 7506 4682 9.

[Kas03] D. Kashchiev and G. M. van Rosmalen. “Review: Nucleation in solutions revisited”. In: *Crystal Research and Technology* 38.7-8 (2003), pp. 555–574.

[Ket01] R. A. Ketcham and W. D. Carlson. “Acquisition, optimization and interpretation of x-ray computed tomographic imagery: Applications to the geosciences”. In: *Computers and Geosciences* 27.4 (2001), pp. 381–400.

[Kha15] P. Khare. “Fluid Dynamics: Part 1: Classical Fluid Dynamics”. In: *Contemporary Physics* 56.3 (2015), pp. 385–387.

[Knü12] A. Knüpfer, C. Rössel, D. an Mey, S. Biersdorff, K. Diethelm, D. Eschweiler, M. Geimer, M. Gerndt, D. Lorenz, A. Malony, W. E. Nagel, Y. Oleynik, P. Philippen, P. Saviankou, D. Schmidl, S. Shende, R. Tschüter, M. Wagner, B. Wesarg, and F. Wolf. “Score-P: A Joint Performance Measurement Run-Time Infrastructure for Periscope, Scalasca, TAU, and Vampir”. In: *Tools for High Performance Computing 2011*. Berlin, Heidelberg: Springer Berlin Heidelberg, 2012, pp. 79–91.

[Krä17] A. Krämer. “Lattice-Boltzmann-Methoden zur Simulation inkompressibler Wirbelströmungen”. PhD thesis. Universität Siegen, 2017.

[Kra18] D. Krause and P. Thörnig. “JURECA: Modular supercomputer at Jülich Supercomputing Centre”. In: *Journal of large-scale research facilities JLSRF* 4 (July 2018), A132.

[Kra21] M. J. Krause, A. Kummerländer, S. J. Avis, H. Kusumaatmaja, D. Dapelo, F. Klemens, M. Gaedtke, N. Hafen, A. Mink, R. Trunk, J. E. Marquardt, M. L. Maier, M. Haussmann, and S. Simonis. “OpenLB—Open source lattice Boltzmann code”. In: *Computers and Mathematics with Applications* 81 (2021), pp. 258–288.

[Kul01] D. A. Kulik and M. Kersten. “Aqueous Solubility Diagrams for Cementitious Waste Stabilization Systems: II, End-Member Stoichiometries of Ideal Calcium Silicate Hydrate Solid Solutions”. In: *Journal of the American Ceramic Society* 84.12 (2001), pp. 3017–3026.

[Kul11] D. A. Kulik. “Improving the structural consistency of C-S-H solid solution thermodynamic models”. In: *Cement and Concrete Research* 41.5 (2011), pp. 477–495.

[Kul12] D. A. Kulik, T. Wagner, S. V. Dmytrieva, G. Kosakowski, F. F. Hingerl, K. V. Chudnenko, and U. R. Berner. “GEM-Selektor geochemical modeling package: revised algorithm and GEMS3K numerical kernel for coupled simulation codes”. In: *Computational Geosciences* 17.1 (2012), pp. 1–24.

[Lal03] P. Lallemand and L. S. Luo. “Lattice Boltzmann method for moving boundaries”. In: *Journal of Computational Physics* 184.2 (2003), pp. 406–421.

[Lal21] E. Laloy and D. Jacques. “Speeding up reactive transport simulations in cement systems by surrogate geochemical modeling: deep neural networks and k-nearest neighbors”. In: *Transport in Porous Media* 143.2 (July 2021), pp. 433–462.

[Lan18] S. Lange. “Structural uptake and retention of safety relevant radionuclides by cementitious materials”. PhD thesis. Rheinisch-Westfälischen Technischen Hochschule Aachen, 2018.

[Las98] A. C. Lasaga. *Kinetic Theory in the Earth Sciences*. Princeton: Princeton University Press, 1998. ISBN: 0-691-03748-5.

[Lat06] J. Latt and B. Chopard. “Lattice Boltzmann method with regularized pre-collision distribution functions”. In: *Mathematics and Computers in Simulation* 72.2-6 (2006), pp. 165–168.

[Lat07] J. Latt. “Technical report: How to implement your DdQq dynamics with only q variables per node (instead of 2q)”. In: 1 (2007), pp. 1–8.

[Lät07] J. Lätt. “Hydrodynamic limit of lattice Boltzmann equations”. PhD thesis. Université de Genève, Aug. 2007, p. 124.

[Lat21] J. Latt, O. Malaspinas, D. Kontaxakis, A. Parmigiani, D. Lagrava, F. Brogi, M. B. Belgacem, Y. Thorimbert, S. Leclaire, S. Li, F. Marson, J. Lemus, C. Kotsalos, R. Conradin, C. Coreixas, R. Petkantchin, F. Raynaud, J. Beny, and B. Chopard. "Palabos: Parallel Lattice Boltzmann Solver". In: *Computers and Mathematics with Applications* 81 (2021), pp. 334–350.

[Lea16] A. M. Leal, D. A. Kulik, G. Kosakowski, and M. O. Saar. "Computational methods for reactive transport modeling: An extended law of mass-action, xLMA, method for multiphase equilibrium calculations". In: *Advances in Water Resources* 96 (2016), pp. 405–422.

[Lea17] A. M. M. Leal, D. A. Kulik, and M. O. Saar. "Ultra-Fast Reactive Transport Simulations When Chemical Reactions Meet Machine Learning: Chemical Equilibrium". In: *arXiv* August (2017).

[Lee05] S. T. Lee, H. Y. Moon, and R. N. Swamy. "Sulfate attack and role of silica fume in resisting strength loss". In: *Cement and Concrete Composites* 27.1 (2005), pp. 65–76.

[LHô16] E. L'Hôpital, B. Lothenbach, D. A. Kulik, and K. Scrivener. "Influence of calcium to silica ratio on aluminium uptake in calcium silicate hydrate". In: *Cement and Concrete Research* 85 (2016), pp. 111–121.

[Li14] Q. Li, A. Fernandez-Martinez, B. Lee, G. A. Waychunas, and Y. S. Jun. "Interfacial energies for heterogeneous nucleation of calcium carbonate on mica and quartz". In: *Environmental Science and Technology* 48.10 (2014), pp. 5745–5753.

[Li17] Q. Li, C. I. Steefel, and Y. S. Jun. "Incorporating Nanoscale Effects into a Continuum-Scale Reactive Transport Model for CO2-Deteriorated Cement". In: *Environmental Science and Technology* 51.18 (2017), pp. 10861–10871.

[Li18] Q. Li and Y.-S. Jun. "The apparent activation energy and pre-exponential kinetic factor for heterogeneous calcium carbonate nucleation on quartz". In: *Communications Chemistry* 1.1 (2018), p. 56.

[Li94] Z. Li, R. F. Giese, and C. J. van Oss. "Surface Thermodynamic Properties of Synthetic Hydrotalcite Compounds". In: *Langmuir* 10.1 (1994), pp. 330–333.

[Lic06] P. C. Lichtner and J. W. Carey. "Incorporating solid solutions in reactive transport equations using a kinetic discrete-composition approach". In: *Geochimica et Cosmochimica Acta* 70.6 (2006), pp. 1356–1378.

[Lic07] P. C. Lichtner and Q. Kang. "Upscaling pore-scale reactive transport equations using a multiscale continuum formulation". In: *Water Resources Research* 43.12 (2007).

[Lio07] M. G. Lioliou, C. A. Paraskeva, P. G. Koutsoukos, and A. C. Payatakes. "Heterogeneous nucleation and growth of calcium carbonate on calcite and quartz". In: *Journal of Colloid and Interface Science* 308.2 (2007), pp. 421–428.

[Lit76] G. G. Litvan. “Variability of the nitrogen surface area of hydrated cement paste”. In: *Cement and Concrete Research* 6.1 (1976), pp. 139–143.

[Liu05] Z. Liu and C. Ma. “A new method for numerical treatment of diffusion coefficients at control-volume surfaces”. In: *Numerical Heat Transfer, Part B: Fundamentals* 47.5 (2005), pp. 491–505.

[Liu17] S. Liu and D. Jacques. “Coupled reactive transport model study of pore size effects on solubility during cement-bicarbonate water interaction”. In: *Chemical Geology* 466.April (2017), pp. 588–599.

[Loc02] D. P. Lockard, L. S. Luo, S. D. Milder, and B. A. Singer. “Evaluation of PowerFLOW for aerodynamic applications”. In: *Journal of Statistical Physics* 107.1-2 (2002), pp. 423–478.

[Lot06] B. Lothenbach and F. Winnefeld. “Thermodynamic modelling of the hydration of Portland cement”. In: *Cement and Concrete Research* 36.2 (2006), pp. 209–226.

[Lot08] B. Lothenbach, T. Matschei, G. Möschner, and F. P. Glasser. “Thermodynamic modelling of the effect of temperature on the hydration and porosity of Portland cement”. In: *Cement and Concrete Research* 38.1 (2008), pp. 1–18.

[Lot15] B. Lothenbach and A. Nonat. “Calcium silicate hydrates: Solid and liquid phase composition”. In: *Cement and Concrete Research* 78 (Dec. 2015), pp. 57–70.

[Lot19] B. Lothenbach, D. A. Kulik, T. Matschei, M. Balonis, L. Baquerizo, B. Dilnesa, G. D. Miron, and R. J. Myers. “Cemdata18: A chemical thermodynamic database for hydrated Portland cements and alkali-activated materials”. In: *Cement and Concrete Research* 115.October 2017 (2019), pp. 472–506.

[Łuk16] G. Łukaszewicz and P. Kalita. *Navier–Stokes Equations*. Advances in Mechanics and Mathematics. Springer International Publishing Switzerland, 2016. ISBN: 978-3-319-27758-5.

[Mad19] J. Maddock and C. Kormanyos. *Boost.Multiprecision*. 2019. URL: `https://www.boost.org/doc/libs/1%7B%5C_%7D71%7B%5C_%7D0/libs/multiprecision/doc/html/index.html`.

[Mar15] N. C. M. Marty, O. Bildstein, P. Blanc, F. Claret, B. Cochepin, E. C. Gaucher, D. Jacques, J.-E. E. Lartigue, S. Liu, K. U. Mayer, J. C. L. Meeussen, I. Munier, I. Pointeau, D. Su, and C. I. Steefel. “Benchmarks for multicomponent reactive transport across a cement/clay interface”. In: *Computational Geosciences* 19.3 (June 2015), pp. 635–653.

[Mat07a] T. Matschei, B. Lothenbach, and F. P. Glasser. “The AFm phase in Portland cement”. In: *Cement and Concrete Research* 37.2 (2007), pp. 118–130.

[Mat07b] T. Matschei, B. Lothenbach, and F. P. Glasser. “Thermodynamic properties of Portland cement hydrates in the system CaO-Al2O3-SiO2-CaSO4-CaCO3-H2O”. In: *Cement and Concrete Research* 37.10 (2007), pp. 1379–1410.

[Mat10] K. Mattila. "Implementation Techniques for the Lattice Boltzmann Method". PhD thesis. University of Jyväskylä, 2010, p. 179. ISBN: 978-951-39-3991-5.

[Max73] J. C. Maxwell. *Treatise on Electricity and Magnetism Vol. 1*. Third edit. New York: Dover publications, 1873, p. 507. ISBN: 486-60636-8.

[Maz08] M. D. Mazzeo and P. V. Coveney. "HemeLB: A high performance parallel lattice-Boltzmann code for large scale fluid flow in complex geometries". In: *Computer Physics Communications* 178.12 (2008), pp. 894–914.

[McD10] P. McDonald, V. Rodin, and A. Valori. "Characterisation of intra- and inter-C–S–H gel pore water in white cement based on an analysis of NMR signal amplitudes as a function of water content". In: *Cement and Concrete Research* 40.12 (2010), pp. 1656–1663.

[McN88] G. R. McNamara and G. Zanetti. "Use of the boltzmann equation to simulate lattice-gas automata". In: *Physical Review Letters* 61.20 (1988), pp. 2332–2335.

[Meh05] P. K. Mehta and P. J. M. Monteiro. *Concrete: Microstructure, Properties, and Materials*. McGraw-Hill Professional, 2005.

[Mel65] T. P. Melia. "Crystal nucleation from aqueous solution". In: *Journal of Biochemical Toxicology* 15.8 (1965), pp. 345–357.

[Mer89] A. B. Mersmann and M. Kind. "Parameters influencing the mean particle size of a crystalline product". In: *Chemical Engineering & Technology* 12.1 (1989), pp. 414–419.

[Mik64] R. S. Mikhail, L. E. Copeland, and S. Brunauer. "Pore structures and surface areas of hardened portland cement pastes by nitrogen adsorption". In: *Canadian Journal of Chemistry* 42.2 (1964), pp. 426–438.

[Mik66] R. S. Mikhail and S. A. Selim. "Adsorption of organic vapors in relation to the pore structure of hardened Portland cement pastes". In: *Proceedings of Symposium on Structure of Portland Cemenet Paste and Concrete*. 90. 1966, pp. 123–134.

[Mil66] R. H. Mills. "Factors Influencing Cessation of Hydration in Water Cured Cement Pastes". In: *Symposium on structure of Portland cement paste and concrete*. 90. Highway Research Board, 1966, pp. 406–424.

[Moh11] A. A. Mohamad. *Lattice Boltzmann Method*. London: Springer London, 2011, p. 175. ISBN: 978-0-85729-454-8.

[Mol15] S. Molins. "Reactive Interfaces in Direct Numerical Simulation of Pore-Scale Processes". In: *Reviews in Mineralogy and Geochemistry* 80.1 (2015), pp. 461–481.

[Mor04] M. Moranville, S. Kamali, and E. Guillon. "Physicochemical equilibria of cement-based materials in aggressive environments - Experiment and modeling". In: *Cement and Concrete Research* 34.9 (2004), pp. 1569–1578.

[Mor73] T. Mori and K. Tanaka. "Average stress in matrix and average elastic energy of materials with misfitting inclusions". In: *Acta Metallurgica* 21.5 (1973), pp. 571–574.

[Nag02] Nagra. *Technical report 02-02: Project Opalinuston - Konzept für die Anlage und den Betrieb eines geologischen Tiefenlagers. Entsorgungsnachweis für abgebrannte Brennelemente, verglaste hochaktive sowie langlebige mittelaktive Abfälle.* Tech. rep. Wetting, Switzerland: Nagra, 2002.

[Nar14] A. Nardi, A. Idiart, P. Trinchero, L. M. De Vries, and J. Molinero. "Interface COMSOL-PHREEQC (iCP), an efficient numerical framework for the solution of coupled multiphysics and geochemistry". In: *Computers and Geosciences* 69 (2014), pp. 10–21.

[Nee22] E. Neeft, D. Jacques, and G. Deissmann. *Initial State of the Art on the assessment of the chemical evolution of ILW and HLW disposal cells. D 2.1 of the HORIZON 2020 project EURAD. EC Grant agreement no: 847593.* Tech. rep. 2022, p. 177.

[Nie71] A. E. Nielsen and O. Söhnel. "Interfacial tensions electrolyte crystal-aqueous solution, from nucleation data". In: *Journal of Crystal Growth* 11.3 (1971), pp. 233–242.

[Noi12] C. Noiriel, C. I. Steefel, L. Yang, and J. Ajo-Franklin. "Upscaling calcium carbonate precipitation rates from pore to continuum scale". In: *Chemical Geology* 318-319 (2012), pp. 60–74.

[Noi21] C. Noiriel and C. Soulaine. "Pore-Scale Imaging and Modelling of Reactive Flow in Evolving Porous Media: Tracking the Dynamics of the Fluid–Rock Interface". In: *Transport in Porous Media* 140.1 (Oct. 2021), pp. 181–213.

[Och16] M. Ochs, D. Mallants, and L. Wang. *Radionuclide and Metal Sorption on Cement and Concrete.* Vol. 9999. Topics in Safety, Risk, Reliability and Quality. Cham: Springer International Publishing, 2016, p. 301. ISBN: 978-3-319-23651-3.

[Ojo05] M. I. Ojovan, W. E. Lee, and W. Lee. *An Introduction to Nuclear Waste Immobilisation.* 2005. ISBN: 9780080444628.

[Ouy88] C. Ouyang, A. Nanni, and W. F. Chang. "Internal and external sources of sulfate ions in portland cement mortar: two types of chemical attack". In: *Cement and Concrete Research* 18.5 (1988), pp. 699–709.

[Par13] D. L. Parkhurst and C. A. J. Appelo. "Description of input and examples for PHREEQC Version 3 — A computer program for speciation, batch-reaction, one-dimensional transport, and inverse geochemical calculations". In: *U.S. Geological Survey Techniques and Methods, book 6, chapter A43* (2013), 6–43A.

[Par15] D. L. Parkhurst and L. Wissmeier. "PhreeqcRM: A reaction module for transport simulators based on the geochemical model PHREEQC". In: *Advances in Water Resources* 83 (2015), pp. 176–189.

[Par99] D. L. Parkhurst and C. Appelo. *User's guide to PHREEQC (Version 2): A computer program for speciation, batch-reaction, one-dimensional transport, and inverse geochemical calculations*. Tech. rep. U.S. Geological Survey, 1999, p. 312.

[Pat14] R. A. Patel, J. Perko, D. Jacques, G. De Schutter, K. Van Breugel, and G. Ye. "A versatile pore-scale multicomponent reactive transport approach based on lattice Boltzmann method: Application to portlandite dissolution". In: *Physics and Chemistry of the Earth* 70-71 (2014), pp. 127–137.

[Pat16a] R. A. Patel. "Lattice Boltzmann Method Based Framework for Simulating Physico-Chemical Processes in Heterogeneous Porous Media and Its Application to Cement Paste". PhD thesis. Gent University, 2016, p. 275. ISBN: 9789085788867.

[Pat16b] R. A. Patel, Q. T. Phung, S. C. Seetharam, J. Perko, D. Jacques, N. Maes, G. De Schutter, G. Ye, and K. Van Breugel. "Diffusivity of saturated ordinary Portland cement-based materials: A critical review of experimental and analytical modelling approaches". In: *Cement and Concrete Research* 90 (2016), pp. 52–72.

[Pat17] R. A. Patel, J. Perko, and D. Jacques. "Yantra: A lattice Boltzmann method based simulation tool modelling physico-chemical processes in concrete at different..." In: August. 2017, pp. 2–4.

[Pat18a] R. A. Patel. *Yantra*. 2018. URL: `https://bitbucket.org/yantralbm/yantra`.

[Pat18b] R. A. Patel, J. Perko, D. Jacques, G. De Schutter, G. Ye, and K. Van Breugel. "A three-dimensional lattice Boltzmann method based reactive transport model to simulate changes in cement paste microstructure due to calcium leaching". In: *Construction and Building Materials* 166 (2018), pp. 158–170.

[Pat18c] R. A. Patel, J. Perko, D. Jacques, G. D. Schutter, G. Ye, and K. V. Bruegel. "Effective diffusivity of cement pastes from virtual microstructures: Role of gel porosity and capillary pore percolation". In: *Construction and Building Materials* 165 (2018), pp. 833–845.

[Pep54] R. Peppler and L. Wells. "The system of lime, alumina, and water from 50-degrees to 250-degrees C". In: *Journal of Research of the National Bureau of Standards* 52.2 (1954), p. 75.

[Per14] J. Perko and R. A. Patel. "Single-relaxation-time lattice Boltzmann scheme for advection-diffusion problems with large diffusion-coefficient heterogeneities and high-advection transport". In: *Physical Review E - Statistical, Nonlinear, and Soft Matter Physics* 89.5 (2014), pp. 1–9.

[Per15] D. A. Perumal and A. K. Dass. "A Review on the development of lattice Boltzmann computation of macro fluid flows and heat transfer". In: *Alexandria Engineering Journal* 54.4 (2015), pp. 955–971.

[Pha00] N. Phan-Thien and D. C. Pham. "Differential multiphase models for polydispersed spheroidal inclusions: Thermal conductivity and effective viscosity". In: *International Journal of Engineering Science* 38.1 (2000), pp. 73–88.

[Phu19] Q. T. Phung, N. Maes, E. Jacops, D. Jacques, G. De Schutter, and G. Ye. "Insights and issues on the correlation between diffusion and microstructure of saturated cement pastes". In: *Cement and Concrete Composites* 96 (Feb. 2019), pp. 106–117.

[Pig16] I. Pignatelli, A. Kumar, R. Alizadeh, Y. Le Pape, M. Bauchy, and G. Sant. "A dissolution-precipitation mechanism is at the origin of concrete creep in moist environments". In: *The Journal of Chemical Physics* 145.5 (2016), p. 054701.

[Pit73] K. S. Pitzer. "Thermodynamics of electrolytes. I. Theoretical basis and general equations". In: *Journal of Physical Chemistry* 77.2 (1973), pp. 268–277.

[Poo16a] J. Poonoosamy. "Dissolution-Precipitation in Porous Media: Experiments and Modelling." PhD thesis. Universität Bern, 2016.

[Poo16b] J. Poonoosamy, E. Curti, G. Kosakowski, D. Grolimund, L. R. Van Loon, and U. Mäder. "Barite precipitation following celestite dissolution in a porous medium: A SEM/BSE and µ-XRD/XRF study". In: *Geochimica et Cosmochimica Acta* 182.April (2016), pp. 131–144.

[Poo22a] J. Poonoosamy, R. Lu, M. I. Lönartz, G. Deissmann, D. Bosbach, and Y. Yang. "A Lab on a Chip Experiment for Upscaling Diffusivity of Evolving Porous Media". In: *Energies* 15.6 (2022), p. 2160.

[Poo22b] J. Poonoosamy, R. Lu, M. I. Lönartz, G. Deissmann, D. Bosbach, and Y. Yang. "A Lab on a Chip Experiment for Upscaling Diffusivity of Evolving Porous Media". In: *Energies* 15.6 (2022).

[Pop92] S. Popovics. *Concrete Materials: Properties, Specifications and Testing*. Second Edi. New Jersey: Noyes Publications, 1992, p. 661. ISBN: O-81.55-1308-9.

[Pra17] N. I. Prasianakis, E. Curti, G. Kosakowski, J. Poonoosamy, and S. V. Churakov. "Deciphering pore-level precipitation mechanisms". In: *Scientific Reports* 7.1 (Dec. 2017), p. 13765.

[Pri14] M. Prieto. "Nucleation and supersaturation in porous media (revisited)". In: *Mineralogical Magazine* 78.6 (2014), pp. 1437–1447.

[Pro10] H. Prommer and V. Post. *PHT3D: A Reactive Multicomponent Transport Model Henning Prommer & Vincent Post*. 2010. URL: `http://gmsdocs.aquaveo.com/PHT3D%7B%5C_%7Dmanual%7B%5C_%7Dv210.pdf`.

[Rid13] K. A. Riding, M. D. Thomas, and K. J. Folliard. "Apparent Diffusivity Model for Concrete Containing Supplementary Cementitious Materials". In: *ACI Materials Journal* 110.6 (2013), pp. 705–713.

[Rij05] L. A. Rijniers, H. P. Huinink, L. Pel, and K. Kopinga. "Experimental evidence of crystallization pressure inside porous media". In: *Physical Review Letters* 94.7 (2005), pp. 23–26.

[Rit11] F. Ritter, T. Boskamp, A. Homeyer, H. Laue, M. Schwier, F. Link, and H.-O. Peitgen. "Medical Image Analysis". In: *IEEE Pulse* 2.6 (2011), pp. 60–70.

[Šav16] B. Šavija and M. Luković. "Carbonation of cement paste: Understanding, challenges, and opportunities". In: *Construction and Building Materials* 117 (2016), pp. 285–301.

[Sch04] G. W. Scherer. "Stress from crystallization of salt". In: *Cement and Concrete Research* 34.9 (2004), pp. 1613–1624.

[Sch06] W. Schroeder, K. Martin, and B. Lorensen. *The Visualization Toolkit*. 4th ed. 2006. ISBN: 978-1-930934-19-1.

[Sch17] S. Schmieschek, L. Shamardin, S. Frijters, T. Krüger, U. D. Schiller, J. Harting, and P. V. Coveney. "LB3D: A parallel implementation of the Lattice-Boltzmann method for simulation of interacting amphiphilic fluids". In: *Computer Physics Communications* 217 (2017), pp. 149–161.

[Sch99] G. W. Scherer. "Crystallization in pores". In: *Cement and Concrete Research* 29.8 (1999), pp. 1347–1358.

[Sei17] N. Seigneur, E. L'Hôpital, A. Dauzères, J. Sammaljärvi, M. Voutilainen, P. E. Labeau, A. Dubus, and V. Detilleux. "Transport properties evolution of cement model system under degradation - Incorporation of a pore-scale approach into reactive transport modelling". In: *Physics and Chemistry of the Earth* 99 (2017), pp. 95–109.

[Sev19] I. Sevostianov, S. G. Mogilevskaya, and V. I. Kushch. "Maxwell's methodology of estimating effective properties: Alive and well". In: *International Journal of Engineering Science* 140 (2019), pp. 35–88.

[Sha09] H. Shao, S. V. Dmytrieva, O. Kolditz, D. A. Kulik, W. Pfingsten, and G. Kosakowski. "Modeling reactive transport in non-ideal aqueous-solid solution system". In: *Applied Geochemistry* 24.7 (2009), pp. 1287–1300.

[Söh82a] O. Söhnel and J. Mullin. "Precipitation of calcium carbonate". In: *Journal of Crystal Growth* 60.2 (1982), pp. 239–250.

[Söh82b] O. Söhnel. "Electrolyte crystal-aqueous solution interfacial tensions from crystallization data". In: *Journal of Crystal Growth* 57.1 (1982), pp. 101–108.

[Spa98] N. Spanos and P. G. Koutsoukos. "Kinetics of Precipitation of Calcium Carbonate in Alkaline pH at Constant Supersaturation. Spontaneous and Seeded Growth". In: *The Journal of Physical Chemistry B* 102.34 (1998), pp. 6679–6684.

[Sta22] V. Starchenko. "Pore-Scale Modeling of Mineral Growth and Nucleation in Reactive Flow". In: *Frontiers in Water* 3 (2022), pp. 1–13.

[Ste05a] C. I. Steefel, D. J. DePaolo, and P. C. Lichtner. "Reactive transport modeling: An essential tool and a new research approach for the Earth sciences". In: *Earth and Planetary Science Letters* 240 (2005), pp. 539–558.

[Ste05b] M. Steiger. "Crystal growth in porous materials - I: The crystallization pressure of large crystals". In: *Journal of Crystal Growth* 282 (2005), pp. 455–469.

[Ste09] C. I. Steefel. *CrunchFlow: User's manual*. Tech. rep. Lawrence Berkeley National Laboratory, 2009, p. 91.

[Ste15] C. I. Steefel, C. A. Appelo, B. Arora, D. Jacques, T. Kalbacher, O. Kolditz, V. Lagneau, P. C. Lichtner, K. U. Mayer, J. C. Meeussen, S. Molins, D. Moulton, H. Shao, J. Šimůnek, N. Spycher, S. B. Yabusaki, and G. T. Yeh. *Reactive transport codes for subsurface environmental simulation*. Vol. 19. 3. 2015, pp. 445–478. ISBN: 1059601494.

[Ste96] C. I. Steefel and K. T. B. Macquarrie. "Approaches to modeling of reactive transport in porous media". In: *Reviews Mineralogy* 34 (1996), pp. 83–125.

[Sto07] E. Stora. "Multi-scale modelling and simulations of the chemo-mechanical behavior of degraded cement-based materials". PhD thesis. Universite Paris-Est, 2007.

[Sto08] E. Stora, B. Bary, and Q. C. He. "On estimating the effective diffusive properties of hardened cement pastes". In: *Transport in Porous Media* 73.3 (2008), pp. 279–295.

[Sto09] E. Stora, B. Bary, Q.-C. He, E. Deville, and P. Montarnal. "Modelling and simulations of the chemo–mechanical behaviour of leached cement-based materials". In: *Cement and Concrete Research* 39.9 (2009), pp. 763–772.

[Suc01] S. Succi. *The Lattice Boltzmann Equation for fluid dynamics and beyond*. Oxford: Oxford University Press, 2001. ISBN: 9780199679249.

[Suk07] M. C. Sukop and D. T. J. Thorne. *Lattice Boltzmann Modeling - An Introduction for Geoscientists An Introduction Geoscientists and Engineers*. 2007. ISBN: 3-540-27981-4.

[Tay97] H. F. W. Taylor. *Cement chemistry*. London: Thomas Telford, 1997, p. 335. ISBN: 0-7277-3945-X.

[Ten00] P. D. Tennis and H. M. Jennings. "A model for two types of calcium silicate hydrate in the microstructure of Portland cement pastes". In: *Cement and Concrete Research* 30.6 (2000), pp. 855–863.

[Tho14] T. Thoenen, W. Hummel, U. Berner, and E. Curti. *The PSI/Nagra Chemical Thermodynamic Database 12/07*. Tech. rep. 04. Villigen: PSI - Laboratory for Waste Management, 2014.

[Tho99] J. J. Thomas, H. M. Jennings, and A. J. Allen. "The Surface Area of Hardened Cement Paste as Measured by Various Techniques". In: *Concrete Science and Engineering* 1.March (1999), pp. 45–64.

[Tor02] S. Torquato. *Random Heterogeneous Materials*. Vol. 16. Interdisciplinary Applied Mathematics. New York, NY: Springer New York, 2002. ISBN: 978-1-4757-6357-7.

[Tri16] P. Trinchero, J. Molinero, G. Deissmann, U. Svensson, B. Gylling, H. Ebrahimi, G. Hammond, D. Bosbach, and I. Puigdomenech. "Implications of Grain-Scale Mineralogical Heterogeneity for Radionuclide Transport in Fractured Media". In: *Transport in Porous Media* (2016).

[Ulm04] F.-J. Ulm, G. Constantinides, and F. H. Heukamp. "Is concrete a poromechanics materials?—A multiscale investigation of poroelastic properties". In: *Materials and Structures* 37.1 (2004), pp. 43–58.

[Van10] M. Vandamme, F.-J. Ulm, and P. Fonollosa. "Nanogranular packing of C-S-H at substochiometric conditions". In: *Cement and Concrete Research* 40.1 (2010), pp. 14–26.

[Vas18] R. Vasconcelos, B. Walkley, N. Hyatt, J. Provis, and C. Corkhill. "The physico-chemical evolution of a low-pH cement in contact with groundwater". In: *Proceedings of the Third Annual Workshop of the HORIZON 2020 CEBAMA Project*. 2018.

[Vas20] R. G. Vasconcelos, B. Walkley, S. Day, C. C. Tang, H. Paraskevoulakos, L. J. Gardner, and C. L. Corkhill. "18-month hydration of a low-pH cement for geological disposal of radioactive waste: The Cebama reference cement". In: *Applied Geochemistry* 116.October 2019 (2020), p. 104536.

[Veh17] T. Vehmas, A. Schnidler, M. Löija, M. Leivo, and E. Holt. "Reference mix design and castings for low-pH concrete for nuclear waste repositories". In: *Proceedings of the First Annual Workshop of the HORIZON 2020 CEBAMA Project*. KIT Scientific Publishing, 2017.

[Ver92] D. Verdoes, D. Kashchiev, and G. M. van Rosmalen. "Determination of nucleation and growth rates from induction times in seeded and unseeded precipitation of calcium carbonate". In: *Journal of Crystal Growth* 118.3-4 (1992), pp. 401–413.

[Vik14] A. Vikhansky and I. Ginzburg. "Taylor dispersion in heterogeneous porous media: Extended method of moments, theory, and modelling with two-relaxation-times lattice Boltzmann scheme". In: *Physics of Fluids* 26.2 (2014).

[Wal09] S. D. C. Walsh, H. Burwinkle, and M. O. Saar. "A new partial-bounceback lattice-Boltzmann method for fluid flow through heterogeneous media". In: *Computers and Geosciences* 35.6 (2009), pp. 1186–1193.

[Wal16] C. S. Walker, S. Sutou, C. Oda, M. Mihara, and A. Honda. "Calcium silicate hydrate (C-S-H) gel solubility data and a discrete solid phase model at 25 °C based on two binary non-ideal solid solutions". In: *Cement and Concrete Research* 79 (2016), pp. 1–30.

[Wit15] T. Witelski and M. Bowen. *Methods of Mathematical Modelling*. Springer Undergraduate Mathematics Series. Cham: Springer International Publishing, 2015. ISBN: 978-3-319-23041-2.

[Wol05] D. A. Wolf-Gladrow. *Lattice-Gas Cellular Automata and Lattice Boltzmann Models - An Introduction*. Berlin: Springer, 2005. ISBN: 3540669736.

[Wor01] E. Worrell, L. Price, N. Martin, C. Hendriks, and L. O. Meida. "Carbon Dioxide Emissions from the Global Cement Industry". In: *Annual Review of Energy and the Environment* 26.1 (2001), pp. 303–329.

[Yan14] X. Yang, B. Shi, Z. Chai, and Z. Guo. "A coupled lattice Boltzmann method to solve Nernst-Planck model for simulating electro-osmotic flows". In: *Journal of Scientific Computing* 61.1 (2014), pp. 222–238.

[Yoo15] H. Yoon, Q. Kang, and A. J. Valocchi. "Lattice Boltzmann-Based Approaches for Pore-Scale Reactive Transport". In: *Reviews in Mineralogy and Geochemistry* 80 (2015), pp. 393–431.

[Yu10] D. Yu and A. J. C. Ladd. "A numerical simulation method for dissolution in porous and fractured media". In: *Journal of Computational Physics* 229.18 (2010), pp. 6450–6465.

[Zem02] V. D. Zementwerke. *Zement Taschenbuch*. 50. Ausgab. Düsseldorf: Verlag Bau+Technik, 2002. ISBN: 3-7640-427-4.

[Zie13] O. Zienkiewicz, R. L. Taylor, and J. Zhu. *The Finite Element Method: Its Basis and Fundamentals*. 7th. Oxford, Butterworth-Heinemann, 2013, p. 753. ISBN: 978-1-85617-633-0.

Appendices

A Chapman-Enscog multi-scale expansion

The detailed derivations about the application of expansion techniques on the Lattice-Boltzmann method used here are scattered among different text books and publications [Che98,Heu10,Moh11,Pat16a,Suc01,Wol05]. Thus, the derivation is compiled here in a consistent nomenclature to improve readability and to allow the reader to understand implications and origins of various mathematical constraining effects.

A.1 Taylor series approximation of the Lattice-Boltzmann equation

As first step, the LHS term of the Lattice-Boltzmann equation 3.35 ($f_i(\vec{x}+\Delta\vec{x}, t+\Delta t)$) is expanded by a Taylor series:

$$f_i(\vec{x}+\Delta\vec{x}, t+\Delta t) = f_i(\vec{x}, t) + \sum_{n=1}^{\infty} \frac{1}{n!} \left(\frac{\partial}{\partial t} + \frac{\partial}{\partial x}\vec{e_i} \right)^n f_i(\vec{x}, t) \tag{A.1}$$

As given by the definition of the Taylor series, the term with order zero is just the function itself which is represented as first term. Each further term in the sum contains partial derivatives of the particle distribution function f_i with respect to time and space, respectively. The terms up to second order are expressed as:

$$f^{(0)} = f_i(\vec{x}, t) \tag{A.2}$$

$$f^{(1)} = \left(\frac{\partial}{\partial t} + \frac{\partial}{\partial x}\vec{e_i} \right) f_i(\vec{x}, t) \tag{A.3}$$

$$f^{(2)} = \frac{1}{2} \left(\frac{\partial^2}{\partial t^2} + 2\frac{\partial^2}{\partial t \partial x} + \frac{\partial^2}{\partial x^2}\vec{e_i}\vec{e_i} \right) f_i(\vec{x}, t) \tag{A.4}$$

Equalizing equation A.1 to the BGK Lattice-Boltzmann equation 3.37 and rearranging yields:

$$\sum_{n=1}^{\infty} \frac{1}{n!} \left(\frac{\partial}{\partial t} + \frac{\partial}{\partial x}\vec{e_i} \right)^n f_i(\vec{x}, t) = \frac{1}{\tau} \left(f_i^{eq}(\vec{x}, t) - f_i(\vec{x}, t) \right) \tag{A.5}$$

It is obvious that the first order term $f^{(1)}$ has canceled out.

A.2 Multi-scale expansion

As next step, the velocity distribution function is approximated by an asymptotic series, which is assumed as perturbation around the equilibrium state $f^{(0)}$ [Suc01, pp.11]:

$$f_i = f_i^{(0)} + \epsilon f_i^{(1)} + \epsilon^2 f_i^{(2)} + ... \tag{A.6}$$

with ϵ related to the Knudsen number, which is a small factor characterizing the deviation of the terms around the equilibrium. The assumption made in the Chapman-Enscog expansion is that $\epsilon < 1$. The indicated exponents are referring to the order of perturbation, thus, the effect to the distribution function decreases with increasing order. The ϵ factor and its exponent allows to keep track of the order of various terms and is used as a kind of label during the derivation. At the final result the factor is set to one [Wol05, p.146]. Similarly, the derivatives with respect to space and time are approximated:

$$\frac{\partial}{\partial x} = \epsilon \frac{\partial}{\partial x_1} + O(\epsilon^2) \tag{A.7}$$

$$\frac{\partial}{\partial t} = \epsilon \frac{\partial}{\partial t_1} + \epsilon^2 \frac{\partial}{\partial t_2} + O(\epsilon^3) \tag{A.8}$$

In equations A.7 and A.8, the O term is the sum of the truncated terms. Essentially, the time derivative is split into two scales in order to analyze slow and fast processes separately. Subsequently, the expanded derivatives are plugged into the Taylor-expanded Lattice-Boltzmann equation A.5. At the same time, terms with a higher order than two are neglected. For simplification $f_i(\vec{x}, t)$ is now short-cut as f_i:

$$\epsilon \frac{\partial f_i}{\partial t_1} + \epsilon^2 \frac{\partial f_i}{\partial t_2} + \epsilon \frac{\partial f_i}{\partial x_1} \vec{e_i} + \frac{1}{2} \epsilon^2 \left(\frac{\partial^2 f_i}{\partial t_1^2} + 2 \frac{\partial^2 f_i}{\partial t_1 \partial x_1} + \frac{\partial^2 f_i}{\partial x_1^2} \vec{e_i} \vec{e_i} \right) = \frac{1}{\tau} \left(f_i^{eq} - f_i \right) \tag{A.9}$$

In this step, the expansion for f_i was not yet substituted. For further derivations only the zeroth order terms are collected, i.e. only terms with the factor $\epsilon^0 = 1$, which are actually terms without any epsilon present:

$$O(\epsilon^0) : \frac{1}{\tau} \left(f_i^{eq} - f_i \right) = 0 \tag{A.10}$$

From this equation it is deducible that the equilibrium function must be the same as the zeroth order value, i.e. $f_i^{eq} = f_i^{(0)}$. Additionally, it is constrained that the sum of all equilibrium values is equal to the density/concentration, thus the sum of higher order terms are deduced as zero. Moreover, for the sake of readability, in the following in this section the sum notation $\sum_{i=0}^{q}$ for the microscopic Lattice-Boltzmann velocities is short-cut to $\sum$:

$$\sum f_i^{(1)} = \sum f_i^{(2)} = 0 \tag{A.11}$$

Another deduction from this is that the collision operator in the Lattice-Boltzmann equation must conserve macroscopic properties as concentration or momentum locally

during the collision process. Thus:

$$\sum \Omega_i = 0 \tag{A.12}$$

Effectively, this means that during collision only the distribution of the non-equilibrium fraction f_i^{neq} will change:

$$f_i = f_i^{eq} + f_i^{neq} \tag{A.13}$$

To continue the expansion procedure f_i is substituted by equation A.6 up to second order, while f_i^{eq} is replaced by $f_i^{(0)}$:

$$\begin{aligned}
&\epsilon\frac{\partial f_i^{(0)}}{\partial t_1}+\epsilon^2\frac{\partial f_i^{(1)}}{\partial t_1}+\epsilon^3\frac{\partial f_i^{(2)}}{\partial t_1}\\
&+\epsilon^2\frac{\partial f_i^{(0)}}{\partial t_2}+\epsilon^3\frac{\partial f_i^{(1)}}{\partial t_2}+\epsilon^4\frac{\partial f_i^{(2)}}{\partial t_2}\\
&+\epsilon\frac{\partial f_i^{(0)}}{\partial x_1}\vec{e_i}+\epsilon^2\frac{\partial f_i^{(1)}}{\partial x_1}\vec{e_i}+\epsilon^3\frac{\partial f_i^{(2)}}{\partial x_1}\vec{e_i}\\
&+\frac{1}{2}\epsilon^2\left(\frac{\partial^2 f_i^{(0)}}{\partial t_1^2}+\epsilon\frac{\partial^2 f_i^{(1)}}{\partial t_1^2}+\epsilon^2\frac{\partial^2 f_i^{(2)}}{\partial t_1^2}\right.\\
&+2\left(\frac{\partial^2 f_i^{(0)}}{\partial t_1\partial x_1}+\epsilon\frac{\partial^2 f_i^{(1)}}{\partial t_1\partial x_1}+\epsilon^2\frac{\partial^2 f_i^{(2)}}{\partial t_1\partial x_1}\right)\vec{e_i}\\
&\left.+\left(\frac{\partial^2 f_i^{(0)}}{\partial x_1^2}+\epsilon\frac{\partial^2 f_i^{(1)}}{\partial x_1^2}+\epsilon^2\frac{\partial^2 f_i^{(2)}}{\partial x_1^2}\right)\vec{e_i}\vec{e_i}\right)\\
&=-\frac{1}{\tau}\left(\epsilon f_i^{(1)}+\epsilon^2 f_i^{(2)}\right)
\end{aligned} \tag{A.14}$$

For simplification all terms above second order are neglected:

$$\begin{aligned}
&\epsilon\frac{\partial f_i^{(0)}}{\partial t_1}+\epsilon^2\frac{\partial f_i^{(1)}}{\partial t_1}+\epsilon^2\frac{\partial f_i^{(0)}}{\partial t_2}+\epsilon\frac{\partial f_i^{(0)}}{\partial x_1}\vec{e_i}+\epsilon^2\frac{\partial f_i^{(1)}}{\partial x_1}\vec{e_i}\\
&\quad+\frac{1}{2}\epsilon^2\left(\frac{\partial^2 f_i^{(0)}}{\partial t_1^2}+2\frac{\partial^2 f_i^{(0)}}{\partial t_1\partial x_1}\vec{e_i}+\frac{\partial^2 f_i^{(0)}}{\partial x_1^2}\vec{e_i}\vec{e_i}\right)=-\frac{1}{\tau}\left(\epsilon f_i^{(1)}+\epsilon^2 f_i^{(2)}\right)
\end{aligned} \tag{A.15}$$

Subsequently, the terms of the equations are sorted by the order, i.e. only the terms with the same exponent in ϵ are selected:

$$O(\epsilon^1): \frac{\partial f_i^{(0)}}{\partial t_1}+\frac{\partial f_i^{(0)}}{\partial x_1}\vec{e_i}=-\frac{1}{\tau}f_i^{(1)} \tag{A.16}$$

$$O(\epsilon^2): \frac{\partial f_i^{(1)}}{\partial t_1}+\frac{\partial f_i^{(0)}}{\partial t_2}+\frac{\partial f_i^{(1)}}{\partial x_1}\vec{e_i}+\frac{1}{2}\left(\frac{\partial^2 f_i^{(0)}}{\partial t_1^2}+2\frac{\partial^2 f_i^{(0)}}{\partial t_1\partial x_1}\vec{e_i}+\frac{\partial^2 f_i^{(0)}}{\partial x_1^2}\vec{e_i}\vec{e_i}\right)=-\frac{1}{\tau}f_i^{(2)} \tag{A.17}$$

Summing up for all velocity distributions f_i of the first order equation gives the first order moment, yielding the form:

$$\sum \frac{\partial f_i^{(0)}}{\partial t_1} + \sum \frac{\partial f_i^{(0)}}{\partial x_1} \vec{e_i} = -\frac{1}{\tau} \sum f_i^{(1)} \tag{A.18}$$

Higher order sums are constrained as $\sum f_i^{(1)} = 0$, thus:

$$\frac{\partial \sum f_i^{(0)}}{\partial t_1} = -\frac{\partial \sum f_i^{(0)} \vec{e_i}}{\partial x_1} \tag{A.19}$$

For equation A.19 it has to be noted that the relation shows an interesting property. Namely, the sums of the spatial and temporal derivatives have the same but negated value. As explained in the derivation above it was defined that $\sum f_i^{(0)} = c$ and $\sum f_i^{(0)} \vec{e_i} = cu$, therefore:

$$\frac{\partial c}{\partial t_1} + \frac{\partial cu}{\partial x_1} = 0 \tag{A.20}$$

Since $cu = j$, i.e. the flux, the differential form of the continuity equation of advection is recovered, which is essentially a mass conservation law:

$$\frac{\partial c}{\partial t} + \frac{\partial j}{\partial x} = 0 \tag{A.21}$$

It is interesting to note, that the time derivative with t_1 shows up in the final equation. This means, that the first term of the time expansion has been resurfaced in the fast process of advection (cf. equation A.8).

A.3 Recast equation to zeroth order

As next step, it will be shown that also the diffusive continuum equation is captured with the Lattice-Boltzmann equation. First, equation A.16 is solved for $f_i^{(0)}$:

$$-\tau \frac{\partial f_i^{(0)}}{\partial t_1} - \tau \frac{\partial f_i^{(0)}}{\partial x_1} \vec{e_i} = f_i^{(1)} \tag{A.22}$$

It is important to recast the equation for $O(\epsilon^2)$ with respect to $f_i^{(0)}$. This is performed by substituting equation A.22 into equation A.17.

$$\begin{aligned} -\tau \frac{\partial^2 f_i^{(0)}}{\partial t_1^2} - \tau \frac{\partial^2 f_i^{(0)}}{\partial x_1 \partial t_1} \vec{e_i} - \tau \frac{\partial^2 f_i^{(0)}}{\partial t_1 \partial x_1} \vec{e_i} - \tau \frac{\partial^2 f_i^{(0)}}{\partial x_1^2} \vec{e_i} \vec{e_i} \\ + \frac{\partial f_i^{(0)}}{\partial t_2} + \frac{1}{2} \frac{\partial^2 f_i^{(0)}}{\partial t_1^2} + \frac{\partial^2 f_i^{(0)}}{\partial t_1 \partial x_1} \vec{e_i} + \frac{1}{2} \frac{\partial^2 f_i^{(0)}}{\partial x_1^2} \vec{e_i} \vec{e_i} = -\frac{1}{\tau} f_i^{(2)} \end{aligned} \tag{A.23}$$

Grouping similar terms and simplifying gives:

$$\frac{\partial f_i^{(0)}}{\partial t_2} + \left(\frac{1}{2} - \tau\right) \frac{\partial^2 f_i^{(0)}}{\partial t_1^2} + \left(\frac{1}{2} - \tau\right) \frac{\partial^2 f_i^{(0)} \vec{e_i} \vec{e_i}}{\partial x_1^2} + (1 - 2\tau) \frac{\partial^2 f_i^{(0)} \vec{e_i}}{\partial t_1 \partial x_1} = -\frac{1}{\tau} f_i^{(2)} \quad \text{(A.24)}$$

Taking zeroth moment, i.e. summing all terms for each velocity vector i, leads to:

$$\frac{\partial \sum f_i^{(0)}}{\partial t_2} + \left(\frac{1}{2} - \tau\right) \frac{\partial^2 \sum f_i^{(0)}}{\partial t_1^2} + \left(\frac{1}{2} - \tau\right) \frac{\partial^2 \sum f_i^{(0)} \vec{e_i} \vec{e_i}}{\partial x_1^2} + (1 - 2\tau) \frac{\partial^2 \sum f_i^{(0)} \vec{e_i}}{\partial t_1 \partial x_1} = -\frac{1}{\tau} \sum f_i^{(2)} \quad \text{(A.25)}$$

There are five types of sums in equation A.25. In order to reduce the number of terms, the second summation term can be recast into a mixed derivative with help of equation A.19:

$$\frac{\partial^2 \sum f_i^{(0)}}{\partial t_1^2} = \frac{\partial}{\partial t_1} \left(\frac{\partial \sum f_i^{(0)}}{\partial t_1} \right) = \frac{\partial}{\partial t_1} \left(-\frac{\partial \sum f_i^{(0)} \vec{e_i}}{\partial x_1} \right) = -\frac{\partial^2 \sum f_i^{(0)}}{\partial t_1 \partial x_1} \quad \text{(A.26)}$$

After substituting into equation A.25 and rearrangement, the equation has simplified to four terms:

$$\frac{\partial \sum f_i^{(0)}}{\partial t_2} + \left(\frac{1}{2} - \tau\right) \frac{\partial^2 \sum f_i^{(0)} \vec{e_i}}{\partial t_1 \partial x_1} + \left(\frac{1}{2} - \tau\right) \frac{\partial^2 \sum f_i^{(0)} \vec{e_i} \vec{e_i}}{\partial x_1^2} = -\frac{1}{\tau} \sum f_i^{(2)} \quad \text{(A.27)}$$

In the following each sum term in equation A.27 will be determined. While the non-zero order term on RHS (fourth term) of A.27 evaluates directly to zero (see A.11), the other terms have to be filled with relations from constraints or derived elsewhere.

A.4 Derivation of sum terms

It is important to recover the right moments out of the separated time scales, i.e. the derivative with ∂t_1 is not the same as ∂t_2. However, the time scales can be converted to the total time derivative again. Following relation is true for the first term:

$$\frac{\partial \sum f_i^{(0)}}{\partial t_2} = \frac{\partial c}{\partial t_2} \quad \text{(A.28)}$$

For finding a definition for $\frac{\partial c}{\partial t_2}$, equation A.8 is rearranged to the t_2 scale

$$\frac{\partial c}{\partial t_2} = \frac{1}{\epsilon^2} \frac{\partial c}{\partial t} - \frac{1}{\epsilon} \frac{\partial c}{\partial t_1} \quad \text{(A.29)}$$

Now substituting the $\frac{\partial c}{\partial t_1}$ term with equation A.19 and using the scale conversion of equation A.7 yields to a definition of the first term in equation A.27:

$$\frac{\partial \sum f_i^{(0)}}{\partial t_2} = \frac{\partial c}{\partial t_2} = \frac{1}{\epsilon^2}\frac{\partial c}{\partial t} + \frac{1}{\epsilon^2}\frac{\partial cu}{\partial x} = \frac{1}{\epsilon^2}\left(\frac{\partial c}{\partial t} + \frac{\partial cu}{\partial x}\right) \tag{A.30}$$

Also, the sum of the mixed derivative (second) term on LHS in equation A.27 needs to be defined. Since $\sum f_i \vec{e_i} = c\,u$ and with help of the product rule the mixed derivative term can be expressed as:

$$\frac{\partial^2 \sum f_i \vec{e_i}}{\partial t_1 \partial x_1} = \frac{\partial}{\partial x_1}\left(c\frac{\partial u}{\partial t_1} + u\frac{\partial c}{\partial t_1}\right) \tag{A.31}$$

Assuming an incompressible fluid, i.e. the advective velocity does not change with time $\left(\frac{\partial u}{\partial t} = 0\right)$, this is simplified to:

$$\frac{\partial^2 \sum f_i \vec{e_i}}{\partial t_1 \partial x_1} = \frac{\partial}{\partial x_1}\left(u\frac{\partial c}{\partial t_1}\right) \tag{A.32}$$

Since an incompressible fluid is assumed, i.e. $\frac{\partial u}{\partial x} = 0$, by further application of the derivative product rule and using equation A.7, it takes the form:

$$\frac{\partial^2 \sum f_i \vec{e_i}}{\partial t_1 \partial x_1} = -\frac{1}{\epsilon^2} u \cdot u \frac{\partial^2 c}{\partial x^2} \tag{A.33}$$

Finally, the third summation term with the second derivative with respect to space in equation A.27 is defined by the type of lattice and equilibrium function used. For sake of simplification, here a linear equilibrium function and an orthogonal lattice type is chosen. Thus, the moment is defined as [Wol05, pp.165] [Mat10]:

$$\frac{\partial^2 \sum f_i^{(0)} \vec{e_i} \vec{e_i}}{\partial x_1^2} = \frac{\partial^2 c}{\partial x^2} e_s^2 \tag{A.34}$$

A.5 Reinserting terms

All four terms derived are inserted into equation A.27, while setting ϵ to unity yields:

$$\frac{\partial c}{\partial t} + \frac{\partial cu}{\partial x} + \left(\frac{1}{2} - \tau\right) u \cdot u \frac{\partial^2 c}{\partial x^2} + \left(\frac{1}{2} - \tau\right) \frac{\partial^2 c}{\partial x^2} e_s^2 = 0 \tag{A.35}$$

Notice that the time scales are again transformed into the ordinary t variable, since ϵ was also substituted back to a value of one. Another rearrangement leads to the form:

$$\frac{\partial c}{\partial t} + \frac{\partial cu}{\partial x} = e_s^2 \left(\tau - \frac{1}{2}\right) \frac{\partial^2 c}{\partial x^2} + \left(\tau - \frac{1}{2}\right) u \cdot u \frac{\partial^2 c}{\partial x^2} \tag{A.36}$$

B Derivation of the geometrical factor for nucleation theory

The classical nucleation theory assumes that a microscopic nucleus is formed as a droplet within the matrix of another phase. Thus, the free energy ΔG of this droplet of arbitrary shape can be written as:

$$\Delta G = V\Delta g + A\sigma \tag{B.1}$$

The volume term is always negative since Δg_v is negative, i.e. energy is released, while the surface term is incorporating the surface tensions σ and is therefore always consuming energy, thus positive. Assuming a spherical nucleus and inserting equations for volume and surface of a sphere yields:

$$\Delta G_s = \frac{4}{3}\pi r^3 \Delta g + 4\pi r^2 \sigma \tag{B.2}$$

Equation B.2 is plotted in figure B.1. The maximum energy barrier is determined by finding the local maximum of the function by differentiation with respect to r and setting to zero:

$$\frac{\partial \Delta G_s}{\partial r} = 4\pi r^2 \Delta g + 8\pi r\sigma = 0 \tag{B.3}$$

Solving for r gives the critical radius r_c:

$$r_c = -2\frac{\sigma}{\Delta g} \tag{B.4}$$

Inserting r_c back into equation B.1 and simplifying yields the maximum energy barrier value:

$$\Delta G_s^{max} = \frac{16\pi}{3}\frac{\sigma^3}{\Delta g} = \beta_s \frac{\sigma^3}{\Delta g} \tag{B.5}$$

Inserting equations for a cubical nucleus with the edge length of a into equation B.1 leads to:

$$\Delta G_c = a^3 r^3 \Delta g + 6a^2\sigma \tag{B.6}$$

In analogy to the derivation for the spherical cluster differentiating with respect to a and setting equal to zero:

$$\frac{\partial \Delta G_c}{\partial a} = 3a^2 \Delta g + 12a\sigma = 0 \tag{B.7}$$

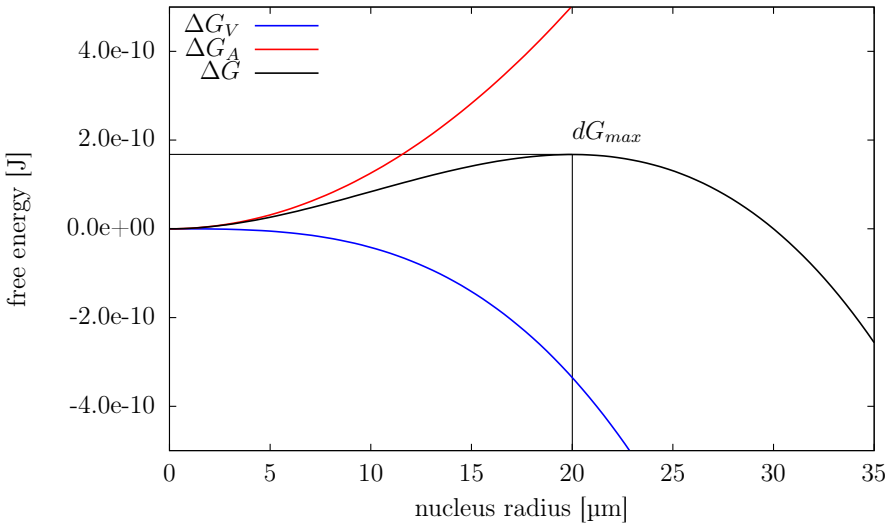

Figure B.1: Energy of a spherical nucleus in dependency of its radius. The total energy ΔG is the sum of the volume energy ΔG_V and the surface energy ΔG_A.

and solving for a yields:

$$a = -4\frac{\sigma}{\Delta g} \tag{B.8}$$

inserting into equation B.6 and simplifying yields the maximum energy barrier of a cubical nucleus which reduces to:

$$\Delta G_c^{max} = 32\frac{\sigma^3}{\Delta g} = \beta_c\frac{\sigma^3}{\Delta g} \tag{B.9}$$

Comparing equations B.5 and B.9:

$$\frac{\Delta G_c^{max}}{\Delta G_s^{max}} = \frac{32\frac{\sigma^3}{\Delta g}}{\frac{16\pi}{3}\frac{\sigma^3}{\Delta g}} = \frac{6}{\pi} \tag{B.10}$$

Accordingly, the energy barrier for a cubical cluster is higher by a factor of $6/\pi$ compared to a spherical one, assuming that the surface tension is identical. This highlights the importance of assumptions regarding the shape of the nucleus when determining nucleation rates and surface tensions from induction time measurements.

C iPP JSON input format

The input files for the IPPIO module are formatted as JSON [Int17] (cf. section 4.4.4.2). Thus, in this section a commented example input file for iPP is shown. The input file depicted here corresponds to the pure equilibrium 2D model to simulate leaching of the low-pH HCP with granite water (cf. section 8.3.2).

```
{
    "maxIter": 10000,                // run for 10000 iterations
    "outputFrequency": 100,          // write output each 100 iteration
    "checkpointingFreq": 1000,       // save checkpoint each 1000 iterations
    // "checkpointingTime": 15,      // minutes calc time
    "diff_coef_reference": 2.2E-9,   // reference diffusion coefficient in m2/s
    "enable_chemistry": true,        // enable chemical equilibration
    "LBCollType": "PTRT",            // set the Lattice-Boltzmann collision
                                     // type vto porosity-TRT
    "tau_reference": 1.0,            // reference Lattice-Boltzmann relaxation time
    "porosity_reference": 1.0,       // reference porosity
    "porosity_low": 0.15,            // cut-off porosity at which nodes
                                     // are considered solid
    "chemistry_tolerance": 1.0E-2,   // run only chemistry equilibration if
                                     // relative concentration changed more than 1%
    "dimensions":
    {
        "dims": [ 251, 250],         // system size is 251 x 250 nodes
        "spatial_resolution": 3E-6, // one reaction cells size is 3 micro meter
        "offset": [ 0, 0],           // offset vector to lower left bottom achor point

        "boundary_conditions":
        {
            "periodic": [false, false], // no periodic boundaries

            // defines a boundary domain at the left which is named "outlet"
            "domains":
                [
                {
                    "name": "outlet",
                    "position": "left",
                    "range": [0, 249]   // define outlet to the total y-range
```

```
            }
        ],

        // defines a boundary condition at the domain named as "outlet"
        // condition is constant concentration with GraniteWater composition
        "diffusive":
            [
            {
                "domain": "outlet",
                "type": "constant",
                "composition": "GraniteWater"
            }
        ]
    }
},

// define thermodynamic database used by PhreeqC
"database": "ThermoChimie_PHREEQC_eDH_v9b0_USFD.dat",

// library extension to retrieve molar volumes of various phases
"database_extension": "molar_volumes.json",

// do not precipitate the following phases in equilibration
"phase_black_list":
    [
    "Dolomite",
    "Epsonite",
    "Fayalite",
    "Afwillite",
    "Anhydrite",
    "Anorthite",
    "Bassanite",
    "Corundum",
    "Foshagite",
    "Gyrolite",
    "Hematite",
    "Hillebrandite",
    "Jaffeite",
    "Jennite",
    "Kaolinite",
    "Okenite",
    "Tobermorite-11A",
    "Tobermorite-14A",
    // etc...
```

```
],

"porosity_model":
{
    "type": "TenJen",           // use the Tennis-Jennings porosity model
    "wc": 0.25,                 // water-to-cement ratio
    "degree_hydration": 0.85,   // degree of hydration as input for the TenJen mo

    "phases":                   // tell iPP which are the CSH phases
        [
        "CSH0.8",
        "CSH1.2",
        "CSH1.6"
    ]
},

"multiscale_func":
{
    "type": "degraded_CSH", // use the degraded CSH diffusivity model

    // diffusion coeffcient of calcium is used as basis
    "free_pore_diff_coef": 2.2E-9
},

// definition of initial compositions
"compositions":
    [
    {
        "name": "GraniteWater", // name of composition
        "temp": 40.0,           // temperature for equilibration
        "pH": 8.2,              // initial pH value
        "units": "mmol/kgw",    // solute concentration unit

        // array of element to concentration value
        "element_concentrations":
            [
            {"name": "Cl", "conc": 3.227 },
            {"name": "C", "conc": 0.86 },
            {"name": "K", "conc": 0.1 },
            {"name": "Na", "conc": 2.8 },
            {"name": "Ca", "conc": 0.5 },
            {"name": "Si", "conc": 0.2 },
            {"name": "S", "conc": 0.1 },
            {"name": "Mg", "conc": 0.2 }
```

```
        ]
    },

    {
        "name": "HydrationProducts",
        "temp": 40.0,
        "pH": 12.053,
        "units": "mol/kgw",

        "element_concentrations":
            [
            { "name": "Al", "conc": 0.00077257},
            { "name": "C", "conc": 0.00069991},
            { "name": "Ca", "conc": 0.00069051},
            { "name": "K", "conc": 0.74112},
            { "name": "Mg", "conc": 3.2518E-09},
            { "name": "Na", "conc": 0.2118},
            { "name": "S", "conc": 0.44446},
            { "name": "Si", "conc": 0.0046202}

        ],

        // amount of phases in mol/liter
        "phases":
            [
            { "name": "CSH0.8", "amount": 1.53877367935862},
            { "name": "CSH1.2", "amount": 6.77758859763773},
            { "name": "Ettringite", "amount": 0.047157753980212},
            { "name": "Calcite", "amount": 0.076913255296354},
            { "name": "Hydrotalcite", "amount": 0.17783117656133},
            { "name": "Stratlingite", "amount": 0.342349030848161}

        ],

        "inert_fraction" : 0.0283   // volume fraction of inert material
    },

    {
        "name": "PoreWater",
        "temp": 40.0,
        "pH": 12.053,
        "units": "mol/kgw",

        // same as hydration products
```

```
        "element_concentrations":
            [
            { "name": "Al", "conc": 0.00077257},
            { "name": "C", "conc": 0.00069991},
            { "name": "Ca", "conc": 0.00069051},
            { "name": "K", "conc": 0.74112},
            { "name": "Mg", "conc": 3.2518E-09},
            { "name": "Na", "conc": 0.2118},
            { "name": "S", "conc": 0.44446},
            { "name": "Si", "conc": 0.0046202}
        ]
    },

    {
        "name": "Inert",
        "units": "mol/kgw",
        "inert_fraction" : 1.0
    }
],

// mapping of the IDs in the geometrical description to compositions
"ID_mapping":
    [
    // usage:
    // {"CompositionName": ID },
    {"PoreWater": 0 },
    {"Inert": 1 },
    {"HydrationProducts": 2 },
    {"Inert": 3 },
    {"Inert": 4 },
    {"Inert": 5 },
    {"Inert": 6 },
    {"Inert": 9 }
],

// read the microstructure definition from an external file
"geometry":
{
    "dims": [ 250, 250],     // dimension of the input geometry
    "origin": [ 1, 0 ],      // shift array by one node towards +x

    // file to read for the geometry array
    "cemhyd_file": "input/slice_1013_square.geo"
},
```

```
    // define the results to write
    "results":
    {
        "results_arrays_enabled":
            [
            "concentrations",
            "phases",
            "porosity"
            "capillary_porosity",
            "diff_coef"
        ],

        // auxilliary output data retrieved from PhreeqC
        "aux_data":
            [
            // usage:
            // { "name_of_output_file": "phreeqc SELECTED_OUTPUT command" }
            { "pH": "pH" },
            { "SI": "saturation_indices Calcite" }
        ]
    }
}
```

List of Figures

List of Tables

Acknowledgment

Ich danke ganz herzlich Herrn Professor Dirk Bosbach mir die Möglichkeit gegeben zu haben, diese Doktorarbeit am Institut IEK-6 des Forschungszentrums Jülich anzufertigen. Herrn Professor Florian Wellmann danke ich für die Übernahme des Korreferats.

Insbesondere möchte ich mich bei Herrn Dr. Guido Deissmann (IEK-6) und Dr. Andres Idiart (Amphos21) für die Betreuung meiner Arbeit bedanken. Ohne die Unterstützung und stete Diskussionsbereitschaft wäre diese Arbeit nicht zustande gekommen.

Zudem danke ich Frau Prof. Claire Corkhill und Frau Dr. Rita Vasconcelos (beide University of Sheffield) für die Bereitstellung von experimentellen Daten, welche unter anderem die μ-XCT Volumendaten der behandelten Zementproben beinhalten.

Darüber hinaus will ich mich zum einen bei meinen Freunden und Kollegen Dr. Steve Lange, Dr. Christian Schreinemachers, Dr. Stephan Schneider, Dr. Klaus Biß, Murat Güngör, Fabian Kreft sowie auch bei allen anderen Kollegen des Instituts IEK-6 bedanken, die mich in dieser Zeit begleitet und unterstützt haben.

Danken möchte ich auch der Europäischen Kommission, da diese Arbeit unter der Zuwendungsvereinbarung Nr. 662147 (CEBAMA) im Rahmen der Horizon 2020 Programme co-finanziert wurde.

Band / Volume 645
Deployment of Fuel Cell Vehicles in Road Transport and the Expansion of the Hydrogen Refueling Station Network: 2024 Update
T. Grube; M. Rex (2024), iii, 26 pp
ISBN: 978-3-95806-786-8

Band / Volume 646
Modellgestützte Analyse treibhausgasneutraler Transformationsstrategien für Deutschland
T. F. Schöb (2024), XII, 228 pp
ISBN: 978-3-95806-789-9

Band / Volume 647
Future Distribution Grids Using Geo-Referenced Synthetic Network Topologies
A. Bandam (2024), ix, 237 pp
ISBN: 978-3-95806-790-5

Band / Volume 648
Multi-scenario, high-resolution Lagrangian transport modeling for the analysis of the Asian tropopause aerosol layer
J. H. Clemens (2024), 143 pp
ISBN: 978-3-95806-792-9

Band / Volume 649
Prospektive Lebenszyklusanalysen von Power-to-Gas-Optionen
J. C. Koj (2024), XVIII, 197 pp
ISBN: 978-3-95806-794-3

Band / Volume 650
Assimilation of groundwater level and cosmic-ray neutron sensor soil moisture measurements into integrated terrestrial system models for better predictions
F. Li (2024), xvii, 172 pp
ISBN: 978-3-95806-796-7

Band / Volume 651
Integration of a rib-channel design to improve air-side contacting in solid oxide cell (SOC) stacks
Y. S. Ayhan (2024), 82 pp
ISBN: 978-3-95806-797-4

Band / Volume 652
Modelling Secondary Circulation in Convective Boundary Layer Using Large Eddy Simulation
L. Zhang (2024), 84 pp
ISBN: 978-3-95806-799-8

Band / Volume 653
Optionen zur Umsetzung der Klimaschutzziele im Verkehrssektor
S. Kraus (2025), XI, 317 pp
ISBN: 978-3-95806-802-5

Band / Volume 654
Modellierung der flächendifferenzierten Grundwasserneubildung für Schleswig-Holstein im Beobachtungszeitraum 1961 – 2021 und für Klimaszenarien bis 2100
I. McNamara, B. Tetzlaff, F. Wendland, T. Wolters (2025), 191 pp
ISBN: 978-3-95806-803-2

Band / Volume 655
Entwicklung alternativer Brenngaselektroden für die Hochtemperatur-Elektrolyse
F. E. Winterhalder (2025), vii, 161 pp
ISBN: 978-3-95806-805-6

Band / Volume 656
Oxide-based All-Solid-State Batteries for and from Recycling Processes
V. M. Kiyek (2025), viii, 128 pp, xix
ISBN: 978-3-95806-806-3

Band / Volume 657
Investigation of current and future anthropogenic chemical regimes in simulation chamber experiments
M. Färber (2025), 213 pp
ISBN: 978-3-95806-809-4

Band / Volume 658
Dynamischer Betrieb von Polymer-Elektrolyt-Membran Wasserelektrolyseuren
E. Rauls (2025), XIV, 239 pp
ISBN: 978-3-95806-811-7

Band / Volume 659
Pore-scale reactive transport modeling in cementitious materials: Development and application of a high-performance computing code based on the Lattice-Boltzmann method
S. Rohmen (2025), X, 295 pp
ISBN: 978-3-95806-812-4

Weitere ***Schriften des Verlags im Forschungszentrum Jülich*** unter
http://wwwzb1.fz-juelich.de/verlagextern1/index.asp

Energie & Umwelt / Energy & Environment
Band / Volume 659
ISBN 978-3-95806-812-4

Mitglied der Helmholtz-Gemeinschaft

JÜLICH
Forschungszentrum